The University of Sheffield

Faculty of Engineering

Department of Mechanical Engineering

Wall-based feedback control of a compressible laminar boundary layer subjected to free-stream vortical disturbances

by

João Miguel da Rocha Pinto

Submitted in partial fulfilment of the requirements for the Doctor of Philosophy Degree in Mechanical Engineering of The University of Sheffield

September 2015

This thesis is dedicated to my wife, Elizabeth.

Abstract

This thesis presents theoretical and numerical results on the penetration of small amplitude free-stream vortical disturbances into a compressible laminar boundary layer, the formation and evolution of streamwise-elongated, low-frequency fluctuations inside the boundary layer and the wall-based feedback control of such disturbances.

The theoretical formulation of the low-frequency disturbances, also called laminar streaks or Klebanoff modes, builds upon the works of Leib, Wundrow & Goldstein [43], Ricco & Wu [58] and Ricco [56], and it is based on the compressible linearised unsteady boundary region equations. For the first time, the incompressible framework by Ricco [56] is extended to the compressible case. The initial and outer boundary conditions for the outer layer compressible disturbances are therefore derived and put into context of the compressible Klebanoff modes analysis by Ricco & Wu [58]. Numerical results on the boundary region equations for the compressible and incompressible cases are presented.

The general adjoint theory is presented and applied to the compressible linear unsteady boundary region equations for the first time. The theoretical formulation considers blowing and suction and wall thermal actuation to attenuate the Klebanoff modes. This further develops the works of Cathalifaud & Luchini [13] on spatial control for the incompressible linear boundary region equations and of Zuccher, Luchini & Bottaro [72] for the incompressible nonlinear boundary region equations. However, the previous studies were limited to the incompressible cases and neglected the free-stream turbulent forcing. Numerical solutions of the attenuated Klebanoff modes via an iterative feedback algorithm are presented, focusing on optimal wall-normal blowing suction.

Acknowledgements

My sincerest thanks to my supervisor, Dr Pierre Ricco for his continuous guidance through the mysterious and marvellous world of asymptotic analysis and fluid mechanics, and for believing in me and challenging me to achieve better. Without him I would not have been able to complete this thesis.

I would like to acknowledge Dr George Papadakis for his insightful suggestions, opinions and comments on this thesis. His guidance is much appreciated.

Thank you to Daniel Wise for always being there to debate and to explore ideas. For enjoyable chess games and valuable advice.

I would like to thank Sohrab Aghdam, for helping to revise the control framework used, the numerous discussions on mathematics and for his friendship.

For interesting discussions and insightful help, I am greatly indebted to Dr Peter Hicks.

I am much obliged to my brother, Pedro da Rocha Pinto, for his constant support and for being an inspiration. For enlightening discussions about mathematics and for his invaluable help with computing.

To my parents, Leonel and Olinda da Rocha Pinto, I owe my deepest gratitude for raising me to be where I am today. Their encouragement has helped me pursue my dreams.

I am most grateful to my wife, Elizabeth Chia, for her unconditional love, patience and understanding throughout this project, and also for proofreading my work.

Finally, I would like to express my appreciation to my family and friends, whose motivation and cheer push me to accomplish my goals.

Contents

1 Introduction **1**

1.1 Laminar regime and bypass transition within boundary layers . . . 3

1.1.1 Experiments . . . 3

1.1.2 Direct Numerical Simulations (DNS) . . . 7

1.1.3 Theory . . . 9

1.2 Adjoint-based methods applied to flow control . . . 13

1.2.1 Linear theory . . . 13

1.2.2 Optimal and robust control in the predictive control framework . . . 14

1.2.3 Temporal growth of laminar disturbances . . . 15

1.2.4 Spatial growth of laminar disturbances . . . 16

1.3 The objectives of the thesis . . . 19

2 Linear response of a compressible boundary layer to free-stream vortical disturbances **21**

2.1 Formulation: scaling and asymptotic structure of flow domain . . . 22

2.2 The mean compressible laminar boundary layer flow . . . 27

2.3 The linear boundary layer flow: region II . . . 29

2.3.1 The unsteady velocity and temperature perturbation flow . 29

2.4 The boundary region flow (region III) and the outer solution (region IV) . . . 32

2.4.1 Region IV: outer flow . . . 35

2.4.2 Outer boundary conditions 36
2.4.3 Upstream behaviour of the boundary region solution 39
2.5 Numerical procedures of the boundary region equations 43
2.6 Numerical solutions of the boundary region equations 47
2.6.1 Response of a two-dimensional free-stream gust 47
2.6.2 Response of a three-dimensional free-stream gust: the Klebanoff modes 50
2.6.3 Asymptotic solution 54
2.6.4 Free-stream turbulence effect 61

3 Wall-based feedback control using the adjoint method 63
3.1 The adjoint method 64
3.1.1 Derivation 65
3.2 Compressible linear unsteady boundary region adjoint 68
3.3 Numerical procedures for the control theory 79
3.4 Controlled numerical results 86
3.4.1 Attenuation parametric study and cost of actuation 86
3.4.2 Optimal wall-based feedback actuation of case 1 97
3.4.3 The effects of the measuring parameters 100
3.5 Alternative controlled numerical results 103

4 Summary and future work 105
4.1 Future work 106

Appendix A Power series solution of the CLUBR equations 117

Appendix B Expansion of adjoint identity 123

Appendix C Incompressible LUBR adjoint 131

Appendix D Alternative actuators for wall-based feedback control 137
D.1 Implementation of the alternative actuators 137

Chapter 1

Introduction

In mechanical, aeronautical, civil and naval engineering systems, it is common to encounter objects moving through fluids. From such interactions, a thin boundary layer forms near the surface, where viscous effects play a crucial role. A boundary layer may experience dynamically different states which can be broadly grouped into the laminar, transitional or fully-developed regimes. In the laminar flow, the fluid layers move parallel to one another without any large-scale, vortical mixing between them. The transitional regime occurs downstream of the laminar regime and is characterised by the breakdown of the laminar flow disturbances. Turbulent spots occur during transition, and, as they merge downstream, the fully-developed turbulent regime ensues. Turbulence displays a spectrum of spatial and temporal scales; it is chaotic in nature and strongly dissipative. Friction and heat transfer increase as the flow evolves from the laminar to the turbulent regime, leading to higher energy required to move an object through the fluid.

The effects of turbulence must be taken into account in wing design, as drag reduction is important for an efficient aircraft. The surface roughness and geometry can be altered to minimise drag. Laminar-turbulent breakdown may occur along the wing, which leads to enhanced drag between the wing and the fluid. Optimal conditions may be achieved by maintaining the laminar regime along the entire wing and fuselage. Therefore, it is of utmost importance to have knowledge of which regime governs the fluid flow.

In the literature, the free-stream disturbances are commonly termed free-stream turbulence (FST), and are usually characterised by the turbulence level Tu (i.e. the root-mean-square value of the velocity fluctuations) and turbulence length scales.

Laminar-turbulent breakdown is believed to result mainly from environmental perturbations affecting the boundary layer, which include the leading edge, surface roughness, pressure gradients, or disturbances coming from the free stream (e.g. acoustic, temperature and vortical fluctuations).

Although laminar-turbulent breakdown has been studied for over a century, the physical mechanisms are yet to be fully understood and it remains a challenge to determine where it occurs.

Dryden [18] discovered that the location of transition moves upstream as Tu increases. From numerous experiments, it is widely accepted that transition is initiated by the growth of Tollmien-Schlichting (TS) waves at a very low turbulence level (i.e. $Tu < 1\%$). As Tu increases, the TS growth rate and wavelength predicted by classical stability theory are altered [68]. At a relatively higher turbulence level (i.e. around $Tu > 5\%$), direct non-linear laminar-turbulent breakdown may occur without apparent involvement of TS waves. The breakdown due to medium-to-high levels of FST is also referred to as bypass transition. This term applies when the main mechanism responsible is not linked to the TS waves predicted by classical stability theory. [51].

A literature review of boundary-layer laminar-turbulent transition induced by free-stream disturbances and feedback flow control of shear flows is presented in chapter 1. The theoretical formulation for the response of a boundary layer subjected to free-stream small vortical disturbances based on the work of Leib, Wundrow & Goldstein [43], Ricco & Wu [58] and Ricco [56] is described and extended in chapter 2. Chapter 3 presents the general adjoint theory, and its application to the compressible boundary region equations is given in chapter 2.

1.1 Laminar regime and bypass transition within boundary layers

1.1.1 Experiments

A review of the literature shows that the first studies of transition in boundary layers under the influence of FST were carried out by Dryden [17] and Taylor [64]. They performed experimental studies on the flat-plate boundary layer at low speed and observed unsteady, streamwise-elongated streaks with spanwise alternatingly low and high streamwise fluctuations. The streamwise velocity fluctuations achieved amplitudes several times larger than those in the free stream. They suggested that these "breathing modes" preceded and caused transition. However, research on breathing modes was not pursued in the subsequent years because Schubauer & Skramstad [61] provided experimental evidence for Tollmien [65] and Schlichting's [60] linear stability theory. This led to the dominance of studies being performed with low levels of FST (i.e. $Tu < 1\%$) to study the existence of Tollmien-Schlichting (TS) waves. Several decades later, Klebanoff's [41] experiments confirmed and expanded Dryden's [17] and Taylor's [64] work. This instigated a renewed interest in the topic (Arnal & Juillen [4], Kendall [37][38][39] and Roach [59]).

Arnal & Juillen [4] obtained the first detailed measurements of a Blasius boundary layer subjected to FST using Tu above 1%, with the objective of investigating the mechanism leading to laminar breakdown. They confirmed that the main disturbances inside the boundary layer were caused by low frequency FST, which led to breathing modes instead of TS waves.

Before the laminar breakdown, the maximum streamwise velocity fluctuations occurred in the middle of the boundary layer, achieving amplitudes of up to $5-7\%$ of the streamwise mean velocity. TS waves reached maximum amplitudes close to the wall with a characteristic streamwise wavelength which was smaller than the one of the breathing modes [49]. They deduced that, even though TS waves

were present, low frequency fluctuations appeared to play the main role in the laminar-turbulent breakdown.

Using hot-wire anemometry and flow visualisation, Kendall [37] carried out further work on the pre-transitional laminar Blasius boundary layer subjected to low level FST generated by a grid upstream. The maximum streamwise velocity fluctuations were found to grow in linear proportion to the boundary layer thickness. He validated the occurrence of the breathing modes and renamed them Klebanoff modes.

Later, Kendall [38][39] studied the receptivity to very low grid-produced FST (i.e. $0.1\% \leq Tu \geq 0.2\%$) and confirmed that TS waves are developed in the Blasius boundary layer. The increase of velocity fluctuations led to turbulent spots further downstream. The effects of different surface roughness on the receptivity subjected to FST was investigated by covering the flat-plate surface with fine and rough sandpaper. The rough surface resulted in turbulent spots that led to turbulence upstream as compared to the fine surface [44].

Westin *et al.* [67] & Boiko *et al.* [9] performed experiments using hot-wire anemometry and smoke flow visualisation in a Blasius boundary layer in a wind tunnel with a turbulence level of below 0.02%. They used flat plates with streamwise lengths of 2.16m and 4.22m and streamwise free-stream velocities between 4ms^{-1} and 8ms^{-1}. A grid was placed 1.5m upstream of the leading edge point to obtain nearly isotropic FST with a 1.5% turbulence level [67]. The measurements were taken between 100mm and 1000mm downstream of the leading edge. To accomplish a uniform pressure gradient at the leading edge, they used two-dimensional potential flow theory to optimise the design of the leading edge together with a trailing edge flap to adjust the pressure stagnation line [67]. Turbulent spots were detected at 1000mm for a streamwise free-stream velocity of 8ms^{-1}, indicating the onset of transition [67]. After inserting a grid upstream, they obtained FST levels between 1.35% and 1.5% for the free-stream streamwise mean velocities of 4ms^{-1} to 8ms^{-1}, respectively. The boundary layer was perturbed by unsteady streaks elongated in the streamwise direction that grew

downstream both in length and amplitude (i.e. Klebanoff modes). The peak value of normalised root-mean-squared streamwise velocity fluctuations increased in linear proportion to the Reynolds number ($R = 1.72\sqrt{U_\infty x/\nu}$, where U_∞ is the free-stream velocity and ν is the kinematic viscosity). Furthermore, no relation was found between the amplitude of the perturbations and the onset of transition [67]. TS waves measurements were carried out during the same experiments. They demonstrated that it was possible to generate and measure TS waves within the boundary layer subjected to FST levels of at least 1.5%. The TS waves subjected to FST were similar to an undisturbed boundary layer by FST; however, the linear amplification rate decreased as FST increased [9].

Experimental studies using flow visualisation and hot-wire anemometry in the same low FST wind tunnel used by Westin *et al.* [67] & Boiko *et al.* [9] were performed by Matsubara & Alfredsson [49] to describe the Blasius boundary layer flow subjected to turbulence levels between 1.5% and 6.6%. Grids with round bars were placed 1.6m upstream of the leading edge to obtain turbulence levels of 1.5% and 2.2%. Another grid with square bars was used 1m upstream of the leading edge to produce the highest turbulence level ($Tu = 6.6\%$). All grids provided nearly homogeneous FST at the leading edge with free-stream velocities of up to 12ms^{-1} [49]. Through smoke flow visualisation, they observed the Klebanoff modes as well defined unsteady streaky structures. These are illustrated in figure 1.1 which displays turbulence levels of 6.6% and free-stream velocities of 2ms^{-1} and 3ms^{-1} for the left and right pictures respectively. The spanwise scale was reported to be close to 1cm. The smoke filled regions represent negative fluctuations of streamwise velocity while the darker regions correspond to positive fluctuations of streamwise velocity [49]. Their measurements confirmed that the spanwise dimensional scale is large compared to the boundary-layer thickness, while further downstream it approaches the boundary-layer thickness. Some streaks exhibited waviness in the streamwise direction that often grew into turbulent spots. These turbulent spots grew and merged, leading to a fully turbulent flow. The measurements showed that the initial growth of the streamwise velocity fluctuations is

proportional to the laminar boundary layer thickness, confirming previous results (e.g. Westin *et al.* [67]).

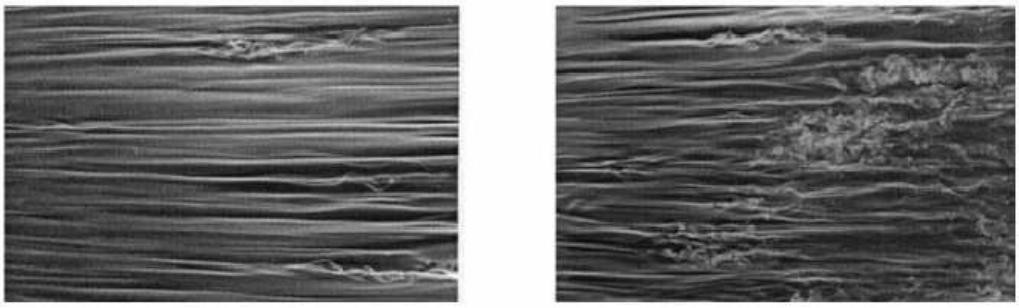

Figure 1.1: The flow direction is from left to right. In the left picture small turbulent spots are shown downstream. In the right picture turbulent spots appear upstream with full developed turbulence downstream. [49].

Fransson [20] used the same low wind tunnel to study the transitional flow exposed to grid-generated free stream turbulence levels from 1.4% to 6.7%. One of the grids was active; it had orifices that injected air jets into the stream, where different jet velocities were induced to increase the FST. As with previous results, the velocity fluctuations within the boundary layer experienced a slower growth close to the leading edge and faster growth downstream. This can be explained by the FST scales requiring some distance to adapt to the boundary layer growth [20]. The transitional Reynolds number was found to be inversely proportional to the square of the turbulence level. The non-dimensional length of the transitional region grew linearly with the transitional Reynolds number and possessed a minimum value for the turbulence levels measured [20]. Fransson concluded that for turbulence levels around or above 2.5%, the relative length of the transitional region increases with the turbulence level. The transitional Reynolds number was related to the turbulence level and the rate of the generated turbulent spots to describe the transitional region more accurately than in previous studies [20].

Similar studies were performed by Mans, Lange, & van Steenhoven [48]. They found that the propagation speed of unstable modes was around 80% of the free-stream streamwise velocity under uncontrolled conditions. Additionally, the

growth rate was about $0.01U_\infty/\delta$, where U_∞ and δ represent the free-stream streamwise mean velocity and the local boundary layer displacement thickness respectively.

Hernon, Walsh & McEligot [32] investigated bypass transition within the Blasius boundary layer subjected to Tu between 1.3% and 6%. They found that the peak of the streamwise velocity fluctuations within the low and high speed streaks shifted location as it approached the laminar-turbulence breakdown. The negative fluctuations moved towards the outer layer, while the positive fluctuations moved towards the wall.

1.1.2 Direct Numerical Simulations (DNS)

To better understand the phenomenon of laminar-turbulent breakdown subjected to FST, Jacobs & Durbin [35] conducted direct numerical simulations of the Blasius boundary layer subjected to FST. A rectangular box was used as the flow domain to study the flow downstream of the leading edge. The incompressible Navier-Stokes equations were solved using a fractional step algorithm. In order to emulate the grid-generated FST commonly used in the experiments, inflow conditions were set using a combination of the Orr-Sommerfeld modes and the Squire modes to model the oncoming isotropic turbulence. Because of these inlet conditions, the streamwise and transverse velocity contours displayed small scale motions near the inlet. The velocity fluctuations contours clearly show the Klebanoff modes and the downstream turbulent spots growing and merging to form fully-developed turbulent flow. These Klebanoff modes were created through the penetration of low frequency fluctuations into the boundary layer. The low velocity streaks eventually lifted to the outer layer and interacted with scales to form the turbulent spots. Jacobs & Durbin argued that the streamwise velocity streaks in the laminar and the turbulent regime might be related. However, it was also observed that the streaks present in the fully turbulent region are not the continuation of the laminar streaks.

Brandt, Schlatter & Henningson [10] also investigated the Blasius boundary

layer subjected to FST via DNS. They studied the relation between the FST integral length scale and the formation of boundary layer disturbances to elucidate the mechanism behind the boundary layer laminar-turbulent breakdown. They noticed that for similar turbulence levels, the transition onset happens further downstream for lower values of the FST integral length scale. They confirmed that the large scales originating from the FST managed to penetrate to the core of the Blasius boundary layer, thereby inducing Klebanoff modes, while small scales tended not to go beyond the outer layer. They also observed that the spanwise scale of the Klebanoff modes was only slightly affected by the FST characteristic scales.

A further DNS study was performed by Zaki & Durbin [71] to investigate bypass transition. Their approach was similar to the previous DNS studies described. They verified the penetration of the low and high frequency disturbances into the boundary layer by neglecting the pressure gradient and using only two modes as inlet flow, one of low and the other of high frequency. They found that the lower frequency mode penetrated the boundary layer and produced Klebanoff modes, while the high frequency mode strongly disturbed the lifted Klebanoff modes, leading to turbulent spots, which merged to generate the fully turbulent flow. To further assess the influence of the modes, they set a high frequency mode with the same amplitude while increasing the low frequency mode; the Klebanoff modes were observed to be more disturbed. When the amplitude of the high frequency mode was kept fixed and the one of the low frequency was decreased, they verified that the high frequencies may not lead to transition as the high frequency disturbance did not penetrate into the core of the boundary layer. They surmised that, for such an interaction, an amplitude threshold for the Klebanoff modes must be met, otherwise transition may be suppressed and occurs further downstream. Higher amplitude streaks were also simulated, leading to less stable Klebanoff modes.

Nagarajan, Lele & Ferziger [52] and Ovchinnikov, Choudhari & Piomelli [53] analysed bypass transition within the Blasius boundary layer via DNS. The lead-

ing edge was included in their simulations. An elliptic leading edge was considered throughout the simulations to investigate the role of the bluntness and integral scale of FST. They also found that for low Tu, the Klebanoff modes are connected to the transition downstream. Turbulent spots were detected without apparent relation to the Klebanoff modes for high values of FST intensity.

1.1.3 Theory

Experimental data and DNS revealed that low-frequency velocity perturbations had the highest penetration level within the Blasius boundary layer. The studies suggest that the Klebanoff modes play a key role for transition for medium-to-high levels of free-stream turbulence, i.e., for Tu between 1% and 6%, while TS waves have a dominant role for lower FST levels. Despite numerous experiments and simulations, the subject of laminar-turbulent breakdown preceded by the Klebanoff modes is yet to be fully understood, although theories have been developed to describe the early pre-transitional formation of streaks.

Nearly a century ago, Taylor [64] derived the first approximation of the mode shape to fit the experimental data, also used by Klebanoff [41]. It considered a perturbed boundary layer, where the streamwise velocity was related to the boundary layer thickness which varied in the spanwise direction. The Taylor expansion for small variations of the boundary layer thickness led to an initial profile of the streaks.

Crow [16] performed an asymptotic linear analysis of the Blasius boundary layer under a steady spanwise disturbance of an otherwise laminar uniform free stream. He obtained a model of the Blasius boundary layer that included streaks. Crow's model becomes invalid when the boundary layer thickness approaches the spanwise length scale, where the Blasius boundary layer is described by the boundary region equations [70]. The term boundary region equations was first introduced by Kemp [36], and they consist of the Navier-Stokes equations with the streamwise derivatives neglected in the viscous and pressure-gradient terms.

By using the linear theory for inviscid incompressible shear flows, Ellingsen

& Palm [19] and Landhal [42] demonstrated that the three-dimensional disturbances can grow at least linearly (algebraically) in time. Landhal showed that the streamwise velocity fluctuations grow algebraically in time to an infinite amplitude when a spanwise velocity remains present [42].

The Blasius boundary layer subjected to steady transversal velocity disturbances interacting nonlinearly to an otherwise uniform laminar free stream was investigated by Goldstein, Leib & Cowley [24]. Goldstein & Leib studied the same problem, but considered streamwise vortical disturbances to an otherwise uniform laminar free stream [23].

Luchini [45] studied a spatially developing Blasius boundary layer subjected to algebraic growth and described a three-dimensional mode of instability. He also suggested that the boundary layer instability was independent of the Reynolds number of the equivalent unperturbed flow because the phenomenon is described by Prandtl's boundary-layer equations.

Andersson, Berggren & Henningson [3] and Luchini [46] further developed the algebraic growth theory of Landhal [42] and Luchini [45] using the linearised boundary region equations to study the spatial growth of steady perturbations. They expanded it by using an iterative adjoint method to find the optimal disturbance that led to maximum perturbation downstream. The maximum perturbation amplification was found to have a null frequency.

A rigorous mathematical asymptotic approach was developed by Leib, Wundrow & Goldstein [43] (referred to hereinafter as LWG) to investigate the signature (i.e. the root-mean-square of the streamwise velocity fluctuation) of the FST within a Blasius boundary layer. The unsteady incompressible boundary region equations were used to obtain the velocity and the pressure fluctuations within the boundary layer. Rapid-distortion theory [21] was used to solve the inviscid flow above the leading edge, and weak turbulence was induced by superimposing FST on the uniform free stream. The FST disturbances were imposed on the boundary layer as a convected gust. The interaction between the boundary layer and the FST was accounted for by matching the boundary region equations

with the inviscid flow on the top of the boundary layer. The asymptotic analysis showed that the low-frequency transversal velocity fluctuations originating from the FST are the main factor for the production of Klebanoff modes. Isotropic turbulence and axisymmetric turbulence with low frequency was used in the simulations to reproduce experimental data. The linear theory was compared with the experimental measurement performed by Kendall using low frequency broadband anisotropic FST. It predicted values of the normalised root-mean-square streamwise velocity slightly below the experimental data, showing good agreement for the low-frequency range, i.e. between 0Hz and 4Hz. For the high frequencies comparison (4Hz to 8Hz), it predicted root-mean-square streamwise velocity with smaller amplitude as it evolves downstream. These differences may be linked to the nonlinear interactions, which are not taken into account by the linear theory.

Wundrow & Goldstein [69] investigated the Klebanoff modes near a finite thickness flat plate originated by small-amplitude streamwise velocity fluctuations imposed on the upstream mean flow. They used the incompressible nonlinear unsteady boundary-region equations. Their predictions showed that the spanwise gradient length scale drives the streamwise velocity perturbations. Initially, the streamwise velocity perturbations growth increases with decreasing spanwise length scale. Further downstream where the boundary-layer thickness becomes of the same order as the spanwise length scale, the growth trend is reversed because of the viscous effects. They suggested that the Klebanoff modes would ultimately run out of energy; this would occur when the spanwise length scale became too short if the viscous effects did not stop the growth of the streamwise velocity fluctuations. The balance of these mechanisms may help to explain whether the spanwise length scale is defined by the FST or by the boundary layer.

Wundrow & Goldstein [70] used the nonlinear boundary region equations to study the effects of small-amplitude, steady, streamwise vortices upstream of the Blasius boundary layer. Their results showed how initially linear perturbations evolve into small-amplitude nonlinear cross-flow far downstream of the leading

edge. They suggested that any cross-flow perturbation introduced within the boundary layer may develop Klebanoff modes because of the lift up mechanism. Ricco, Luo & Wu [57] expanded the LWG theory to the nonlinear case using the incompressible nonlinear unsteady boundary region equations to investigate the evolution and instability of Klebanoff modes subjected to free-stream vortical disturbances.

Most of the experiments, DNS and theoretical studies on Klebanoff modes were conducted for incompressible flows. However, the LWG theory was expanded to the compressible case by Ricco & Wu [58]. They investigated the penetration of low-frequency vortical free-stream disturbances into the boundary layer using the compressible linearised boundary region equations. They discovered that the low-frequency vortical disturbances penetrate the boundary layer to generate thermal streaks in addition to the Klebanoff modes. The temperature fluctuations induced by the FST may trigger a second instability that leads to laminar-turbulence breakdown. They reported that for a vortical disturbance with a comparatively large spanwise wavelength, the induced boundary-layer fluctuations eventually evolve into an amplifying wave because of a receptivity mechanism. The mechanism consists of a vortical disturbance which excites a decaying quasi-three-dimensional Lam-Rott eigensolution. Then, the decaying eigensolution undergoes wavelength shortening to form a spanwise pressure gradient. Furthermore, the pressure gradient balances with inertia in a viscous sublayer which leads to an exponential growth.

A different framework is also available for the study of boundary layers that can be considered as an intermediate method between the described theories and DNS. This framework is known as the Parabolised Stability Equations (PSE). They account for non-parallel effects and have been used vastly to study the stability of boundary layers, e.g. Bertolloti *et al.* [6], Airiau [2], *et al.* [54].

The PSE include both growth mechanisms; the algebraic transient growth and exponential growth through primary and higher instabilities. PSE differs from the previous equations as they include weak ellipticity. A thorough literature

review of the PSE was conducted by Herbert [31] where the advantages and issues of this method are demonstrated and explained.

1.2 Adjoint-based methods applied to flow control

In literature, the process of controlling a fluid flow is termed flow control, and it is a multidisciplinary field that includes disciplines such as control theory, applied mathematics and fluid mechanics.

With the objective of attenuating the Klebanoff modes in the Blasius boundary layer subjected to environmental disturbances to delay laminar-turbulent breakdown, some concepts regarding flow control and its applications to linear models are revised, so that they may be applied to the boundary layer theory to meet this project's aims.

1.2.1 Linear theory

To perform control using linearised equations, two main approaches are available; the iterative approach (i.e. adjoint-based) and the direct approach (i.e. Riccati-based) [40]. The two approaches are related and are designed to control a state system in order to optimise pre-defined parameters, i.e. an objective functional. The adjoint-based methods perform a linearisation about a trajectory of the system, then determine how to update the control variables to achieve optimal solutions. The process iterates until the nullified gradient is obtained throughout the interval of actuation defined. These methods can be applied to nonlinear systems; however, the solution may only be locally optimal instead of a globally optimal solution.

On the contrary, the direct approaches perform a single linearisation about a representative mean flow state. It is important to note that it does not have to be a solution of the governing equation. This leads to a unique optimal point of the mean flow optimisation. The Riccati-based methods impose the gradient equal to zero and then solve the state and adjoint fields that result from that. This often

requires more computational resources than the adjoint methods. Therefore, the adjoint-based and Riccati-based approaches both rely on linearisation to achieve optimisation. However, the Riccati-based methods are only suitable for linear systems [40].

The Riccati-based methods are in fact derived from the adjoint-methods using the linear map between the adjoint variables and the state variables that lead to the Riccati equation. Riccati equations can be solved by numerous algorithms available in commercial packages such as MATLAB.

1.2.2 Optimal and robust control in the predictive control framework

Bewley *et al.* [7] described several relevant temporal objective functionals that can be used with the adjoint-based methods to control turbulent flows. In many applications, reducing drag is very important. The optimisation of drag reduction using actuation profiles derived from adjoint-based methods requires the future state of the flow. Such an analysis may require the computation of the flow in a large interval of time, which is not always feasible. For turbulence, drag reduction is often seen as the end goal; thus, investigating the causes of drag may allow optimisation to be done for smaller intervals of time. The turbulence itself causes wall-normal convective transport that leads to higher values of drag; therefore, regulating the time-averaged turbulent kinetic energy can achieve drag reduction while saving computational power. Furthermore, Bewley *et al.* [7] suggested regulation of large-scale and intermediate-scale structures because of the physics and computational power available at the moment. Thus, controlling the larger structures that feed the smaller structures may be more effective in achieving drag reduction.

Bewley *et al.* [7] performed simulations by applying DNS to a turbulent channel flow and using the receding-horizon predictive control framework to reduce drag. The computation of the adjoint field is of the same order as the physical flow field for a similar time interval. The simulations performed were of very

high dimensions to identify different characteristics of methods and control approaches in order to compare them. The algorithm may be slightly modified to include both far temporal and intermediate intervals in the optimisation. Better understanding of the physics may help in defining an appropriate cost functional. The strategies that are designed for long temporal intervals prove to be better than the strategies for shorter temporal intervals. The strategies that focus on the end result while sacrificing intermediate temporal results are more effective than simply regulating the quantity that is intended to be optimised. The control of the terminal values of turbulent kinetic energy has a bigger impact on the flow than the control of drag. Bewley *et al.* [7] concluded that by using wall transpiration by small amounts of blowing and suction (i.e. the actuators do not change the mass flow rate of the system), it is possible to fully relaminarise low Reynolds number turbulent channel flows, which may result in a drag reduction of over 50%. The computational resources required to run such simulations makes it more difficult for the strategies to be implemented on current systems to provide real-time control. However, as the computational resources increase and faster algorithms appear, it may become possible to compute such flows on closed-loop real systems.

1.2.3 Temporal growth of laminar disturbances

Högberg & Henningson [34] used DNS to study linear optimal control applied to temporal growing Falkner-Scan-Cooke boundary layers. They derived the stationary Riccati equation from the adjoint system by considering an infinitely large time scale for the measured parameters. Using blowing and suction as the actuator and assuming non-parallel effects to be small, the controller was extended to spatially developing boundary layers. The tests performed in a Blasius boundary layer showed that TS waves were fully stabilised and the transient growth was attenuated by the controller. Furthermore, the control was applied to a spatial Falkner-Scan-Cooke flow with unstable perturbations where the linear controller was able to attenuate the growth of cross-flow vortices and delay secondary

instabilities. Additionally, their results suggest that the controller works for stationary, time-varying perturbations and for relatively high levels of nonlinearity.

Monokrousos, Åkervik, Brandt & Henningson [50] used an adjoint-based method to study the global linear stability of the Blasius boundary layer subjected to three-dimensional disturbances upstream. The optimisation was to maximise the energy growth of the perturbations. Therefore, the initial conditions were optimised using an adjoint-based method to obtain the largest growth for different finite times. Time-periodic wall forcing was added to amplify the growth rate of the perturbations. They found that the optimal initial conditions for spanwise wavelengths of the order of the boundary-layer thickness are finite-length vortices that exploit the lift-up mechanism to generate Klebanoff modes. For long spanwise wavelengths, the perturbations growth is caused by the Orr mechanism combined with oblique waves. They verified that the lift-up mechanism is most efficient for small frequencies.

1.2.4 Spatial growth of laminar disturbances

The strategies suggested by Bewley *et al.* [7] may be modified to work on spatial instead of temporal control. Similar work was performed by researchers on the pre-transitional Blasius layer to attenuate the streaks and thus delay the laminar breakdown into transition.

Cathalifaud & Luchini [13] applied control theory to the algebraic growth theory (e.g. [46]). They defined an optimal perturbation as the input disturbance of the boundary layer that maximises the output disturbance energy. As shown by Luchini [46], the optimal upstream disturbance consists of stationary streamwise vortices. The attenuation of the steady perturbations originating from the optimal upstream disturbance within the boundary layer was performed using blowing and suction as actuators. The method used was an adjoint-based strategy that considered optimal control as the minimisation of a given objective functional [13]. The framework proposed is described for a chosen objective functional that is minimised through a formal procedure to obtain the state and

adjoint equations along with the conditions of optimality. The solutions of such a system result in the optimal controller [13]. The optimal control profiles for flat and curved plates showed that the portion of wall near the leading edge was where the actuation was highest, especially for curved geometries. They suggested that blowing and suction can be highly effective for large curvatures. The disturbances within the boundary layer were successfully dampened. However, special care should be taken while attenuating the flow with objective functionals that only optimise the end of the interval of actuation, i.e. only guarantee attenuation shortly downstream of the actuators. This may result in an increase of the velocity fluctuations within the interval of actuation which may possibly lead to undesired transition. This can be avoided by considering the energy of the velocity fluctuations throughout the whole interval of actuation in the objective functional. Alternatively, a limited energy input may be introduced at the actuators to obtain a smooth attenuation of the steady fluctuations.

Zuccher, Luchini & Bottaro [72] expanded the work of Cathalifaud & Luchini [13] for the Blasius boundary layer using the incompressible nonlinear boundary-region equations. Their results also showed that increased actuation is necessary close to the leading edge, compared to further downstream, to attenuate the flow.

A different approach was taken by Cathalifaud & Bewley [11], who proposed a noncausal framework that attenuates developing boundary-layers using active and closed-loop control. They considered a linear boundary layer subjected to small, spatially developing, three-dimensional perturbations with blowing and suction distribution over a portion of the wall as actuators. A state estimation is performed by collecting measurements of skin friction and pressure over the same region. The proposed new framework uses a Riccati-based feedback control approach that considers the parabolic feature in the streamwise direction of the linear boundary-layer equations. The framework was implemented and the simulations led to an attenuated flow [12].

Chevalier *et al.* [15] extended the work of Högberg & Henningson [34] by running DNS on spatially developing boundary layers with restrained information

for the controller. A thin strip of measurements were taken at the wall. In addition, noise was added to the wall measurements. Followed by the sensors, a thin strip of unsteady blowing and suction actuators was added to attenuate the flow. Also, stochastic perturbations were generated upstream.

Semeraro *et al.* [62] studied the active linear control applied to a flat-plate boundary layer with the objective of delaying the onset of turbulence. They carried out DNS of the nonlinear, transitional regime of the boundary layer, while employing a three-dimensional, localised initial condition that triggered TS waves of finite amplitude to numerically simulate the transition to turbulence. They also used reduced-order models of the linearised Navier-Stokes equations to design linear quadratic Gaussian controllers. Their optimisation was done through a parametric study that changed the direction and magnitude of the actuators and the weight of the controllers. They concluded that the fully linear control approach was effective in delaying the onset of turbulence in the presence of the created disturbances that had an amplitude of approximately 1% of the free-stream velocity at the location of the actuator.

Belson *et al.* [5] used DNS to study the effects of different types and positions of actuators and sensors on the controllers' performance and robustness in the linearised 2D Blasius boundary layer. They considered two different configurations, one where the sensor is upstream of the actuator, and another where the sensor is placed after the actuator. Their findings revealed that when the sensors are placed upstream of the actuator, the performance is increased, as observed in previous works. However, when the sensor is placed after the actuator, they demonstrated that the performance was degraded by the additional disturbances and uncertainties in the plant model.

A different approach to delay the onset of turbulence in a Blasius boundary layer was investigated by Hanson *et al.* [30]. They performed experiments using a spanwise array of symmetric plasma actuators that had the capacity to form spanwise-periodic counter-rotating vortices. The disturbances in the boundary layer were generated by an array of rough elements, and after improving the

geometry of the array of actuators, they obtained up to 70% energy reduction of the total disturbance energy.

Their work was further expanded by Hanson *et al.* [29] by modifying the experiment to a closed loop, using feedback from wall-shear stress measurements. This significantly increased the energy reduction to over 95%, with the initial control iteration already showing over 89% reduction.

Hack & Zaki [28] used DNS to study the influence of harmonic spanwise wall motion on bypass transition in incompressible boundary layers. They found that with optimal wall-oscillation parameters, attenuation of the laminar flow regime was achieved, and that the cost of actuation was worth the reduction in propulsion power. However, further forcing amplitudes resulted in an upstream onset of turbulence.

An expansion of the work conducted by Hack & Zaki [28] was carried out by Hicks & Ricco [33] by employing a Wentzel-Kramers-Brillouin-Jeffrey analysis to investigate the effects of wall oscillation on the incompressible Blasius flow above an otherwise stationary flat-plate described by LWG [43]. They obtained Klebanoff modes energy reduction of up to 90% which indicates that actuation in the spanwise direction can be very effective in controlling the Klebanoff modes.

Luchini & Bottaro [47] performed a thorough review of the use of adjoint equations in hydrodynamic stability theory. They demonstrated the powerful capabilities of the adjoint-based methods both in analytical and numerical applications applied to the scope of fluid mechanics, not only to optimal perturbations, but also with the opposite application, i.e. to disrupt the base flow.

1.3 The objectives of the thesis

- To extend the incompressible framework by Ricco [56] to the compressible case for the first time by including the components $\{\bar{u}^{(0)}, \bar{v}^{(0)}, \bar{w}^{(0)}, \bar{\tau}^{(0)}, \bar{p}^{(0)}\}$. This provides a correct prediction for the velocity, pressure and temperature fluctuations in the outer layer of the compressible Blasius boundary

layer.

- To apply control to the theoretical formulation of the compressible boundary layer subjected to free-stream small vortical disturbances based on the work of LWG [43], and Ricco & Wu [58], with the objective of attenuating the streaks.

- To apply control to the extension of the theoretical formulation of the incompressible framework by Ricco [56] derived in the present work, with the same objective of reducing the amplitude of the streaks.

- The objectives for the control framework are described below:

  - To obtain the adjoint compressible linear unsteady boundary region equations for the first time.

  - To design a controller to attenuate the streamwise velocity fluctuations and temperature fluctuations within the compressible boundary layer.

  - To apply feedback control by the use of wall actuators.

  - To study the viability of alternative wall actuators: heat transfer actuators, and a blowing and suction mechanism with an angle of attack.

Chapter 2

Linear response of a compressible boundary layer to free-stream vortical disturbances

In this chapter, based on the work of Leib, Wundrow & Goldstein (LWG) [43], Ricco [55][56] and Ricco & Wu [58], the theoretical formulation of the compressible boundary layer subjected to free-stream small vortical disturbances is described. The incompressible framework by Ricco [56] is extended to the compressible case for the first time.

The formulation and scaling are introduced in §2.1. The flow above the boundary layer, and in the proximity of the leading edge is described in LWG [43]. The flow within the boundary layer, including its boundary and initial conditions, is shown in §2.2, §2.3 and §2.4. The numerical procedures are then presented in §2.5, together with the numerical solutions of the boundary region in §2.6.

2.1 Formulation: scaling and asymptotic structure of flow domain

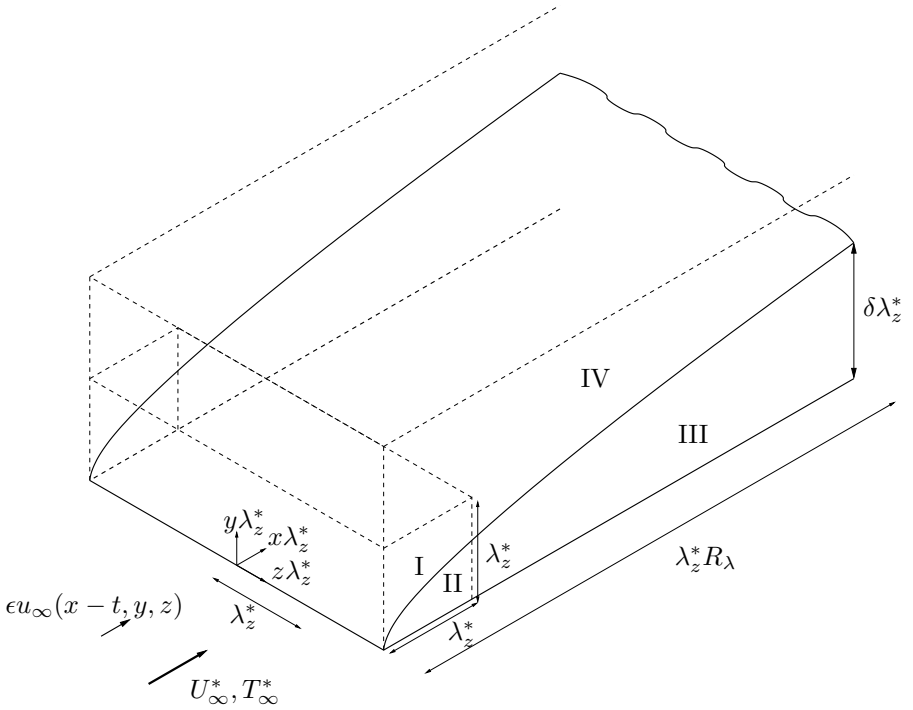

Figure 2.1: A schematic illustration of the different asymptotic regions of the flow.

This formulation is closely guided by Ricco & Wu [58] and LWG [43]. Consider an air flow with uniform velocity U_∞^* and constant temperature T_∞^* passing over an infinitely thin flat plate. The plate is regarded as an adiabatic wall, and the air, a perfect gas with the speed of sound in the free stream, described as:

$$c_\infty^* = \sqrt{\gamma R^* T_\infty^*}, \tag{2.1}$$

where γ is the ratio of the specific heats and R^* the universal gas constant defined as $\gamma = 1.4$ and $R^* = 287.05$ N m kg^{-1} K^{-1} respectively. A diagram of this flow is shown in figure 2.1. The Mach number M is defined in the usual way as:

$$M \equiv \frac{U_\infty^*}{c_\infty^*} \tag{2.2}$$

and is taken to be of $\mathcal{O}(1)$.

Vortical disturbances originating from the free stream are superimposed on U^*_∞ to represent weak turbulence in the FST. The vortical disturbances are of the convected gust type and are treated as statistically-stationary, homogeneous turbulent vortical fluctuations.

A Cartesian coordinate system is used to represent the flow where a point is described by a position vector $\mathbf{x} = x\hat{\mathbf{i}} + y\hat{\mathbf{j}} + z\hat{\mathbf{k}}$, where x, y and z describe the streamwise, wall normal and spanwise directions. The space coordinates are non-dimensionalised by the spanwise integral length scale of the free-stream turbulence λ^*_z. For the special case of a single Fourier component, λ^*_z is the spanwise wavelength of the free-stream vortical disturbance.

The symbol * is used to represent dimensional quantities. The velocities are non-dimensionalised by U^*_∞, the temperature by T^*_∞ and the pressure by $\rho^*_\infty U^{*2}_\infty$. Time is normalised by λ^*_z/U^*_∞. The fluid properties are made dimensionless by their values in the free stream, i.e., the density, dynamic viscosity and thermal conductivity are normalised by ρ^*_∞, μ^*_∞ and k^*_∞ respectively.

The intensity of the turbulent velocity fluctuations is assumed to be small so that the flow can be considered as a linear perturbation of the mean flow. As in LWG [43], the perturbations are viewed as a superposition of sinusoidal disturbances:

$$\mathbf{u} - \hat{\mathbf{i}} = \epsilon \mathbf{u}_\infty(x - t, y, z) = \epsilon \hat{\mathbf{u}}^\infty e^{i(\mathbf{k}\cdot\mathbf{x} - k_x t)} + c.c., \tag{2.3}$$

where $c.c.$ is the complex conjugate and $\hat{\mathbf{u}}^\infty$ and $\mathbf{k}$ are real vectors defined as:

$$\hat{\mathbf{u}}^\infty = \begin{bmatrix} \hat{u}^\infty_x \\ \hat{u}^\infty_y \\ \hat{u}^\infty_z \end{bmatrix} \tag{2.4}$$

and

$$\mathbf{k} = \begin{bmatrix} k_x \\ k_y \\ k_z \end{bmatrix} \tag{2.5}$$

respectively. The components $\hat{u}_x^\infty$, $\hat{u}_y^\infty$ and $\hat{u}_z^\infty$ are of $\mathcal{O}(1)$, $\epsilon \ll 1$ is a measure of turbulent intensity and $\mathbf{k}$ is the wavenumber vector. The continuity equation reads:

$$\hat{\mathbf{u}}^\infty \cdot \mathbf{k} = 0. \tag{2.6}$$

Experiments show that low-frequency (i.e. long wave-length) vortical turbulence penetrates the boundary layer to form Klebanoff modes. Therefore, components with $k_x \ll 1$ are considered. Due to the linearity, each Fourier mode can be analysed individually and the sum of the Fourier modes leads to the continuous free-stream turbulence spectrum.

According to LWG [43], a turbulent Reynolds number is defined as:

$$r_t = \epsilon R_\lambda = \mathcal{O}(1) \tag{2.7}$$

with:

$$R_\lambda \equiv \frac{U_\infty^* \lambda_z^*}{\nu_\infty^*} \tag{2.8}$$

and:

$$R_\lambda \gg 1, \tag{2.9}$$

where ν_∞^* is the kinematic viscosity of the fluid in the free stream. Goldstein [22] has considered an asymptotically large R_λ and taken a small ϵ while keeping $r_t = \mathcal{O}(1)$; this leads to a flow that can be divided into four asymptotic regions, as illustrated in figure 2.1.

Region I: it is an inviscid region located above the boundary layer and around the leading edge. The solution of this region is described in LWG [43].

Region II: it is viscous in nature and located below region I where the unsteady perturbations are characterised by the linearised unsteady boundary layer equations (LUBL) described by Gulyaev *et al.* [26] and LWG [43] for the incompressible case and by Ricco [55] and Ricco & Wu [58] for the compressible case, in which their compressible formulation is used here. Within this region, the boundary layer thickness δ^* is related to the location x^* by:

$$\delta^* = \mathcal{O}\left(\frac{x^*}{\sqrt{R_\infty}}\right), \tag{2.10}$$

where:

$$R_\infty \equiv \frac{U_\infty^* x^*}{\nu_\infty^*}. \tag{2.11}$$

The LUBL equations are valid while the boundary layer thickness δ^* is smaller than the spanwise length scale λ_z^*, which leads to:

$$x^* \ll \mathcal{O}\left(\lambda_z^* R_\lambda\right) \tag{2.12}$$

or

$$\frac{x}{R_\lambda} \ll \mathcal{O}(1). \tag{2.13}$$

Goldstein's [22] numerical solutions of the LUBL equations show that the maximum value of the velocity perturbations occur when $x = \mathcal{O}\left(k_x^{-1}\right)$. Thus, the following scaling is done:

$$k_x = \mathcal{O}\left(R_\lambda^{-1}\right), \tag{2.14}$$

which can also be written as:

$$\bar{x} \equiv k_x x = \mathcal{O}(1). \tag{2.15}$$

Therefore, the boundary layer thickness δ^* becomes

$$\delta^* = \mathcal{O}(\lambda_z^*) \tag{2.16}$$

as:

$$\frac{x}{R_\lambda} = \mathcal{O}(1). \tag{2.17}$$

This invalidates the solution of the LUBL equations as the diffusion in the spanwise direction becomes of the same order of magnitude as the wall-normal direction.

Region III: it is the viscous region that follows downstream of region II becomes invalid, i.e., at $\mathcal{O}\left(\lambda_z^* R_\lambda\right)$ from the leading edge. It has a width of $\mathcal{O}(\lambda_z^*)$ and its unsteady flow is described by the boundary region equations [36], i.e., Navier-Stokes equations while neglecting the streamwise viscous diffusion and streamwise pressure-gradient. The boundary region equations are parabolic in

the streamwise direction and elliptic in the spanwise direction. Similar to region II, the terms (2.14) and (2.15) are used; however, equation (2.13) becomes $x/R_\lambda = \mathcal{O}(1)$.

Using the above assumptions, the compressible boundary region equations can be deduced from the compressible Navier-Stokes equations (cf. Ricco [55]). Considering x scaled by:

$$\tilde{x} = \frac{x}{R_\lambda}, \tag{2.18}$$

and time t^* by:

$$\tilde{t} = \frac{t^* \nu_\infty^*}{\lambda_z^{*2}}, \tag{2.19}$$

keeping y scaled by λ_z^* because $\delta^* = \mathcal{O}(\lambda_z^*)$ and taking into account that $R_\lambda \gg 1$, leading to:

$$u = \tilde{u}\left(\tilde{x}, y, z, \tilde{t}\right) + \ldots \tag{2.20a}$$

$$v = R_\lambda^{-1}\tilde{v}\left(\tilde{x}, y, z, \tilde{t}\right) + \ldots \tag{2.20b}$$

$$w = R_\lambda^{-1}\tilde{w}\left(\tilde{x}, y, z, \tilde{t}\right) + \ldots \tag{2.20c}$$

$$p = R_\lambda^{-2}\tilde{p}\left(\tilde{x}, y, z, \tilde{t}\right) + \ldots \tag{2.20d}$$

$$\tau = \tilde{T}\left(\tilde{x}, y, z, \tilde{t}\right) + \ldots \tag{2.20e}$$

$$\rho = \tilde{\rho}\left(\tilde{x}, y, z, \tilde{t}\right) + \ldots \tag{2.20f}$$

and:

continuity equation

$$\frac{\partial \tilde{\rho}}{\partial \tilde{t}} + \frac{\partial}{\partial \tilde{x}}\left(\tilde{\rho}\tilde{u}\right) + \frac{\partial}{\partial y}\left(\tilde{\rho}\tilde{v}\right) + \frac{\partial}{\partial z}\left(\tilde{\rho}\tilde{w}\right) = 0; \tag{2.21}$$

x-momentum equation

$$\tilde{\rho}\left(\frac{\partial \tilde{u}}{\partial \tilde{t}} + \tilde{u}\frac{\partial \tilde{u}}{\partial \tilde{x}} + \tilde{v}\frac{\partial \tilde{u}}{\partial y} + \tilde{w}\frac{\partial \tilde{u}}{\partial z}\right) = \frac{\partial}{\partial y}\left(\mu\frac{\partial \tilde{u}}{\partial y}\right) + \frac{\partial}{\partial z}\left(\mu\frac{\partial \tilde{u}}{\partial z}\right); \tag{2.22}$$

y-momentum equation

$$\begin{aligned}\tilde{\rho}\left(\frac{\partial \tilde{v}}{\partial \tilde{t}} + \tilde{u}\frac{\partial \tilde{v}}{\partial \tilde{x}} + \tilde{v}\frac{\partial \tilde{v}}{\partial y} + \tilde{w}\frac{\partial \tilde{v}}{\partial z}\right) &= -\frac{\partial \tilde{p}}{\partial y} + \frac{\partial}{\partial \tilde{x}}\left(\mu\frac{\partial \tilde{u}}{\partial y}\right) \\ + \frac{\partial}{\partial y}\left[\mu\left(-\frac{2}{3}\frac{\partial \tilde{u}}{\partial \tilde{x}} + \frac{4}{3}\frac{\partial \tilde{v}}{\partial y} - \frac{2}{3}\frac{\partial \tilde{w}}{\partial z}\right)\right] &+ \frac{\partial}{\partial z}\left[\mu\left(\frac{\partial \tilde{v}}{\partial z} + \frac{\partial \tilde{w}}{\partial y}\right)\right];\end{aligned} \tag{2.23}$$

z-momentum equation

$$\tilde{\rho}\left(\frac{\partial\tilde{w}}{\partial\tilde{t}}+\tilde{u}\frac{\partial\tilde{w}}{\partial\tilde{x}}+\tilde{v}\frac{\partial\tilde{w}}{\partial y}+\tilde{w}\frac{\partial\tilde{w}}{\partial z}\right)=-\frac{\partial\tilde{p}}{\partial z}+\frac{\partial}{\partial\tilde{x}}\left(\mu\frac{\partial\tilde{u}}{\partial z}\right)$$
$$+\frac{\partial}{\partial y}\left[\mu\left(\frac{\partial\tilde{v}}{\partial z}+\frac{\partial\tilde{w}}{\partial y}\right)\right]+\frac{\partial}{\partial z}\left[\mu\left(-\frac{2}{3}\frac{\partial\tilde{u}}{\partial\tilde{x}}-\frac{2}{3}\frac{\partial\tilde{v}}{\partial y}+\frac{4}{3}\frac{\partial\tilde{w}}{\partial z}\right)\right]; \tag{2.24}$$

energy equation

$$\tilde{\rho}\left(\frac{\partial\tilde{T}}{\partial\tilde{t}}+\tilde{u}\frac{\partial\tilde{T}}{\partial\tilde{x}}+\tilde{v}\frac{\partial\tilde{T}}{\partial y}+\tilde{w}\frac{\partial\tilde{T}}{\partial z}\right)=\frac{1}{\mathrm{Pr}}\left[\frac{\partial}{\partial y}\left(k\frac{\partial\tilde{T}}{\partial y}\right)+\frac{\partial}{\partial z}\left(k\frac{\partial\tilde{T}}{\partial z}\right)\right]$$
$$+(\gamma-1)M^2\mu\left(\frac{\partial\tilde{u}}{\partial y}\right)^2; \tag{2.25}$$

where k is the thermal conductivity of air and Pr is the Prandtl number which is set to $\mathrm{Pr}=0.7$.

The $\mathcal{O}(\epsilon)$ fluctuations in the free stream lead to $\mathcal{O}\left(\epsilon/k_x\right)$ streamwise velocity disturbances in the boundary layer [43]. Consistent with LWG [43], $\epsilon/k_x \ll 1$ is used together with equation (2.14) to obtain the linearisation condition:

$$\epsilon R_\lambda = r_t \ll 1, \tag{2.26}$$

which is used throughout this chapter. The linearisation condition (2.26) is employed to linearise the boundary region equations to obtain the linearised unsteady boundary region equations.

Region IV: above region III, there is also a viscous flow. Region IV is influenced by the displacement of the flow underneath, i.e., region III. Logically, the flow differs at subsonic, transonic or supersonic speeds. Region IV is treated according to the LWG [43] formulation.

2.2 The mean compressible laminar boundary layer flow

Consider the flow above a flat plate and further downstream, i.e. $x > 0$. The equations to describe the steady compressible laminar boundary layer equations are derived from the steady Navier-Stokes equations, similar to the incompressible case. However, the simplification of the x-momentum and energy equa-

tions to a system of ordinary differential equations (ODE) requires the Howarth-Dorodnitsyn coordinate transformation [63]:

$$\bar{Y} = \bar{Y}(x, y) \equiv \int_0^y \rho\,(x, \tilde{y})\,\mathrm{d}\tilde{y}. \tag{2.27}$$

When the pressure gradient is not present, a similarity solution is obtained by using the similarity variable:

$$\eta \equiv \bar{Y}\sqrt{\frac{R_\lambda}{2x}}. \tag{2.28}$$

Assuming a constant Prandlt number Pr, the similarity solution leads to the coupled ODE system:

$$FF'' + \left(\frac{\mu}{T}F''\right)' = 0, \tag{2.29}$$

$$\frac{1}{\mathrm{Pr}}\left(\frac{\mu}{T}T'\right)' + T'F + (\gamma - 1)M^2\frac{\mu}{T}(F'')^2 = 0, \tag{2.30}$$

where:

$$F = F(\eta), \tag{2.31}$$

$$T = T(\eta), \tag{2.32}$$

$$\mu = \mu(T), \tag{2.33}$$

with the following boundary conditions:

$$F(0) = 0, \tag{2.34}$$

$$F'(0) = 0, \tag{2.35}$$

$$T'(0) = 0, \tag{2.36}$$

$$F' \to 1 \quad \text{as} \quad \eta \to \infty, \tag{2.37}$$

$$T \to 1 \quad \text{as} \quad \eta \to \infty. \tag{2.38}$$

Equation (2.36) is obtained by considering an adiabatic wall. From equations (2.29) and (2.30), the steady streamwise velocity U, steady wall-normal velocity V and steady temperature T can be obtained:

$$U = F', \tag{2.39}$$

$$V = \frac{1}{\sqrt{2xR_\lambda}} \left(\eta_c T F' - T F \right), \tag{2.40}$$

$$T = T(\eta), \tag{2.41}$$

where:

$$\eta_c \equiv \frac{1}{T} \int_0^\eta T\left(\breve{\eta}\right) d\breve{\eta}. \tag{2.42}$$

The boundary conditions (2.34) and (2.35) are found from the no-slip condition at the wall, i.e.:

$$U = V = 0, \tag{2.43}$$

and equations (2.28), (2.39) and (2.40). The relation between viscosity μ and the temperature T is assumed to be given by the power law [14]:

$$\mu = T^\omega, \quad \text{with} \quad \omega = 0.76, \tag{2.44}$$

as is appropriate for a $M < 4$ [63].

2.3 The linear boundary layer flow: region II

Region II originates from the inviscid flow described in LWG [43] as region I, which encounters the wall that imposes a no-slip condition, i.e., the velocities are nullified at the wall. This leads to the viscous region II, which is commonly known as the boundary layer.

The unsteady perturbations are linearised about the steady laminar compressible boundary layer. In this section, the steady flow is considered first, followed by the unsteady perturbations (cf. Ricco & Wu [58]).

2.3.1 The unsteady velocity and temperature perturbation flow

Considering that the flow is periodic in time and in the spanwise direction, the solution for the velocities u, v, w and temperature τ can be given by a single

Fourier component of the disturbance:

$$\begin{bmatrix} u \\ v \\ w \\ \tau \end{bmatrix} = \begin{bmatrix} U \\ V \\ 0 \\ T \end{bmatrix} + \epsilon \begin{bmatrix} \bar{u}_0(\bar{x},\eta) \\ \sqrt{\frac{2\bar{x}k_x}{R_\lambda}}\bar{v}_0(\bar{x},\eta) \\ \bar{w}_0(\bar{x},\eta) \\ \bar{\tau}_0(\bar{x},\eta) \end{bmatrix} e^{i(k_z z - k_x t)} + c.c. \tag{2.45}$$

Substituting equation (2.45) into equations (2.21)-(2.25) and linearising the equations yields the LUBL equations:

continuity equation

$$\begin{aligned} \frac{\eta_c}{2\bar{x}}\frac{T'}{T}\bar{u}_0 + \frac{\partial \bar{u}_0}{\partial \bar{x}} - \frac{\eta_c}{2\bar{x}}\frac{\partial \bar{u}_0}{\partial \eta} - \frac{T'}{T^2}\bar{v}_0 + \frac{1}{T}\frac{\partial \bar{v}_0}{\partial \eta} + \frac{ik_z}{k_x}\bar{w}_0 + \left(\frac{i}{T} - \frac{1}{2\bar{x}}\frac{T'F}{T^2}\right)\bar{\tau}_0 \\ -\frac{F'}{T}\frac{\partial \bar{\tau}_0}{\partial \bar{x}} + \frac{1}{2\bar{x}}\frac{F}{T}\frac{\partial \bar{\tau}_0}{\partial \eta} = 0; \end{aligned} \tag{2.46}$$

x-momentum equation

$$\begin{aligned} \left(-i - \frac{\eta_c}{2\bar{x}}F''\right)\bar{u}_0 + F'\frac{\partial \bar{u}_0}{\partial \bar{x}} + \frac{1}{2\bar{x}}\left(\frac{\mu T'}{T^2} - F - \frac{\mu' T'}{T}\right)\frac{\partial \bar{u}_0}{\partial \eta} \\ -\frac{1}{2\bar{x}}\frac{\mu}{T}\frac{\partial^2 \bar{u}_0}{\partial \eta^2} + \frac{F''}{T}\bar{v}_0 + \frac{1}{2\bar{x}}\left(\frac{FF''}{T} - \frac{\mu' F'''}{T} - \frac{\mu'' T' F''}{T} + \frac{\mu' T' F''}{T^2}\right)\bar{\tau}_0 \\ -\frac{1}{2\bar{x}}\frac{\mu' F''}{T}\frac{\partial \bar{\tau}_0}{\partial \eta} = 0; \end{aligned} \tag{2.47}$$

z-momentum equation

$$-i\bar{w}_0 + F'\frac{\partial \bar{w}_0}{\partial \bar{x}} + \frac{1}{2\bar{x}}\left(\frac{\mu T'}{T^2} - \frac{\mu' T'}{T} - F\right)\frac{\partial \bar{w}_0}{\partial \eta} - \frac{1}{2\bar{x}}\frac{\mu}{T}\frac{\partial^2 \bar{w}_0}{\partial \eta^2} = 0; \tag{2.48}$$

energy equation

$$\begin{aligned} -\frac{\eta_c}{2\bar{x}}T'\bar{u}_0 - (\gamma-1)M^2\frac{1}{\bar{x}}\frac{\mu F''}{T}\frac{\partial \bar{u}_0}{\partial \eta} + \frac{T'}{T}\bar{v}_0 \\ + \left(-i + \frac{1}{2\bar{x}}\frac{T'F}{T} - \frac{1}{2\bar{x}}\frac{1}{\mathrm{Pr}}\frac{\mu''(T')^2}{T} - \frac{1}{2\bar{x}}\frac{1}{\mathrm{Pr}}\frac{\mu' T''}{T} + \frac{1}{2\bar{x}}\frac{1}{\mathrm{Pr}}\frac{\mu'(T')^2}{T^2}\right. \\ \left. -(\gamma-1)M^2\frac{1}{2\bar{x}}\frac{\mu'(F'')^2}{T}\right)\bar{\tau}_0 + F'\frac{\partial \bar{\tau}_0}{\partial \bar{x}} \\ + \frac{1}{2\bar{x}}\left(-F - \frac{2}{\mathrm{Pr}}\frac{\mu' T'}{T} + \frac{1}{\mathrm{Pr}}\frac{\mu T'}{T^2}\right)\frac{\partial \bar{\tau}_0}{\partial \eta} - \frac{1}{2\bar{x}}\frac{1}{\mathrm{Pr}}\frac{\mu}{T}\frac{\partial^2 \bar{\tau}_0}{\partial \eta^2} = 0; \end{aligned} \tag{2.49}$$

with boundary conditions:

$$\bar{u}_0 = 0 \quad \text{at} \quad \eta = 0, \tag{2.50}$$

$$\bar{v}_0 = 0 \quad \text{at} \quad \eta = 0, \tag{2.51}$$

$$\bar{w}_0 = 0 \quad \text{at} \quad \eta = 0, \tag{2.52}$$

$$\frac{\partial \bar{\tau}_0}{\partial \eta} = 0 \quad \text{at} \quad \eta = 0, \tag{2.53}$$

$$\bar{\tau}_0 \to 0 \quad \text{as} \quad \eta \to \infty. \tag{2.54}$$

Similar to the steady flow, the no-slip condition at the wall is imposed by (2.50)-(2.52) and the adiabatic condition at the wall by (2.53). Due to the lack of temperature forcing from the free stream, the temperature fluctuations must vanish in the free stream, i.e. (2.54). Considering that the LUBL equations require seven boundary conditions, the remaining two are given by the kinematic forcing at the free stream. According to LWG [43], Ricco & Wu [58] and Ricco [56], the remaining boundary conditions are found by expressing the solution as in Gulyaev *et al.* [26]:

$$\begin{bmatrix} \bar{u}_0 \\ \bar{v}_0 \\ \bar{w}_0 \\ \bar{\tau}_0 \end{bmatrix} = C^{(0)} \begin{bmatrix} \bar{u}^{(0)} \\ \bar{v}^{(0)} \\ -\frac{ik_x}{k_z}\bar{w}^{(0)} \\ \bar{\tau}^{(0)} \end{bmatrix} + C \begin{bmatrix} \frac{ik_z}{k_x}\bar{u} \\ \frac{ik_z}{k_x}\bar{v} \\ \bar{w} \\ \frac{ik_z}{k_x}\bar{\tau} \end{bmatrix} \tag{2.55}$$

with:

$$C^{(0)} \equiv \hat{u}_x^{\infty} + \frac{ik_x}{\sqrt{k_x^2 + k_z^2}}\hat{u}_y^{\infty} \tag{2.56}$$

and:

$$C \equiv \hat{u}_z^{\infty} + \frac{ik_z}{\sqrt{k_x^2 + k_z^2}}\hat{u}_y^{\infty}. \tag{2.57}$$

The continuity equation (2.46) simplifies to:

$$\begin{aligned} \frac{\eta_c}{2\bar{x}}\frac{T'}{T}\bar{u} + \frac{\partial \bar{u}}{\partial \bar{x}} - \frac{\eta_c}{2\bar{x}}\frac{\partial \bar{u}}{\partial \eta} - \frac{T'}{T^2}\bar{v} + \frac{1}{T}\frac{\partial \bar{v}}{\partial \eta} + \bar{w} + \left(\frac{i}{T} - \frac{1}{2\bar{x}}\frac{T'F}{T^2}\right)\bar{\tau} \\ - \frac{F'}{T}\frac{\partial \bar{\tau}}{\partial \bar{x}} + \frac{1}{2\bar{x}}\frac{F}{T}\frac{\partial \bar{\tau}}{\partial \eta} = 0. \end{aligned} \tag{2.58}$$

The matching of the kinematic components $\bar{u}$ and $\bar{w}$ with the region I described in LWG [43] yields:

$$\bar{u} \to 0 \quad \text{as} \quad \eta \to \infty, \tag{2.59}$$

$$\bar{w} \to e^{i\bar{x}} \quad \text{as} \quad \eta \to \infty. \tag{2.60}$$

The procedure to obtain the initial conditions for the LUBL equations can be found on page 24 and Appendix A of Ricco [55].

2.4 The boundary region flow (region III) and the outer solution (region IV)

The boundary layer equations fail to describe the flow when the spanwise diffusion cannot be neglected, i.e., the boundary layer thickness δ^* becomes of the same order of magnitude as the spanwise length scale in the free-stream disturbance λ_z^*. The location where it occurs is given by equation (2.17).

The boundary region equations are used to describe the flow in region III. The unsteady streaks generated in the boundary layer lead to an unsteady pressure in region IV. The new unknown is treated in a similar way to the velocities and temperature fluctuations. In line with LWG [43], Ricco & Wu [58] and Ricco [56], the pressure p is written according to Gulyaev [26]:

$$p = -\frac{1}{2} + \epsilon \bar{p}_0 \left(\bar{x}, \eta\right) e^{i(k_z z - k_x t)} + c.c., \tag{2.61}$$

where:

$$\bar{p}_0 = \frac{k_x}{R_\lambda} C^{(0)} \bar{p}^{(0)} + i\kappa_z \sqrt{\frac{k_x}{R_\lambda}} C \bar{p}, \tag{2.62}$$

with:

$$\kappa_z \equiv \frac{k_z}{\sqrt{k_x R_\lambda}}. \tag{2.63}$$

$C^{(0)}$ and C are given by equations (2.56) and (2.57) respectively.

The terms proportional to the components $\bar{u}$, $\bar{v}$, $\bar{w}$, $\bar{\tau}$ and $\bar{p}$ are analysed in LWG [43] for the incompressible case, and in Ricco [55] and Ricco & Wu [58] for the compressible case. They represent the dominant part of the velocities, pressure and temperature fluctuations within the core of the boundary layer, i.e., in the middle and close to the wall within the boundary layer. The terms proportional to the components $\bar{u}^{(0)}$, $\bar{v}^{(0)}$, $\bar{w}^{(0)}$, $\bar{\tau}^{(0)}$ and $\bar{p}^{(0)}$ were studied for the

incompressible case by Ricco [56] and for the first time, the compressible case is solved in the present study. These represent second order components of the Klebanoff modes within the core of the boundary layer, and because of that, have been neglected in previous works [43][58]. However, in the outer layer, they are the dominant components of the Klebanoff modes, and thus the components $\bar{u}^{(0)}$, $\bar{v}^{(0)}$, $\bar{w}^{(0)}$, $\bar{\tau}^{(0)}$ and $\bar{p}^{(0)}$ are important to obtain more realistic profiles along the wall-normal direction.

The components $\{\bar{u}, \bar{v}, \bar{w}, \bar{\tau}, \bar{p}\}$ and the components $\left\{\bar{u}^{(0)}, \bar{v}^{(0)}, \bar{w}^{(0)}, \bar{\tau}^{(0)}, \bar{p}^{(0)}\right\}$ satisfy the compressible linear unsteady boundary region (referred to hereinafter as CLUBR) equations (cf. Ricco & Wu [58]):
continuity equation

$$\begin{aligned}\frac{\eta_c}{2\bar{x}}\frac{T'}{T}\bar{u} + \frac{\partial\bar{u}}{\partial\bar{x}} - \frac{\eta_c}{2\bar{x}}\frac{\partial\bar{u}}{\partial\eta} - \frac{T'}{T^2}\bar{v} + \frac{1}{T}\frac{\partial\bar{v}}{\partial\eta} + \bar{w} + \left(\frac{i}{T^2} - \frac{1}{2\bar{x}}\frac{T'F}{T^2}\right)\bar{\tau} \\ -\frac{F'}{T}\frac{\partial\bar{\tau}}{\partial\bar{x}} + \frac{1}{2\bar{x}}\frac{F}{T}\frac{\partial\bar{\tau}}{\partial\eta} = 0;\end{aligned} \tag{2.64}$$

x-momentum equation

$$\begin{aligned}\left(-i - \frac{\eta_c}{2\bar{x}}F'' + \kappa_z^2\mu T\right)\bar{u} + F'\frac{\partial\bar{u}}{\partial\bar{x}} + \frac{1}{2\bar{x}}\left(\frac{\mu T'}{T^2} - F - \frac{\mu' T'}{T}\right)\frac{\partial\bar{u}}{\partial\eta} \\ -\frac{1}{2\bar{x}}\frac{\mu}{T}\frac{\partial^2\bar{u}}{\partial\eta^2} + \frac{F''}{T}\bar{v} + \frac{1}{2\bar{x}}\left(\frac{FF''}{T} - \frac{\mu' F'''}{T} - \frac{\mu'' T' F''}{T} + \frac{\mu' T' F''}{T^2}\right)\bar{\tau} \\ -\frac{1}{2\bar{x}}\frac{\mu' F''}{T}\frac{\partial\bar{\tau}}{\partial\eta} = 0;\end{aligned} \tag{2.65}$$

y-momentum equation

$$\begin{aligned}
&\frac{1}{(2\bar{x})^2}\left(TF-\eta_c TF'+\eta_c T'F-{\eta_c}^2 TF''\right)\bar{u}+\frac{1}{3\bar{x}}\mu'T'\frac{\partial\bar{u}}{\partial\bar{x}}-\frac{1}{6\bar{x}}\mu\frac{\partial}{\partial\bar{x}}\left(\frac{\partial\bar{u}}{\partial\eta}\right)\\
&+\frac{1}{12\bar{x}^2}\left(\eta_c\mu'T'-\eta_c\frac{\mu T'}{T}+\mu\right)\frac{\partial\bar{u}}{\partial\eta}+\frac{\eta_c}{12\bar{x}^2}\mu\frac{\partial^2\bar{u}}{\partial\eta^2}+\left(-i+\frac{\eta_c}{2\bar{x}}F''\right.\\
&\left.-\frac{1}{2\bar{x}}\frac{T'F}{T}+\frac{1}{2\bar{x}}F'+\kappa_z^2\mu T\right)\bar{v}+F'\frac{\partial\bar{v}}{\partial\bar{x}}+\left(-\frac{1}{2\bar{x}}F-\frac{2}{3\bar{x}}\frac{\mu'T'}{T}\right.\\
&\left.+\frac{2}{3\bar{x}}\frac{\mu T'}{T^2}\right)\frac{\partial\bar{v}}{\partial\eta}-\frac{4}{3}\frac{1}{2\bar{x}}\frac{\mu}{T}\frac{\partial^2\bar{v}}{\partial\eta^2}+\frac{2}{3}\frac{1}{2\bar{x}}\mu'T'\bar{w}-\frac{1}{3}\frac{1}{2\bar{x}}\mu\frac{\partial\bar{w}}{\partial\eta}\\
&+\left(-FF'+\eta_c(F')^2-\frac{T'F^2}{T}+\eta_cFF''+\frac{1}{3\bar{x}^2}\frac{\mu'T''F}{T}-\frac{1}{3\bar{x}^2}\frac{\mu'(T')^2F}{T^2}\right.\\
&+\frac{1}{3\bar{x}^2}\frac{\mu''(T')^2F}{T}+\frac{1}{3\bar{x}^2}\frac{\mu'T'F'}{T}+\frac{\eta_c}{4\bar{x}^2}\frac{\mu'T'F''}{T}-\frac{1}{4\bar{x}^2}\mu'F''-\frac{\eta_c}{4\bar{x}^2}\mu''T'F''\\
&\left.-\frac{\eta_c}{4\bar{x}^2}\mu'F'''\right)\bar{\tau}-\frac{1}{2\bar{x}}\mu'F''\frac{\partial\bar{\tau}}{\partial\bar{x}}+\left(-\frac{\eta_c}{4\bar{x}^2}\mu'F''+\frac{1}{3\bar{x}^2}\frac{\mu'T'F}{T}\right)\frac{\partial\bar{\tau}}{\partial\eta}\\
&+\frac{1}{2\bar{x}}\frac{\partial\bar{p}}{\partial\eta}=0;
\end{aligned}\tag{2.66}$$

z-momentum equation

$$\begin{aligned}
&-\frac{\eta_c}{2\bar{x}}\kappa_z^2\mu'TT'\bar{u}+\frac{1}{3}\kappa_z^2\mu T\frac{\partial\bar{u}}{\partial\bar{x}}-\frac{\eta_c}{6\bar{x}}\kappa_z^2\mu T\frac{\partial\bar{u}}{\partial\eta}+\kappa_z^2\mu'T'\bar{v}+\frac{1}{3}\kappa_z^2\mu\frac{\partial\bar{v}}{\partial\eta}\\
&+\left(\frac{4}{3}\kappa_z^2\mu T-i\right)\bar{w}+F'\frac{\partial\bar{w}}{\partial\bar{x}}+\frac{1}{2\bar{x}}\left(\frac{\mu T'}{T^2}-\frac{\mu'T'}{T}-F\right)\frac{\partial\bar{w}}{\partial\eta}-\frac{1}{2\bar{x}}\frac{\mu}{T}\frac{\partial^2\bar{w}}{\partial\eta^2}\\
&+\frac{1}{3\bar{x}}\kappa_z^2\mu'T'F\bar{\tau}-\kappa_z^2T\bar{p}=0;
\end{aligned}\tag{2.67}$$

energy equation

$$\begin{aligned}
&-\frac{\eta_c}{2\bar{x}}T'\bar{u}-(\gamma-1)M^2\frac{1}{\bar{x}}\frac{\mu F''}{T}\frac{\partial\bar{u}}{\partial\eta}+\frac{T'}{T}\bar{v}\\
&+\left(-i+\frac{1}{2\bar{x}}\frac{T'F}{T}-\frac{1}{2\bar{x}}\frac{1}{\mathrm{Pr}}\frac{\mu''(T')^2}{T}\right.\\
&\left.-\frac{1}{2\bar{x}}\frac{1}{\mathrm{Pr}}\frac{\mu'T''}{T}+\frac{1}{2\bar{x}}\frac{1}{\mathrm{Pr}}\frac{\mu'(T')^2}{T^2}+\frac{1}{\mathrm{Pr}}\kappa_z^2\mu T-(\gamma-1)M^2\frac{1}{2\bar{x}}\frac{\mu'(F'')^2}{T}\right)\bar{\tau}\\
&+F'\frac{\partial\bar{\tau}}{\partial\bar{x}}+\frac{1}{2\bar{x}}\left(-F-\frac{2}{\mathrm{Pr}}\frac{\mu'T'}{T}+\frac{1}{\mathrm{Pr}}\frac{\mu T'}{T^2}\right)\frac{\partial\bar{\tau}}{\partial\eta}-\frac{1}{2\bar{x}}\frac{1}{\mathrm{Pr}}\frac{\mu}{T}\frac{\partial^2\bar{\tau}}{\partial\eta^2}=0.
\end{aligned}\tag{2.68}$$

The boundary conditions for the CLUBR at the wall are obtained through the no-slip condition, which imposes:

$$\bar{u}=\bar{v}=\bar{w}=\bar{u}^{(0)}=\bar{v}^{(0)}=\bar{w}^{(0)}=0,\tag{2.69}$$

while the adiabatic wall leads to:

$$\frac{\partial\bar{\tau}}{\partial\eta}=\frac{\partial\bar{\tau}^{(0)}}{\partial\eta}=0.\tag{2.70}$$

The outer boundary conditions, i.e. $\eta \to \infty$, requires the CLUBR to match the outer flow above (region IV).

2.4.1 Region IV: outer flow

The velocity field in region IV is expanded as (cf. LWG [43] and Ricco & Wu [58]):

$$\mathbf{u} = \begin{bmatrix} \frac{\partial \Psi}{\partial y} \\ -\frac{\partial \Psi}{\partial x} \\ 0 \end{bmatrix} + \epsilon \mathbf{u}^{(\mathbf{0})} e^{i(k_z z - k_x t)} + c.c. + \dots \tag{2.71}$$

where the stream function Ψ is given by Ricco [55] for the compressible case as:

$$\Psi = y - (\beta_c + \gamma_c)\mathrm{Re}\left[\sqrt{\frac{2\left(x + iy\sqrt{1-M^2}\right)}{R_\lambda}}\right], M < 1, M = \mathcal{O}(1) \tag{2.72}$$

and

$$\Psi = y - (\beta_c + \gamma_c)\mathrm{Re}\left[\sqrt{\frac{2\left(x + iy\sqrt{M^2-1}\right)}{R_\lambda}}\right], M > 1, M = \mathcal{O}(1), \tag{2.73}$$

where Re denotes the real part and:

$$\beta_c \equiv \lim_{\eta \to \infty} \eta - F, \tag{2.74}$$

$$\gamma_c \equiv \lim_{\eta \to \infty} \eta_c - \eta. \tag{2.75}$$

The second terms of Ψ in equations (2.72) and (2.73) represent the viscous displacement. Despite the differences of Ψ according to subsonic or supersonic flow, for $y \ll 0$ it approximates to:

$$\Psi \sim y - (\beta_c + \gamma_c)\sqrt{\frac{2x}{R_\lambda}}, \tag{2.76}$$

which can be rewritten as:

$$\Psi \to \frac{y^{(0)}}{\sqrt{k_x R_\lambda}} \quad \text{as} \quad y \to 0, \tag{2.77}$$

where:

$$y^{(0)} \equiv \sqrt{2\bar{x}}\bar{\eta} \tag{2.78}$$

and

$$\bar{\eta} \equiv \eta - \beta_c. \tag{2.79}$$

Taking into account that the pressure and temperature fluctuations vanish in region IV, the equation (2.71) is substituted into the momentum equations (2.65)-(2.67) to find the velocity disturbance $\mathbf{u^{(0)}}\left(\bar{x}, y\right)$ obtained by:

$$\left(-i + \frac{\partial}{\partial \bar{x}} - \frac{\partial \Psi}{\partial x}\frac{\partial}{\partial y} - \frac{1}{k_x R_\lambda}\frac{\partial^2}{\partial y^2} + \kappa_z^2\right)\mathbf{u^{(0)}} = 0. \tag{2.80}$$

Introducing Ψ as a new independent variable into equation (2.80) leads to:

$$\left(-i + \frac{\partial}{\partial \bar{x}} - \frac{1}{k_x R_\lambda}\frac{\partial^2}{\partial \Psi^2} + \kappa_z^2\right)\mathbf{u^{(0)}} = \mathcal{O}\left(\frac{k_x}{R_\lambda}\right). \tag{2.81}$$

The solution of (2.81) that satisfies the upstream boundary condition in (2.3) (LWG [43]) is:

$$\mathbf{u^{(0)}} = \hat{\mathbf{u}}^\infty e^{i\left(\bar{x} + k_y \Psi\right) - \left(\kappa_z^2 + \kappa_y^2\right)\left(\bar{x} - \bar{x}_L^\dagger\right)}, \tag{2.82}$$

where:

$$\bar{x}_L^\dagger \equiv k_x x_L^\dagger \tag{2.83}$$

and

$$\kappa_y \equiv \frac{k_y}{\sqrt{k_x R_\lambda}}. \tag{2.84}$$

The solution (2.82) can be further simplified using equations (2.77) and (2.78) to:

$$\mathbf{u^{(0)}} = \hat{\mathbf{u}}^\infty e^{i\left(\bar{x} + \kappa_y y^{(0)}\right) - \left(\kappa_z^2 + \kappa_y^2\right)\bar{x}}. \tag{2.85}$$

2.4.2 Outer boundary conditions

The outer boundary conditions, i.e. $\eta \to \infty$, of the CLUBR equations (2.64)-(2.68) are found by matching the large-η limit of the CLUBR equations with the outer flow. Both components $\{\bar{u}, \bar{v}, \bar{w}, \bar{\tau}, \bar{p}\}$ and $\left\{\bar{u}^{(0)}, \bar{v}^{(0)}, \bar{w}^{(0)}, \bar{\tau}^{(0)}, \bar{p}^{(0)}\right\}$ satisfy the large-η limit of the CLUBR equations (2.64)-(2.68), which can be read in terms of $y^{(0)}$ as (cf. Ricco [55]):

large-η limit of the continuity equation

$$\frac{\partial \bar{u}}{\partial \bar{x}} - \frac{\beta_c + \gamma_c}{\sqrt{2\bar{x}}}\frac{\partial \bar{u}}{\partial y^{(0)}} + \sqrt{2\bar{x}}\frac{\partial \bar{v}}{\partial y^{(0)}} + \bar{w} + i\bar{\tau} - \frac{\partial \bar{\tau}}{\partial \bar{x}} = 0; \tag{2.86}$$

large-η limit of the x-momentum equation

$$\left(-i+\kappa_z^2\right)\bar{u}+\frac{\partial\bar{u}}{\partial\bar{x}}-\frac{\partial^2\bar{u}}{\partial y^{(0)2}}=0; \tag{2.87}$$

large-η limit of the y-momentum equation

$$\begin{aligned}-\frac{\beta_c+\gamma_c}{\left(2\bar{x}\right)^2}\bar{u}+\left(-i+\frac{1}{2\bar{x}}+\kappa_z^2\right)\bar{v}+\frac{\partial\bar{v}}{\partial\bar{x}}-\frac{\partial^2\bar{v}}{\partial y^{(0)2}}+\frac{1}{\sqrt{2\bar{x}}}\frac{\partial\bar{p}}{\partial y^{(0)}}\\ +\left(\beta_c+\gamma_c\right)\bar{\tau}-\frac{1}{3\sqrt{2\bar{x}}}\frac{\partial}{\partial\bar{x}}\left(\frac{\partial\bar{\tau}}{\partial y^{(0)}}\right)+\frac{i}{3\sqrt{2\bar{x}}}\frac{\partial\bar{\tau}}{\partial y^{(0)}};\end{aligned} \tag{2.88}$$

large-η limit of the z-momentum equation

$$\left(-i+\kappa_z^2\right)\bar{w}+\frac{\partial\bar{w}}{\partial\bar{x}}-\frac{\partial^2\bar{w}}{\partial y^{(0)2}}-\frac{1}{3}\kappa_z^2 i\bar{\tau}+\frac{1}{3}\kappa_z^2\frac{\partial\bar{\tau}}{\partial\bar{x}}-\kappa_z^2\bar{p}=0; \tag{2.89}$$

large-η limit of the energy equation

$$\left(-i+\frac{\kappa_z^2}{\mathrm{Pr}}\right)\bar{\tau}+\frac{\partial\bar{\tau}}{\partial\bar{x}}-\frac{1}{\mathrm{Pr}}\frac{\partial^2\bar{\tau}}{\partial y^{(0)2}}=0. \tag{2.90}$$

The solutions of the large-η limit equations (2.86)-(2.90) that match the outer solution (2.85) are:

$$\bar{u}=0, \tag{2.91}$$

$$\begin{aligned}\bar{v}=&\frac{ie^{i\bar{x}}}{\left(\kappa_y-i|\kappa_z|\right)\sqrt{2\bar{x}}}\left[e^{i\kappa_y y^{(0)}-\left(\kappa_z^2+\kappa_y^2\right)\bar{x}}-e^{-|\kappa_z|y^{(0)}}\right]\\ &+\frac{|\kappa_z|e^{i\bar{x}-|\kappa_z|y^{(0)}}}{\sqrt{2\bar{x}}}\int_0^{\bar{x}}g\left(\breve{x}\right)e^{-i\breve{x}}d\breve{x},\end{aligned} \tag{2.92}$$

$$\begin{aligned}\bar{w}=&\frac{e^{i\bar{x}}}{\kappa_y-i|\kappa_z|}\left[\kappa_y e^{i\kappa_y y^{(0)}-\left(\kappa_z^2+\kappa_y^2\right)\bar{x}}-i|\kappa_z|e^{-|\kappa_z|y^{(0)}}\right]\\ &+\kappa_z^2 e^{i\bar{x}-|\kappa_z|y^{(0)}}\int_0^{\bar{x}}g\left(\breve{x}\right)e^{-i\breve{x}}d\breve{x},\end{aligned} \tag{2.93}$$

$$\bar{\tau}=0, \tag{2.94}$$

$$\bar{p}=g\left(\bar{x}\right)e^{-|\kappa_z|y^{(0)}}, \tag{2.95}$$

and

$$\bar{u}^{(0)}=\frac{e^{i\bar{x}}}{\kappa_y-i|\kappa_z|}\left[\kappa_y e^{i\kappa_y y^{(0)}-\left(\kappa_z^2+\kappa_y^2\right)\bar{x}}-i|\kappa_z|e^{-|\kappa_z|y^{(0)}}\right], \tag{2.96}$$

$$\begin{aligned}\bar{v}^{(0)}=&\frac{e^{i\bar{x}-|\kappa_z|y^{(0)}}}{\kappa_y-i|\kappa_z|}\left[-2i\left|\kappa_z\right|^3\left(\beta_c+\gamma_c\right)+\frac{1}{\sqrt{2\bar{x}}}+\frac{\beta_c+\gamma_c}{4\bar{x}}i|\kappa_z|\left(1+2|\kappa_z|y^{(0)}\right)\right]\\ &+\frac{e^{i\bar{x}+i\kappa_y y^{(0)}-\left(\kappa_z^2+\kappa_y^2\right)\bar{x}}}{\kappa_y-i|\kappa_z|}\left[\frac{\kappa_y\left(\beta_c+\gamma_c\right)\left(\kappa_y^2-\kappa_z^2\right)}{2\bar{x}\left(\kappa_z^2+\kappa_y^2\right)}-\frac{1+i\left(\kappa_z^2+\kappa_y^2\right)}{\sqrt{2\bar{x}}}\right]\\ &+\frac{|\kappa_z|}{\sqrt{2\bar{x}}}e^{i\bar{x}-|\kappa_z|y^{(0)}}\int_0^{\bar{x}}g^{(0)}\left(\breve{x}\right)e^{-i\breve{x}}d\breve{x},\end{aligned} \tag{2.97}$$

$$\begin{aligned}\bar{w}^{(0)} =&\frac{2i\left(\beta_c+\gamma_c\right)\kappa_y^2\kappa_z^2}{\sqrt{2\bar{x}}\left(\kappa_z^2+\kappa_y^2\right)\left(\kappa_y-i|\kappa_z|\right)}e^{i\bar{x}+i\kappa_y y^{(0)}-\left(\kappa_z^2+\kappa_y^2\right)\bar{x}}\\&+\frac{i\kappa_z^2\left(\beta_c+\gamma_c\right)}{\kappa_y-i|\kappa_z|}e^{i\bar{x}-|\kappa_z|y^{(0)}}\left[\frac{1}{2\sqrt{2\bar{x}}}+\frac{|\kappa_z|y^{(0)}}{\sqrt{2\bar{x}}}-2\kappa_z^2\sqrt{2\bar{x}}\right]\\&+\kappa_z^2e^{i\bar{x}-|\kappa_z|y^{(0)}}\int_0^{\bar{x}}g^{(0)}\left(\breve{x}\right)e^{-i\breve{x}}d\breve{x},\end{aligned}\tag{2.98}$$

$$\bar{\tau}^{(0)}=0,\tag{2.99}$$

$$\begin{aligned}\bar{p}^{(0)} =&-\frac{i\left(\beta_c+\gamma_c\right)e^{i\bar{x}}}{\left(2\bar{x}\right)^{\frac{3}{2}}\left(\kappa_y-i|\kappa_z|\right)}\left[\left(\frac{1}{2}+|\kappa_z|y^{(0)}\right)e^{-|\kappa_z|y^{(0)}}\right.\\&\left.+\frac{2\kappa_y^2}{\kappa_z^2+\kappa_y^2}e^{i\kappa_y y^{(0)}-\left(\kappa_z^2+\kappa_y^2\right)\bar{x}}\right]+g^{(0)}\left(\bar{x}\right)e^{-|\kappa_z|y^{(0)}},\end{aligned}\tag{2.100}$$

where the functions $g\left(\bar{x}\right)$ and $g^{(0)}\left(\bar{x}\right)$ are unknown functions. However, its behaviour can be determined as $\bar{x}\to 0$ by matching with region I (see LWG [43] and Ricco [56]). The solutions (2.91)-(2.99) match the ones found by Ricco [56] for the incompressible case. Based on LWG [43], $g\left(\bar{x}\right)$ and $g^{(0)}\left(\bar{x}\right)$ can be eliminated from the solutions (2.92), (2.93), (2.95), (2.97), (2.98) and (2.100) by imposing the mixed type boundary conditions as $\eta\to\infty$:

$$\bar{u}=0,\tag{2.101}$$

$$\frac{\partial\bar{v}}{\partial\eta}+|\kappa_z|\sqrt{2\bar{x}}\bar{v}\to-e^{\left(i-\kappa_z^2-\kappa_y^2\right)\bar{x}+i\kappa_y\sqrt{2\bar{x}}\bar{\eta}},\tag{2.102}$$

$$\frac{\partial\bar{w}}{\partial\eta}+|\kappa_z|\sqrt{2\bar{x}}\bar{w}\to i\kappa_y\sqrt{2\bar{x}}e^{\left(i-\kappa_z^2-\kappa_y^2\right)\bar{x}+i\kappa_y\sqrt{2\bar{x}}\bar{\eta}},\tag{2.103}$$

$$\bar{\tau}=0,\tag{2.104}$$

$$\frac{\partial\bar{p}}{\partial\eta}+|\kappa_z|\sqrt{2\bar{x}}\bar{p}\to 0,\tag{2.105}$$

and

$$\frac{\partial\bar{u}^{(0)}}{\partial\eta}+|\kappa_z|\sqrt{2\bar{x}}\bar{u}^{(0)}\to 0,\tag{2.106}$$

$$\begin{aligned}\frac{\partial\bar{v}^{(0)}}{\partial\eta}+|\kappa_z|\sqrt{2\bar{x}}\bar{v}^{(0)}\to&\frac{i\kappa_z^2\left(\beta_c+\gamma_c\right)e^{i\bar{x}-|\kappa_z|\sqrt{2\bar{x}}\bar{\eta}}}{\sqrt{2\bar{x}}\left(\kappa_y-i|\kappa_z|\right)}\\&\times\left[\frac{1}{\sqrt{2\bar{x}}}\frac{i\kappa_y\left(\beta_c+\gamma_c\right)\left(\kappa_y^2-\kappa_z^2\right)}{\kappa_z^2+\kappa_y^2}-i+\kappa_z^2+\kappa_y^2\right]\\&\times e^{i\kappa_y\sqrt{2\bar{x}}\bar{\eta}+i\bar{x}-\left(\kappa_z^2+\kappa_y^2\right)\bar{x}},\end{aligned}\tag{2.107}$$

$$\frac{\partial \bar{w}^{(0)}}{\partial \eta} + |\kappa_z|\sqrt{2\bar{x}}\bar{w}^{(0)} \rightarrow \frac{i\,|\kappa_z|^3\,(\beta_c+\gamma_c)\,e^{i\bar{x}-|\kappa_z|\sqrt{2\bar{x}}\bar{\eta}}}{\kappa_y - i|\kappa_z|} - \frac{1}{\kappa_z^2+\kappa_y^2} 2\kappa_z^2\kappa_y^2\,(\beta_c+\gamma_c)\,e^{i\kappa_y\sqrt{2\bar{x}}\bar{\eta}+i\bar{x}-\left(\kappa_z^2+\kappa_y^2\right)\bar{x}}, \tag{2.108}$$

$$\bar{\tau}^{(0)} = 0, \tag{2.109}$$

$$\frac{\partial \bar{p}^{(0)}}{\partial \eta} + |\kappa_z|\sqrt{2\bar{x}}\bar{p}^{(0)} \rightarrow -\frac{i\kappa_z\,(\beta_c+\gamma_c)\,e^{i\bar{x}-|\kappa_z|\sqrt{2\bar{x}}\bar{\eta}}}{2\bar{x}\,(\kappa_y - i\kappa_z)} + \frac{\kappa_y^2\,(\beta_c+\gamma_c)\,e^{i\kappa_y\sqrt{2\bar{x}}\bar{\eta}+i\bar{x}-\bar{x}\left(\kappa_z^2+\kappa_y^2\right)}}{\bar{x}\left(\kappa_z^2+\kappa_y^2\right)}. \tag{2.110}$$

The external vortical forcing disturbances from the outer flow are represented as the non-zero terms on the right-hand-side of the boundary conditions.

2.4.3 Upstream behaviour of the boundary region solution

The appropriate initial conditions for the CLUBR equations (2.64)-(2.68) are obtained by seeking the power series solutions for $\eta = \mathcal{O}(1)$ and $\bar{x} \ll \mathcal{O}(1)$:

$$\{\bar{u},\bar{v},\bar{w},\bar{\tau},\bar{p}\} = \sum_{n=0}^{\infty} (2\bar{x})^{\frac{n}{2}} \times \left\{2\bar{x}\tilde{U}_n(\eta), \tilde{V}_n(\eta), \tilde{W}_n(\eta), 2\bar{x}\tilde{T}_n(\eta), \frac{1}{\sqrt{2\bar{x}}}\tilde{P}_n(\eta)\right\}, \tag{2.111}$$

$$\left\{\bar{u}^{(0)},\bar{v}^{(0)},\bar{w}^{(0)},\bar{\tau}^{(0)},\bar{p}^{(0)}\right\} = \sum_{n=0}^{\infty} (2\bar{x})^{\frac{n}{2}} \times \left\{U_n(\eta), \frac{1}{2\bar{x}}V_n(\eta), \frac{1}{\sqrt{2\bar{x}}}W_n(\eta), T_n(\eta), \frac{1}{(2\bar{x})^{\frac{3}{2}}}P_n(\eta)\right\}. \tag{2.112}$$

The first two terms of the power series (2.111) are substituted into the CLUBR equations (2.64)-(2.68), and collecting the like powers of $\bar{x}$ results in two systems of ordinary differential equations, which are shown in Appendix D of Ricco [55]. The two sets of differential equations are solved to reach their solutions, which will be used to obtain the initial conditions of the components denoted as $\{\bar{u},\bar{v},\bar{w},\bar{\tau},\bar{p}\}$, as $\bar{x} \ll 1$. Similarly, to achieve the initial conditions for the components expressed as $\left\{\bar{u}^{(0)},\bar{v}^{(0)},\bar{w}^{(0)},\bar{\tau}^{(0)},\bar{p}^{(0)}\right\}$, as $\bar{x} \ll 1$, the power series (2.112) is expanded and the first three terms are substituted into the CLUBR

equations (2.64)-(2.68), and collecting like powers of $\bar{x}$ results in three sets of ordinary differential equations included in Appendix A, together with its boundary conditions. The additive rule is then used to construct a composite solution that is valid for every value of η. The composite solution is achieved by adding the first two terms of the power series (2.111) and the first three terms of the power series (2.112) to the equations (2.91)-(2.95) and (2.96)-(2.100), respectively, and subtracting their common parts. The initial conditions to be imposed for $\bar{x} \ll 1$ are:

$$\bar{u} \to 2\bar{x}\tilde{U}_0 + (2\bar{x})^{\frac{3}{2}}\,\tilde{U}_1, \tag{2.113}$$

$$\begin{aligned}\bar{v} \to & \tilde{V}_0 + \sqrt{2\bar{x}}\tilde{V}_1 + \frac{i}{(\kappa_y - i|\kappa_z|)\sqrt{2\bar{x}}}\left[e^{-\left(\kappa_z^2+\kappa_y^2\right)\bar{x}+i\kappa_y\sqrt{2\bar{x}}\bar{\eta}} - e^{-|\kappa_z|\sqrt{2\bar{x}}\bar{\eta}}\right] \\ & - \left(\frac{3}{4}\beta - \frac{|\kappa_z|}{2}g_1\sqrt{2\bar{x}}\right)e^{-|\kappa_z|\sqrt{2\bar{x}}\bar{\eta}} - \bar{v}_c,\end{aligned} \tag{2.114}$$

$$\begin{aligned}\bar{w} \to & \tilde{W}_0 + \sqrt{2\bar{x}}\tilde{W}_1 + \frac{1}{\kappa_y - i|\kappa_z|}\left[\kappa_y e^{-\left(\kappa_z^2+\kappa_y^2\right)\bar{x}+i\kappa_y\sqrt{2\bar{x}}\bar{\eta}} - i|\kappa_z|e^{-|\kappa_z|\sqrt{2\bar{x}}\bar{\eta}}\right] \\ & - \frac{3}{4}\beta|\kappa_z|\sqrt{2\bar{x}}e^{-|\kappa_z|\sqrt{2\bar{x}}\bar{\eta}} - \bar{w}_c,\end{aligned} \tag{2.115}$$

$$\bar{\tau} \to 2\bar{x}\tilde{T}_0 + (2\bar{x})^{\frac{3}{2}}\,\tilde{T}_1, \tag{2.116}$$

$$\bar{p} \to \frac{\tilde{P}_0}{\sqrt{2\bar{x}}} + \tilde{P}_1 + \left(g_1 - \frac{V_c}{|\kappa_z|\sqrt{2\bar{x}}}\right)e^{-|\kappa_z|\sqrt{2\bar{x}}\bar{\eta}} - \bar{p}_c, \tag{2.117}$$

and

$$\begin{aligned}\bar{u}^{(0)} \to & U_0 + \sqrt{2\bar{x}}U_1 + 2\bar{x}U_2 \\ & + \frac{e^{i\bar{x}}}{\kappa_y - i|\kappa_z|}\left[\kappa_y e^{i\kappa_y y^{(0)} - \left(\kappa_z^2+\kappa_y^2\right)\bar{x}} - i|\kappa_z|e^{-|\kappa_z|y^{(0)}}\right] \\ & - \left[1 + \sqrt{2\bar{x}}\left(-|\kappa_z| + i\kappa_y\right)\bar{\eta} + \bar{x}\left(i - i|\kappa_z|\kappa_y - \kappa_y^2 + \left(\kappa_z^2 - i|\kappa_z|\kappa_y - \kappa_y^2\right)\bar{\eta}^2\right)\right],\end{aligned} \tag{2.118}$$

$$
\begin{aligned}
\bar{v}^{(0)} \to & \frac{1}{2\bar{x}} V_{0,0} + \frac{1}{\sqrt{2\bar{x}}} V_1 + V_2 \\
& + \frac{e^{i\bar{x} - |\kappa_z| y^{(0)}}}{\kappa_y - i|\kappa_z|} \left(-2i \left|\kappa_z\right|^3 \left(\beta_c + \gamma_c\right) + \frac{1}{\sqrt{2\bar{x}}} + \frac{\beta_c + \gamma_c}{4\bar{x}} i|\kappa_z| \left(1 + 2|\kappa_z| y^{(0)}\right) \right) \\
& + \frac{e^{i\bar{x} + i\kappa_y y^{(0)} - \left(\kappa_z^2 + \kappa_y^2\right)\bar{x}}}{\kappa_y - i|\kappa_z|} \left(\frac{\kappa_y \left(\beta_c + \gamma_c\right) \left(\kappa_y^2 - \kappa_z^2\right)}{2\bar{x} \left(\kappa_z^2 + \kappa_y^2\right)} - \frac{1 + i \left(\kappa_z^2 + \kappa_y^2\right)}{\sqrt{2\bar{x}}} \right) \\
& + \frac{|\kappa_z|}{\sqrt{2\bar{x}}} e^{i\bar{x} - |\kappa_z| y^{(0)}} \left[\frac{1}{|\kappa_z| \sqrt{2\bar{x}}} \left(V_{0,0} - \left(\beta_c + \gamma_c\right) \frac{i \left|\kappa_z\right|^3 + i|\kappa_z| \kappa_y^2 + 2\kappa_y^3 - 2\kappa_z^2 \kappa_y}{2 \left(\kappa_y - i|\kappa_z|\right) \left(\kappa_z^2 + \kappa_y^2\right)} \right) \right. \\
& \left. + \frac{g_1^{(0)}}{|\kappa_z|} + \frac{g_2^{(0)}}{|\kappa_z|} \sqrt{2\bar{x}} \right] \\
& - \left[\frac{1}{2\bar{x}} V_{0,0} + \frac{1}{\sqrt{2\bar{x}}} \left(|\kappa_z| - i\kappa_y + g_1^{(0)} + \left(-V_{0,0} |\kappa_z| \right. \right. \right. \\
& \left. \left. \left. - \frac{\left(\beta_c + \gamma_c\right) \left(\kappa_z^2 - i|\kappa_z| \kappa_y - \kappa_y^2\right)}{|\kappa_z| - i\kappa_y} \right) \bar{\eta} \right) + g_2^{(0)} + V_{0,0} \frac{i}{2} \right. \\
& + \frac{\left(\beta_c + \gamma_c\right) \left(4 \left|\kappa_z\right|^3 + i\kappa_z^2 \kappa_y - i\kappa_y^3\right)}{2 \left(|\kappa_z| + i\kappa_y\right)} + \left(-i - |\kappa_z| g_1^{(0)} + i|\kappa_z| \kappa_y + \kappa_y^2 \right) \bar{\eta} \\
& \left. + \frac{1}{2} \left(\kappa_z^2 V_{0,0} + \left(\beta_c + \gamma_c\right) \left(2\kappa_z^2 - i|\kappa_z| \kappa_y - \kappa_y^2\right) \right) \bar{\eta}^2 \right],
\end{aligned}
\tag{2.119}
$$

$$
\begin{aligned}
\bar{w}^{(0)} \to & \frac{1}{\sqrt{2\bar{x}}} W_0 + W_1 + \sqrt{2\bar{x}} W_2 \\
& + \frac{2i \left(\beta_c + \gamma_c\right) \kappa_y^2 \kappa_z^2}{\sqrt{2\bar{x}} \left(\kappa_z^2 + \kappa_y^2\right) \left(\kappa_y - i|\kappa_z|\right)} e^{i\bar{x} + i\kappa_y y^{(0)} - \left(\kappa_z^2 + \kappa_y^2\right)\bar{x}} \\
& + \frac{i\kappa_z^2 \left(\beta_c + \gamma_c\right)}{\kappa_y - i|\kappa_z|} e^{i\bar{x} - |\kappa_z| y^{(0)}} \left(\frac{1}{2\sqrt{2\bar{x}}} + \frac{|\kappa_z| y^{(0)}}{\sqrt{2\bar{x}}} - 2\kappa_z^2 \sqrt{2\bar{x}} \right) \\
& + \kappa_z^2 e^{i\bar{x} - |\kappa_z| y^{(0)}} \left[\frac{1}{|\kappa_z| \sqrt{2\bar{x}}} \left(V_{0,0} - \left(\beta_c + \gamma_c\right) \frac{i \left|\kappa_z\right|^3 + i|\kappa_z| \kappa_y^2 + 2\kappa_y^3 - 2\kappa_z^2 \kappa_y}{2 \left(\kappa_y - i|\kappa_z|\right) \left(\kappa_z^2 + \kappa_y^2\right)} \right) \right. \\
& \left. + \frac{g_1^{(0)}}{|\kappa_z|} + \frac{g_2^{(0)}}{|\kappa_z|} \sqrt{2\bar{x}} \right] - \left[\frac{1}{\sqrt{2\bar{x}}} \left(V_{0,0} |\kappa_z| + \frac{\left(\beta_c + \gamma_c\right) i|\kappa_z| \kappa_y}{\left(|\kappa_z| - i\kappa_y\right)} \right) \right. \\
& + |\kappa_z| g_1^{(0)} - \kappa_z^2 \left(V_{0,0} \ \left(\beta_c + \gamma_c\right) \right) \bar{\eta} + \sqrt{2\bar{x}} \left(|\kappa_z| g_2^{(0)} + \frac{i|\kappa_z|}{2} V_{0,0} \right. \\
& + \frac{\left(\beta_c + \gamma_c\right)}{2 \left(\kappa_z^2 + \kappa_y^2\right)} \left(-\kappa_z^2 \kappa_y - i|\kappa_z| \kappa_y^2 + 2 \left(|\kappa_z|^3 \kappa_y^2 - i\kappa_z^2 \kappa_y^3 \right) + 4 \left(|\kappa_z|^5 - i\kappa_z^4 \kappa_y \right) \right) \\
& \left. \left. - \kappa_z^2 g_1^{(0)} \bar{\eta} + \left(\frac{|\kappa_z|^3}{2} V_{0,0} + \frac{\left(\beta_c + \gamma_c\right) \left(2\kappa_z^4 - 3i \left|\kappa_z\right|^3 \kappa_y - 2\kappa_z^2 \kappa_y^2\right)}{2 \left(|\kappa_z| - i\kappa_y\right)} \right) \bar{\eta}^2 \right) \right],
\end{aligned}
\tag{2.120}
$$

$$\bar{\tau}^{(0)} \to T_0 + \sqrt{2\bar{x}} T_1 + 2\bar{x} T_2, \tag{2.121}$$

$$\begin{aligned}
\bar{p}^{(0)} \to & \frac{1}{(2\bar{x})^{\frac{3}{2}}} P_0 + \frac{1}{2\bar{x}} P_1 + \frac{1}{\sqrt{2\bar{x}}} P_2 \\
& + \left[-\frac{1}{|\kappa_z| (2\bar{x})^{3/2}} \left(V_{0,0} - (\beta_c + \gamma_c) \frac{i |\kappa_z|^3 + i|\kappa_z|\kappa_y^2 + 2\kappa_y^3 - 2\kappa_z^2 \kappa_y}{2 (\kappa_y - i|\kappa_z|) \left(\kappa_z^2 + \kappa_y^2\right)} \right) + \frac{g_2^{(0)}}{|\kappa_z| \sqrt{2\bar{x}}} \right. \\
& \left. - \frac{i}{2|\kappa_z| \sqrt{2\bar{x}}} \left(V_{0,0} - (\beta_c + \gamma_c) \frac{i |\kappa_z|^3 + i|\kappa_z|\kappa_y^2 + 2\kappa_y^3 - 2\kappa_z^2 \kappa_y}{2 (\kappa_y - i|\kappa_z|) \left(\kappa_z^2 + \kappa_y^2\right)} \right) \right] e^{-|\kappa_z| y^{(0)}} \\
& - \frac{i (\beta_c + \gamma_c) e^{i\bar{x}}}{(2\bar{x})^{\frac{3}{2}} (\kappa_y - i|\kappa_z|)} \left[\left(\frac{1}{2} + |\kappa_z| y^{(0)} \right) e^{-|\kappa_z| y^{(0)}} + \frac{2\kappa_y^2}{\kappa_z^2 + \kappa_y^2} e^{i\kappa_y y^{(0)} - \left(\kappa_z^2 + \kappa_y^2\right)\bar{x}} \right] \\
& - \left[\frac{1}{(2\bar{x})^{3/2}} \left(-\frac{1}{|\kappa_z|} V_{0,0} - \frac{(\beta_c + \gamma_c) i\kappa_y}{|\kappa_z| (|\kappa_z| - i\kappa_y)} \right) \right. \\
& + \frac{1}{2\bar{x}} \left((V_{0,0} + (\beta_c + \gamma_c)) \bar{\eta} \right) + \frac{1}{\sqrt{2\bar{x}}} \left(-\frac{i}{2\kappa_z} V_{0,0} \right. \\
& + \frac{g_2^{(0)}}{|\kappa_z|} - \frac{(\beta_c + \gamma_c) \left(2\kappa_z^2 \kappa_y^2 - |\kappa_z|\kappa_y - i\kappa_y^2 - 2i|\kappa_z|\kappa_y^3\right)}{2|\kappa_z| (|\kappa_z| - i\kappa_y) (|\kappa_z| + i\kappa_y)} \\
& \left. \left. - \left(\frac{|\kappa_z|}{2} V_{0,0} + \frac{(\beta_c + \gamma_c) \left(2\kappa_z^2 - 3i|\kappa_z|\kappa_y - 2\kappa_y^2\right)}{2 (|\kappa_z| - i\kappa_y)} \right) \bar{\eta}^2 \right) \right],
\end{aligned} \tag{2.122}$$

where V_c, g_1 along with the common parts $\bar{v}_c$, $\bar{w}_c$ and $\bar{p}_c$ are found to be (cf. Appendix D in Ricco [55]):

$$V_c = -\lim_{\eta \to \infty} \left(V_0 - \bar{\eta} \right), \tag{2.123}$$

$$g_1 = \frac{2c_1}{|\kappa_z|} + 2V_c \beta_c + i \left(\beta_c^2 + 1\right) \left(\frac{\kappa_y}{|\kappa_z|} + i \right), \tag{2.124}$$

$$\bar{v}_c = -\bar{\eta} - V_c + \sqrt{2\bar{x}} \left(-\frac{i}{2} (\kappa_y + i|\kappa_z|) \left(\bar{\eta}^2 + 1\right) + V_c |\kappa_z| \bar{\eta} + \frac{1}{2} |\kappa_z| g_1 \right), \tag{2.125}$$

$$\bar{w}_c = 1 + \sqrt{2\bar{x}} \left(-i (\kappa_y + i|\kappa_z|) \bar{\eta} - V_c |\kappa_z| \right), \tag{2.126}$$

$$\bar{p}_c = \frac{P_0}{\sqrt{2\bar{x}}} + g_1 + V_c \bar{\eta}. \tag{2.127}$$

The limit $V_{0,0}$ and the constants $g_1^{(0)}$ and $g_2^{(0)}$ can be found in Appendix A.

2.5 Numerical procedures of the boundary region equations

The Blasius mean-flow momentum equation (2.29) and energy equation (2.30) are decomposed into five ordinary differential equations, and their solutions are subsequently found using an implicit second-order finite-difference numerical scheme. The nonlinear system is solved using the Newton-Raphson method (see Cebeci [14]).

The CLUBR equations (2.64)-(2.68) are elliptic in the spanwise direction and parabolic in the streamwise direction, and thus they can be marched downstream with only having knowledge of the initial, outer and wall boundary conditions. At the wall, the no-slip condition is used together with an adiabatic wall.

The components $\bar{u}$, $\bar{v}$, $\bar{w}$, $\bar{\tau}$ and $\bar{p}$ are found by solving the boundary region system (2.64)-(2.68) with the boundary conditions (2.101)-(2.105) and the initial conditions (2.113)-(2.117). The system is solved by a second-order finite difference scheme which is central in η and backward in $\bar{x}$. The stencil is illustrated in figure 2.2. The derivatives of the velocity and temperature fluctuations are approximated as:

$$\frac{\partial u}{\partial \eta} \approx \frac{u_{i,j+1} - u_{i,j-1}}{2\Delta\eta}, \tag{2.128}$$

$$\frac{\partial^2 u}{\partial \eta^2} \approx \frac{u_{i,j+1} - 2u_{i,j} + u_{i,j-1}}{(\Delta\eta)^2}, \tag{2.129}$$

$$\frac{\partial u}{\partial \bar{x}} \approx \frac{a u_{i,j} + b u_{i-1,j} + c u_{i-2,j}}{\Delta\bar{x}}, \tag{2.130}$$

$$\frac{\partial^2 u}{\partial \bar{x}\partial \eta} \approx \frac{a\left(u_{i,j+1} - u_{i,j-1}\right) + b\left(u_{i-1,j+1} - u_{i-1,j-1}\right) + c\left(u_{i-2,j+1} - u_{i-2,j-1}\right)}{2\Delta\bar{x}\Delta\eta}, \tag{2.131}$$

where $a = 3/2$, $b = -2$ and $c = 1/2$. To avoid the pressure decoupling phenomenon, the pressure is calculated using a staggered grid in the η direction with respect to the grid of the velocities and temperature. The pressure and its derivative is approximated as:

$$p \approx \frac{p_{i,j+1/2} + p_{i,j-1/2}}{2}, \tag{2.132}$$

$$\frac{\partial p}{\partial \eta} \approx \frac{p_{i,j+1/2} - p_{i,j-1/2}}{\Delta \eta}. \tag{2.133}$$

Due to the second-order numerical method used in the streamwise direction to

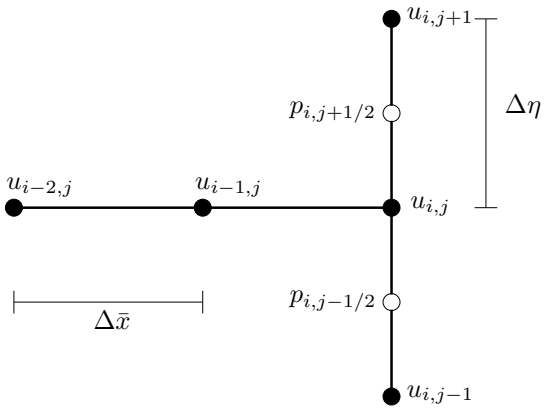

Figure 2.2: The second-order stencil in $\bar{x}$ and η used to compute the boundary region equations.

obtain the solutions of $\bar{u}$, $\bar{v}$, $\bar{w}$, $\bar{\tau}$ and $\bar{p}$, the initial conditions (2.113)-(2.117) were computed at the locations $\bar{x}_0$ and $\bar{x}_0 + \Delta\bar{x}$, where $\bar{x}_0 =$ indicates the initial location of $\bar{x}$ and is prescribed as $\bar{x}_0 = 10^(-9)$.

After performing mesh independence checks on the solutions $\bar{u}$, $\bar{v}$, $\bar{w}$, $\bar{\tau}$ and $\bar{p}$, the appropriate values were determined to be $\Delta\bar{x} = 0.0005$ and $\Delta\eta = 0.03$.

For the components $\bar{u}^{(0)}$, $\bar{v}^{(0)}$, $\bar{w}^{(0)}$, $\bar{\tau}^{(0)}$ and $\bar{p}^{(0)}$, the boundary region equations (2.64)-(2.68) are solved with the initial conditions (2.118)-(2.122) and boundary conditions (3.3)-(2.110) using a similar finite difference scheme in η but using a third-order backwards scheme in $\bar{x}$, as shown in figure 2.3. The derivatives in $\bar{x}$ are approximated as:

$$\frac{\partial u}{\partial \bar{x}} \approx \frac{a_3 u_{i,j} + b_3 u_{i-1,j} + c_3 u_{i-2,j} + d_3 u_{i-3,j}}{\Delta\bar{x}}, \tag{2.134}$$

and

$$\begin{aligned}\frac{\partial^2 u}{\partial \bar{x} \partial \eta} \approx & \frac{a\left(u_{i,j+1} - u_{i,j-1}\right) + b\left(u_{i-1,j+1} - u_{i-1,j-1}\right)}{2\Delta\bar{x}\Delta\eta} \\ & + \frac{c\left(u_{i-2,j+1} - u_{i-2,j-1}\right) + d\left(u_{i-3,j+1} - u_{i-3,j-1}\right)}{2\Delta\bar{x}\Delta\eta},\end{aligned} \tag{2.135}$$

where $a_3 = 11/6$, $b_3 = -3$, $c_3 = 3/2$ and $d_3 = -1/3$.

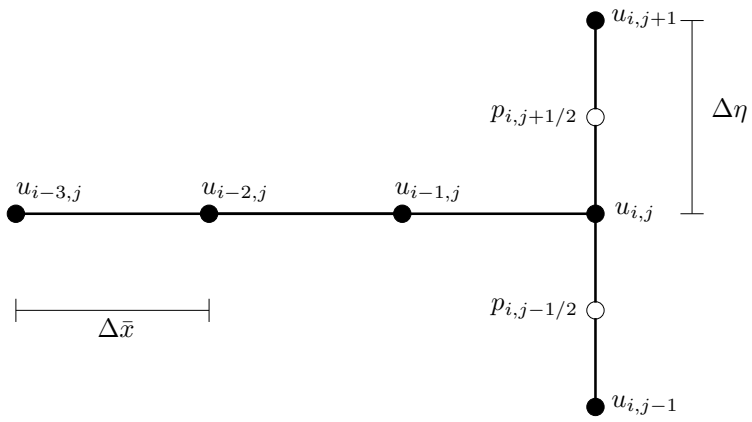

Figure 2.3: The third-order stencil in $\bar{x}$ and second-order in η used to compute the boundary region equations.

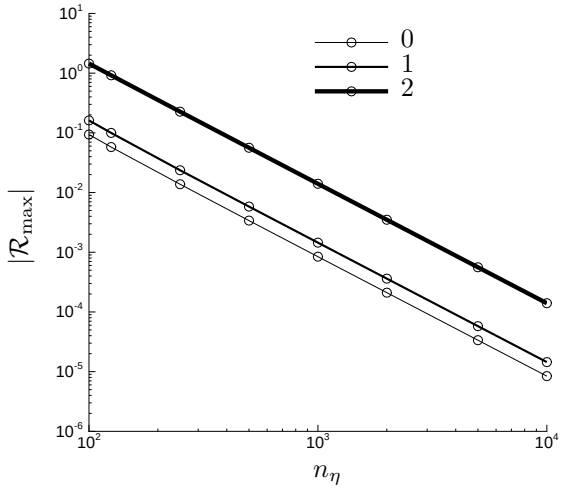

Figure 2.4: The plot shows the maximum residual error per number of points used in the η direction to compute the power series solutions for $M = 3$, $\kappa_z = 1$ and $\kappa_y = 1$. The legend indicates the power series coefficient number for the components $\bar{u}^{(0)}$, $\bar{v}^{(0)}$, $\bar{w}^{(0)}$, $\bar{\tau}^{(0)}$ and $\bar{p}^{(0)}$.

The increased order in the streamwise direction is necessary because $\bar{v}^{(0)}$ and $\bar{w}^{(0)}$ are singular for $\bar{x} \ll 1$; this can be seen in equation (2.112). In both systems, the pressure components $\bar{p}$ and $\bar{p}^{(0)}$ are singular for $\bar{x} \ll 1$, but do not affect the marching scheme because the streamwise pressure gradient term is not present in CLUBR equations. The third-order numerical scheme also requires the initial conditions (2.113)-(2.117) to be computed at the locations $\bar{x}_0$, $\bar{x}_0 + \Delta\bar{x}$ and $\bar{x}_0 + 2\Delta\bar{x}$. Due to the singularities as $\bar{x} \ll 1$, the initial location is set to $\bar{x}_0 = 0.0009$. In addition, the mesh independence checks revealed that the previous value of $\Delta\bar{x}$ was not enough to ensure mesh independence as $\bar{x} \ll 1$, and thus the values $\Delta\bar{x} = 0.00005$ and $\Delta\eta = 0.03$ were used instead.

The power series terms (2.111) and (2.112) for the CLUBR system initial conditions were computed using an implicit centred second-order scheme in η. For the components $\bar{u}^{(0)}$, $\bar{v}^{(0)}$, $\bar{w}^{(0)}$, $\bar{\tau}^{(0)}$ and $\bar{p}^{(0)}$, the error based on the absolute residual $|\mathcal{R}_{\max}|$ is plotted with the number of points in η for a fixed maximum $\eta = 15$, as shown in figure 2.4. All three series showed a -2 slope in the logarithm scale, as expected by the second-order scheme. The definition of the absolute residual $|\mathcal{R}_{\max}|$ is the absolute maximum residual for each power series equations system, i.e. equations (A.1)-(A.5), (A.6)-(A.10) and (A.11)-(A.15).

Resolution checks were performed on all numerical schemes to ensure mesh independence. The code was also validated by comparison with all the results displayed in LWG [43], Ricco & Wu [58] and Ricco [56]; the results were perfectly matched because the numerical schemes used are identical, and thus this work is also comparable to the experiments matched in the aforementioned papers. The numerical procedure used to find the numerical solutions of the boundary region equations and power series terms is fully described in Cebeci [14] from pages 260-264. Further information about the numerical simulations of the components $\{\bar{u}, \bar{v}, \bar{w}, \bar{\tau}, \bar{p}\}$ is found in Ricco [55] and in [56] for the components denoted as $\left\{\bar{u}^{(0)}, \bar{v}^{(0)}, \bar{w}^{(0)}, \bar{\tau}^{(0)}, \bar{p}^{(0)}\right\}$.

2.6 Numerical solutions of the boundary region equations

2.6.1 Response of a two-dimensional free-stream gust

The compressible boundary layer disturbances $\bar{u}^{(0)}$, $\bar{v}^{(0)}$, $\bar{\tau}^{(0)}$ and $\bar{p}^{(0)}$ induced by a free-stream two-dimensional gust is studied to extend the incompressible results obtained by Ricco [56]. The boundary layer response to the gust is evaluated by considering a wall-normal wavelength comparable with the boundary-layer thickness, i.e. $\kappa_z \to 0$ at $\bar{x} = \mathcal{O}(1)$ or $\lambda_z^* \gg \delta^*$. Hereinafter the notation $\kappa_z = 0$ is adopted to describe $\kappa_z = 10^{-5}$. A value of zero cannot be assigned to κ_z because it appears as a denominator in the initial conditions for the pressure component (2.122).

The streamwise velocity $|\bar{u}^{(0)}|$ and temperature $\bar{\tau}^{(0)}$ fluctuations for $M = 3$, $\kappa_z = 0$ and $\kappa_y = 1$ are plotted in the left and right of figure 2.5, respectively. The streamwise velocity $|\bar{u}^{(0)}|$ fluctuations in the free-stream decay faster downstream than the fluctuations within the boundary layer. The peak also shifts from approximately $\eta \approx 3.5$ at $\bar{x} = 0.1$ to $\eta \approx 2.5$ at $\bar{x} = 2.5$. The magnitude of $\bar{\tau}^{(0)}$ decays faster close to the wall than further away from it as the flow evolves downstream. The amplitude of the wall-normal $\bar{v}^{(0)}$ velocity fluctuations for $M = 3$, $\kappa_z = 0$ and $\kappa_y = 1$ are plotted in figure 2.6. The wall-normal velocity $|\bar{v}^{(0)}|$ peak within the boundary layer shifts from the edge of the boundary layer approximately $\eta \approx 4.5$ to the centre at $\eta \approx 2.5$ as the flow develops downstream, and the frequency of the peaks increases. As expected, the spanwise velocity magnitude $|\bar{w}^{(0)}|$ is very small because $\kappa_z \to 0$.

The evolution of the streamwise velocity $\bar{u}^{(0)}$ and temperature $\bar{\tau}^{(0)}$ perturbation magnitude for $M = 3$, $\kappa_z = 0$ and $\kappa_y = 2$ are shown in the left and right of figure 2.7, respectively. The amplitude of the velocity $\bar{u}^{(0)}$ decays at a faster rate in the free stream than within the boundary layer core. This disparity increases with κ_y and additionally, the peak of the streamwise velocity $\bar{u}^{(0)}$ magnitude

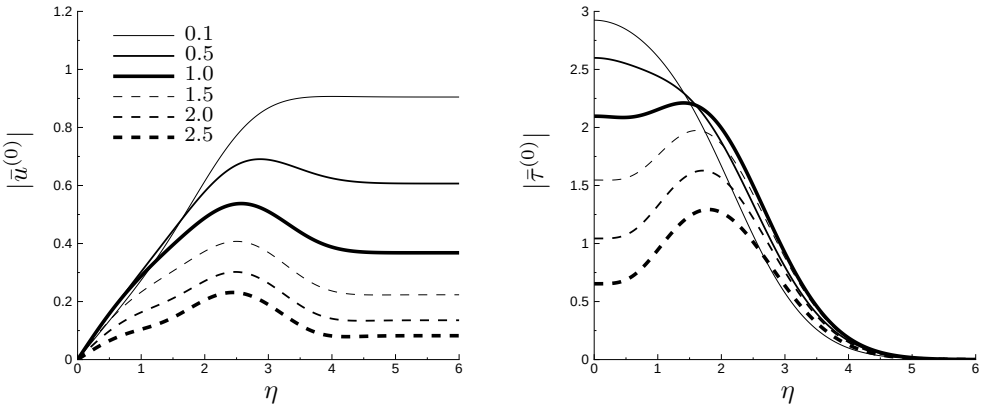

Figure 2.5: Amplitude of the streamwise velocity $\bar{u}^{(0)}$ (left) and temperature $\bar{\tau}^{(0)}$ (right) fluctuations for $M = 3$, $\kappa_z = 0$ and $\kappa_y = 1$ at the indicated values of $\bar{x}$.

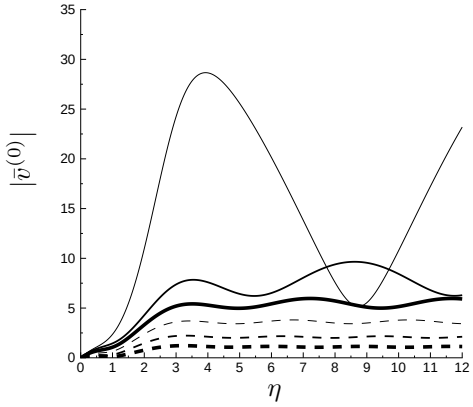

Figure 2.6: Amplitude of the wall-normal $\bar{v}^{(0)}$ velocity fluctuations for $M = 3$, $\kappa_z = 0$ and $\kappa_y = 1$ at the indicated values of $\bar{x}$ in figure 2.5.

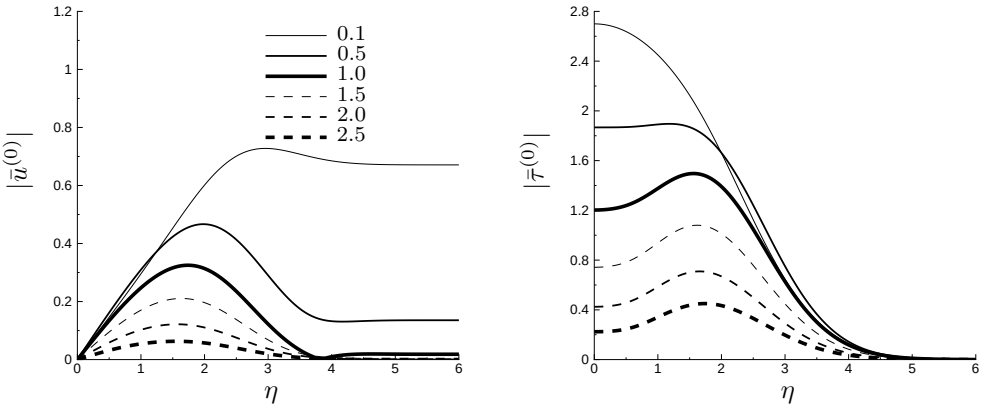

Figure 2.7: Amplitude of the streamwise velocity $\bar{u}^{(0)}$ (left) and temperature $\bar{\tau}^{(0)}$ (right) fluctuations for $M = 3$, $\kappa_z = 0$ and $\kappa_y = 2$ at the indicated values of $\bar{x}$.

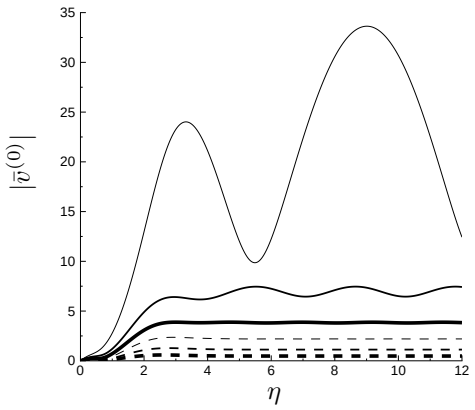

Figure 2.8: Amplitude of the wall-normal $\bar{v}^{(0)}$ velocity fluctuations for $M = 3$, $\kappa_z = 0$ and $\kappa_y = 2$ at the indicated values of $\bar{x}$ in figure 2.7.

shifts to the wall as κ_y increases. At small values of $\bar{x}$, i.e. $\bar{x} \leq 0.1$ the magnitude peak of the temperature $\bar{\tau}^{(0)}$ perturbations appears at the wall or nearby. As the flow evolves downstream, the magnitude at the wall decays faster than the rest of the boundary layer, which leads to a peak at around $\eta \approx 1.5$ at $\bar{x} > 0.5$. Further downstream, the peak shifts slowly to the middle of the boundary layer. The emerging peak decays downstream in a similar way to the streamwise velocity $\bar{u}^{(0)}$. As κ_y increases, the rate of decaying increases due to the viscous effect. Due to the forcing from the free-stream being of the kinematic type, there are no temperature fluctuations outside of the boundary layer, and thus the temperature fluctuations $\bar{\tau}^{(0)}$ within the boundary layer are generated by the mean-flow shear and the kinematic disturbances.

The amplitude of the wall-normal component $\bar{v}^{(0)}$ for the same conditions $M = 3$, $\kappa_z = 0$ and $\kappa_y = 2$ are plotted in figure 2.8. The magnitude of $\bar{v}^{(0)}$ has a peak within the boundary layer located around the same η as the magnitude of the streamwise velocity $\bar{u}^{(0)}$ at the same $\bar{x}$. Consistent with the $|\bar{u}^{(0)}|$ behaviour, the peak magnitude of the component $\bar{v}^{(0)}$ is shifted closer to the wall as κ_y increases. For small $\bar{x}$ values, the magnitude of the wall-normal velocity $\bar{v}^{(0)}$ uniformly decays in the free stream and within the boundary layer. This suggests that the mean-flow shear acts mainly on the streamwise velocity $\bar{u}^{(0)}$ and the temperature $\bar{\tau}^{(0)}$. Downstream of $\bar{x} \approx 0.1$, $|\bar{v}^{(0)}|$ has a wavy modulation in the free stream with decreasing wavelength and amplitude as the flow evolves downstream.

2.6.2 Response of a three-dimensional free-stream gust: the Klebanoff modes

The evolution of the boundary layer disturbances generated by a three-dimensional gust is investigated for the compressible case by presenting the full solution of $\bar{u}_0$, $\bar{v}_0$, $\bar{w}_0$, $\bar{\tau}_0$ and $\bar{p}_0$ in (2.55). Two different cases are shown. Case 1 focuses on conditions of $\kappa_z = \kappa_y = \mathcal{O}(1)$ and would ideally represent a flow at high Reynolds number that is typical in wind tunnel supersonic flows. However, to the best of the author's knowledge, the $\bar{u}^{(0)}$ component only becomes relevant

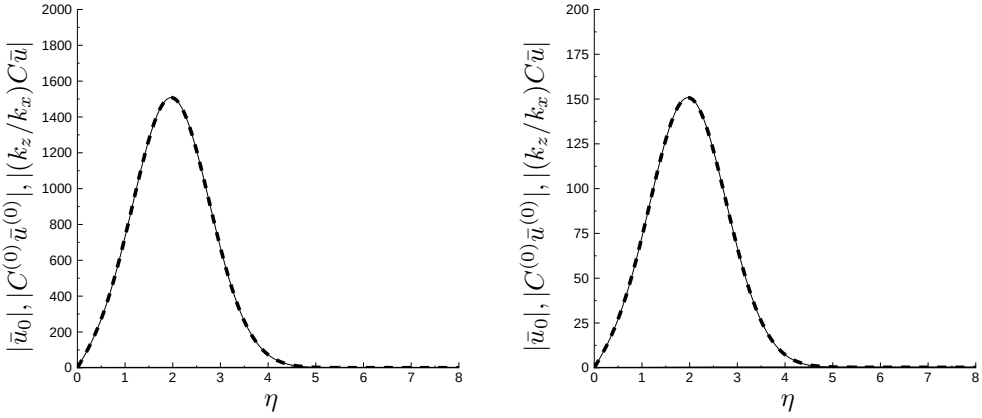

Figure 2.9: Amplitude of the streamwise velocity profiles $|\bar{u}_0|$ (dashed lines), $|C^{(0)}\bar{u}^{(0)}|$ (solid thicker lines) and $|(k_z/k_x)C\bar{u}|$ (solid thinner lines) for cases 1-A (left) and 1-B (right) at $\bar{x} = 0.5$, for $M = 3$ and $\kappa_z = \kappa_y = 1$.

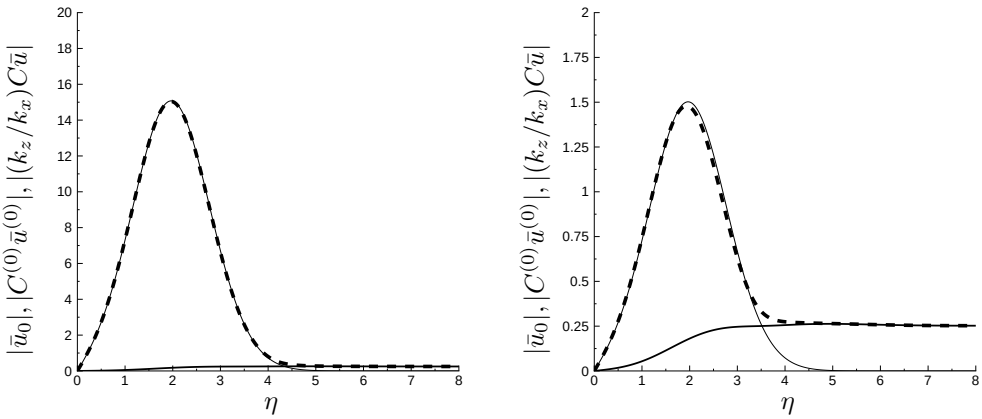

Figure 2.10: Amplitude of the streamwise velocity profiles $|\bar{u}_0|$ (dashed lines), $|C^{(0)}\bar{u}^{(0)}|$ (solid thicker lines) and $|(k_z/k_x)C\bar{u}|$ (solid thinner lines) for cases 1-C (left) and 1-D (right) at $\bar{x} = 0.5$, for $M = 3$ and $\kappa_z = \kappa_y = 1$.

with respect to $\bar{u}$ as the Reynolds number decreases. This is explained by the condition $k_x \ll k_z$, and k_z being fixed. As k_x increases, R_λ has to decrease because of $\kappa \sim 1/k_1\, R_\Lambda$. This is demonstrated by the cases plotted in figures 2.9 and 2.10 and described in table 2.1. All cases in table 2.1 are consistent with LWG [43] and Ricco & Wu [58] where the component $\bar{u}^{(0)}$ can be neglected, with the exception of case 1-D where the component $\bar{u}^{(0)}$ becomes comparable with the component $\bar{u}$. Therefore, for most compressible supersonic practical scenarios with $\kappa_z = \kappa_y = \mathcal{O}(1)$, the component $\bar{u}$ is sufficient to describe the flow correctly, and with the interest of studying the physics for the cases where $\bar{u}^{(0)}$ becomes important, Case 1 is taken for a relatively small Reynolds number. Case 1 focuses

Case	κ_z	k_x	$\hat{u}_x^\infty$	$\hat{u}_y^\infty$	R_λ
1-A	1	10^{-5}	0.959179	0.199998	3947842
1-B	1	10^{-4}	0.959292	0.199985	394784
1-C	1	10^{-3}	0.960423	0.1998476	39478
1-D	1	10^{-2}	0.971732	0.198453	3948

Table 2.1: Properties of convective gust with $k_y = k_z = 2\pi$, $\kappa_z = \kappa_y$, $\lambda_y^* = \lambda_z^*$, $\hat{u}_z^\infty = -0.2$ and similar conditions to case 1 shown in table 2.2.

on the high frequency part of the spectrum, and has similar gust conditions as the three-dimensional incompressible case studied by Ricco [56], with the difference that $M = 3$ is taken.

Case	κ_z	k_x	$\hat{u}_x^\infty$	$\hat{u}_y^\infty$	R_λ	f^*(Hz)	λ_x^*(m)	λ_z^*(m)
1	1	0.1	1.084714	0.182736	395	68971.5	0.008874	0.000141232
2	0.027	0.4	1.459967	0.107056	135386	653.8	0.936162	0.0595979

Table 2.2: Properties of convective gust with $k_y = k_z = 2\pi$, $\kappa_z = \kappa_y$, $\lambda_y^* = \lambda_z^*$, $\hat{u}_z^\infty = -0.2$ and $U_\infty^* \approx 612.046$ m s^{-1}

Case 2 aims to predict the low frequency spectrum in the laboratory experiments, both case 1 and 2 use the data in Graziosi & Brown [25] to obtain the gust properties. The temperature of the gust is obtained by use of

$T^*_\infty = 2T^*_0/\left[2+(\gamma-1)M^2\right] \approx 103.571$ K where $T^*_0 = 290$ K. This yields $c^*_\infty \approx 204.015$ m s^{-1} and $U^*_\infty \approx 612.046$ m s^{-1}. The kinematic viscosity $\nu^* \approx 2.67907\times10^{-4}$ m^2 s^{-1} was found by interpolating the known values of the Reynolds number in Graziosi & Brown [25], to obtain a value of the kinematic viscosity at $x^* = 0.15$ m. Then $k_x = 0.4$ is set, and $x^* = 0.15$ m is assumed to correspond to $\bar{x} = 1$ m in order to calculate κ_z. Furthermore, $\kappa_z = \kappa_y$ and $\hat{u}^\infty_z = -0.2$ are also set. The remaining values, $\hat{u}^\infty_x$ and $\hat{u}^\infty_y$ are calculated using the continuity equation (2.6) and $\left((\hat{u}^\infty_x)^2 + \left(\hat{u}^\infty_y\right)^2 + (\hat{u}^\infty_z)^2\right)^{1/2} = 1$. The values of each parameter are shown in table 2.2 for both cases.

Firstly, case 1 is analysed. The amplitude of the streamwise velocity $\bar{u}_0$ is plotted in figure 2.11 (left) at different values of $\bar{x}$. At $\bar{x} = 0.25$, there is a peak around $\eta \approx 1.5$ which disappears downstream. The peak is related to the $\bar{u}$ which decays faster than the outer part of the boundary layer. The correctly weighted components $\bar{u}$ and $\bar{u}^{(0)}$ are displayed along with their sum, $\bar{u}_0$, in figure 2.11 (right) to demonstrate the relevance of the component $\bar{u}^{(0)}$ in the core of the boundary layer. Unlike the incompressible case studied by Ricco [56], the weighted amplitude of $\bar{u}^{(0)}$ does not confine itself to the outer part of the boundary layer, and instead is significant in describing the velocity fluctuations in the core of the boundary layer as well as matching the free-stream velocity. The wall-normal $\bar{v}_0$ and spanwise $\bar{w}_0$ velocity magnitudes are shown in figure 2.12 at different values of $\bar{x}$. The peak of the $|\bar{v}_0|$ shifts slightly to the centre of the boundary layer as the flow develops downstream, and the peak decays faster than the outer part of the boundary layer. The term $|\bar{w}_0|$ has a peak that shifts slightly from $\eta \approx 1.5$ to $\eta \approx 2$ as the flow evolves downstream from $\bar{x} = 0.25$ to $\bar{x} = 2$ respectively. The temperature $|\bar{\tau}_0|$ and $|\bar{p}_0|$ profiles are plotted in figure 2.13. Both temperature and pressure peaks shift to the centre of the boundary layer as the flow develops downstream. The temperature fluctuations $|\bar{\tau}_0|$ display profile shapes similar to that of the streamwise velocity fluctuations $\bar{u}$ which are characteristic of the thermal streaks profiles found in Ricco & Wu [58]. The pressure peak decays faster than the pressure magnitude at the wall as the flow evolves in $\bar{x}$.

Lastly, case 2 is studied. In this case, the streamwise velocity magnitude $|\bar{u}_0|$ is shown in figure 2.14 (left) at different $\bar{x}$ locations. The term proportional to $\bar{u}$ grows in magnitude as the flow evolves downstream, and at $\bar{x} \gg 1$, it becomes noticeably larger than the term proportional to $\bar{u}^{(0)}$ in the inner part of the boundary layer. In figure 2.14 (right) the different proportional terms are presented at $\bar{x} = 0.5$. The term proportional to $\bar{u}$ has a peak in the inner part of the boundary layer at approximately $\eta \approx 1.75$. Also at $\bar{x} = 0.5$, the streamwise velocity magnitude $|\bar{u}_0|$ is close to $|C^{(0)}\bar{u}^{(0)}|$ for $\eta > 1.75$. This shows the relevance of the terms proportional to $\bar{u}^{(0)}$ in the core of the boundary layer. The wall-normal $|\bar{v}_0|$ and spanwise $|\bar{w}_0|$ velocity profiles are plotted in figure 2.15. In both profiles, the velocity magnitude decays faster with $\bar{x}$ in the outer part of the boundary layer than in the inner part. As the outer part of $|\bar{w}_0|$ decays, there is an emerging peak around $\eta \approx 2$. The temperature $\bar{\tau}_0$ and pressure $\bar{p}_0$ fluctuation amplitudes are presented in figure 2.16. The temperature $|\bar{\tau}_0|$ decays close to the wall across $\bar{x}$ for the $\bar{x}$ displayed, with the peak shifting to the centre of the boundary layer as the decay occurs. The pressure $\bar{p}_0$ magnitude decays slowly compared to case 1 because κ_z is small.

2.6.3 Asymptotic solution

In line with LWG and page 22 of Ricco [56], the boundary region solution for the components $\bar{u}^{(0)}$, $\bar{v}^{(0)}$, $\bar{w}^{(0)}$, $\bar{\tau}^{(0)}$ and $\bar{p}^{(0)}$ can be expressed through an asymptotic solution in the limit $\kappa_z \to \infty$ as $\left\{\bar{u}^{(0)}, \bar{\tau}^{(0)}\right\} = \left\{\hat{u}^{(0)}, \hat{\tau}^{(0)}\right\}\left(\kappa_z^2\bar{x}, \eta; \kappa_y/\kappa_z\right)$ and $\left\{\bar{v}^{(0)}, \bar{w}^{(0)}, \bar{p}^{(0)}\right\} = \kappa_z^2\left\{\hat{v}^{(0)}, \hat{w}^{(0)}, \hat{p}^{(0)}\right\}\left(\kappa_z^2\bar{x}, \eta; \kappa_y/\kappa_z\right)$ where $\kappa_y/\kappa_z = \mathcal{O}(1)$. The scaled components $\hat{u}^{(0)}$, $\hat{v}^{(0)}$, $\hat{w}^{(0)}$, $\hat{\tau}^{(0)}$ and $\hat{p}^{(0)}$ satisfy the boundary region equations and collapse on one another as κ_z grows, see figure 2.17 for Mach 3. Similar collapsing curves were found for different Mach numbers (cf. Ricco [56] for $M = 0$).

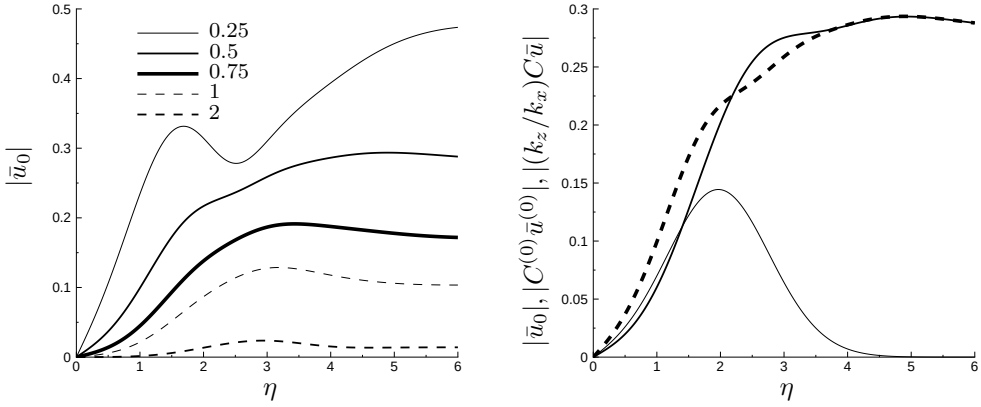

Figure 2.11: Case 1 - Amplitude of the streamwise velocity profiles $\bar{u}_0$ at the indicated values of $\bar{x}$ (left) and the streamwise velocity profiles $|\bar{u}_0|$ (dashed lines), $|C^{(0)}\bar{u}^{(0)}|$ (solid thicker lines) and $|(k_z/k_x)C\bar{u}|$ (solid thinner lines) at $\bar{x} = 0.5$ (right) for $M = 3$ and $\kappa_z = \kappa_y = 1$.

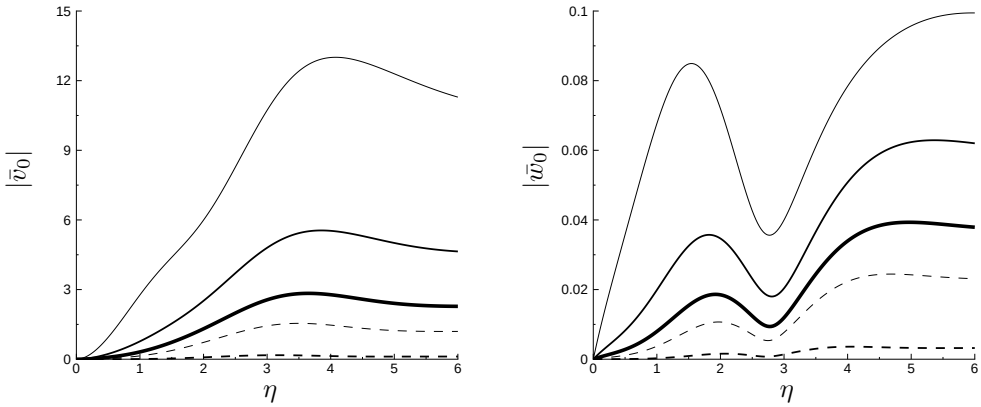

Figure 2.12: Case 1 - Amplitude of the wall-normal $\bar{v}_0$ (left) and spanwise $\bar{w}_0$ (right) velocity profiles for $M = 3$ and $\kappa_z = \kappa_y = 1$ at the indicated values of $\bar{x}$ in figure 2.11.

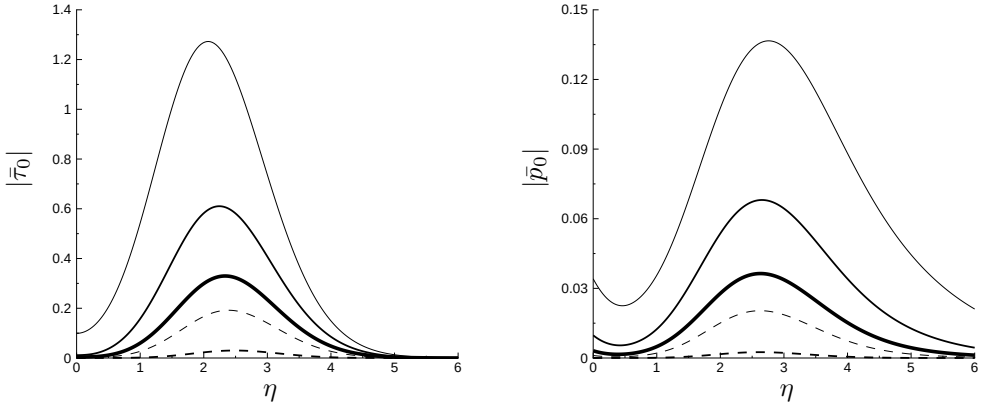

Figure 2.13: Case 1 - Amplitude of the temperature $\bar{\tau}_0$ (left) and pressure $\bar{p}_0$ (right) profiles for $M = 3$ and $\kappa_z = \kappa_y = 1$ at the indicated values of $\bar{x}$ in figure 2.11.

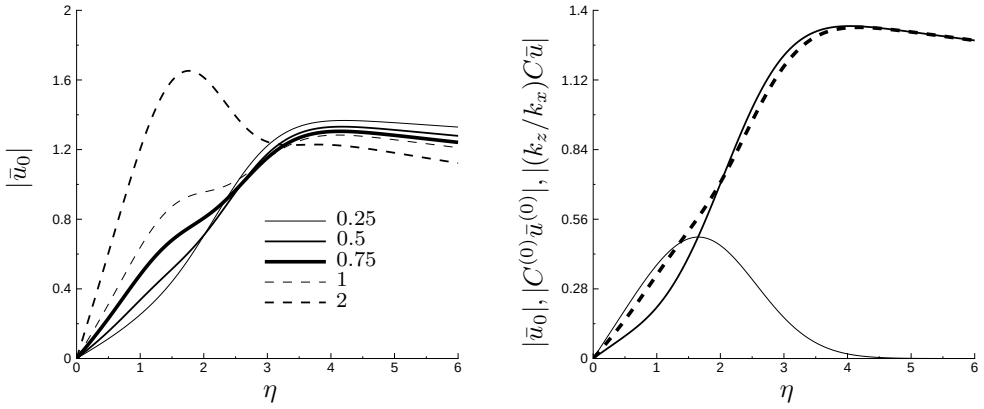

Figure 2.14: Case 2 - Amplitude of the streamwise velocity profiles $\bar{u}_0$ at the indicated values of $\bar{x}$ (left) and the streamwise velocity profiles $|\bar{u}_0|$ (dashed lines), $|C^{(0)}\bar{u}^{(0)}|$ (solid thicker lines) and $|(k_z/k_x)C\bar{u}|$ (solid thinner lines) at $\bar{x} = 0.5$ (right) for $M = 3$ and $\kappa_z = \kappa_y = 0.027$.

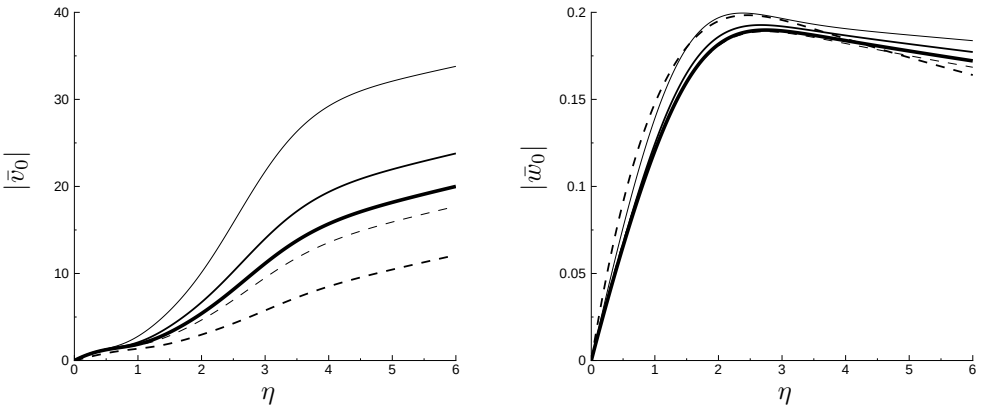

Figure 2.15: Case 2 - Amplitude of the wall-normal $\bar{v}_0$ (left) and spanwise $\bar{w}_0$ (right) velocity profiles for $M = 3$ and $\kappa_z = \kappa_y = 0.027$ at the indicated values of $\bar{x}$ in figure 2.14.

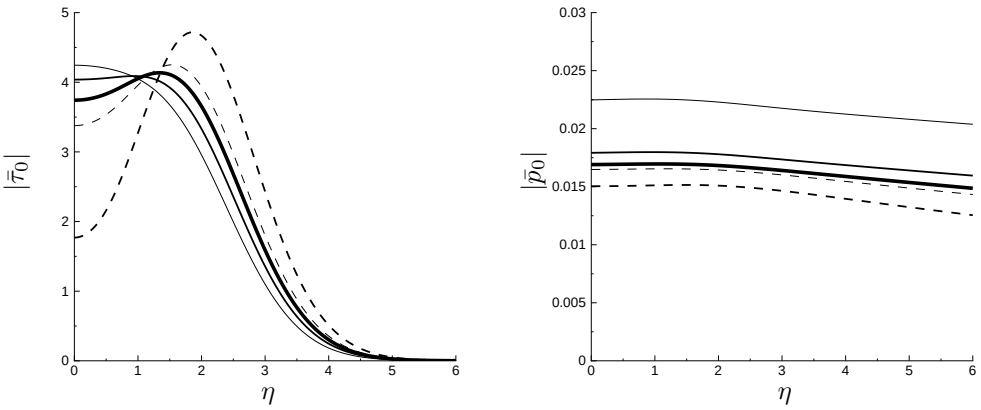

Figure 2.16: Case 2 - Amplitude of the temperature $\bar{\tau}_0$ (left) and pressure $\bar{p}_0$ (right) profiles for $M = 3$ and $\kappa_z = \kappa_y = 0.027$ at the indicated values of $\bar{x}$ in figure 2.14.

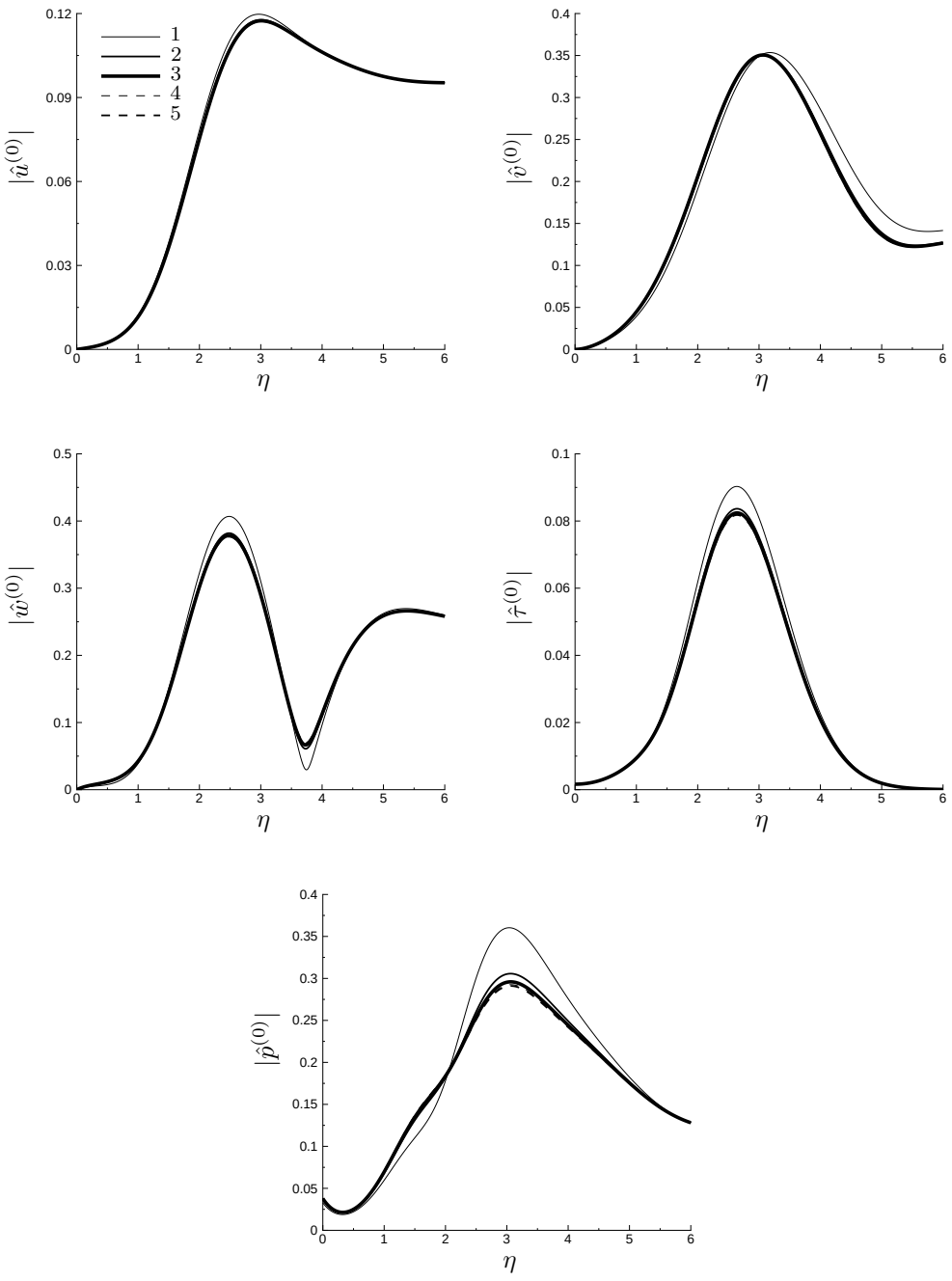

Figure 2.17: Asymptotic scaling for $\kappa_z \gg 1$ and Mach 3 with $\kappa_z/\kappa_y = 1$ at $\kappa_z^2 \bar{x} = 1$. The legend indicates the values of κ_z.

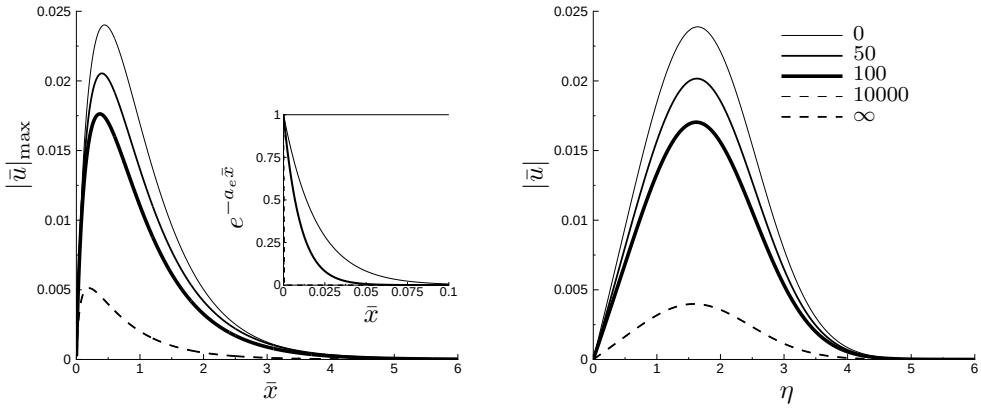

Figure 2.18: Amplitude of the streamwise velocity profiles $|\bar{u}|_{\max}$ across $\bar{x}$ (left) and the streamwise velocity profiles $|\bar{u}|$ at $\bar{x} = 0.5$ (right) for $M = 0$ and $\kappa_z = -\kappa_y = 1$. The evolution of the exponent $e^{-a_e\bar{x}}$ is shown in the smaller plot (left). The legend indicates different values of a_e for all three plots.

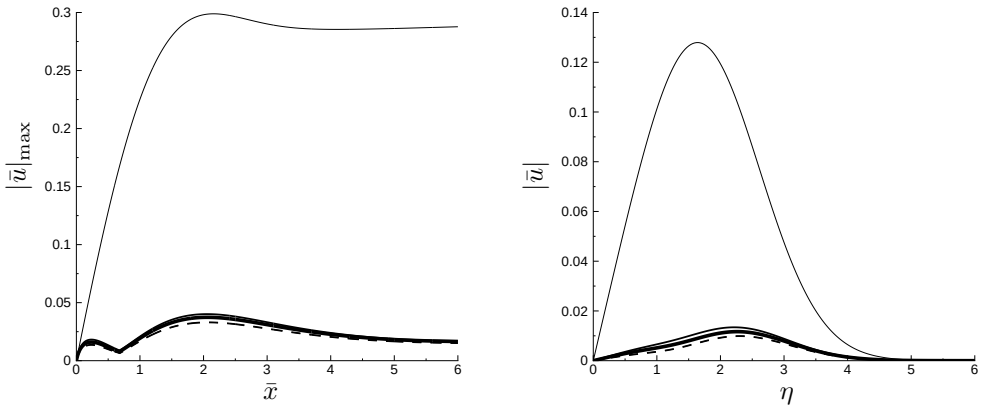

Figure 2.19: Amplitude of the streamwise velocity profiles $|\bar{u}|_{\max}$ across $\bar{x}$ (left) and the streamwise velocity profiles $|\bar{u}|$ at $\bar{x} = 0.5$ (right) for $M = 0$ and $\kappa_z = -\kappa_y = 0.01$. The values of a_e for both plots are indicated in the legend in figure 2.18.

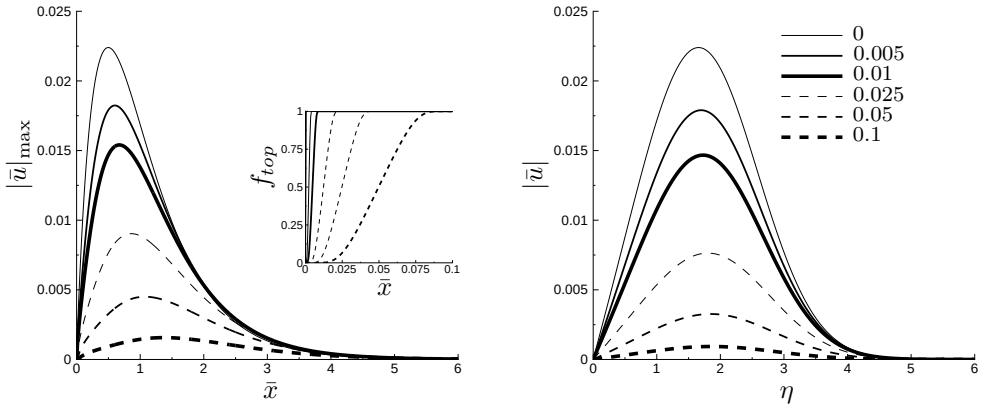

Figure 2.20: Amplitude of the streamwise velocity profiles $|\bar{u}|_{\max}$ across $\bar{x}$ (left) and the streamwise velocity profiles $|\bar{u}|$ at $\bar{x} = 0.5$ (right) for $M = 0$ and $\kappa_z = -\kappa_y = 1$. The evolution of the function f_{top} is shown in the smaller plot (left). The legend indicates different values of $\bar{x}_2$ for all three plots.

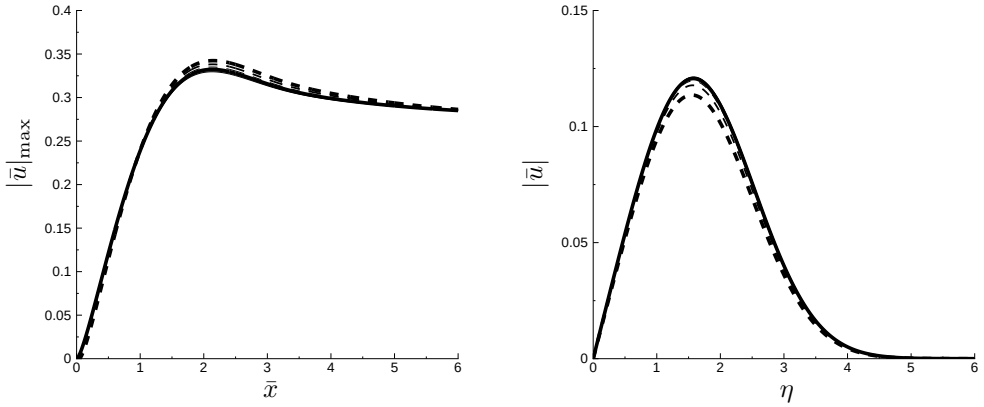

Figure 2.21: Amplitude of the streamwise velocity profiles $|\bar{u}|_{\max}$ across $\bar{x}$ (left) and the streamwise velocity profiles $|\bar{u}|$ at $\bar{x} = 0.5$ (right) for $M = 0$ and $\kappa_z = -\kappa_y = 0.01$. The values of $\bar{x}_2$ for both plots are indicated in the legend in figure 2.20.

2.6.4 Free-stream turbulence effect

With the intention of demonstrating the importance of the free-stream turbulence in the core of the boundary layer, the components $\{\bar{u}, \bar{v}, \bar{w}, \bar{\tau}, \bar{p}\}$ are solved with modified outer boundary conditions. The former boundary conditions (2.101)-(2.105) were modified by multiplying the right-hand-side terms with an exponent defined as $e^{-a_e \bar{x}}$. The exponent decays with $\bar{x}$, and as a_e increases, the decay occurs faster. For a large value of a_e, the outer boundary conditions forcing can be neglected and the flow is solely driven by the initial conditions. The influence of the velocity fluctuations $\bar{v}$ and $\bar{w}$ as $\eta \to \infty$ onto the streamwise velocity fluctuation $\bar{u}$ within the boundary layer is shown in figures 2.18 and 2.19 for $\kappa_z = 1$ and $\kappa_z = 0.01$, respectively.

As a_e increases, the inertia from the initial conditions becomes the main factor in generating the fluctuations, which results in much smaller magnitude of $\bar{u}$ for both cases. The top boundary conditions at small $\bar{x}$ are more important for $\kappa_z = 1$ than for $\kappa_z \ll 1$; the growth of $\bar{u}$ for $\kappa_z = 0.01$ does not change significantly when a_e increases. This is because the growth of $\bar{u}$ occurs faster for $\kappa_z = \mathcal{O}(1)$, and then it decays. However, for $\kappa_z \ll 1$, the flow takes longer to develop.

To investigate the effect of the initial conditions, the initial conditions (2.113)-(2.117) are set to zero, and the right-hand-side of the boundary conditions (2.101)-(2.105) were multiplied by a function f_{top} defined as

$$f_{\text{top}} = \begin{cases} \frac{e}{e+e^{\frac{\bar{x}}{\bar{x}-\bar{x}_2}+\frac{\bar{x}_2}{\bar{x}}}} & \text{if } \bar{x} < \bar{x}_2 \\ 1 & \text{if } \bar{x} \geq \bar{x}_2 \end{cases}$$

where $\bar{x}_2$ is the $\bar{x}$ location where the modified outer boundary conditions match the original ones. The maximum streamwise velocity $\bar{u}$ magnitude and the streamwise velocity $|\bar{u}|$ at $\bar{x} = 0.5$ are plotted for $\kappa_z = -\kappa_y = 1$ and $\kappa_z = -\kappa_y = 0.01$ in figures 2.20 and 2.21, respectively. The shape of the streamwise velocity $|\bar{u}|$ fluctuations remains similar to the different values of $\bar{x}_2$ considered for both cases $\kappa_z = 1$ and $\kappa_z = 0.01$. The nullified initial conditions with $\bar{x}_2 = 0$

leads to a slightly decreased magnitude peak for $\kappa_z = 1$ and a slightly larger magnitude for $\kappa_z = 0.01$ than the original cases. The peak of $|\bar{u}_{\max}|$ along $\bar{x}$ decreases with the increase of $\bar{x}_2$ for $\kappa_z = 1$ and increases slightly for $\kappa_z = 0.01$. Therefore, both the initial conditions and outer boundary conditions are very important to the magnitude of $|\bar{u}|$ for $\kappa_z = \mathcal{O}(1)$. For $\kappa_z \ll 1$, the outer boundary conditions are still important, while the initial conditions do not change the results significantly.

Chapter 3

Wall-based feedback control using the adjoint method

The theoretical formulation of the Klebanoff modes was derived in the previous chapter, and thus, a control method can be selected to attenuate the Klebanoff modes.

The control of partial differential equation systems can be complex and difficult to achieve. The two common approaches to these problems are adjoint-based (iterative) and Riccati-based (direct) methods. A major difference between these methods is that the Riccati approach allows for faster results, given that there is sufficient computational power to solve the problem, while the adjoint approach permits the solution of larger systems and is not restricted to linear problems. In this thesis, an iterative adjoint method is used to achieve attenuation of the Klebanoff modes.

The general adjoint theory is derived in §3.1 and is applied to the CLUBR equations for the first time in §3.2. The numerical procedures employed to resolve the optimisation problem is described in §3.3, and the numerical solutions in §3.4. This develops the research on spatial control by Cathalifaud & Luchini [13] for the incompressible steady linear boundary region equations.

3.1 The adjoint method

The adjoint or Lagrangian multipliers method is a mathematical approach used to determine the extrema of a function subject to constraints. The optimisation is performed on a function that represents physical quantities or other parameters to be controlled; in the particular case of minimisation. It is often called "cost functional" or "objective functional".

Consider the adjoint method for a general minimisation problem (cf. Gunzburger [27]; Bewley, Moin & Temam [7] and Abergel & Temam [1] for the mathematical proof). Let $\mathbf{q} = \mathbf{q}(\mathbf{c})$ represent the state variables and $\mathbf{c}$ the control variables, where $\mathbf{q} \in \mathbb{C}^n$ and $\mathbf{c} \in \mathbb{C}^m$, and a cost functional $\mathcal{J} = \mathcal{J}(\mathbf{q}, \mathbf{c})$ defined as $\mathcal{J} : \mathbb{C}^n \times \mathbb{C}^m \to \mathbb{J}$, subject to constraints $\mathbf{F} = \mathbf{F}(\mathbf{q}, \mathbf{c})$ as $\mathbf{F} : \mathbb{C}^n \times \mathbb{C}^m \to \mathbb{C}^n$, where $(m, n) \in \mathbb{N}^3$.

The matrix $\partial\mathbf{F}/\partial\mathbf{q}$ must be nonsingular and the constraint equations are expressed as equal to zero, i.e.:

$$\mathbf{F}(\mathbf{q}, \mathbf{c}) = 0, \tag{3.1}$$

where:

$$\mathbf{F} = \begin{bmatrix} \mathbf{Q}(\mathbf{q}) \\ \mathbf{C}(\mathbf{c}) \end{bmatrix}.$$

The vectors $\mathbf{Q}$ and $\mathbf{C}$ represent the constraints related to the state and control variables, $\mathbf{q}$ and $\mathbf{c}$ respectively (i.e. the constraint equations $\mathbf{Q}(\mathbf{q}) = 0$ and $\mathbf{C}(\mathbf{c}) = 0$).

The optimisation problem is formally defined as the minimisation of the cost functional $\mathcal{J}$ through the control variables $\mathbf{c}$, while taking into account the constraint equations (3.1). The solution to the minimisation problem is to find the controls $\mathbf{c}$ that nullify the $\mathrm{d}\mathcal{J}/\mathrm{d}\mathbf{c}$, i.e.:

$$\frac{\mathrm{d}\mathcal{J}}{\mathrm{d}\mathbf{c}} = 0,$$

where

$$\frac{\mathrm{d}\mathcal{J}}{\mathrm{d}\mathbf{c}} = \frac{\partial\mathcal{J}}{\partial\mathbf{q}}\frac{\mathrm{d}\mathbf{q}}{\mathrm{d}\mathbf{c}} + \frac{\partial\mathcal{J}}{\partial\mathbf{c}}. \tag{3.2}$$

For complex problems as the ones typically found in flow control, the term $\mathrm{d}\mathbf{q}/\mathrm{d}\mathbf{c}$ is difficult to compute and therefore, it becomes convenient to derive another set of equations that avoid the computation of $\mathrm{d}\mathbf{q}/\mathrm{d}\mathbf{c}$ instead. The derivation is shown below in §3.1.1.

3.1.1 Derivation

The set of equations are found by rearranging equation (3.2) to write the differential of $\mathcal{J}$ as

$$\mathrm{d}\mathcal{J} = \frac{\partial \mathcal{J}}{\partial \mathbf{q}}\mathrm{d}\mathbf{q} + \frac{\partial \mathcal{J}}{\partial \mathbf{c}}\mathrm{d}\mathbf{c} \tag{3.3}$$

and similarly, by taking the differential of the constraint equations (3.1) as

$$\mathrm{d}\mathbf{F} = \frac{\partial \mathbf{F}}{\partial \mathbf{q}}\mathrm{d}\mathbf{q} + \frac{\partial \mathbf{F}}{\partial \mathbf{c}}\mathrm{d}\mathbf{c}.$$

The differential of $\mathbf{F}$ is $\mathrm{d}\mathbf{F} = 0$ because of the equation $\mathbf{F} = 0$, which can be expanded as

$$\frac{\partial \mathbf{F}}{\partial \mathbf{q}}\mathrm{d}\mathbf{q} + \frac{\partial \mathbf{F}}{\partial \mathbf{c}}\mathrm{d}\mathbf{c} = 0.$$

Solving the differential $\mathrm{d}\mathbf{F}$ for $\mathrm{d}\mathbf{q}$ to get

$$\mathrm{d}\mathbf{q} = -\left(\frac{\partial \mathbf{F}}{\partial \mathbf{q}}\right)^{-1}\frac{\partial \mathbf{F}}{\partial \mathbf{c}}\mathrm{d}\mathbf{c}. \tag{3.4}$$

The term $\mathrm{d}\mathbf{q}$ in equation (3.4) can then be substituted in equation (3.3) yielding

$$\mathrm{d}\mathcal{J} = -\frac{\partial \mathcal{J}}{\partial \mathbf{q}}\left(\frac{\partial \mathbf{F}}{\partial \mathbf{q}}\right)^{-1}\frac{\partial \mathbf{F}}{\partial \mathbf{c}}\mathrm{d}\mathbf{c} + \frac{\partial \mathcal{J}}{\partial \mathbf{c}}\mathrm{d}\mathbf{c}. \tag{3.5}$$

Let $\mathbf{r}$ be a vector defined as

$$\mathbf{r} = \frac{\partial \mathcal{J}}{\partial \mathbf{q}}\left(\frac{\partial \mathbf{F}}{\partial \mathbf{q}}\right)^{-1} \tag{3.6}$$

and substituting equation (3.6) in equation (3.5), one finds

$$\mathrm{d}\mathcal{J} = \left(\frac{\partial \mathcal{J}}{\partial \mathbf{c}} - \mathbf{r}\frac{\partial \mathbf{F}}{\partial \mathbf{c}}\right)\mathrm{d}\mathbf{c}. \tag{3.7}$$

The extrema of the cost functional $\mathcal{J}$ is found by searching $\mathrm{d}\mathcal{J} = 0$, and thus from equation (3.7), the optimality conditions can be written as

$$\frac{\partial \mathcal{J}}{\partial \mathbf{c}} - \mathbf{r}\frac{\partial \mathbf{F}}{\partial \mathbf{c}} = 0, \tag{3.8}$$

and also, the adjoint equations are obtained by rearranging equation (3.6), yielding

$$\frac{\partial \mathcal{J}}{\partial \mathbf{q}} - \mathbf{r}\frac{\partial \mathbf{F}}{\partial \mathbf{q}} = 0, \tag{3.9}$$

where $\mathbf{r}$ is the adjoint vector.

The similarity of the optimality conditions and the adjoint equations suggest that the optimisation problem can be written in terms of a Lagrangian functional, and thus the adjoint framework or Lagrangian multipliers method is derived below for a Lagrangian functional.

Let a Lagrangian functional be defined as:

$$\mathcal{L}(\mathbf{q}, \mathbf{c}, \mathbf{r}) = \mathcal{J}(\mathbf{q}, \mathbf{c}) - \langle \mathbf{r}, \mathbf{F}(\mathbf{q}, \mathbf{c}) \rangle, \tag{3.10}$$

where $\mathbf{r}$ is a vector of adjoint variables or Lagrange multipliers (in optimal control theory, it is called costate vector) defined as:

$$\mathbf{r} = \begin{bmatrix} \mathbf{r_q} \\ \mathbf{r_c} \end{bmatrix},$$

and $\langle \cdot, \cdot \rangle$ denotes an inner product between the space of the adjoint variables $\{\mathbf{r_q}, \mathbf{r_c}\}$ and the constraints $\{\mathbf{Q}, \mathbf{C}\}$. The adjoint vectors $\mathbf{r_q}$ and $\mathbf{r_c}$ have the same dimensions as $\mathbf{Q}$ and $\mathbf{C}$ respectively (i.e. there are as many adjoint variables as there are constraints). There is freedom to define the inner product because of equation (3.1). See equations (3.60) for the inner product definition used in the CLUBR system optimisation problem.

Equation (3.1) implies that the Lagrangian functional (3.10) can be written as:

$$\mathcal{L}(\mathbf{q}, \mathbf{c}, \mathbf{r}) = \mathcal{J}(\mathbf{q}, \mathbf{c}),$$

and its gradient can be expressed as:

$$\frac{\mathrm{d}\mathcal{J}}{\mathrm{d}\mathbf{c}} = \frac{\mathrm{d}\mathcal{L}}{\mathrm{d}\mathbf{c}}.$$

The optimisation problem then, can be seen as finding the minima of the Lagrangian functional with respect to the control variables, i.e.:

$$\frac{\mathrm{d}\mathcal{L}}{\mathrm{d}\mathbf{c}} = 0, \tag{3.11}$$

where

$$\frac{\mathrm{d}\mathcal{L}}{\mathrm{d}\mathbf{c}} = \frac{\partial \mathcal{L}}{\partial \mathbf{c}} + \frac{\partial \mathcal{L}}{\partial \mathbf{q}}\frac{\mathrm{d}\mathbf{q}}{\mathrm{d}\mathbf{c}} + \frac{\partial \mathcal{L}}{\partial \mathbf{r}}\frac{\mathrm{d}\mathbf{r}}{\mathrm{d}\mathbf{c}}. \tag{3.12}$$

The equation (3.12) can then be rearranged to give the differential of the Lagrangian functional $\mathcal{L}$ as

$$\mathrm{d}\mathcal{L} = \frac{\partial \mathcal{L}}{\partial \mathbf{c}}\mathrm{d}\mathbf{c} + \frac{\partial \mathcal{L}}{\partial \mathbf{q}}\mathrm{d}\mathbf{q} + \frac{\partial \mathcal{L}}{\partial \mathbf{r}}\mathrm{d}\mathbf{r}, \tag{3.13}$$

where equation (3.11) implies

$$\mathrm{d}\mathcal{L} = 0. \tag{3.14}$$

Using the procedure to find (3.8) (3.9) and from equations (3.13) and (3.14), it is clear that the solution for the optimisation problem is found by seeking $\mathbf{c}$, $\mathbf{q}$ and $\mathbf{r}$, such that the Lagrangian functional $\mathcal{L}(\mathbf{c}, \mathbf{q}, \mathbf{r})$ is stationary, i.e.:

$$\frac{\partial \mathcal{L}}{\partial \mathbf{c}} = 0 \Rightarrow \text{optimality conditions} \Rightarrow \frac{\partial \mathcal{J}}{\partial \mathbf{c}} - \left\langle \mathbf{r}, \frac{\partial \mathbf{F}}{\partial \mathbf{c}} \right\rangle = 0, \tag{3.15a}$$

$$\frac{\partial \mathcal{L}}{\partial \mathbf{q}} = 0 \Rightarrow \text{adjoint equations} \Rightarrow \frac{\partial \mathcal{J}}{\partial \mathbf{q}} - \left\langle \mathbf{r}, \frac{\partial \mathbf{F}}{\partial \mathbf{q}} \right\rangle = 0, \tag{3.15b}$$

$$\frac{\partial \mathcal{L}}{\partial \mathbf{r}} = 0 \Rightarrow \text{constraint equations} \Rightarrow \mathbf{F} = 0. \tag{3.15c}$$

These equations constitute an optimality system which can be used to determine the optimal controls and states to the optimisation problem. From equations (3.7) and (3.8) it was also shown that solving the optimality conditions is equivalent to solving $\mathrm{d}\mathcal{J}/\mathrm{d}\mathbf{c} = 0$. In the following section, this formulation will be applied to the CLUBR equations with the aim of reducing the magnitude of the Klebanoff modes. To give some physical insight to the application of this general formulation to a flow control problem, it is important to understand that taking the Fréchet differential of the Lagrangian (3.10) to obtain (3.1.1) can be physically interpreted as linearising the Lagrangian in the direction of an arbitrary control perturbation $\mathbf{c}'$. Thus, substituting $\mathbf{c} = \mathbf{c} + \mathbf{c}'$ and $\mathbf{q} + \mathbf{q}'$ as $\mathbf{q} = \mathbf{q}(\mathbf{c})$ in the Lagrangian (3.10) and collecting the terms with respect to $\mathbf{c}'$ and $\mathbf{q}'$ leads to an equivalent formulation. In the equivalent formulation, $\mathbf{q}'$ denotes the change or perturbation of the state vector $\mathbf{q}$ to an arbitrary change of the controls $\mathbf{c}$ in the direction $\mathbf{c}'$. This alternative formulation will be used throughout the next section to

make evident the physical meaning of the cost functional and CLUBR system differentials.

3.2 Compressible linear unsteady boundary region adjoint

The CLUBR equations (2.64)-(2.68) that describe the pressure, velocities and temperature fluctuations within the Blasius boundary layer are expressed in the form of an operator for the components $\{\bar{p}, \bar{u}, \bar{v}, \bar{w}, \bar{\tau}\}$ and for the components $\left\{\bar{p}^{(0)}, \bar{u}^{(0)}, \bar{v}^{(0)}, \bar{w}^{(0)}, \bar{\tau}^{(0)}\right\}$ as

$$\bar{\mathbf{Q}}\left(\bar{\mathbf{q}}\right) = 0 \tag{3.16}$$

and

$$\bar{\mathbf{Q}}\left(\bar{\mathbf{q}}^{(\mathbf{0})}\right) = 0 \tag{3.17}$$

respectively. The vectors $\bar{\mathbf{q}}$ and $\bar{\mathbf{q}}^{(\mathbf{0})}$ are the state vectors expressed as

$$\bar{\mathbf{q}} = \begin{bmatrix} \bar{p} \\ \bar{u} \\ \bar{v} \\ \bar{w} \\ \bar{\tau} \end{bmatrix}$$

and

$$\bar{\mathbf{q}}^{(\mathbf{0})} = \begin{bmatrix} \bar{p}^{(0)} \\ \bar{u}^{(0)} \\ \bar{v}^{(0)} \\ \bar{w}^{(0)} \\ \bar{\tau}^{(0)} \end{bmatrix}$$

respectively.

For the present problem, wall-normal blowing and suction, also known as wall-normal transpiration, is chosen as the actuation method and thus, it needs to be included in the formulation. The former boundary conditions (2.69) are

modified to

$$\bar{v} = \bar{v}_w \quad \text{at} \quad \eta = 0, \tag{3.18}$$

$$\bar{v}^{(0)} = \bar{v}_w^{(0)} \quad \text{at} \quad \eta = 0, \tag{3.19}$$

and

$$\bar{u} = \bar{w} = \bar{u}^{(0)} = \bar{w}^{(0)} = 0 \quad \eta = 0, \tag{3.20}$$

to include the actuation. The remaining boundary conditions (2.70), (2.101)-(2.110) and initial conditions (2.113)-(2.122) for both systems remain unchanged.

The actuation optimisation problem is therefore defined as the minimisation of the cost functional $\mathcal{J}$ through the control variables $\bar{v}_w(x)$ or $\bar{v}_w^{(0)}(x)$, while taking into account the CLUBR equations as constraints. The solution to this problem is obtained by finding the controls $\bar{v}_w(x)$ and $\bar{v}_w^{(0)}(x)$ that nullify $\mathrm{d}\mathcal{J}/\mathrm{d}\bar{v}_w$ and $\mathrm{d}\mathcal{J}^{(0)}/\mathrm{d}\bar{v}_w^{(0)}$ respectively.

Due to the linearity of the components $\{\bar{u}, \bar{v}, \bar{w}, \bar{\tau}, \bar{p}\}$ and the components $\left\{\bar{u}^{(0)}, \bar{v}^{(0)}, \bar{w}^{(0)}, \bar{\tau}^{(0)}, \bar{p}^{(0)}\right\}$, both control problems are solved independently and their solutions summed as a linear solution in the end. This may not be acceptable in terms of measuring the kinetic energy in the system, but it is accepted in terms of the minimisation problem at hand because attenuating both systems independently and then summing their solution leads to the same result as attenuating both systems simultaneously.

With the objective of measuring the Klebanoff modes, the kinetic energy of the streamwise velocity fluctuations is chosen as the parameter to be measured in the cost functionals. In addition, the temperature fluctuations can be measured to attenuate the thermal modes for $M > 0$. The cost functionals are defined as:

$$\mathcal{J} = \alpha_1\mathcal{J}_1 + \alpha_2\mathcal{J}_2 + \alpha_3\mathcal{J}_3 + \alpha_4\mathcal{J}_4 + \frac{\theta_v^2}{2}\int_{\bar{x}_i}^{\bar{x}_f}\left(\bar{v}_w^H\mathbf{Q_v}\bar{v}_w\right)\mathrm{d}\bar{x} \tag{3.21}$$

and

$$\mathcal{J}^{(0)} = \alpha_2^{(0)}\mathcal{J}_2^{(0)} + \alpha_4^{(0)}\mathcal{J}_4^{(0)} + \frac{\theta_v^{(0)2}}{2}\int_{\bar{x}_i}^{\bar{x}_f}\left(\bar{v}_w^{(0)H}\mathbf{Q_v^{(0)}}\bar{v}_w^{(0)}\right)\mathrm{d}\bar{x}, \tag{3.22}$$

where

$$\mathcal{J}_1 = \frac{1}{2}\int_0^\infty \left(\bar{u}^H\mathbf{Q_1}\bar{u}\right)_{\bar{x}=\bar{x}_f} d\eta, \tag{3.23}$$

$$\mathcal{J}_2 = \frac{1}{2}\int_{\bar{x}_i}^{\bar{x}_f}\int_0^{\infty}\left(\bar{u}^H\mathbf{Q_2}\bar{u}\right)\mathrm{d}\eta\mathrm{d}\bar{x}, \tag{3.24}$$

$$\mathcal{J}_3 = \frac{1}{2}\int_0^{\infty}\left(\bar{\tau}^H\mathbf{Q_3}\bar{\tau}\right)_{\bar{x}=\bar{x}_f}\mathrm{d}\eta, \tag{3.25}$$

$$\mathcal{J}_4 = \frac{1}{2}\int_{\bar{x}_i}^{\bar{x}_f}\int_0^{\infty}\left(\bar{\tau}^H\mathbf{Q_4}\bar{\tau}\right)\mathrm{d}\eta\mathrm{d}\bar{x}, \tag{3.26}$$

$$\mathcal{J}_2^{(0)} = \frac{1}{2}\int_{\bar{x}_i}^{\bar{x}_f}\int_0^{\infty}\left(\bar{u}^{(0)H}\mathbf{Q_2^{(0)}}\bar{u}^{(0)}\right)\mathrm{d}\eta\mathrm{d}\bar{x}, \tag{3.27}$$

$$\mathcal{J}_4^{(0)} = \frac{1}{2}\int_{\bar{x}_i}^{\bar{x}_f}\int_0^{\infty}\left(\bar{\tau}^{(0)H}\mathbf{Q_4^{(0)}}\bar{\tau}^{(0)}\right)\mathrm{d}\eta\mathrm{d}\bar{x}, \tag{3.28}$$

and the terms $\mathbf{Q_1}$, $\mathbf{Q_2}$, $\mathbf{Q_3}$, $\mathbf{Q_4}$, $\mathbf{Q_v}$, $\mathbf{Q_2^{(0)}}$, $\mathbf{Q_4^{(0)}}$, $\mathbf{Q_v^{(0)}}$ are weighing Hermitian matrices that satisfy $\mathbf{Q_1} \geq 0$, $\mathbf{Q_2} \geq 0$, $\mathbf{Q_3} \geq 0$, $\mathbf{Q_4} \geq 0$, $\mathbf{Q_v} > 0$, $\mathbf{Q_2^{(0)}} \geq 0$, $\mathbf{Q_4^{(0)}} \geq 0$, $\mathbf{Q_v^{(0)}} > 0$. The coefficients α_1, α_2, α_3, α_4 and $\alpha_2^{(0)}$, $\alpha_4^{(0)}$ satisfy the equations

$$\alpha_1 + \alpha_2 + \alpha_3 + \alpha_4 = 1, \quad \alpha_1, \alpha_2, \alpha_3, \alpha_4 \in \mathbb{R}_0^+$$

and

$$\alpha_2^{(0)} + \alpha_4^{(0)} = 1, \quad \alpha_2^{(0)}, \alpha_4^{(0)} \in \mathbb{R}_0^+$$

respectively, and are used to select which cost functionals are used. The coefficients θ_v and $\theta_v^{(0)}$ define the weight of the cost of actuation. The cost of actuation is measured by the kinetic energy of the input variables $\bar{v}_w$ and $\bar{v}_w(0)$. The superscript $(\cdot)^H$ denotes the conjugate transpose.

The cost functional $\mathcal{J}_1$ measures the terminal kinetic energy of the streamwise velocity $\bar{u}$, while $\mathcal{J}_2$ and $\mathcal{J}_2^{(0)}$ measure the kinetic energy along the interval $[\bar{x}_i, \bar{x}_f]$ of the streamwise velocities $\bar{u}$ and $\bar{u}^{(0)}$ respectively. The temperature fluctuations $\bar{\tau}$ are measured by the cost functional $\mathcal{J}_3$ at the terminal distance $\bar{x}_f$, and cost functionals $\mathcal{J}_4$ and $\mathcal{J}_4^{(0)}$ measure the temperature fluctuations $\bar{\tau}$ and $\bar{\tau}^{(0)}$ along the interval $[\bar{x}_i, \bar{x}_f]$. The terminal kinetic energies of the components $\bar{u}^{(0)}$ and $\bar{\tau}^{(0)}$ are not considered within the cost functional as these terms are not of leading order close the wall, where the actuators are implemented.

The cost functionals (3.21) and (3.22) may be rewritten as a sum of inner products as follows

$$\mathcal{J} = \frac{\alpha_1}{2}\left\langle\bar{u},\bar{u}\right\rangle_{\mathbf{Q_1}} + \frac{\alpha_2}{2}\left\langle\bar{u},\bar{u}\right\rangle_{\mathbf{Q_2}} + \frac{\alpha_3}{2}\left\langle\bar{\tau},\bar{\tau}\right\rangle_{\mathbf{Q_3}} + \frac{\alpha_4}{2}\left\langle\bar{\tau},\bar{\tau}\right\rangle_{\mathbf{Q_4}} + \frac{\theta_v^2}{2}\left\langle\bar{v}_w,\bar{v}_w\right\rangle_{\mathbf{Q_v}} \tag{3.29}$$

and

$$\begin{aligned}\mathcal{J}^{(0)} = &\frac{\alpha_2^{(0)}}{2}\left\langle \bar{u}^{(0)}, \bar{u}^{(0)} \right\rangle_{\mathbf{Q_2^{(0)}}} + \frac{\alpha_4^{(0)}}{2}\left\langle \bar{\tau}^{(0)}, \bar{\tau}^{(0)} \right\rangle_{\mathbf{Q_4^{(0)}}} \\ &+ \frac{\theta_v^{(0)}2}{2}\left\langle \bar{v}_w^{(0)}, \bar{v}_w^{(0)} \right\rangle_{\mathbf{Q_v^{(0)}}}\end{aligned} \tag{3.30}$$

where $\langle \cdot, \cdot \rangle_{\mathbf{M}}$ denotes an inner product with a generic Hermitian weighting matrix $\mathbf{M}$, defined as

$$\langle \bar{\mathbf{q}}, \bar{\mathbf{q}} \rangle_{\mathbf{M}} = \int_{\bar{x}_i}^{\bar{x}_f} \int_0^{\infty} \bar{\mathbf{q}}^H \mathbf{M} \bar{\mathbf{q}} \mathrm{d}\eta \mathrm{d}\bar{x}, \tag{3.31}$$

when the weighting matrices $\mathbf{Q_2}$, $\mathbf{Q_4}$, $\mathbf{Q_2^{(0)}}$ and $\mathbf{Q_4^{(0)}}$ are present. The inner product for the weighting matrices $\mathbf{Q_1}$ and $\mathbf{Q_3}$ is defined as

$$\langle \bar{\mathbf{q}}, \bar{\mathbf{q}} \rangle_{\mathbf{M}} = \int_0^{\infty} \left[\bar{\mathbf{q}}^H \mathbf{M} \bar{\mathbf{q}} \right]_{\bar{x}=\bar{x}_f} \mathrm{d}\eta, \tag{3.32}$$

and for the control weighting matrices $\mathbf{Q_v}$ and $\mathbf{Q_v^{(0)}}$ as

$$\langle \bar{\mathbf{v}}_{\mathbf{w}}, \bar{\mathbf{v}}_{\mathbf{w}} \rangle_{\mathbf{M}} = \int_{\bar{x}_i}^{\bar{x}_f} \bar{\mathbf{v}}_{\mathbf{w}}^H \mathbf{M} \bar{\mathbf{v}}_{\mathbf{w}} \mathrm{d}\bar{x}. \tag{3.33}$$

The cost functionals expressed as the sum of the inner products makes them easier to be differentiated as the inner product properties can be used.

With the actuator and the cost functionals defined, the next step towards the solution of the minimisation problem is to find the gradients of the cost functionals $\mathcal{J}$ and $\mathcal{J}^{(0)}$ with respect to the control variables $\bar{v}_w$ and $\bar{v}_w^{(0)}$ respectively, that are equal to zero, i.e:

$$\frac{\mathrm{d}\mathcal{J}}{\mathrm{d}\bar{v}_w} = 0 \tag{3.34}$$

and

$$\frac{\mathrm{d}\mathcal{J}^{(0)}}{\mathrm{d}\bar{v}_w^{(0)}} = 0. \tag{3.35}$$

These equations were described in the previous section as the optimality conditions. The solution of these gradients leads to minima or maximum points, depending on the problem. In this thesis, the focus is on attenuating the Klebanoff modes and finding the minima points of the cost functionals.

The problem can also be posed as Lagragian functionals defined as

$$\mathcal{L}(\bar{\mathbf{q}}, \bar{v}_w, \bar{\mathbf{r}}) = \mathcal{J}(\bar{\mathbf{q}}, \bar{v}_w) - \langle \bar{\mathbf{r}}, \bar{\mathbf{Q}}(\bar{\mathbf{q}}) \rangle_{\mathbf{M}}$$

and

$$\mathcal{L}^{(0)}(\bar{\mathbf{q}}^{(\mathbf{0})}, \bar{v}_w^{(0)}, \bar{\mathbf{r}}) = \mathcal{J}^{(0)}(\bar{\mathbf{q}}^{(\mathbf{0})}, \bar{v}_w^{(0)}) - \langle \bar{\mathbf{r}}, \bar{\mathbf{Q}}\left(\bar{\mathbf{q}}^{(\mathbf{0})}\right)\rangle_{\mathbf{M}},$$

where $\bar{\mathbf{r}}$ is an adjoint vector defined further on in the formulation, along with th inner products.

In order to determine the sensitivity of the cost functionals $\mathcal{J}$ and $\mathcal{J}^{(0)}$ to small modifications of the control $\bar{v}_w$ and $\bar{v}_w^{(0)}$ respectively, the approach of Abergel & Temam [1] and Bewley, Moin & Temam [7] which is valid for nonlinear and linear systems is closely followed.

Let $\mathcal{J}'$ be the perturbation to the cost functional $\mathcal{J}$ that results from the perturbation $\bar{v}_w$ in an arbitrary direction $\bar{v}'_w$, where $\mathcal{J}'$ is the Fréchet differential [66] of the cost functional $\mathcal{J}$, defined as

$$\mathcal{J}' \equiv \lim_{h\to 0} \frac{\mathcal{J}\left(\bar{v}_w + h\bar{v}'_w\right) - \mathcal{J}\left(\bar{v}_w\right)}{h}. \tag{3.36}$$

The definition of the functional differential, called Fréchet differential because the space of the functions is a Banach space, can also be written using the gradient $\mathrm{d}\mathcal{J}/\mathrm{d}\bar{v}_w$ as

$$\begin{aligned} \mathcal{J}' &\equiv \left\langle \frac{\mathrm{d}\mathcal{J}\left(\bar{v}_w\right)}{\mathrm{d}\bar{v}_w}, \bar{v}'_w \right\rangle_{\mathbf{I}} \\ &\equiv \int_{\bar{x}_i}^{\bar{x}_f} \left(\frac{\mathrm{d}\mathcal{J}\left(\bar{v}_w\right)}{\mathrm{d}\bar{v}_w}\right)^H \mathbf{I}\bar{v}'_w \mathrm{d}\bar{x}, \end{aligned} \tag{3.37}$$

where $\mathbf{I}$ represents the identity matrix. It is important to mention that the gradients could be preconditioned using a weighting matrix other than the identity matrix $\mathbf{I}$ (e.g. [40]).

The formulation can be used in an analogous way to define the perturbation of the cost functional $\mathcal{J}^{(0)}$ to the perturbation $\bar{v}_w^{(0)}$ in the arbitrary direction $\bar{v}_w^{(0)\prime}$ and its gradient $\mathrm{d}\mathcal{J}^{(0)}/\mathrm{d}\bar{v}_w^{(0)}$ as

$$\mathcal{J}^{(0)\prime} \equiv \lim_{h\to 0} \frac{\mathcal{J}^{(0)}\left(\bar{v}_w^{(0)} + h\bar{v}_w^{(0)\prime}\right) - \mathcal{J}^{(0)}\left(\bar{v}_w^{(0)}\right)}{h} \tag{3.38}$$

and

$$\begin{aligned}\mathcal{J}^{(0)\prime} &\equiv \left\langle \frac{\mathrm{d}\mathcal{J}^{(0)}\left(\bar{v}_w^{(0)}\right)}{\mathrm{d}\bar{v}_w^{(0)}}, \bar{v}_w^{(0)\prime} \right\rangle_{\mathbf{I}} \\ &\equiv \int_{\bar{x}_i}^{\bar{x}_f} \left(\frac{\mathrm{d}\mathcal{J}^{(0)}\left(\bar{v}_w^{(0)}\right)}{\mathrm{d}\bar{v}_w^{(0)}} \right)^H \mathbf{I}\bar{v}_w^{(0)\prime}\mathrm{d}\bar{x}\end{aligned} \tag{3.39}$$

respectively. The cost functionals perturbations $\mathcal{J}'$ and $\mathcal{J}^{(0)\prime}$ can be expressed from (3.29) and (3.30) using the definitions (3.36)-(3.37) and (3.38)-(3.39) respectively, and applying the chain rule (3.2). For instance, the inner product $\langle \bar{v}_w, \bar{v}_w \rangle_{\mathbf{Q_v}}$ can be differentiated as $\langle \bar{v}_w, \bar{v}_w \rangle_{\mathbf{Q_v}} = \langle \bar{v}_w, \bar{v}'_w \rangle_{\mathbf{Q_v}} + \langle \bar{v}'_w, \bar{v}_w \rangle_{\mathbf{Q_v}} = 2\langle \bar{v}_w, \bar{v}'_w \rangle_{\mathbf{Q_v}}$, and thus the cost functionals perturbations $\mathcal{J}'$ and $\mathcal{J}^{(0)\prime}$ are written as

$$\mathcal{J}' = \alpha_1 \left\langle \bar{u}, \bar{u}' \right\rangle_{\mathbf{Q_1}} + \alpha_2 \left\langle \bar{u}, \bar{u}' \right\rangle_{\mathbf{Q_2}} + \alpha_3 \left\langle \bar{\tau}, \bar{\tau}' \right\rangle_{\mathbf{Q_3}} + \alpha_4 \left\langle \bar{\tau}, \bar{\tau}' \right\rangle_{\mathbf{Q_4}} + \theta_v^2 \left\langle \bar{v}_w, \bar{v}'_w \right\rangle_{\mathbf{Q_v}}$$

and

$$\mathcal{J}^{(0)\prime} = \alpha_2^{(0)} \left\langle \bar{u}^{(0)}, \bar{u}^{(0)\prime} \right\rangle_{\mathbf{Q_2^{(0)}}} + \alpha_4^{(0)} \left\langle \bar{\tau}^{(0)}, \bar{\tau}^{(0)\prime} \right\rangle_{\mathbf{Q_4^{(0)}}} + \theta_v^{(0)} 2 \left\langle \bar{v}_w^{(0)}, \bar{v}_w^{(0)\prime} \right\rangle_{\mathbf{Q_v^{(0)}}},$$

or in the expanded form as

$$\mathcal{J}' = \alpha_1 \mathcal{J}'_1 + \alpha_2 \mathcal{J}'_2 + \alpha_3 \mathcal{J}'_3 + \alpha_4 \mathcal{J}'_4 + \theta_v^2 \int_{\bar{x}_i}^{\bar{x}_f} \left(\bar{v}_w^H \mathbf{Q_v} \bar{v}'_w \right) \mathrm{d}\bar{x} \tag{3.40}$$

and

$$\mathcal{J}^{(0)\prime} = \alpha_2^{(0)} \mathcal{J}_2^{(0)\prime} + \alpha_4^{(0)} \mathcal{J}_4^{(0)\prime} + \theta_v^{(0)2} \int_{\bar{x}_i}^{\bar{x}_f} \left(\bar{v}_w^{(0)H} \mathbf{Q_v^{(0)}} \bar{v}_w^{(0)\prime} \right) \mathrm{d}\bar{x}, \tag{3.41}$$

where

$$\mathcal{J}'_1 = \int_0^\infty \left(\bar{u}^H \mathbf{Q_1} \bar{u}' \right)_{\bar{x}=\bar{x}_f} d\eta, \tag{3.42}$$

$$\mathcal{J}'_2 = \int_{\bar{x}_i}^{\bar{x}_f} \int_0^\infty \left(\bar{u}^H \mathbf{Q_2} \bar{u}' \right) \mathrm{d}\eta \mathrm{d}\bar{x}, \tag{3.43}$$

$$\mathcal{J}'_3 = \int_0^\infty \left(\bar{\tau}^H \mathbf{Q_3} \bar{\tau}' \right)_{\bar{x}=\bar{x}_f} \mathrm{d}\eta, \tag{3.44}$$

$$\mathcal{J}'_4 = \int_{\bar{x}_i}^{\bar{x}_f} \int_0^\infty \left(\bar{\tau}^H \mathbf{Q_4} \bar{\tau}' \right) \mathrm{d}\eta \mathrm{d}\bar{x}, \tag{3.45}$$

$$\mathcal{J}_2^{(0)\prime} = \int_{\bar{x}_i}^{\bar{x}_f} \int_0^{\infty} \left(\bar{u}^{(0)H} \mathbf{Q_2^{(0)}} \bar{u}^{(0)\prime} \right) \mathrm{d}\eta \mathrm{d}\bar{x}, \tag{3.46}$$

$$\mathcal{J}_4^{(0)\prime} = \int_{\bar{x}_i}^{\bar{x}_f} \int_0^{\infty} \left(\bar{\tau}^{(0)H} \mathbf{Q_4^{(0)}} \bar{\tau}^{(0)\prime} \right) \mathrm{d}\eta \mathrm{d}\bar{x}, \tag{3.47}$$

where the linear perturbations $\bar{\mathbf{q}}'$ and $\bar{\mathbf{q}}^{(\mathbf{0})\prime}$ to the solutions $\bar{\mathbf{q}}$ and $\bar{\mathbf{q}}^{(\mathbf{0})}$ that arise from the variations $\bar{v}_w'$ and $\bar{v}_w^{(0)\prime}$ to the controls $\bar{v}_w$ and $\bar{v}_w^{(0)}$ are defined in a similar way to the perturbations of the cost functional $\mathcal{J}'$ and $\mathcal{J}^{(0)\prime}$, and are given by the definition of the Fréchet differential as

$$\bar{\mathbf{q}}' \equiv \lim_{h \to 0} \frac{\bar{\mathbf{q}}\left(\bar{v}_w + h\bar{v}_w'\right) - \bar{\mathbf{q}}\left(\bar{v}_w\right)}{h} \tag{3.48}$$

and

$$\bar{\mathbf{q}}^{(\mathbf{0})\prime} \equiv \lim_{h \to 0} \frac{\bar{\mathbf{q}}^{(\mathbf{0})}\left(\bar{v}_w^{(0)} + h\bar{v}_w^{(0)\prime}\right) - \bar{\mathbf{q}}^{(\mathbf{0})}\left(\bar{v}_w^{(0)}\right)}{h}, \tag{3.49}$$

and expressed as

$$\bar{\mathbf{q}}' = \begin{bmatrix} \bar{p}' \\ \bar{u}' \\ \bar{v}' \\ \bar{w}' \\ \bar{\tau}' \end{bmatrix} \tag{3.50}$$

and

$$\bar{\mathbf{q}}^{(0)\prime} = \begin{bmatrix} \bar{p}^{(0)\prime} \\ \bar{u}^{(0)\prime} \\ \bar{v}^{(0)\prime} \\ \bar{w}^{(0)\prime} \\ \bar{\tau}^{(0)\prime} \end{bmatrix}, \tag{3.51}$$

respectively. To obtain the system of equations that describe the vectors $\bar{\mathbf{q}}'$ and $\bar{\mathbf{q}}^{(\mathbf{0})\prime}$ to the control variations $\bar{v}_w'$ and $\bar{v}_w^{(0)\prime}$ respectively, the Fréchet differential of the CLUBR equations (3.16) and (3.17) and its respective boundary conditions (2.70), (3.18)-(3.20), (2.91)-(2.100) and initial conditions (2.113)-(2.122) are taken. This leads to

$$\bar{\mathbf{Q}}\left(\bar{\mathbf{q}}'\right) = 0 \tag{3.52}$$

and

$$\bar{\mathbf{Q}}\left(\bar{\mathbf{q}}^{(\mathbf{0})\prime}\right) = 0. \tag{3.53}$$

This means that the CLUBR equations (2.64)-(2.68) because of linearity are equally valid for the state vectors $\bar{\mathbf{q}}$ and $\bar{\mathbf{q}}^{(\mathbf{0})}$ as well as their linear perturbations $\bar{\mathbf{q}}'$ and $\bar{\mathbf{q}}^{(\mathbf{0})\prime}$. The boundary conditions for the latter are expressed as

$$\bar{v}' = \bar{v}'_w \quad \text{at} \quad \eta = 0, \tag{3.54}$$

$$\bar{v}^{(0)\prime} = \bar{v}_w^{(0)\prime} \quad \text{at} \quad \eta = 0, \tag{3.55}$$

$$\bar{u}' = \bar{w}' = \frac{\partial \bar{\tau}'}{\partial \eta} = \bar{u}^{(0)\prime} = \bar{w}^{(0)\prime} = \frac{\partial \bar{\tau}^{(0)\prime}}{\partial \eta} = 0 \quad \text{at} \quad \eta = 0, \tag{3.56}$$

$$\begin{aligned} \bar{p}' = \bar{u}' = \bar{v}' = \bar{w}' = \bar{\tau}' = \bar{p}^{(0)\prime} = \bar{u}^{(0)\prime} \\ = \bar{v}^{(0)\prime} = \bar{w}^{(0)\prime} = \bar{\tau}^{(0)\prime} = 0 \quad \text{at} \quad \eta \to \infty, \end{aligned} \tag{3.57}$$

and initial conditions

$$\bar{p}' = \bar{u}' = \bar{v}' = \bar{w}' = \bar{\tau}' = \bar{p}^{(0)\prime} = \bar{u}^{(0)\prime} = \bar{v}^{(0)\prime} = \bar{w}^{(0)\prime} = \bar{\tau}^{(0)\prime} = 0 \quad \text{as} \quad \bar{x} \to 0. \tag{3.58}$$

The solutions of the perturbations $\bar{\mathbf{q}}'$ and $\bar{\mathbf{q}}^{(\mathbf{0})\prime}$ represent the effects of the control perturbations $\bar{v}'_w$ and $\bar{v}_w^{(0)\prime}$ respectively, within the boundary layer. However, it is difficult to directly derive the gradients $\mathrm{d}\mathcal{J}/\mathrm{d}\bar{v}_w$ and $\mathrm{d}\mathcal{J}^{(0)}/\mathrm{d}\bar{v}_w^{(0)}$ from these perturbations, defined implicitly in (3.37) and (3.39) respectively, as the linear relationships $\bar{\mathbf{q}}' = \bar{\mathbf{q}}'\left(\bar{v}'_w\right)$ and $\bar{\mathbf{q}}^{(\mathbf{0})\prime} = \bar{\mathbf{q}}^{(\mathbf{0})\prime}\left(\bar{v}_w^{(0)\prime}\right)$ are implicit. Therefore, the adjoint identity is introduced and defined as

$$\left\langle \bar{\mathbf{r}}, \bar{\mathbf{Q}}\left(\bar{\mathbf{q}}'\right)\right\rangle_{\mathbf{M}} = \left\langle \bar{\mathbf{R}}\left(\bar{\mathbf{r}}\right), \bar{\mathbf{q}}'\right\rangle_{\mathbf{M}} + b, \tag{3.59}$$

where $\langle \cdot, \cdot \rangle$ denotes an inner product between the perturbed state vector $\bar{\mathbf{q}}'$ and the adjoint vector $\bar{\mathbf{r}}$ or Lagrange multipliers (in optimal control theory, it is also called costate vector), defined as:

$$\left\langle \bar{\mathbf{r}}, \bar{\mathbf{Q}}\left(\bar{\mathbf{q}}'\right)\right\rangle_{\mathbf{M}} = \int_{\bar{x}_i}^{\bar{x}_f} \int_0^{\infty} \bar{\mathbf{r}}^H \mathbf{M} \bar{\mathbf{Q}}\left(\bar{\mathbf{q}}'\right) \mathrm{d}\eta \mathrm{d}\bar{x}, \tag{3.60}$$

where

$$\bar{\mathbf{r}} = \begin{bmatrix} \bar{r}_c \\ \bar{r}_x \\ \bar{r}_y \\ \bar{r}_z \\ \bar{r}_e \end{bmatrix}$$

and $\bar{\mathbf{R}}(\cdot)$ represents the adjoint operator that can be used to nullify the gradients of the cost functionals with respect to the control variables. The boundary terms b are used to obtain the boundary conditions and initial conditions of the adjoint equations. Due to the nature of the adjoint system, the initial conditions are in fact terminal conditions since the system is marched backwards from $\bar{x}_f$ to $\bar{x}_i$.

The expansion adjoint identity (3.59) and the method to obtain the adjoint equation systems is shown in Appendix B with a Hermitian weight matrix $\mathbf{M}$ defined as the identity matrix. The equations (B.13) and (B.20) are used to rewrite the gradients (3.34) and (3.35) using the definitions (3.37) and (3.39) to yield

$$\frac{\mathrm{d}\mathcal{J}}{\mathrm{d}\bar{v}_w} = \left[\frac{1}{T}\bar{r}_c + \theta_v^2 \mathbf{Q}_{\mathbf{v}} \bar{v}_w\right]_{\eta=0} \tag{3.61}$$

and

$$\frac{\mathrm{d}\mathcal{J}^{(0)}}{\mathrm{d}\bar{v}_w^{(0)}} = \left[\frac{1}{T}\bar{r}_c + \theta_v^{(0)2} \mathbf{Q}_{\mathbf{v}}^{(\mathbf{0})} \bar{v}_w^{(0)}\right]_{\eta=0} \tag{3.62}$$

respectively. For the gradient (3.61), $\bar{r}_c$ is obtained from solving the adjoint equations (B.5), expanded as

$$-\frac{1}{2\bar{x}}\frac{\partial \bar{r}_y}{\partial \eta} - \kappa_z^2 T \bar{r}_z = 0; \tag{3.63}$$

$$
\begin{aligned}
&\frac{1}{2\bar{x}}\bar{r}_c - \frac{\partial \bar{r}_c}{\partial \bar{x}} + \frac{\eta_c}{2\bar{x}}\frac{\partial \bar{r}_c}{\partial \eta} + \left(i + \kappa_z^2 \mu T + \frac{F'}{2\bar{x}} - \frac{\eta_c F''}{2\bar{x}}\right)\bar{r}_x - F'\frac{\partial \bar{r}_x}{\partial \bar{x}} \\
&\qquad + \frac{1}{2\bar{x}}\left(F + \frac{\mu T'}{T^2} - \frac{\mu' T'}{T}\right)\frac{\partial \bar{r}_x}{\partial \eta} - \frac{1}{2\bar{x}}\frac{\mu}{T}\frac{\partial^2 \bar{r}_x}{\partial \eta^2} \\
&+ \frac{1}{(2\bar{x})^2}\left(TF + 2\mu' T' - \eta_c TF' + \eta_c T' F - \eta_c^2 TF''\right)\bar{r}_y - \frac{\mu' T'}{2\bar{x}}\frac{\partial \bar{r}_y}{\partial \bar{x}} \\
&- \frac{\mu}{6\bar{x}}\frac{\partial}{\partial \bar{x}}\left(\frac{\partial \bar{r}_y}{\partial \eta}\right) + \frac{1}{(2\bar{x})^2}\left(\mu - \frac{\eta_c \mu T'}{3T} + \frac{\eta_c \mu' T'}{3}\right)\frac{\partial \bar{r}_y}{\partial \eta} + \frac{\eta_c \mu}{12\bar{x}^2}\frac{\partial^2 \bar{r}_y}{\partial \eta^2} \\
&\qquad + \frac{1}{6\bar{x}}\left(\kappa_z^2 \mu T - 3\eta_c \kappa_z^2 \mu' T T'\right)\bar{r}_z - \frac{1}{3}\kappa_z^2 \mu T \frac{\partial \bar{r}_z}{\partial \bar{x}} + \frac{\eta_c \kappa_z^2 \mu T}{6\bar{x}}\frac{\partial \bar{r}_z}{\partial \eta} \\
&\qquad + \left(-\frac{\eta_c T'}{2\bar{x}} + \frac{1}{\bar{x}}(\gamma - 1)M^2\left[\frac{\mu F'''}{T} - \frac{\mu T' F''}{T^2} + \frac{\mu' T' F''}{T}\right]\right)\bar{r}_e \\
&\qquad\qquad + \frac{1}{\bar{x}}(\gamma - 1)M^2 \frac{\mu F''}{T}\frac{\partial \bar{r}_e}{\partial \eta} = \alpha_2 \mathbf{Q_2}\bar{u};
\end{aligned}
\tag{3.64}
$$

$$
\begin{aligned}
&-\frac{1}{T}\frac{\partial \bar{r}_c}{\partial \eta} + \frac{F''}{T}\bar{r}_x + \left(i + \kappa_z^2 \mu T + \frac{1}{2\bar{x}}\left[2F' - \frac{T' F}{T} + \eta_c F''\right]\right)\bar{r}_y \\
&\qquad - F'\frac{\partial \bar{r}_y}{\partial \bar{x}} + \left(\frac{F}{2\bar{x}} + \frac{2}{3\bar{x}}\left[\frac{\mu T'}{T^2} - \frac{\mu' T'}{T}\right]\right)\frac{\partial \bar{r}_y}{\partial \eta} - \frac{2}{3\bar{x}}\frac{\mu}{T}\frac{\partial^2 \bar{r}_y}{\partial \eta^2} \\
&\qquad\qquad + \frac{2}{3}\kappa_z^2 \mu' T' \bar{r}_z - \frac{1}{3}\kappa_z^2 \mu \frac{\partial \bar{r}_z}{\partial \eta} + \frac{T'}{T}\bar{r}_e = 0;
\end{aligned}
\tag{3.65}
$$

$$
\begin{aligned}
&\bar{r}_c + \frac{\mu' T'}{2\bar{x}}\bar{r}_y + \frac{\mu}{6\bar{x}}\frac{\partial \bar{r}_y}{\partial \eta} + \left(i + \frac{4}{3}\kappa_z^2 \mu T + \frac{F'}{2\bar{x}}\right)\bar{r}_z - F'\frac{\partial \bar{r}_z}{\partial \bar{x}} \\
&\qquad + \frac{1}{2\bar{x}}\left(F + \frac{\mu T'}{T^2} - \frac{\mu' T'}{T}\right)\frac{\partial \bar{r}_z}{\partial \eta} - \frac{1}{2\bar{x}}\frac{\mu}{T}\frac{\partial^2 \bar{r}_z}{\partial \eta^2} = 0;
\end{aligned}
\tag{3.66}
$$

$$
\begin{aligned}
&\left(-\frac{i}{T^2} - \frac{1}{2\bar{x}}\frac{F'}{T}\right)\bar{r}_c + \frac{F'}{T}\frac{\partial \bar{r}_c}{\partial \bar{x}} - \frac{1}{2\bar{x}}\frac{F}{T}\frac{\partial \bar{r}_c}{\partial \eta} + \frac{1}{2\bar{x}}\frac{FF''}{T}\bar{r}_x \\
&+ \frac{1}{2\bar{x}}\frac{\mu' F''}{T}\frac{\partial \bar{r}_x}{\partial \eta} + \left(-FF' + \eta_c (F')^2 - \frac{T' F^2}{T} + \eta_c FF'' - \frac{\mu' F''}{2\bar{x}^2}\right)\bar{r}_y \\
&\qquad + \frac{\mu' F''}{2\bar{x}}\frac{\partial \bar{r}_y}{\partial \bar{x}} + \left(-\frac{1}{3\bar{x}^2}\frac{\mu' T' F}{T} + \frac{\eta_c \mu' F''}{4\bar{x}^2}\right)\frac{\partial \bar{r}_y}{\partial \eta} + \frac{\kappa_z^2 \mu' T' F}{3\bar{x}}\bar{r}_z \\
&\qquad + \left(i + \frac{\kappa_z^2 \mu T}{\mathrm{Pr}} + \frac{1}{2\bar{x}}\left[F' + \frac{T' F}{T} - (\gamma - 1)M^2 \frac{\mu'(F'')^2}{T}\right]\right)\bar{r}_e \\
&\qquad - F'\frac{\partial \bar{r}_e}{\partial \bar{x}} + \frac{1}{2\bar{x}}\left(F + \frac{\mu T'}{\mathrm{Pr}\, T^2}\right)\frac{\partial \bar{r}_e}{\partial \eta} - \frac{1}{2\bar{x}}\frac{\mu}{\mathrm{Pr}\, T}\frac{\partial^2 \bar{r}_e}{\partial \eta^2} = \alpha_4 \mathbf{Q_4}\bar{\tau},
\end{aligned}
\tag{3.67}
$$

with boundary conditions (B.7) and (B.8), and terminal conditions (B.9)-(B.11).

Likewise, for the gradient (3.62), $\bar{r}_c$ is obtained from solving the adjoint equations (B.14), expanded as follows

$$
-\frac{1}{2\bar{x}}\frac{\partial \bar{r}_y}{\partial \eta} - \kappa_z^2 T \bar{r}_z = 0; \tag{3.68}
$$

$$\frac{1}{2\bar{x}}\bar{r}_c - \frac{\partial \bar{r}_c}{\partial \bar{x}} + \frac{\eta_c}{2\bar{x}}\frac{\partial \bar{r}_c}{\partial \eta} + \left(i + \kappa_z^2 \mu T + \frac{F'}{2\bar{x}} - \frac{\eta_c F''}{2\bar{x}}\right)\bar{r}_x - F'\frac{\partial \bar{r}_x}{\partial \bar{x}}$$
$$+\frac{1}{2\bar{x}}\left(F + \frac{\mu T'}{T^2} - \frac{\mu' T'}{T}\right)\frac{\partial \bar{r}_x}{\partial \eta} - \frac{1}{2\bar{x}}\frac{\mu}{T}\frac{\partial^2 \bar{r}_x}{\partial \eta^2}$$
$$+\frac{1}{(2\bar{x})^2}\left(TF + 2\mu' T' - \eta_c TF' + \eta_c T'F - \eta_c^2 TF''\right)\bar{r}_y - \frac{\mu' T'}{2\bar{x}}\frac{\partial \bar{r}_y}{\partial \bar{x}}$$
$$-\frac{\mu}{6\bar{x}}\frac{\partial}{\partial \bar{x}}\left(\frac{\partial \bar{r}_y}{\partial \eta}\right) + \frac{1}{(2\bar{x})^2}\left(\mu - \frac{\eta_c \mu T'}{3T} + \frac{\eta_c \mu' T'}{3}\right)\frac{\partial \bar{r}_y}{\partial \eta} + \frac{\eta_c \mu}{12\bar{x}^2}\frac{\partial^2 \bar{r}_y}{\partial \eta^2} \tag{3.69}$$
$$+\frac{1}{6\bar{x}}\left(\kappa_z^2 \mu T - 3\eta_c \kappa_z^2 \mu' T T'\right)\bar{r}_z - \frac{1}{3}\kappa_z^2 \mu T\frac{\partial \bar{r}_z}{\partial \bar{x}} + \frac{\eta_c \kappa_z^2 \mu T}{6\bar{x}}\frac{\partial \bar{r}_z}{\partial \eta}$$
$$+\left(-\frac{\eta_c T'}{2\bar{x}} + \frac{1}{\bar{x}}(\gamma - 1)M^2\left[\frac{\mu F'''}{T} - \frac{\mu T' F''}{T^2} + \frac{\mu' T' F''}{T}\right]\right)\bar{r}_e$$
$$+\frac{1}{\bar{x}}(\gamma - 1)M^2\frac{\mu F''}{T}\frac{\partial \bar{r}_e}{\partial \eta} = \alpha_2^{(0)}\mathbf{Q_2^{(0)}}\bar{u}^{(0)};$$

$$-\frac{1}{T}\frac{\partial \bar{r}_c}{\partial \eta} + \frac{F''}{T}\bar{r}_x + \left(i + \kappa_z^2 \mu T + \frac{1}{2\bar{x}}\left[2F' - \frac{T'F}{T} + \eta_c F''\right]\right)\bar{r}_y$$
$$-F'\frac{\partial \bar{r}_y}{\partial \bar{x}} + \left(\frac{F}{2\bar{x}} + \frac{2}{3\bar{x}}\left[\frac{\mu T'}{T^2} - \frac{\mu' T'}{T}\right]\right)\frac{\partial \bar{r}_y}{\partial \eta} - \frac{2}{3\bar{x}}\frac{\mu}{T}\frac{\partial^2 \bar{r}_y}{\partial \eta^2} \tag{3.70}$$
$$+\frac{2}{3}\kappa_z^2 \mu' T'\bar{r}_z - \frac{1}{3}\kappa_z^2 \mu\frac{\partial \bar{r}_z}{\partial \eta} + \frac{T'}{T}\bar{r}_e = 0;$$

$$\bar{r}_c + \frac{\mu' T'}{2\bar{x}}\bar{r}_y + \frac{\mu}{6\bar{x}}\frac{\partial \bar{r}_y}{\partial \eta} + \left(i + \frac{4}{3}\kappa_z^2 \mu T + \frac{F'}{2\bar{x}}\right)\bar{r}_z - F'\frac{\partial \bar{r}_z}{\partial \bar{x}}$$
$$+\frac{1}{2\bar{x}}\left(F + \frac{\mu T'}{T^2} - \frac{\mu' T'}{T}\right)\frac{\partial \bar{r}_z}{\partial \eta} - \frac{1}{2\bar{x}}\frac{\mu}{T}\frac{\partial^2 \bar{r}_z}{\partial \eta^2} = 0; \tag{3.71}$$

$$\left(-\frac{i}{T^2} - \frac{1}{2\bar{x}}\frac{F'}{T}\right)\bar{r}_c + \frac{F'}{T}\frac{\partial \bar{r}_c}{\partial \bar{x}} - \frac{1}{2\bar{x}}\frac{F}{T}\frac{\partial \bar{r}_c}{\partial \eta} + \frac{1}{2\bar{x}}\frac{FF''}{T}\bar{r}_x$$
$$+\frac{1}{2\bar{x}}\frac{\mu' F''}{T}\frac{\partial \bar{r}_x}{\partial \eta} + \left(-FF' + \eta_c(F')^2 - \frac{T'F^2}{T} + \eta_c FF'' - \frac{\mu' F''}{2\bar{x}^2}\right)\bar{r}_y$$
$$+\frac{\mu' F''}{2\bar{x}}\frac{\partial \bar{r}_y}{\partial \bar{x}} + \left(-\frac{1}{3\bar{x}^2}\frac{\mu' T' F}{T} + \frac{\eta_c \mu' F''}{4\bar{x}^2}\right)\frac{\partial \bar{r}_y}{\partial \eta} + \frac{\kappa_z^2 \mu' T' F}{3\bar{x}}\bar{r}_z \tag{3.72}$$
$$+\left(i + \frac{\kappa_z^2 \mu T}{\mathrm{Pr}} + \frac{1}{2\bar{x}}\left[F' + \frac{T'F}{T} - (\gamma - 1)M^2\frac{\mu'(F'')^2}{T}\right]\right)\bar{r}_e$$
$$-F'\frac{\partial \bar{r}_e}{\partial \bar{x}} + \frac{1}{2\bar{x}}\left(F + \frac{\mu T'}{\mathrm{Pr}\, T^2}\right)\frac{\partial \bar{r}_e}{\partial \eta} - \frac{1}{2\bar{x}}\frac{\mu}{\mathrm{Pr}\, T}\frac{\partial^2 \bar{r}_e}{\partial \eta^2} = \alpha_4^{(0)}\mathbf{Q_4^{(0)}}\bar{\tau}.$$

with boundary conditions (B.15) and (B.16), and terminal conditions (B.17)-(B.19).

The controls $\bar{v}_w$ and $\bar{v}_w^{(0)}$ are obtained independently as shown, and then summed using the decomposition (2.55) as

$$\bar{v}_0 = C^{(0)}\bar{v}_w^{(0)} + C\frac{ik_z}{k_x}\bar{v}_w \quad \text{at} \quad \eta = 0.$$

The formulation of this optimisation problem for the particular case of the incompressible LUBR equations is provided in Appendix C.

3.3 Numerical procedures for the control theory

The strategy to numerically implement the control theory for the minimisation of the cost functionals $\mathcal{J}$ defined in (3.21) and $\mathcal{J}^{(0)}$ defined in (3.22) is identical in both cases. The adjoint components $\bar{r}_x$, $\bar{r}_y$, $\bar{r}_z$, $\bar{r}_e$ and $\bar{r}_c$ are obtained by solving the systems of adjoint equations described in the previous section. The adjoint equations (3.63)-(3.67) and (3.68)-(3.72) are solved using a backwards march, i.e. from $\bar{x}_f$ to $\bar{x}_i$, as opposed to the forward march for the solution of the numerical boundary region equations. This is the natural direction for the solution of the adjoint equations (e.g. Bewley [8]). Both adjoint equation systems are solved using a second-order finite difference scheme which is central in η and backward in $\bar{x}$. The stencil is shown in figure 3.1. The derivatives of the adjoint components $\bar{r}_x$, $\bar{r}_z$ and $\bar{r}_e$ are approximated as:

$$\frac{\partial r_x}{\partial \eta} \approx \frac{(r_x)_{i,j+1} - (r_x)_{i,j-1}}{2\Delta\eta}, \tag{3.73}$$

$$\frac{\partial^2 r_x}{\partial \eta^2} \approx \frac{(r_x)_{i,j+1} - 2(r_x)_{i,j} + (r_x)_{i,j-1}}{(\Delta\eta)^2}, \tag{3.74}$$

$$\frac{\partial r_x}{\partial \bar{x}} \approx \frac{a(r_x)_{i,j} + b(r_x)_{i+1,j} + c(r_x)_{i+2,j}}{\Delta\bar{x}}, \tag{3.75}$$

where $a = 3/2$, $b = -2$ and $c = 1/2$. In order to avoid the equivalent of the pressure decoupling phenomenon, the components $\bar{r}_y$ and $\bar{r}_c$ are computed using a staggered grid in the η direction with respect to the grid of the remaining components $\bar{r}_x$, $\bar{r}_z$ and $\bar{r}_e$. The components $\bar{r}_y$ and $\bar{r}_c$ and their derivatives are approximated as:

$$r_c \approx \frac{(r_c)_{i,j+1/2} + (r_c)_{i,j-1/2}}{2}, \tag{3.76}$$

$$\frac{\partial r_c}{\partial \eta} \approx \frac{(r_c)_{i,j+1/2} - (r_c)_{i,j-1/2}}{\Delta\eta}, \tag{3.77}$$

$$\frac{\partial^2 r_c}{\partial \eta^2} \approx \frac{(r_c)_{i,j+3/2} - 2(r_c)_{i,j+1/2} + (r_c)_{i,j-1/2}}{(\Delta\eta)^2}, \tag{3.78}$$

$$\frac{\partial r_c}{\partial x} \approx \frac{a\left((r_c)_{i,j+1/2} + (r_c)_{i,j-1/2}\right) + b\left((r_c)_{i+1,j+1/2} + (r_c)_{i+1,j-1/2}\right)}{2\Delta\bar{x}} + \frac{c\left((r_c)_{i+2,j+1/2} + (r_c)_{i+2,j-1/2}\right)}{2\Delta\bar{x}}, \tag{3.79}$$

$$\frac{\partial^2 r_c}{\partial\bar{x}\partial\eta} \approx \frac{a\left((r_c)_{i,j+1/2} - (r_c)_{i,j-1/2}\right) + b\left((r_c)_{i+1,j+1/2} - (r_c)_{i+1,j-1/2}\right)}{\Delta\bar{x}\Delta\eta} + \frac{c\left((r_c)_{i+2,j+1/2} - (r_c)_{i+2,j-1/2}\right)}{\Delta\bar{x}\Delta\eta}. \tag{3.80}$$

With regard to the implementation of the terminal conditions (B.9)-(B.11),

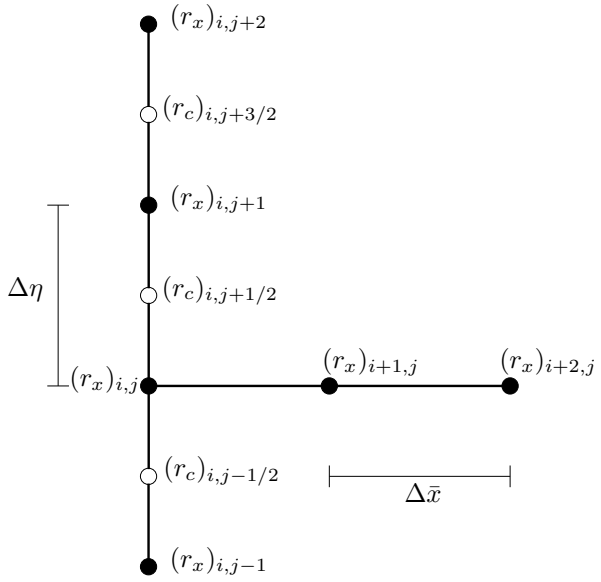

Figure 3.1: The second-order stencil in $\bar{x}$ and η used to compute the adjoint equations.

(B.17)-(B.19), a second-order method in $\bar{x}$ is replaced by a first-order scheme for the first backwards iteration, and this is done by setting $a = 1$, $b = -1$ and $c = 0$.

Due to the boundary condition being different from zero as $\eta \to \infty$, the matrix $\mathbf{Q_2^{(0)}}$ is defined as a diagonal matrix with the function

$$e^{-b_e\eta}$$

at each entry, and with $b_e = 1$. This ensures that the integrals of the cost functional (3.22) converge independently of the simulation size. In addition, the right-hand-side forcing of the adjoint equation (3.69) can be expressed as

$\alpha_2^{(0)} e^{-b_e \eta} \bar{u}^{(0)}$. The remaining Hermitian matrices $\mathbf{Q_1}$, $\mathbf{Q_2}$, $\mathbf{Q_4}$, $\mathbf{Q_v}$, $\mathbf{Q_3^{(0)}}$, $\mathbf{Q_4^{(0)}}$ and $\mathbf{Q_v^{(0)}}$ were defined as identity matrices for all simulations in this thesis.

The $[\bar{x}_i, \bar{x}_f]$ domain for the actuation varied with the simulation. The initial $\bar{x}$ location was set to $\bar{x}_i = 10^{-9}$ and $\bar{x}_i = 0.0009$ for the solution of the cost functionals $\mathcal{J}$ (3.21) and $\mathcal{J}^{(0)}$ (3.22) respectively. The final location of $\bar{x}$ was defined according to the value of κ_z as shown in table 3.1, unless otherwise specified.

κ_z	$\bar{x}_f$
0	50
0.027	50
0.5	20
1	5
1.5	5
2	5

Table 3.1: The list of streamwise final locations of the actuation $\bar{x}_f$ according to the value of κ_z used in the simulation.

Numerical checks were conducted using the right-hand-side forcing described in the previous section to ensure mesh independence. Further checks were done using the equation (4.13) in LWG, as the predefined values of $\bar{u} = \frac{1}{2}\bar{x}\eta F''$ in equation (3.64). This extra check was performed to study the robustness of the numerical method in solving the adjoint equations, in such a way that the numerical error is independent of the boundary region numerical solutions.

As in the boundary region numerical procedures, extra information for the solution of the adjoint equations can be found in Cebeci [14] from pages 260-264.

In the numerical search for the gradients (3.61) and (3.62) that minimise the optimisation problem, the steepest descent method was implemented to update the wall-boundary conditions (3.18) and (3.19) in each iteration. The steepest descent was implemented as

$$\bar{v}_w^{N+1} = \bar{v}_w^N - \alpha^N \frac{\mathrm{d}\mathcal{J}^N}{\mathrm{d}\bar{v}_w} \tag{3.81}$$

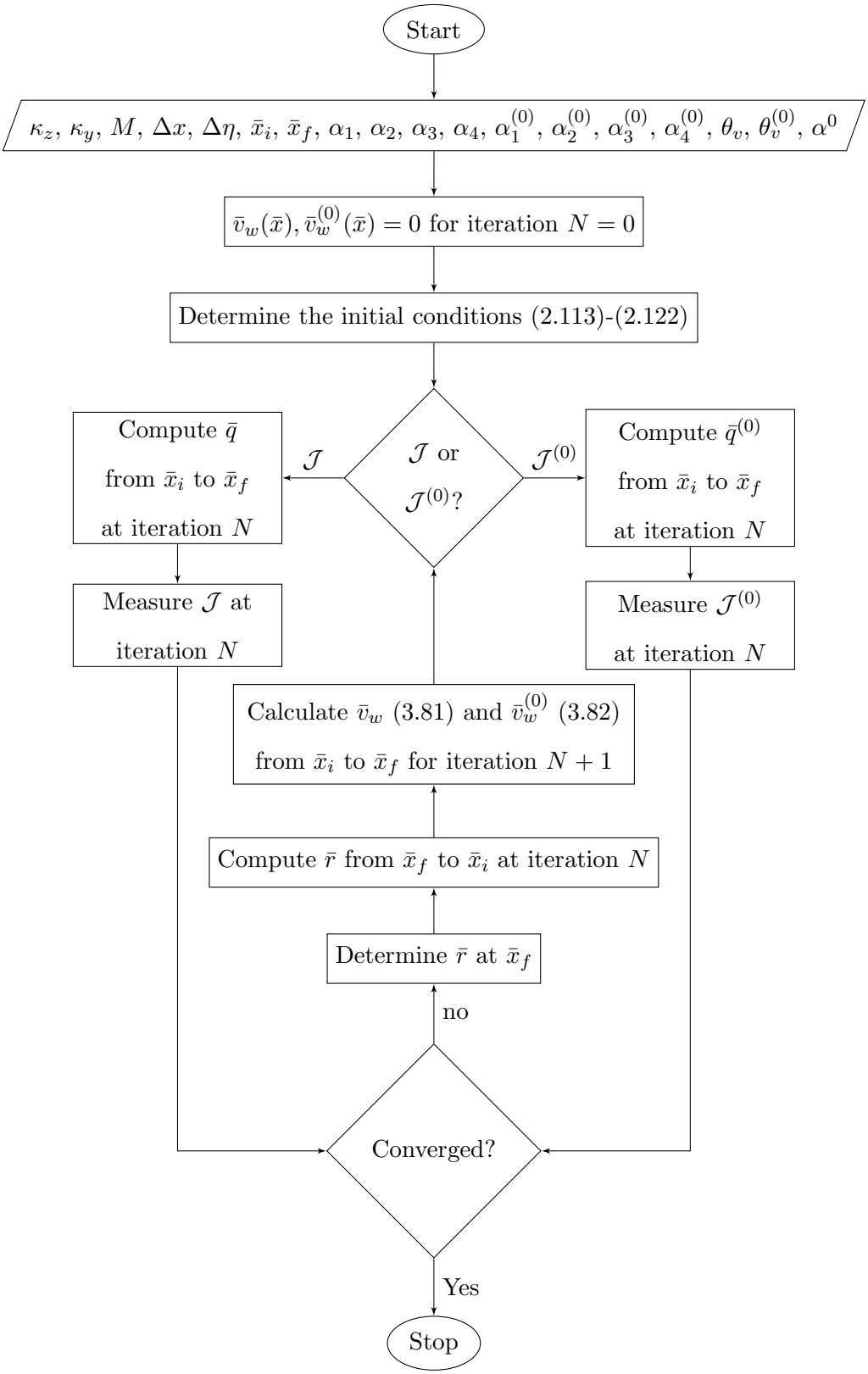

Figure 3.2: Flowchart of the algorithm employed to minimise the cost functionals.

and

$$\bar{v}_w^{(0)N+1} = \bar{v}_w^{(0)N} - \alpha^N \frac{\mathrm{d}\mathcal{J}^{(0)N}}{\mathrm{d}\bar{v}_w} \tag{3.82}$$

from $\bar{x}_i$ to $\bar{x}_f$, where N indicates the number of iterations and α^N is a parameter that controls how large the "step" is given in the gradient direction. A value of $\alpha^N = \pm 2048$ was used to start all simulations, and in each iteration the value is corrected to ensure minimisation of the cost functionals $\mathcal{J}$ and $\mathcal{J}^{(0)}$. In each iteration, the steepest descent method updates the actuators in the direction which maximises the cost functionals $\mathcal{J}$ and $\mathcal{J}^{(0)}$ with respect to $\bar{v}_w$ and $\bar{v}_w^{(0)}$ respectively. If a sufficiently large value of iterations is considered, i.e. $k \to \infty$, the algorithm should find a local minimum of the system. Due to the nature of the cost functionals $\mathcal{J}$ (3.21), $\mathcal{J}^{(0)}$ (3.22), and the CLUBR equations, the solutions should approximate the global minimum.

In addition, the following convergence criteria:

$$\frac{\mathcal{J}^N - \mathcal{J}^{N-1}}{\mathcal{J}^{N-1}} < \epsilon_c, \tag{3.83}$$

was put into effect to detect the convergence of the steepest descent method, where ϵ_c is a convergence parameter set to 10^{-7} in all simulations. When the $\mathcal{J}^N - \mathcal{J}^{N-1}/\mathcal{J}^{N-1}$ becomes smaller than the parameter ϵ_c, it is assumed that the method converged, and thus the iterative procedure stops.

The full algorithm for the optimisation strategy is illustrated in figure 3.2 and is described briefly in the following steps:

1. The unperturbed flow equations (2.29) and (2.30) are solved.

2. The power-series (2.111) and (2.112) are obtained.

3. The control actuators $\bar{v}_w$ or $\bar{v}_w^{(0)}$, implemented by the boundary conditions (3.18) and (3.19) respectively, are initiated as zero across $\bar{x}$ for iteration $N = 0$.

4. The initial conditions (2.113)-(2.122) are determined and stored to initiate every forward march.

5. The CLUBR equations (2.64)-(2.68) are solved using the modified wall boundary condition (3.18) or (3.19), in a forward march from $\bar{x}_i$ to $\bar{x}_f$.

6. The cost functionals $\mathcal{J}$ (3.21) or $\mathcal{J}^{(0)}$ (3.22) are computed for iteration N.

7. If $N > 0$, the convergence criteria (3.83) is checked. If it is satisfied, the simulation stops, otherwise it continues.

8. The terminal conditions (B.9)-(B.11) or (B.17)-(B.19) are calculated.

9. The adjoint equations (3.63)-(3.67) or (3.68)-(3.72) are computed from $\bar{x}_f$ to $\bar{x}_i$ in a backwards march.

10. The control actuators $\bar{v}_w$ or $\bar{v}_w^{(0)}$ are updated for iteration $N+1$ using the steepest descent method (3.81) or (3.82).

11. The process iterates from step 4.

It is important to mention that in our simulations, we have full information of our system and thus the control is robust. This was further verfied from the numerous simulations performed, where a smooth convergence was obtained to a minimum value of the cost functionals.

If the knowledge of the flow had been partial, some noise should be added in the input loop to ensure the controller is robust and that the optimal wall profiles resultant from the in-house code would perform well for a disturbed flow model.

The code was verified several times and compared to the independent in-house code of Dr. Liang and Dr. Papadakis from Imperial College London, which solves an incompressible Blasius boundary layer using a Riccati framework. The magnitude of the uncontrolled and controlled velocity and pressure perturbations can be seen in figures 3.3 and 3.4 for $\kappa_z = -\kappa_y = 1$ and $M = 0$, where the delta and circle symbols represent the uncontrolled and controlled profiles, respectively, of the Imperial College London in-house code.

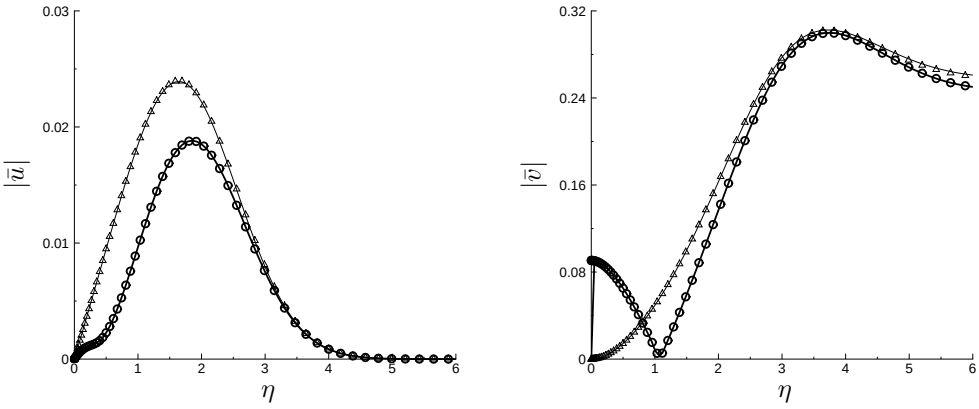

Figure 3.3: The magnitude of the streamwise velocity $|\bar{u}|$ (left) and wall-normal velocity $|\bar{v}|$ (right) fluctuations along η at $\bar{x} = 0.5$ of the uncontrolled profiles (thinner solid lines and delta symbols) versus the optimal controlled profiles (thicker solid lines and circle symbols) for $M = 0$, $\alpha_1 = \alpha_3 = \alpha_4 = 0$, $\alpha_2 = 1$, $\theta_v^2 = 10^{-3}$, $\kappa_z = 1$ and $\kappa_y = -1$.

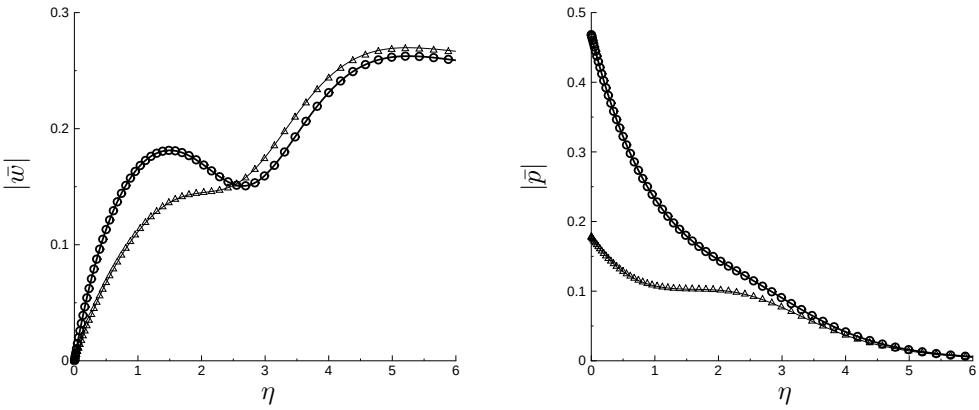

Figure 3.4: The magnitude of the spanwise velocity $|\bar{w}|$ (left) and pressure $|\bar{p}|$ (right) fluctuations along η at $\bar{x} = 0.5$ of the uncontrolled profiles (thinner solid lines and delta symbols) versus the optimal controlled profiles (thicker solid lines and circle symbols) for $M = 0$, $\alpha_1 = \alpha_3 = \alpha_4 = 0$, $\alpha_2 = 1$, $\kappa_z = 1$, $\theta_v^2 = 10^{-3}$ and $\kappa_y = -1$.

3.4 Controlled numerical results

3.4.1 Attenuation parametric study and cost of actuation

The wall-normal blowing and suction actuators are enabled at this point in an attempt to attenuate the Klebanoff modes.

In order to investigate which modes κ_z, κ_y can be attenuated, a parametric mapping is carried out for the energy reduction of $\mathcal{J}$, with $\alpha_1 = \alpha_3 = \alpha_4 = 0$, $\alpha_2 = 1$ and the cost of actuation neglected as $\theta_v^2 \to 0$. The energy reduction is calculated as

$$\text{Energy reduction} = 1 - \frac{\mathcal{J}^N}{\mathcal{J}^0},$$

and the cost functional $\mathcal{J}^{(0)}$ is not considered at this stage. This is because the actuation is implemented at the wall, where the components $\bar{p}^{(0)}$, $\bar{u}^{(0)}$, $\bar{v}^{(0)}$, $\bar{w}^{(0)}$ and $\bar{\tau}^{(0)}$ are typically of second order, as shown in the previous chapter. These components will be attenuated further into the study, once the possibility of attenuating the modes κ_z, κ_y is confirmed.

The results of the parametric mapping are shown in figure 3.5, where energy reduction was achieved for all modes in the study. The grey region denominated as TS waves in the figure also includes a region of large-λ_z Klebanoff modes from $\kappa_z = 0$ to $\kappa_z = 10^{-3}$. Further details are found in Ricco & Wu [58]. The grey zone was avoided in the parametric mapping as the target of the control are the Klebanoff modes.

In order to investigate the effects of the actuation cost, κ_z and κ_y are set to recreate cases 1, 1-A to 1-D, i.e. with $\kappa_z = \kappa_y = 1$. From the parametric study, it is already known that the actuation is viable, and thus the simulations are performed with similar conditions to the parametric study but with different values of θ_v.

The energy reduction obtained for different values of θ_v is shown in table 3.2, and as predicted, there is an insignificant energy reduction for large values of $\theta_v^2 > 10^{-2}$. Additionally, the theoretical maximum energy reduction is achieved for values of $\theta_v^2 < 10^{-7}$.

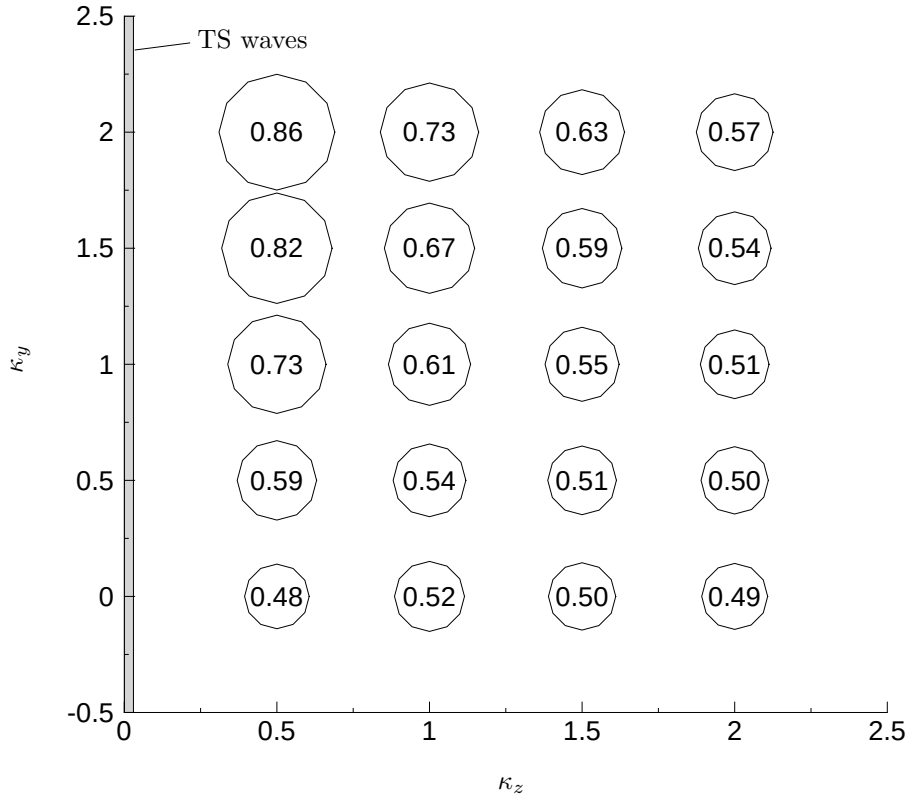

Figure 3.5: The mapping shows the energy reduction of $\mathcal{J}$ achieved for different values of κ_z and κ_y for $M = 3$, $\alpha_1 = \alpha_3 = \alpha_4 = 0$, $\alpha_2 = 1$ and $\theta_v^2 \to 0$. The grey area indicates the region where TS-waves develop early along $\bar{x}$ as shown in Ricco & Wu [58].

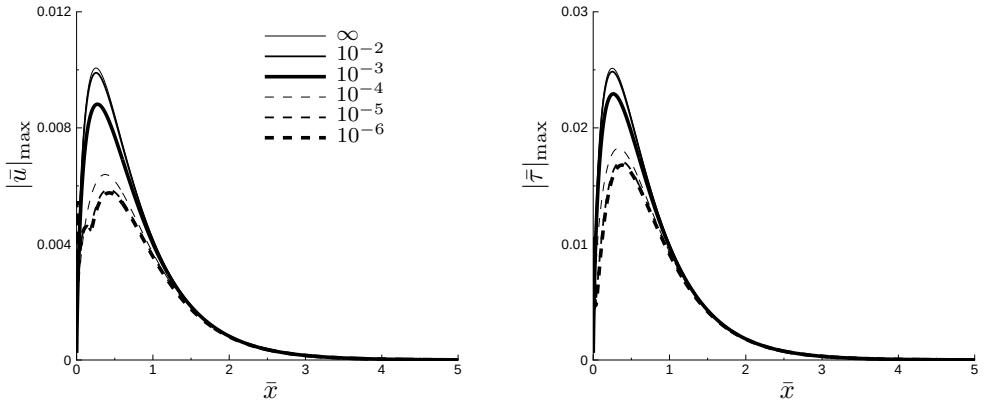

Figure 3.6: Amplitude of the streamwise velocity $|\bar{u}|_{\max}$ (left) and temperature $|\bar{\tau}|_{\max}$ (right) fluctuations for $M = 3$, $\alpha_1 = \alpha_3 = \alpha_4 = 0$, $\alpha_2 = 1$, $\kappa_z = 1$ and $\kappa_y = 1$. The legend indicates the different weights θ_v^2 used, and $\theta_v^2 = \infty$ designates the uncontrolled case.

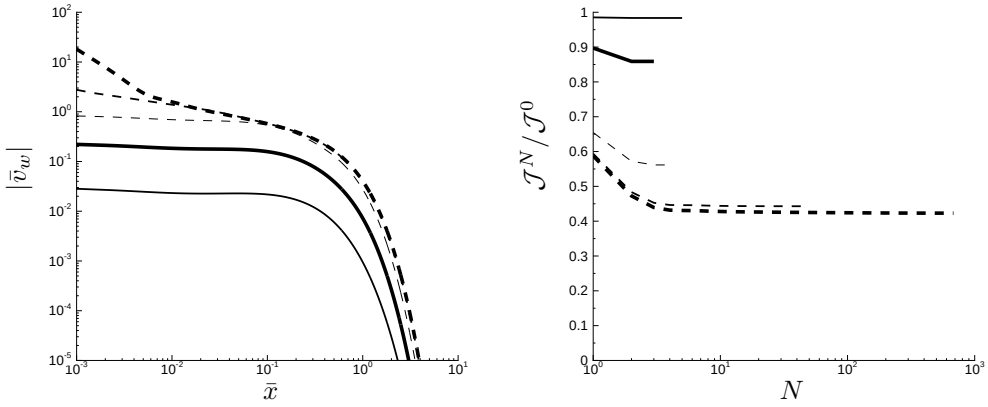

Figure 3.7: Amplitude of the control $\bar{v}_w$ (left) across $\bar{x}$ (left) and the normalised cost functional $\mathcal{J}^N/\mathcal{J}^0$ per iteration N (right) for $M = 3$, $\alpha_1 = \alpha_3 = \alpha_4 = 0$, $\alpha_2 = 1$, $\kappa_z = 1$ and $\kappa_y = 1$ with the indicated values of θ_v^2 in figure 3.6.

κ_z	κ_y	θ_v^2	Energy reduction
1	1	10^0	0.00
1	1	10^{-1}	0.00
1	1	10^{-2}	0.02
1	1	10^{-3}	0.16
1	1	10^{-4}	0.46
1	1	10^{-5}	0.57
1	1	10^{-6}	0.59
1	1	10^{-7}	0.60
1	1	10^{-8}	0.61

Table 3.2: The list of energy reductions achieved for $M = 3$, $\alpha_1 = \alpha_3 = \alpha_4 = 0$ and $\alpha_2 = 1$ according to the value of θ_v^2 used in the simulation.

The analysis shows that the appropriate values of θ_v^2 to be used are between 10^{-2} and 10^{-6}, and the maximum amplitude of the streamwise velocity $\bar{u}$ and temperature $\bar{\tau}$ along $\bar{x}$ are plotted in figure 3.6 for such values. The respective optimal actuation $|\bar{v}_w|$ profiles and the normalised cost functionals for each case are shown in figure 3.7. In cases with $\theta_v^2 = 10^{-2}$ and $\theta_v^2 = 10^{-3}$, the curves of the streamwise velocity $|\bar{u}|_{\max}$ and temperature $|\bar{\tau}|_{\max}$ have a similar shape to the uncontrolled case, and showing that the physics remains similar with small reductions, as is verified in table 3.2. The results of $\theta_v^2 = 10^{-4}$ illustrate a strong attenuation and a fast convergence of the algorithm. The cases with $\theta_v^2 = 10^{-5}$ and $\theta_v^2 = 10^{-6}$ are nearly identical and reveal the limits of optimal attenuation of the Klebanoff modes. Due to the faster convergence, the value of $\theta_v^2 = 10^{-5}$ will be used to further investigate the physics involved in the optimal attenuation of the Klebanoff modes.

The extreme cases of the parametric study are then examined and the energy reductions obtained are shown in table 3.3. The cases with $\kappa_z = 2$ have displayed a higher sensitivity to the actuation cost parameters as the energy reduction was slightly less than the cases with $\theta_v^2 \to 0$. Further investigation is conducted by studying their velocity and temperature profiles.

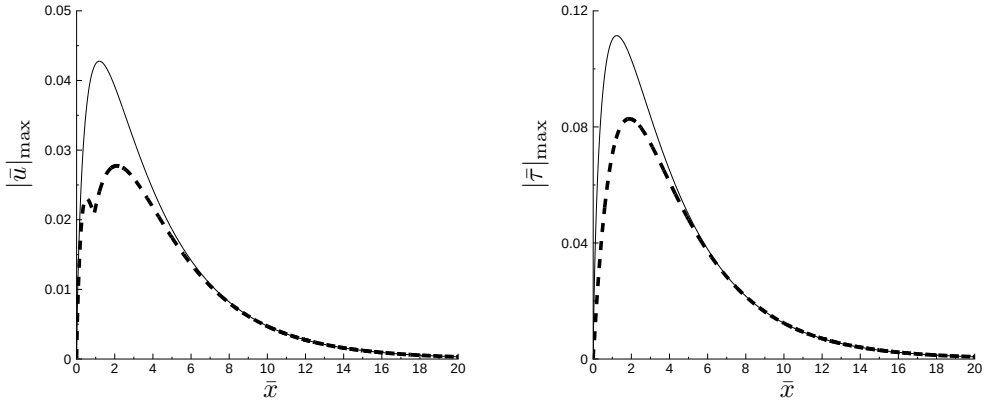

Figure 3.8: The maximum magnitude of the streamwise velocity $|\bar{u}|_{\max}$ (left) and temperature $|\bar{\tau}|_{\max}$ (right) fluctuations along the streamwise direction $\bar{x}$ of the uncontrolled profiles (solid lines) versus the optimal controlled profiles (dashed lines) for $M = 3$, $\alpha_1 = \alpha_3 = \alpha_4 = 0$, $\alpha_2 = 1$, $\kappa_z = 0.5$ and $\kappa_y \to 0$.

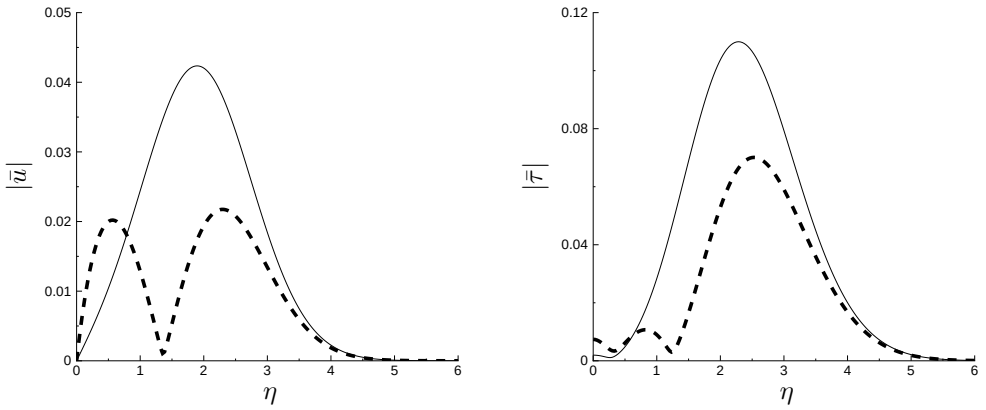

Figure 3.9: The magnitude of the streamwise velocity $|\bar{u}|$ (left) and temperature $|\bar{\tau}|$ (right) fluctuations along η at $\bar{x} = 1$ of the uncontrolled profiles (solid lines) versus the optimal controlled profiles (dashed lines) for $M = 3$, $\alpha_1 = \alpha_3 = \alpha_4 = 0$, $\alpha_2 = 1$, $\kappa_z = 0.5$ and $\kappa_y \to 0$.

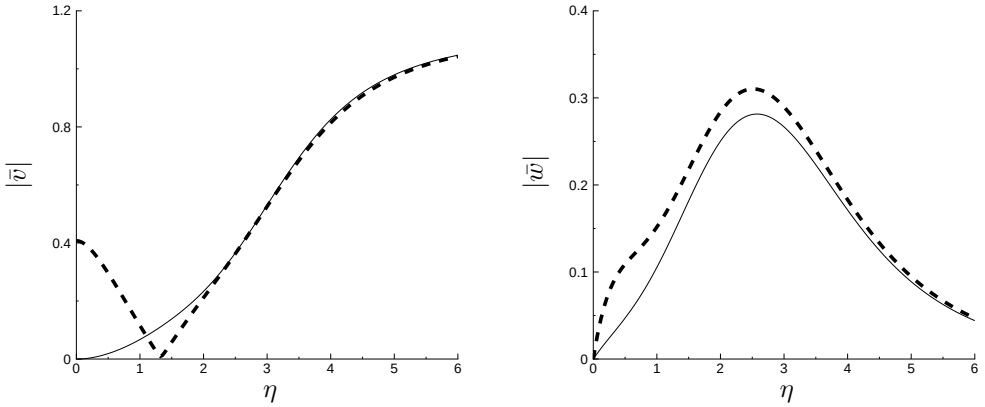

Figure 3.10: The magnitude of the wall-normal $|\bar{v}|$ (left) and spanwise $|\bar{w}|$ (right) velocity fluctuations along η at $\bar{x} = 1$ of the uncontrolled profiles (solid lines) versus the optimal controlled profiles (dashed lines) for $M = 3$, $\alpha_1 = \alpha_3 = \alpha_4 = 0$, $\alpha_2 = 1$, $\kappa_z = 0.5$ and $\kappa_y \to 0$.

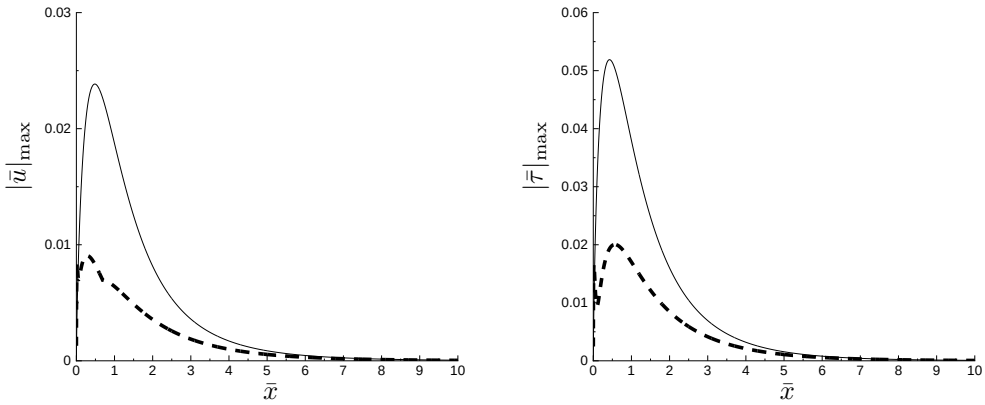

Figure 3.11: The maximum magnitude of the streamwise velocity $|\bar{u}|_{\max}$ (left) and temperature $|\bar{\tau}|_{\max}$ (right) fluctuations along the streamwise direction $\bar{x}$ of the uncontrolled profiles (solid lines) versus the optimal controlled profiles (dashed lines) for $M = 3$, $\alpha_1 = \alpha_3 = \alpha_4 = 0$, $\alpha_2 = 1$, $\kappa_z = 0.5$ and $\kappa_y = 2$.

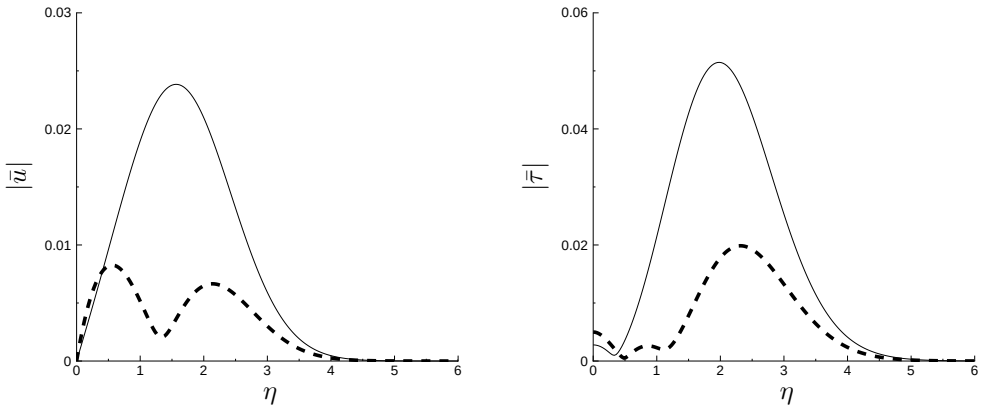

Figure 3.12: The magnitude of the streamwise velocity $|\bar{u}|$ (left) and temperature $|\bar{\tau}|$ (right) fluctuations along η at $\bar{x} = 0.5$ of the uncontrolled profiles (solid lines) versus the optimal controlled profiles (dashed lines) for $M = 3$, $\alpha_1 = \alpha_3 = \alpha_4 = 0$, $\alpha_2 = 1$, $\kappa_z = 0.5$ and $\kappa_y = 2$.

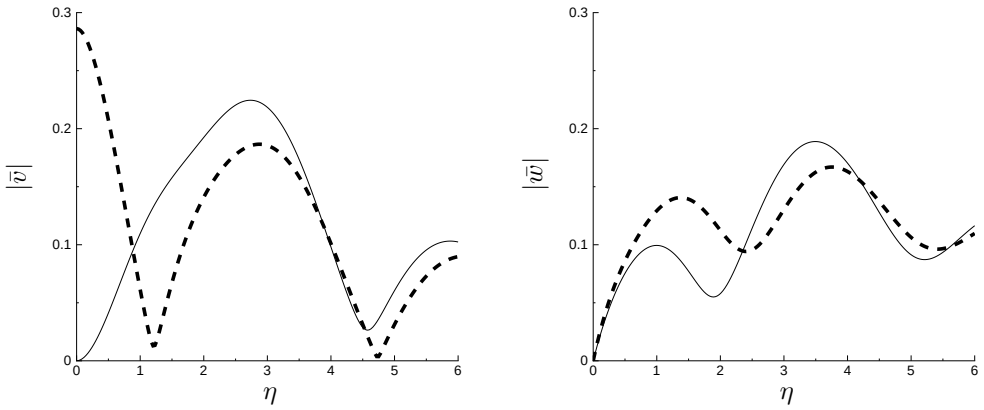

Figure 3.13: The magnitude of the wall-normal $|\bar{v}|$ (left) and spanwise $|\bar{w}|$ (right) velocity fluctuations along η at $\bar{x} = 0.5$ of the uncontrolled profiles (solid lines) versus the optimal controlled profiles (dashed lines) for $M = 3$, $\alpha_1 = \alpha_3 = \alpha_4 = 0$, $\alpha_2 = 1$, $\kappa_z = 0.5$ and $\kappa_y = 2$.

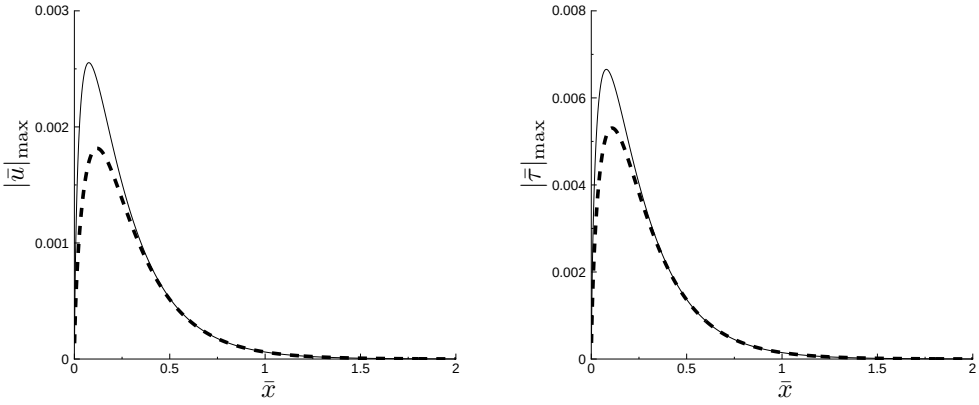

Figure 3.14: The maximum magnitude of the streamwise velocity $|\bar{u}|_{\max}$ (left) and temperature $|\bar{\tau}|_{\max}$ (right) fluctuations along the streamwise direction $\bar{x}$ of the uncontrolled profiles (solid lines) versus the optimal controlled profiles (dashed lines) for $M = 3$, $\alpha_1 = \alpha_3 = \alpha_4 = 0$, $\alpha_2 = 1$, $\kappa_z = 2$ and $\kappa_y \to 0$.

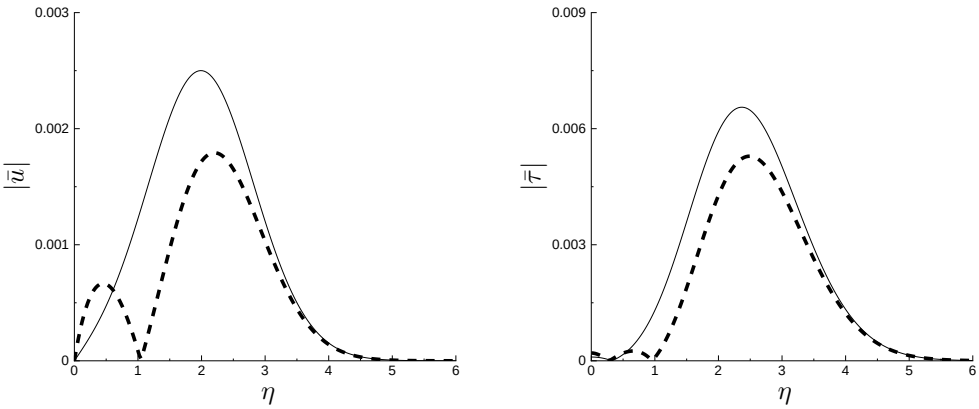

Figure 3.15: The magnitude of the streamwise velocity $|\bar{u}|$ (left) and temperature $|\bar{\tau}|$ (right) fluctuations along η at $\bar{x} = 0.1$ of the uncontrolled profiles (solid lines) versus the optimal controlled profiles (dashed lines) for $M = 3$, $\alpha_1 = \alpha_3 = \alpha_4 = 0$, $\alpha_2 = 1$, $\kappa_z = 2$ and $\kappa_y \to 0$.

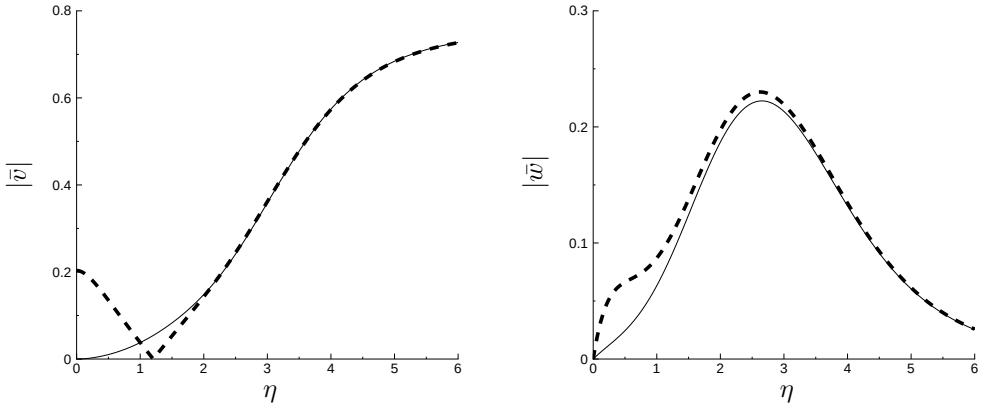

Figure 3.16: The magnitude of the wall-normal $|\bar{v}|$ (left) and spanwise $|\bar{w}|$ (right) velocity fluctuations along η at $\bar{x} = 0.1$ of the uncontrolled profiles (solid lines) versus the optimal controlled profiles (dashed lines) for $M = 3$, $\alpha_1 = \alpha_3 = \alpha_4 = 0$, $\alpha_2 = 1$, $\kappa_z = 2$ and $\kappa_y \to 0$.

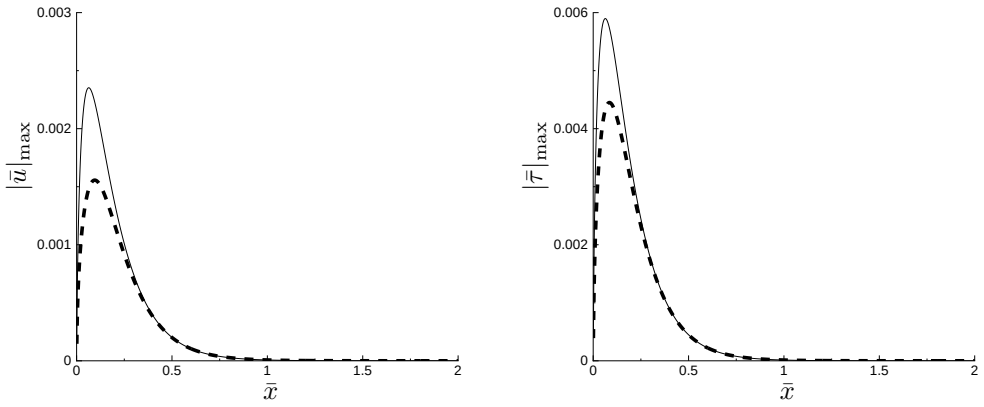

Figure 3.17: The maximum magnitude of the streamwise velocity $|\bar{u}|_{\max}$ (left) and temperature $|\bar{\tau}|_{\max}$ (right) fluctuations along the streamwise direction $\bar{x}$ of the uncontrolled profiles (solid lines) versus the optimal controlled profiles (dashed lines) for $M = 3$, $\alpha_1 = \alpha_3 = \alpha_4 = 0$, $\alpha_2 = 1$ and $\kappa_z = \kappa_y = 2$.

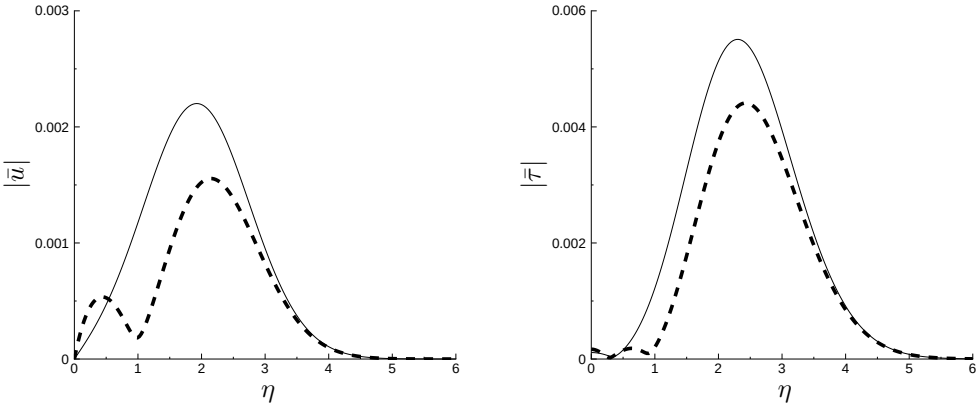

Figure 3.18: The magnitude of the streamwise velocity $|\bar{u}|$ (left) and temperature $|\bar{\tau}|$ (right) fluctuations along η at $\bar{x} = 0.1$ of the uncontrolled profiles (solid lines) versus the optimal controlled profiles (dashed lines) for $M = 3$, $\alpha_1 = \alpha_3 = \alpha_4 = 0$, $\alpha_2 = 1$ and $\kappa_z = \kappa_y = 2$.

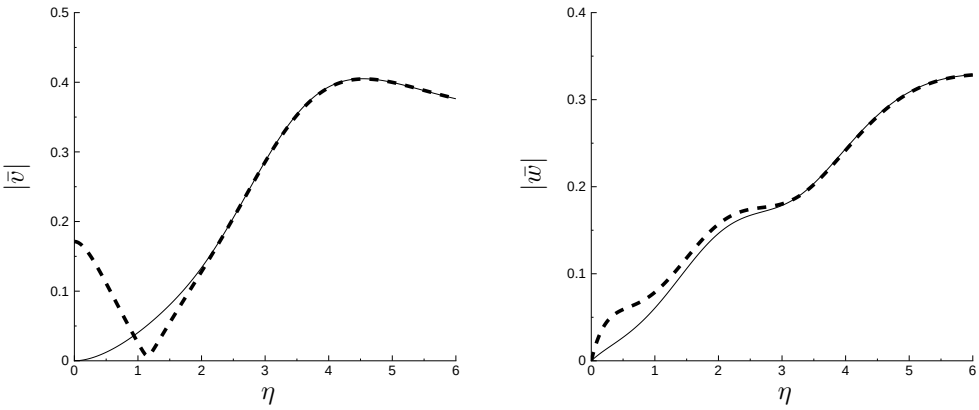

Figure 3.19: The magnitude of the wall-normal $|\bar{v}|$ (left) and spanwise $|\bar{w}|$ (right) velocity fluctuations along η at $\bar{x} = 0.1$ of the uncontrolled profiles (solid lines) versus the optimal controlled profiles (dashed lines) for $M = 3$, $\alpha_1 = \alpha_3 = \alpha_4 = 0$, $\alpha_2 = 1$ and $\kappa_z = \kappa_y = 2$.

κ_z	κ_y	Energy reduction	Figures
0.5	0	0.48	3.8-3.10
0.5	2	0.86	3.11-3.13
2	0	0.34	3.14-3.16
2	2	0.39	3.17-3.19

Table 3.3: The list of the energy reductions achieved for $M = 3$, $\alpha_1 = \alpha_3 = \alpha_4 = 0$, $\alpha_2 = 1$ using $\theta_v^2 = 10^{-5}$.

The maximum magnitude of the velocities and temperature fluctuations along $\bar{x}$ are plotted in figures 3.8 and 3.11 for the two extreme cases with $\kappa_z = 0.5$. For the case with $\kappa_z = 0.5$ and $\kappa_y \to 0$, the velocity and temperature profiles at $\bar{x} = 1$ are shown in figures 3.9 and 3.10, while for the case with $\kappa_z = 0.5$ and $\kappa_y = 2$, the velocity and temperature profiles are displayed at $\bar{x} = 0.5$ in figures 3.12 and 3.13. The $\bar{x}$ locations were chosen to approximate the peak of the Klebanoff modes along the streamwise direction $\bar{x}$. Both cases demonstrate that when the actuators are active, the otherwise solo peak in the streamwise velocity fluctuations $\bar{u}$ is greatly attenuated around $\eta = 1.25$, resulting in two smaller magnitude peaks. This is consistent with the reduction of the temperature streaks, where a similar reduction is found around $\eta = 1.25$. The wall-normal velocity $\bar{v}$ increases close to the wall due to the introduction of the actuators, but it then decreases around $\eta = 1.25$, which corresponds to the resulting reductions in the laminar and thermal streaks.

For the cases with $\kappa_z = 2$, the maximum magnitude of the velocity and temperature fluctuations along $\bar{x}$ are displayed in figures 3.14 and 3.17, and the velocity and temperature profiles at $\bar{x} = 0.1$ are plotted in figures 3.15 and 3.16 for the case with $\kappa_z = 2$ and $\kappa_y \to 0$, and in figures 3.18 and 3.19 for the case with $\kappa_z = \kappa_y = 2$. The maximum streamwise velocity magnitude occurs around $\bar{x} = 0.1$ in these two extreme cases. Similar to the two extreme cases with $\kappa_z = 0.5$, there is an increase of the wall-normal velocity fluctuations near the wall due to the actuation. This results in a sudden drop around $\eta = 1$, which

is connected to the local minima in the streamwise velocity and temperature profiles. The main difference to the previous cases is that the unattenuated streamwise velocity peak leads to a smaller magnitude peak close to the wall with the addition of actuation, and a medium magnitude peak in the outer portion of the boundary layer. With the extrema of the parametric study analysed, case 1 is investigated.

3.4.2 Optimal wall-based feedback actuation of case 1

The cases 1, 1-A to 1-D from tables 2.1 and 2.2 fall within the controllable domain as shown by the parametric study, and were chosen to investigate the physics involved in the control. The magnitude of the unattenuated and attenuated profiles of the streamwise and wall normal velocity fluctuations are plotted in figures 3.20 and 3.21 for cases 1-A to 1-D. In these cases, the $\bar{u}^{(0)}$ components are of second order throughout and thus only the component $\bar{u}$ is shown. The plots reveal that the initial peak in the centre of the boundary layer is successfully attenuated to two smaller peaks. The increase of the wall-normal velocity $|\bar{v}|$ at the wall results in a decrease of wall-normal velocity at the same η location. This is connected to the local minimum value of the streamwise velocity $|\bar{u}|$. The resulting peaks of the attenuated streamwise velocity behave differently. The outer peak remains around $\bar{x} \approx 1.4$ and the peak closer to the wall moves slightly closer to the wall as the flow evolves downstream. This is the opposite of the uncontrolled case which shifts slightly towards the outer part from the inner boundary layer. It is clearly shown by these plots that the lift up mechanism is attenuated by the optimal actuation.

Furthermore, the unattenuated and attenuated profiles of the spanwise velocity $|\bar{w}|$ and temperature $|\bar{\tau}|$ are plotted in figures 3.22 and 3.23, where a slight increase of the spanwise velocity occurs close to the wall. The temperature fluctuations follow the streamwise velocity fluctuations closely, exhibiting a solo peak for the uncontrolled case to two smaller peaks about the minimum wall-normal velocity around $\eta \approx 1.1$. This shows that both the Klebanoff modes and thermal

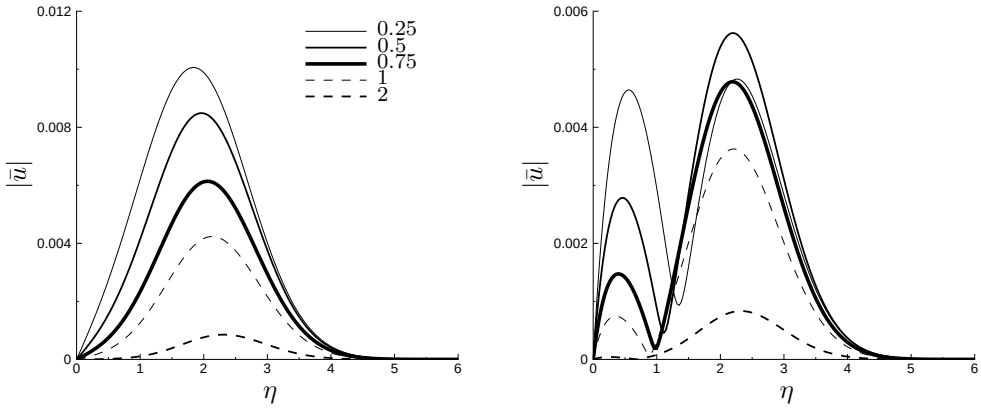

Figure 3.20: Amplitude of the uncontrolled (left) and controlled (right) streamwise velocity profiles $|\bar{u}|$ for $M = 3$, $\alpha_1 = \alpha_3 = \alpha_4 = 0$, $\alpha_2 = 1$, $\kappa_z = \kappa_y = 1$ at the indicated values of $\bar{x}$.

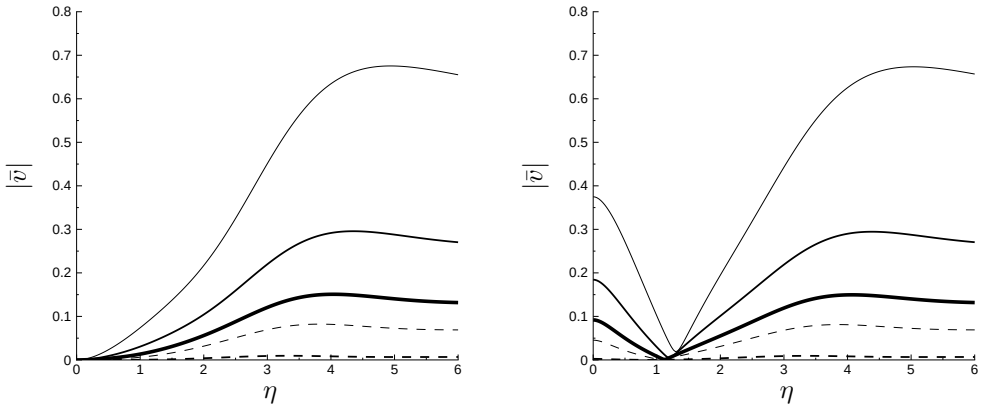

Figure 3.21: Amplitude of the uncontrolled (left) and controlled (right) wall-normal velocity profiles $|\bar{v}|$ for $M = 3$, $\alpha_1 = \alpha_3 = \alpha_4 = 0$, $\alpha_2 = 1$, $\kappa_z = \kappa_y = 1$ at the indicated values of $\bar{x}$ in figure 3.20.

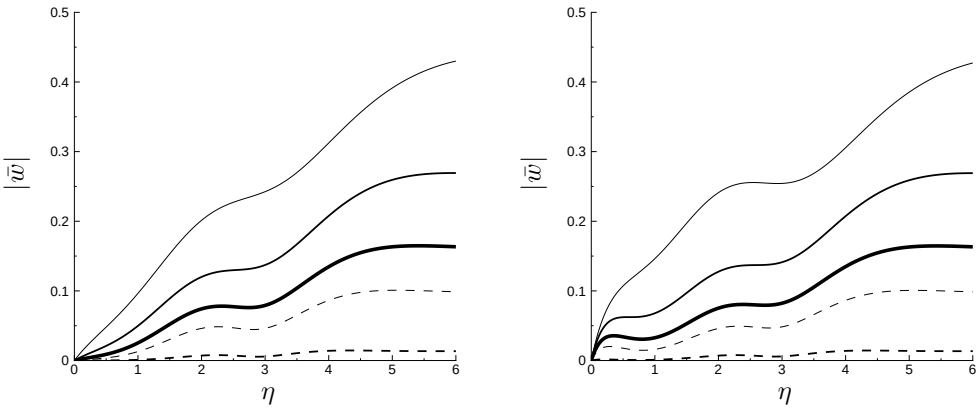

Figure 3.22: Amplitude of the uncontrolled (left) and controlled (right) spanwise velocity profiles $|\bar{w}|$ for $M = 3$, $\alpha_1 = \alpha_3 = \alpha_4 = 0$, $\alpha_2 = 1$, $\kappa_z = \kappa_y = 1$ at the indicated values of $\bar{x}$ in figure 3.20.

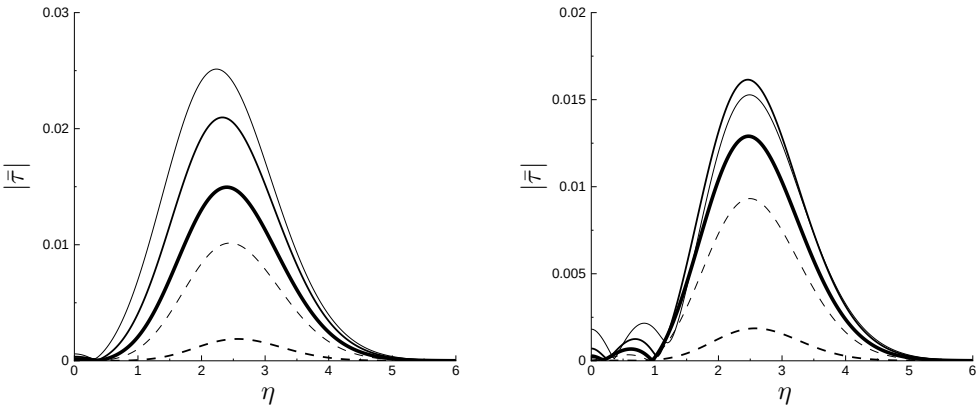

Figure 3.23: Amplitude of the uncontrolled (left) and controlled (right) temperature profiles $|\bar{\tau}|$ for $M = 3$, $\alpha_1 = \alpha_3 = \alpha_4 = 0$, $\alpha_2 = 1$, $\kappa_z = \kappa_y = 1$ at the indicated values of $\bar{x}$ in figure 3.20.

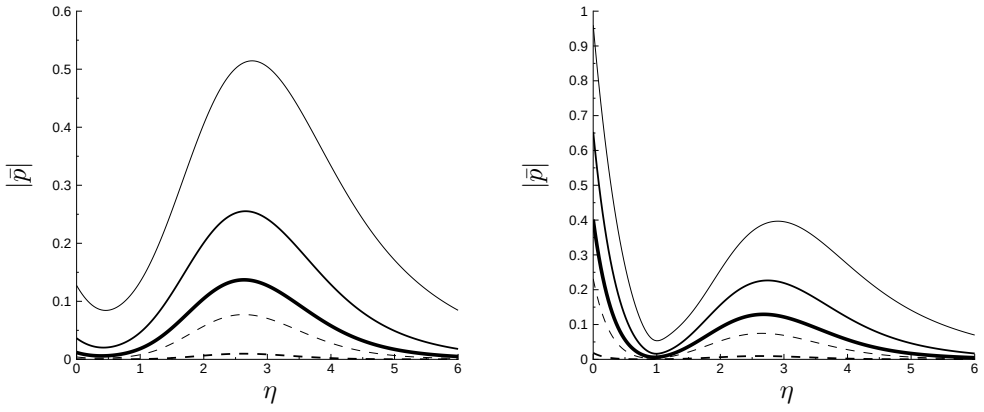

Figure 3.24: Amplitude of the uncontrolled (left) and controlled (right) pressure profiles $|\bar{p}|$ for $M = 3$, $\alpha_1 = \alpha_3 = \alpha_4 = 0$, $\alpha_2 = 1$, $\kappa_z = \kappa_y = 1$ at the indicated values of $\bar{x}$ in figure 3.20.

streaks attenuation is caused by disrupting the lift up mechanism that generates the Klebanoff modes. The profiles of uncontrolled and controlled pressure are displayed in figure 3.24, where an expected increase of pressure in the actuated profiles occurs close to the wall; it is related to the introduction of the wall-normal blowing and suction.

Case 1 can be now solved by taking into account the linearity of the problem, i.e. the control of $\bar{u}$ and $\bar{u}^{(0)}$ can be solved independently and summed in the end. The results are shown in figures 3.25 and 3.26 at $\bar{x} = 0.5$. Results for Case 1 are similar to the cases 1-A to 1-D; the streamwise velocity fluctuations are also attenuated up to $\eta = 4$ which indicates that blowing and suction actuation can successfully be used, even when the component $\bar{u}^{(0)}$ is of the first order within the boundary layer.

3.4.3 The effects of the measuring parameters

Throughout this paper, the regulation of the kinetic energy along $\bar{x}$ of $\bar{u}$ and $\bar{u}^{(0)}$ was considered. The inclusion of the other control parameters such as terminal kinetic energy and the evaluation of the thermal streaks were tested during the

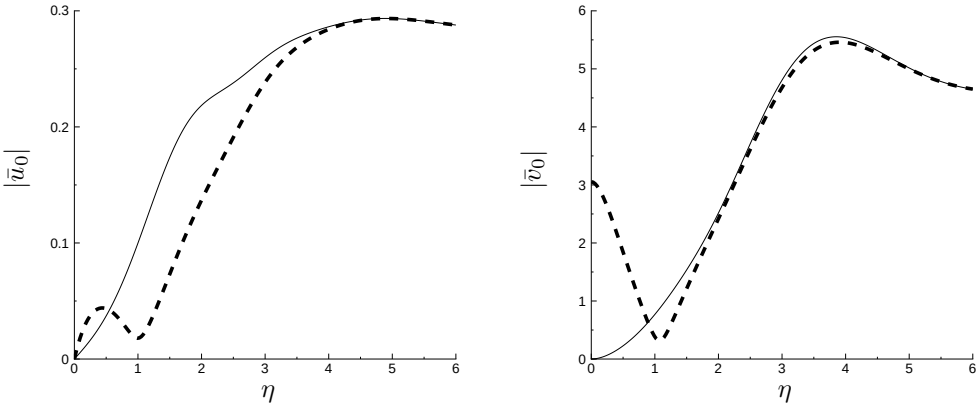

Figure 3.25: Magnitude of the streamwise $\bar{u}_0$ (left) and wall-normal $\bar{v}_0$ (right) velocity fluctuations along η at $\bar{x} = 0.5$ of the unattenuated profiles (solid lines) versus the optimal attenuation profiles (dashed lines), for $M = 3$, $\alpha_1 = \alpha_3 = \alpha_4 = 0$, $\alpha_2 = 1$, $\kappa_z = 1$ and $\kappa_y = 1$.

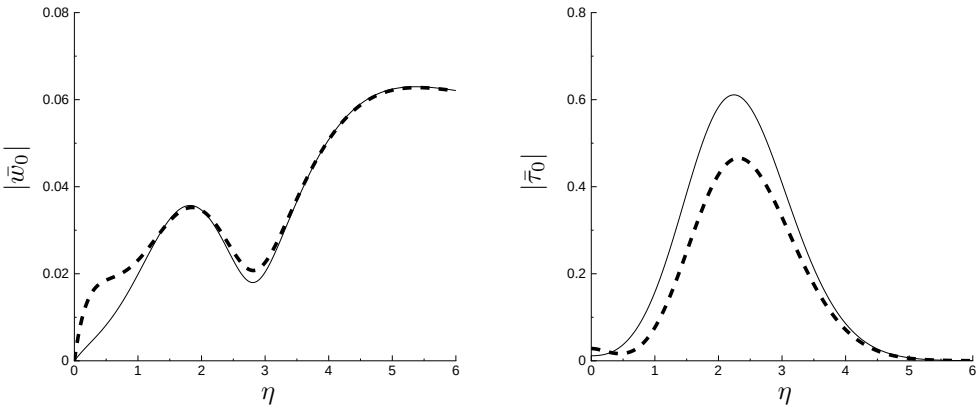

Figure 3.26: Magnitude of the spanwise velocity $\bar{w}_0$ (left) and temperature $\bar{\tau}_0$ (right) fluctuations along η at $\bar{x} = 0.5$ of the unattenuated profiles (solid lines) versus the optimal attenuation profiles (dashed lines), for $M = 3$, $\alpha_1 = \alpha_3 = \alpha_4 = 0$, $\alpha_2 = 1$, $\kappa_z = 1$ and $\kappa_y = 1$.

development of this thesis and resulted in a significant increase of magnitude of the streamwise velocity fluctuations upstream of the value of $\bar{x}$ being measured. The increase could result in upstream transition to turbulence, and due to the linear equations being used, it would be impossible to evaluate that. Thus the focus will be on measuring the energy along the entire domain for both the Klebanoff and thermal streaks.

α_2	α_4	θ_v^2	$\mathcal{J}_2^N/\mathcal{J}_2^0$	$\mathcal{J}_4^N/\mathcal{J}_4^0$	$\mathcal{J}_v$	Energy reduction
1	0	10^{-5}	0.411359	0.480876	8.62379×10^{-7}	0.57
0.5	0.5	10^{-5}	0.608223	0.349213	2.08074×10^{-6}	0.60
0	1	10^{-5}	0.962108	0.324683	2.86460×10^{-6}	0.67

Table 3.4: The list of energy reductions achieved while measuring the energy reduction according to the values of α_2 and α_4 used in each case, for $M = 3$, $\kappa_z = \kappa_y = 1$, and $\alpha_1 = \alpha_3 = 0$.

To ensure local minimisation, all cases were performed with small steps of optimisation, i.e. considering the regulation of the kinetic energy for $\bar{u}$ and $\alpha_2 = 1$, and with $\bar{x}_i$ and $\bar{x}_f = \bar{x}_i + \mathrm{d}\bar{x}$ being evaluated as it marches downstream along the whole domain.

Unlike the previous simulations that focused on measuring the Klebanoff modes to achieve their attenuation, the thermal streaks will also be measured by using a value of θ_τ other than zero. Table 3.4 displays combinations of measuring Klebanoff modes and thermal streaks and their energy reduction for different normalised cost functionals. It is clear from the results that the Klebanoff modes benefit more from being measured by the energy of the streamwise velocity fluctuations, i.e. $\mathcal{J}_2^N/\mathcal{J}_2^0$, than the thermal streaks benefit from being measured by the energy of the temperature fluctuations, i.e. $\mathcal{J}_4^N/\mathcal{J}_4^0$. Moreover, in order to achieve optimal actuation when the cost functional measures the thermal streaks energy, an increased in the cost of actuation is incurred. Therefore, setting $\alpha_2 = 1$ and $\alpha_1 = \alpha_3 = \alpha_4 = 0$ is an appropriate way to attenuate both the Klebanoff and thermal streaks by disrupting the lift up mechanism that generates them.

The formulation for the extension of this work to multiple actuation directions is initialised and verified to be a viable option in Appendix D. The preliminary results shown in the section below reveals that the wall-normal and spanwise directions are optimal to attenuate Klebanoff modes, but even fast fluctuations of the temperature at the wall can attenuate Klebanoff modes

3.5 Alternative controlled numerical results

κ_z	κ_y	$\bar{u}_w^2$	$\bar{v}_w^2$	$\bar{w}_w^2$	$\bar{\tau}_w^2$	Energy reduction
1	1	1	0	0	0	0.31
1	1	0	1	0	0	0.58
1	1	0	0	1	0	0.67
1	1	0	0	0	1	0.27
1	1	$1/\sqrt{2}$	$1/\sqrt{2}$	0	0	0.31
1	1	$-1/\sqrt{2}$	$1/\sqrt{2}$	0	0	0.32
1	1	0	$1/\sqrt{2}$	$1/\sqrt{2}$	0	0.25
1	1	0	$1/\sqrt{2}$	$-1/\sqrt{2}$	0	0.63
1	1	$1/\sqrt{2}$	0	$1/\sqrt{2}$	0	0.32
1	1	$1/\sqrt{2}$	0	$-1/\sqrt{2}$	0	0.31

Table 3.5: The list of energy reductions achieved for different combinations of actuators for $M = 3$, $\alpha_1 = \alpha_3 = \alpha_4 = 0$, $\alpha_2 = 1$ and $\theta_v^2 \to 0$.

The formulation described is now used to perform a parametric study on the possible actuators to attenuate the Klebanoff modes. The study is performed by taking into account the knowledge gained in chapter 3, i.e. measuring energy from the Klebanoff modes instead of the energy from the thermal streaks, and focusing on the $\bar{u}$ component.

The combination of actuators tested are described in table 3.5 without considering the actuation cost, to explore the theoretical maximum attenuation. The results reveal that wall-normal blowing and suction is an excellent direction to attenuate the Klebanoff modes. It was only surpassed by the spanwise blowing and suction at the wall or a combination of wall-normal and spanwise blowing

and suction. This is consistent with the work of Hicks & Ricco [33] who obtained up to 90% laminar streaks energy reduction.

An investigation of the actuation weights for the spanwise direction actuators revealed results similar to those found for the wall-normal direction actuators. The spanwise actuators also displayed the same physical effects as the wall-normal actuators, i.e. the introduction of a spanwise velocity $\bar{w}$ at the wall induced an increase of the amplitude wall-normal velocity $\bar{v}$ near the wall, followed by a reduction with a minimum located at $\eta \approx 1.3$. The reduction is consistent with figures 3.20-3.21 and results in a minimum peak of the amplitude of streamwise velocity $\bar{u}$ around $\eta \approx 1.3$.

This analysis has proven the possibility for the theoretical attenuation of the Klebanoff modes and thermal streaks via other directions of actuation, even though the spanwise direction for blowing and suction would be immensely difficult to implement in a laboratory. The current formulation for multiple actuators does not set a static orientation between wall-normal and spanwise, instead it attempts to optimise two actuators working simultaneously, i.e. wall-normal and spanwise actuators.

It is important in future work, to find a healthy relationship between the chosen actuators and combine them using an equation or in a predetermined direction. This would allow for a smoother and easier practical implementation. The same framework could be easily extended to consider speakers, which would be adequate actuators in attaining frequencies involved in optimal control of the compressible boundary layers.

Chapter 4

Summary and future work

The work of LWG [43], Ricco [55][56] and Ricco & Wu [58] on the theoretical formulation of the compressible boundary layer subjected to free-stream small vortical disturbances was described and expanded. The incompressible framework by Ricco [56] was extended to the compressible case for the first time, namely, the inclusion of the components $\bar{u}^{(0)}$, $\bar{v}^{(0)}$, $\bar{w}^{(0)}$, $\bar{\tau}^{(0)}$ and $\bar{p}^{(0)}$.

The components $\bar{u}^{(0)}$, $\bar{v}^{(0)}$, $\bar{w}^{(0)}$, $\bar{\tau}^{(0)}$ and $\bar{p}^{(0)}$ should allow the formulation to match the experiments in the outer layer of the boundary layer such as with previous theoretical results for the incompressible case [56]. Thus far, to the best of the author's knowledge, existing compressible experimental measurements lack the data to match the theoretical results obtained when the components were included.

Numerical results for the components $\{\bar{u}^{(0)}, \bar{v}^{(0)}, \bar{w}^{(0)}, \bar{\tau}^{(0)}, \bar{p}^{(0)}\}$ were obtained for the compressible case for the first time. The results showed that for $\kappa_y = \kappa_z = \mathcal{O}(1)$, this component only becomes significant at low Reynolds numbers, more common at lower speeds than $M = 3$.

The importance of the initial and top boundary conditions was also investigated, and it was subsequently demonstrated that the framework designed by LWG [43] to obtain the initial and boundary conditions greatly affects the results.

The general adjoint theory was derived and applied to the CLUBR equations for the first time, with the objective of attenuating the laminar flow. A spatial

controller was specifically designed to attenuate the Klebanoff modes and the thermal streaks. In addition, it should also work with other instabilities such as TS waves.

The controller designed focuses on the minimisation of the streamwise velocity fluctuations and temperature fluctuations. These are measured within the boundary layer over an interval and at a specific cross section at $\bar{x}_f$. The actuation method used was wall-blowing and suction. The results revealed that an increase of wall-normal velocity fluctuations close to the wall is followed by a decrease in local minimum around $\eta \approx 1.1$, and that resulted in a local minimum of the streamwise velocity fluctuations around the same value of η. The optimal wall-normal blowing and suction proved that it is possible to successfully attenuate the Klebanoff modes and the thermal streaks by disrupting the lift up mechanism.

Further investigations were carried out to study combinations of two different types of wall actuators, namely, heat transfer and blowing and suction. All of the combinations were able to attenuate the Klebanoff modes, but only the wall-normal and spanwise directions of blowing and suction indicated major attenuation, which was consistent with the studies of Hack & Zaki [28] and Hicks & Ricco [33] that used spanwise wall oscillation to attenuate the Klebanoff modes, although in the work of Hicks & Ricco [33] the actuator was on the base flow.

4.1 Future work

This work has accurately described the compressible and incompressible flows and has successfully attenuated laminar and thermal streaks. This sets the ground for future research to explore other controllers and actuators with the purpose of widening its industrial applications. A summary is provided below on some of the potential methods to test other controllers:

- Add constraints to the combination of wall-normal and spanwise blowing and suction method to normalise both components, i.e. restrict the angle

of attack along $\bar{x}$ to a constant.

- Explore the control of TS waves.

- Experiment with other cost functionals and different actuators to compare their effectiveness. For instance:

  - Regulation of the dissipation energy

$$\mathcal{J}\left(\bar{\mathbf{q}},\bar{\mathbf{c}}\right)=\frac{1}{2}\int_{\bar{x}_{\text{in}}}^{\bar{x}_{\text{fin}}}\int_{0}^{\infty}\left|\frac{\partial\bar{u}\left(\bar{x},\eta\right)}{\partial\eta}\right|^{2}\mathrm{d}\eta\mathrm{d}\bar{x} \tag{4.1}$$

  - Terminal control of the dissipation energy

$$\mathcal{J}\left(\bar{\mathbf{q}},\bar{\mathbf{c}}\right)=\frac{1}{2}\int_{0}^{\infty}\left|\frac{\partial\bar{u}\left(\bar{x}_{f},\eta\right)}{\partial\eta}\right|^{2}\mathrm{d}\eta \tag{4.2}$$

  - Regulation of the wall-normal velocity fluctuations energy

$$\mathcal{J}\left(\bar{\mathbf{q}},\bar{\mathbf{c}}\right)=\frac{1}{2}\int_{\bar{x}_{\text{in}}}^{\bar{x}_{\text{fin}}}\int_{0}^{\infty}\left|\bar{v}\left(\bar{x},\eta\right)\right|^{2}\mathrm{d}\eta\mathrm{d}\bar{x} \tag{4.3}$$

  - Terminal control of the wall-normal velocity fluctuations energy

$$\mathcal{J}\left(\bar{\mathbf{q}},\bar{\mathbf{c}}\right)=\frac{1}{2}\int_{0}^{\infty}\left|\bar{v}\left(\bar{x}_{f},\eta\right)\right|^{2}\mathrm{d}\eta \tag{4.4}$$

- Noise can be added to the outer flow to simulate the uncertainties originated in the free-stream turbulence; this leads to a Gaussian 3D function of κ and κ_2. The spectrum of solutions can be summed to obtain the response of the system for the full spectrum of κ and κ_2, while taking the noise into account.

- The cost functional can be modified to include only information at the wall, which is used to recreate data measured through sensors. This would verify the effectiveness of the method when applied to limited information such as:

  - Regulation along the wall of the wall-normal gradient of the streamwise velocity fluctuations

$$\mathcal{J}\left(\bar{\mathbf{q}},\bar{\mathbf{c}}\right)=\frac{1}{2}\int_{\bar{x}_{\text{in}}}^{\bar{x}_{\text{fin}}}\left|\frac{\partial\bar{u}\left(\bar{x},0\right)}{\partial\eta}\right|^{2}\mathrm{d}\bar{x} \tag{4.5}$$

– Regulation along the wall of the wall-normal gradient of the wall-normal velocity fluctuations

$$\mathcal{J}\left(\bar{\mathbf{q}},\bar{\mathbf{c}}\right)=\frac{1}{2}\int_{\bar{x}_{\mathrm{in}}}^{\bar{x}_{\mathrm{fin}}}\left|\frac{\partial\bar{v}\left(\bar{x},0\right)}{\partial\eta}\right|^{2}\mathrm{d}\bar{x} \tag{4.6}$$

– Regulation along the wall pressure fluctuations

$$\mathcal{J}\left(\bar{\mathbf{q}},\bar{\mathbf{c}}\right)=\frac{1}{2}\int_{\bar{x}_{\mathrm{in}}}^{\bar{x}_{\mathrm{fin}}}\left|\bar{p}\left(\bar{x},0\right)\right|^{2}\mathrm{d}\bar{x} \tag{4.7}$$

Bibliography

[1] F. Abergel and R. Temam. On some control problems in fluid mechanics. *Theoretical and Computational Fluid Dynamics*, 1(6):303–325, 1990.

[2] C. Airiau. Non-parallel acoustic receptivity of a blasius boundary layer using an adjoint approach. *Flow, Turbulence and Combustion*, 65:347–367, 2000.

[3] P. Andersson, M. Berggren, and D. S. Henningson. Optimal disturbances and bypass transition in boundary layers. *Phys. Fluids*, 11(1):134–150, 1999.

[4] D. Arnal and J. C. Juillen. Contribution expérimental a l'etude de la receptivite d'une couche limite laminaire, a la turbulence de l'ecoulement general. *CERT RT 1/5018 AYD - ONERA*, 1978.

[5] B. A. Belson, O. Semeraro, C. W. Rowley, and D. S. Henningson. Feedback control of instabilities in the two-dimensional Blasius boundary layer: The role of sensors and actuators. *Phys. Fluids*, 25(5), 2013.

[6] F. P. Bertolotti, T. Herbert, and P. R. Spalart. Linear and non linear stability of the blasius boundary layer. *J. Fluid Mech.*, 242:441–474, 1992.

[7] T. Bewley, P. Moin, and R. Temam. DNS-based predictive control of turbulence: an optimal benchmark for feedback algorithms. *J. Fluid Mech.*, 447:179–225, 2001.

[8] T. R. Bewley. Flow control: new challenges for a new Reinaissance. *Prog. Aero. Sc.*, 37:21–58, 2001.

[9] A. V. Boiko, K. J. A. Westin, K. G. B. Klingmann, V. V. Kozlov, and P. H. Alfredsson. Experiments in a boundary layer subjected to free stream turbulence. Part 2. The role of TS-waves in the transition process. *J. Fluid Mech.*, 281:219–245, 1994.

[10] L. Brandt, P. Schlatter, and D. S. Henningson. Transition in boundary layers subject to free-stream turbulence. *J. Fluid Mech.*, 517:167–198, 2004.

[11] P. Cathalifaud and T. R. Bewley. A noncausal framework for model-based feedback control of spatially developing perturbations in boundary-layer flow systems. Part I: formulation. *Syst. Control Letters*, 51:1–13, 2004.

[12] P. Cathalifaud and T. R. Bewley. A noncausal framework for model-based feedback control of spatially developing perturbations in boundary-layer flow systems. Part II: numerical simulations using state feedback. *Syst. Control Letters*, 51:15–22, 2004.

[13] P. Cathalifaud and P. Luchini. Algebraic growth in boundary layers: optimal control by blowing and suction at the wall. *Eur. J. Mech. - B Fluids*, 19:469–490, 2000.

[14] T. Cebeci. *Convective Heat Transfer*. Springer-Verlag, 2002.

[15] M. Chevalier, J. Hoepffner, E. Akervik, and D. S. Henningson. Linear feedback control and estimation applied to instabilities in spatially developing boundary layers. *J. Fluid Mech.*, 588:163–187, 2007.

[16] S. C. Crow. The spanwise perturbation of two-dimensional boundary-layers. *J. Fluid Mech.*, 24:153–164, 1966.

[17] H. L. Dryden. Air flow in the boundary layer near a plate. *NACA Rep.*, 562, 1936.

[18] H. L. Dryden. Transition from laminar to turbulent flow at subsonic and supersonic speeds. *Conference on High-Speed Aeronautics, 41, Polytechnic of Brooklyn, New York*, 1955.

[19] T. Ellingsen and E. Palm. Stability of linear flow. *Phys. Fluids*, 18(4):487–488, 1975.

[20] J. Fransson, M. Matsubara, and P. H. Alfredsson. Transition induced by free-stream turbulence. *J. Fluid Mech.*, 527:1–25, 2005.

[21] M. E. Goldstein. Unsteady vortical and entropic distortions of potential flows round arbitrary obstacles. *J. Fluid Mech.*, 89:433–468, 1978.

[22] M. E. Goldstein. Response of the pre-transitional laminar boundary layer to free-stream turbulence - Otto Laporte Lecture. *Bull. Am. Phys. Soc.*, 42:2150, 1997.

[23] M. E. Goldstein and S. J. Leib. Three-dimensional boundary layer instability and separation induced by small-amplitude streamwise vorticity in the upstream flow. *J. Fluid Mech.*, 246:21–41, 1993.

[24] M. E. Goldstein, S. J. Leib, and S. J. Cowley. Distortion of a flat plate boundary layer by free stream vorticity normal to the plate. *J. Fluid Mech.*, 237:231–260, 1992.

[25] P. Graziosi and G. Brown. Experiments on stability and transition at Mach 3. *J. Fluid Mech.*, 472:83–124, 2002.

[26] A. N. Gulyaev, V. E. Kozlov, V. R. Kuzenetsov, B. I. Mineev, and A. N. Sekundov. Interaction of a laminar boundary layer with external turbulence. *Fluid Dynamics. Translated from Izv, Akad. Navk. SSSR Mekh. Zhid. Gaza 6, vol. 5, pp. 55-65.*, 24(5):700–710, 1989.

[27] M. Gunzburger. Adjoint equation-based methods for control problems in incompressible, viscous flows. *Flow, Turbulence and Combustion*, 65:249–272, 2000.

[28] M. Hack and T. Zaki. The influence of harmonic wall motion on transitional boundary layers. *J. Fluid Mech.*, 760, Pages = 63-94, year = 2014.

[29] R. E. Hanson, P. Lavoie, K. M. Blade, and A. M. Naguib. Steady-state closed-loop control of bypass boundary layer transition using plasma actuators. *50th AIAA Aerospace Sciences Meeting Including the New Horizons Forum and Aerospace Exposition*, AIAA 2012-1140, 2012.

[30] R. E. Hanson, P. Lavoie, A. M. Naguib, and J. F. Morrison. Transient growth instability cancelation by a plasma actuator array. *Exp. Fluids*, 49(6):1339–1348, 2010.

[31] T. Herbert. Parabolized stability equations. *Ann. Rev. Fluid Mech.*, 29:245–283, 1997.

[32] D. Hernon, E. J. Walsh, and D. M. McEligot. Experimental investigation into the routes to bypass transition and the shear-sheltering phenomenon. *J. Fluid Mech.*, 591:461–479, 2007.

[33] P. Hicks and P. Ricco. Laminar streaks growth above a spanwise oscillation wall. *J. Fluid Mech.*, 768:348–374, 2015.

[34] M. Hogberg and D. S. Henningson. Linear optimal control applied to instabilities in spatially developing boundary layers. *J. Fluid Mech.*, 470:151–179, 2002.

[35] R. G. Jacobs and P. A. Durbin. Simulation of bypass transition. *J. Fluid Mech.*, 428:185–212, 2001.

[36] N. Kemp. The laminar three-dimensional boundary layer and a study of the flow past a side edge. *MSc Thesis, Cornell University*, 1951.

[37] J. M. Kendall. Experimental study of disturbances produced in a pre-transitional boundary layer. *AIAA Paper 85-1695*, 1985.

[38] J. M. Kendall. Boundary layer receptivity to free stream turbulence. *AIAA Paper*, 90-1504, 1990.

[39] J. M. Kendall. Studies on laminar boundary layer receptivity to free-stream turbulence near a leading edge. *In Boundary Layer Stability and Transition to Turbulence (ed. D.C. Reda, H. L. Reed & R. Kobayashi). ASME FED*, 114:23–30, 1991.

[40] J. Kim and T. R. Bewley. A linear systems approach to flow control. *Ann. Rev. Fluid Mech.*, 39:383–417, 2007.

[41] P. S. Klebanoff. Effect of free-stream turbulence on a laminar boundary layer. *Bull. Am. Phys. Soc.*, 16:1323, 1971.

[42] M. Landahl. A note on an algebraic instability of inviscid parallel shear flows. *J. Fluid Mech.*, 98:243–251, 1980.

[43] S. J. Leib, D. W. Wundrow, and M. E. Goldstein. Effect of free-stream turbulence and other vortical disturbances on a laminar boundary layer. *J. Fluid Mech.*, 380:169–203, 1999.

[44] L. Leventhal and E. Reshotko. Preliminary experimental study of disturbances in a laminar boundary-layer due to distributed surface roughness. *Final Report Case Inst. of Tech., Cleveland, OH. Dept. of Mechanical and Aerospace Engineering.*, 1981.

[45] P. Luchini. Reynolds-number-independent instability of the boundary layer over a flat surface. *J. Fluid Mech.*, 327:101–115, 1996.

[46] P. Luchini. Reynolds-number-independent instability of the boundary layer over a flat surface: optimal perturbations. *J. Fluid Mech.*, 404:289–309, 2000.

[47] P. Luchini and A. Bottaro. Adjoint equations in stability analysis. *Ann. Rev. Fluid Mech.*, 46:493–517, 2014.

[48] J. Mans, H. C. de Lange, and A. A. van Steenhoven. Sinuous breakdown in a flat plate boundary layer exposed to free-stream turbulence. *Phys. Fluids*, 19(088101), 2007.

[49] M. Matsubara and P. H. Alfredsson. Disturbance growth in boundary layers subjected to free-stream turbulence. *J. Fluid Mech.*, 430:149–168, 2001.

[50] A. Monokrousos, E. Åkervik, L. Brandt, and D. S. Henningson. Global three-dimensional optimal disturbances in the Blasius boundary-layer flow using time-steppers. *J. Fluid Mech.*, 650:181–214, 2010.

[51] M. V. Morkovin. Critical evaluation of transition for laminar to turbulent shear layers with emphasis on hypersonically traveling bodies. Technical report, Air Force Flight Dynamics Laboratory, 1969.

[52] S. Nagarajan, S. K. Lele, and J. H. Ferziger. Leading-edge effects in bypass transition. *J. Fluid Mech.*, 572:471–504, 2007.

[53] V. Ovchinnikov, M. M. Choudhari, and U. Piomelli. Numerical simulations of boundary-layer bypass transition due to high-amplitude free-stream turbulence. *J. Fluid Mech.*, 613:135–169, 2008.

[54] J. O. Pralits, A. Hanifi, and D. S. Henningson. Adjoint-based optimization of steady suction for disturbance control in incompressible flows. *J. Fluid Mech.*, 467:129–161, 2002.

[55] P. Ricco. Response of a compressible laminar boundary layer to free-stream turbulence. *PhD Thesis, University of London*, 2006.

[56] P. Ricco. The pre-transitional Klebanoff modes and other boundary layer disturbances induced by small-wavelength free-stream vorticity. *J. Fluid Mech.*, 638:267–303, 2009.

[57] P. Ricco, J. Luo, and X. Wu. Evolution and instability of unsteady nonlinear streaks generated by free-stream vortical disturbances. *J. Fluid Mech.*, 677:1–38, 2011.

[58] P. Ricco and X. Wu. Response of a compressible laminar boundary layer to free-stream vortical disturbances. *J. Fluid Mech.*, 587:97–138, 2007.

[59] P. Roach. The generation of nearly isotropic turbulence by means of grids. *Int. J. Heat Fluid Flow*, 8:82–92, 1987.

[60] H. Schlichting. Zur Entstehung der Turbulenz bei der Plattenströmung. *Math. Phys. Klasse. Nach. Ges. Wiss. Göttingen*, pages 181–208, 1933.

[61] G. Schubauer and H. Skramstad. Laminar boundary-layer oscillations and transition on a flat plate. *NACA TN 909*, 1947.

[62] O. Semeraro, S. Bagheri, L. Brandt, and D. Henningson. Transition delay in a boundary layer flow using active control. *J. Fluid Mech.*, 731:288–311, 2013.

[63] K. Stewartson. *The theory of laminar boundary layers in compressible fluids.* Oxford at the Claredon Press, 1964.

[64] G. I. Taylor. Some recent developments in the study of turbulence. *Fifth Intl. Congr. for Appl. Mech. (ed. J.P. Den Hartog & Peters) - Wiley/Chapman and Hall, New York-London*, pages 294–310, 1939.

[65] W. Tollmien. Uber die Entstehung der Turbulenz 1. Mitteilung. in Math. Phys. Kl. (pp. 21–44). Nach. Ges. Wiss. Göttingen (Translated into English as NACA TM 609 (1931)). 1929.

[66] M. M. Vaĭnberg. *Variational methods for the study of nonlinear operators.* Holden-Day series in mathematical physics. Holden-Day, 1964.

[67] K. J. A. Westin, A. V. Boiko, B. G. B. Klingmann, V. V. Kozlov, and P. H. Alfredsson. Experiments in a boundary layer subjected to free stream turbulence. Part 1. Boundary layer structure and receptivity. *J. Fluid Mech.*, 281:193–218, 1994.

[68] X. Wu and M. Choudhari. Linear and non-linear instabilities of a Blasius boundary layer perturbed by streamwise vortices. Part 2. Intermittent instability induced by long-wavelength Klebanoff modes. *J. Fluid Mech.*, 483:249–286, 2003.

[69] D. W. Wundrow and M. E. Goldstein. On the environmental realizability of algebraically growing disturbances and their relation to Klebanoff modes. *Th. Comp. Fluid Dyn.*, 10:171–186, 1998.

[70] D. W. Wundrow and M. E. Goldstein. Effect on a laminar boundary layer of small-amplitude streamwise vorticity in the upstream flow. *J. Fluid Mech.*, 426:229–262, 2001.

[71] T. Zaki and P. A. Durbin. Continuous mode transition and the effects of pressure gradient. *J. Fluid Mech.*, 563:357–388, 2006.

[72] S. Zuccher, P. Luchini, and A. Bottaro. Algebraic growth in a Blasius boundary layer: optimal and robust control by mean suction in the nonlinear regime. *J. Fluid Mech.*, 513:135–160, 2004.

Appendix A

Power series solution of the CLUBR equations

In LWG and Ricco & Wu [58], the collection of two terms of the power series (2.111) is sufficient. Ricco [56] required three terms to resolve the no-slip condition at the wall for the components denoted as $\bar{v}^{(0)}$ and $\bar{w}^{(0)}$. In the present work, three terms were also sufficient in the solution of the power series terms (2.112). The equations of the first three terms of the power series (2.112) are

$$\eta_c \frac{T'}{T} U_0 - \eta_c U_0' - \frac{T'}{T^2} V_0 + \frac{1}{T} V_0' - \frac{T'F}{T^2} T_0 + \frac{F}{T} T_0' = 0, \tag{A.1}$$

$$\begin{aligned} &-\eta_c F'' U_0 + \left(\frac{\mu T'}{T^2} - F - \frac{\mu' T'}{T} \right) U_0' - \frac{\mu}{T} U_0'' + \frac{F''}{T} V_0 \\ &+ \left(\frac{FF''}{T} - \frac{\mu' F'''}{T} - \frac{\mu'' T' F''}{T} + \frac{\mu' T' F''}{T^2} \right) T_0 - \frac{\mu' F''}{T} T_0' = 0, \end{aligned} \tag{A.2}$$

$$P_0' = 0, \tag{A.3}$$

$$-F' W_0 + \left(\frac{\mu T'}{T^2} - \frac{\mu' T'}{T} - F \right) W_0' - \frac{\mu}{T} W_0'' - \kappa_z^2 T P_0 = 0, \tag{A.4}$$

$$\begin{aligned} &-\eta_c T' U_0 - (\gamma - 1) M^2 2 \frac{\mu F''}{T} U_0' + \frac{T'}{T} V_0 \\ &+ \left(\frac{T'F}{T} - \frac{1}{\mathrm{Pr}} \frac{\mu''(T')^2}{T} - \frac{1}{\mathrm{Pr}} \frac{\mu' T''}{T} + \frac{1}{\mathrm{Pr}} \frac{\mu'(T')^2}{T^2} - (\gamma - 1) M^2 \frac{\mu'(F'')^2}{T} \right) T_0 \\ &+ \left(-F - 2 \frac{1}{\mathrm{Pr}} \frac{\mu' T'}{T} + \frac{1}{\mathrm{Pr}} \frac{\mu T'}{T^2} \right) T_0' - \frac{1}{\mathrm{Pr}} \frac{\mu}{T} T_0'' = 0, \end{aligned} \tag{A.5}$$

and

$$\left(\eta_c\frac{T'}{T}+1\right)U_1-\eta_cU_1'-\frac{T'}{T^2}V_1+\frac{1}{T}V_1'+W_0-\left(\frac{T'F}{T^2}+\frac{F'}{T}\right)T_1+\frac{F}{T}T_1'=0, \tag{A.6}$$

$$\begin{aligned}&\left(-\eta_cF''+F'\right)U_1+\left(\frac{\mu T'}{T^2}-F-\frac{\mu'T'}{T}\right)U_1'-\frac{\mu}{T}U_1''+\frac{F''}{T}V_1\\&+\left(\frac{FF''}{T}-\frac{\mu'F'''}{T}-\frac{\mu''T'F''}{T}+\frac{\mu'T'F''}{T^2}\right)T_1-\frac{\mu'F''}{T}T_1'=0,\end{aligned} \tag{A.7}$$

$$\begin{aligned}&\left(TF-\eta_cTF'+\eta_cT'F-{\eta_c}^2TF''\right)U_0+\left(\frac{\eta_c}{3}\mu'T'-\frac{\eta_c}{3}\frac{\mu T'}{T}+\frac{1}{3}\mu\right)U_0'+\frac{\eta_c}{3}\mu U_0''\\&+\left(\eta_cF''-\frac{T'F}{T}-F'\right)V_0+\left(-F-\frac{4}{3}\frac{\mu'T'}{T}+\frac{4}{3}\frac{\mu T'}{T^2}\right)V_0'-\frac{4}{3}\frac{\mu}{T}V_0''\\&+\left(\frac{4}{3}\frac{\mu'T''F}{T}-\frac{4}{3}\frac{\mu'(T')^2F}{T^2}+\frac{4}{3}\frac{\mu''(T')^2F}{T}+\frac{4}{3}\frac{\mu'T'F'}{T}+\eta_c\frac{\mu'T'F''}{T}\right.\\&\left.-\mu'F''-\eta_c\mu''T'F''-\eta_c\mu'F'''\right)T_0+\left(-\eta_c\mu'F''+\frac{4}{3}\frac{\mu'T'F}{T}\right)T_0'+P_1'=0,\end{aligned} \tag{A.8}$$

$$\begin{aligned}&-\eta_c\kappa_z^2\mu'TT'U_0-\frac{\eta_c}{3}\kappa_z^2\mu TU_1'+\kappa_z^2\mu'T'V_0+\frac{1}{3}\kappa_z^2\mu V_0'\\&+\left(\frac{\mu T'}{T^2}-\frac{\mu'T'}{T}-F\right)W_1'-\frac{\mu}{T}W_1''+\frac{2}{3}\kappa_z^2\mu'T'FT_0-\kappa_z^2TP_1=0,\end{aligned} \tag{A.9}$$

$$\begin{aligned}&-\eta_cT'U_1-(\gamma-1)M^2 2\frac{\mu F''}{T}U_1'+\frac{T'}{T}V_1\\&+\left(\frac{T'F}{T}-\frac{1}{\mathrm{Pr}}\frac{\mu''(T')^2}{T}-\frac{1}{\mathrm{Pr}}\frac{\mu'T''}{T}+\frac{1}{\mathrm{Pr}}\frac{\mu'(T')^2}{T^2}-(\gamma-1)M^2\frac{\mu'(F'')^2}{T}+F'\right)T_1\\&+\left(-F-2\frac{1}{\mathrm{Pr}}\frac{\mu'T'}{T}+\frac{1}{\mathrm{Pr}}\frac{\mu T'}{T^2}\right)T_1'-\frac{1}{\mathrm{Pr}}\frac{\mu}{T}T_1''=0,\end{aligned} \tag{A.10}$$

and

$$\begin{aligned}&\left(\eta_c\frac{T'}{T}+2\right)U_2-\eta_cU_2'-\frac{T'}{T^2}V_2+\frac{1}{T}V_2'+W_1\\&+\frac{i}{T^2}T_0+\left(-\frac{T'F}{T^2}-2\frac{F'}{T}\right)T_2+\frac{F}{T}T_2'=0,\end{aligned} \tag{A.11}$$

$$\begin{aligned}&\left(-i+\kappa_z^2\mu T\right)U_0+\left(-\eta_cF''+2F'\right)U_2+\left(\frac{\mu T'}{T^2}-F-\frac{\mu'T'}{T}\right)U_2'-\frac{\mu}{T}U_2''\\&+\frac{F''}{T}V_2+\left(\frac{FF''}{T}-\frac{\mu'F'''}{T}-\frac{\mu''T'F''}{T}+\frac{\mu'T'F''}{T^2}\right)T_2-\frac{\mu'F''}{T}T_2'=0,\end{aligned} \tag{A.12}$$

$$\left(TF - \eta_c TF' + \eta_c T'F - \eta_c{}^2 TF'' + \frac{2}{3}\mu' T'\right) U_1$$
$$+\frac{1}{3}\left(-\mu + \eta_c \mu' T' - \eta_c \frac{\mu T'}{T} + \mu\right) U_1' + \frac{\eta_c}{3}\mu U_1'' + \left(\eta_c F'' - \frac{T'F}{T}\right) V_1$$
$$+\left(-F - \frac{4}{3}\frac{\mu' T'}{T} + \frac{4}{3}\frac{\mu T'}{T^2}\right) V_1' - \frac{4}{3}\frac{\mu}{T} V_1'' + \frac{2}{3}\mu' T' W_0 - \frac{1}{3}\mu W_0'$$
$$+\left(\frac{4}{3}\frac{\mu' T'' F}{T} - \frac{4}{3}\frac{\mu'(T')^2 F}{T^2} + \frac{4}{3}\frac{\mu''(T')^2 F}{T} + \frac{4}{3}\frac{\mu' T' F'}{T} + \eta_c \frac{\mu' T' F''}{T}\right.$$
$$\left. -2\mu' F'' - \eta_c \mu'' T' F'' - \eta_c \mu' F'''\right) T_1 + \left(-\eta_c \mu' F'' + \frac{4}{3}\frac{\mu' T' F}{T}\right) T_1' + P_2' = 0, \tag{A.13}$$

$$\left(-\eta_c \kappa_z^2 \mu' T T' + \frac{1}{3}\kappa_z^2 \mu T\right) U_1 - \frac{\eta_c}{3}\kappa_z^2 \mu T U_1' + \kappa_z^2 \mu' T' V_1 + \frac{1}{3}\kappa_z^2 \mu V_1'$$
$$+\left(\frac{4}{3}\kappa_z^2 \mu T - i\right) W_0 + F' W_2 + \left(\frac{\mu T'}{T^2} - \frac{\mu' T'}{T} - F\right) W_2' - \frac{\mu}{T} W_2''$$
$$+\frac{2}{3}\kappa_z^2 \mu' T' F T_1 - \kappa_z^2 T P_2 = 0, \tag{A.14}$$

$$-\eta_c T' U_2 - (\gamma - 1) M^2 2 \frac{\mu F''}{T} U_2' + \frac{T'}{T} V_2 - i T_0$$
$$+\left(\frac{T'F}{T} - \frac{1}{\mathrm{Pr}}\frac{\mu''(T')^2}{T} - \frac{1}{\mathrm{Pr}}\frac{\mu' T''}{T} + \frac{1}{\mathrm{Pr}}\frac{\mu'(T')^2}{T^2} + 2F'\right) T_2$$
$$+\left(-F - 2\frac{1}{\mathrm{Pr}}\frac{\mu' T'}{T} + \frac{1}{\mathrm{Pr}}\frac{\mu T'}{T^2}\right) T_2' - \frac{1}{\mathrm{Pr}}\frac{\mu}{T} T_2'' = 0. \tag{A.15}$$

The equations (A.1)-(A.15) satisfy the following boundary conditions at the wall:

$$\bar{u}^{(0)} = \bar{v}^{(0)} = \bar{w}^{(0)} = \frac{\partial \bar{\tau}^{(0)}}{\partial \eta} = 0 \quad \text{at} \quad \eta = 0. \tag{A.16}$$

The boundary conditions for the power series $\bar{u}^{(0)}$ as $\eta \to \infty$ are found by matching the first, second and third term of the power series with the leading order, second-order and third-order of the Frobenius series of the large-η solution (2.96) as $\bar{x} \ll 1$ respectively, to yield:

$$U_0 = 1,\ U_1 = \left(-|\kappa_z| + i\kappa_y\right)\bar{\eta} \quad as \quad \eta \to \infty$$

$$U_2 = \frac{1}{2}\left[i - i|\kappa_z|\kappa_y - \kappa_y^2 + \left(\kappa_z^2 - i|\kappa_z|\kappa_y - \kappa_y^2\right)\bar{\eta}^2\right] \quad as \quad \eta \to \infty.$$

Matching the large-η solution (2.99) with the power series expansion for $\bar{\tau}^{(0)}$ gives

$$T_0 = T_1 = T_2 = 0 \quad as \quad \eta \to \infty.$$

The equations (A.1), (A.2) and (A.5) are decoupled from (A.3) and (A.4). They can be solved to numerically obtain the outer boundary condition for V_0 as $\eta \to \infty$, defined as

$$V_{0,0} = \lim_{\eta\to\infty} V_0.$$

Matching the power series terms as $\eta \to \infty$, namely V_0, V_1 and V_2 with the leading order, second-order and third order terms respectively, in the expansion of (2.97) for $\bar{x} \ll 1$ leads to

$$\int_0^{\bar{x}} g^{(0)}(\hat{x})\, e^{-i\hat{x}} d\hat{x} = \frac{1}{|\kappa_z|\sqrt{2\bar{x}}} \left[V_{0,0} - (\beta_c+\gamma_c) \frac{i\left|\kappa_z\right|^3 + i\left|\kappa_z\right|\kappa_y^2 + 2\kappa_y^3 - 2\kappa_z^2\kappa_y}{2\left(\kappa_y - i|\kappa_z|\right)\left(\kappa_z^2+\kappa_y^2\right)} \right] + \frac{g_1^{(0)}}{|\kappa_z|} + \frac{g_2^{(0)}}{|\kappa_z|}\sqrt{2\bar{x}},$$

where the constants $g_1^{(0)}$ and $g_2^{(0)}$ are (cf. Appendix A in [56] for the incompressible case)

$$g_1^{(0)} = V_{1,0} - |\kappa_z| + i\kappa_y + \beta_c \left[-|\kappa_z| V_{0,0} - \frac{\kappa_z^2(\beta_c+\gamma_c)}{|\kappa_z| - i\kappa_y} + i(\beta_c+\gamma_c)\kappa_y \right],$$

$$\begin{aligned} g_2^{(0)} = {} & V_{2,0} - \frac{i}{2} V_{0,0} - \frac{(\beta_c+\gamma_c)\left(4\left|\kappa_z\right|^3 + i\kappa_z^2\kappa_y - i\kappa_y^3\right)}{2\left(|\kappa_z| + i\kappa_y\right)} \\ & + \beta_c\left(-i - |\kappa_z| g_1^{(0)} + i|\kappa_z|\kappa_y + \kappa_y^2\right) \\ & - \frac{1}{2}\beta_c^2\left[\kappa_z^2 V_{0,0} + (\beta_c+\gamma_c)\left(2\kappa_z^2 - i|\kappa_z|\kappa_y - \kappa_y^2\right)\right], \end{aligned}$$

where:

$$V_{1,0} = \lim_{\eta\to\infty}\left[V_1 + \left(|\kappa_z| V_0 + \frac{\kappa_z^2(\beta_c+\gamma_c)}{|\kappa_z| - i\kappa_y} - i(\beta_c+\gamma_c)\kappa_y \right)\eta \right],$$

$$V_{2,0} = \lim_{\eta\to\infty}\left(V_2 - V_{2,1}\eta - V_{2,2}\eta^2\right),$$

$$V_{2,1} = -i - |\kappa_z| g_1^{(0)} + i|\kappa_z|\kappa_y + \kappa_y^2 - 2\beta_c V_{2,2},$$

$$V_{2,2} = \frac{1}{2}\left[\kappa_z^2 V_{0,0} + (\beta_c+\gamma_c)\left(2\kappa_z^2 - i|\kappa_z|\kappa_y - \kappa_y^2\right)\right].$$

Analogous to (A.16), the terms in the power series of $\bar{w}^{(0)}$ and $\bar{p}^{(0)}$ are matched with the expansion of the large-η solution (2.98) and (2.100) respectively, as $\bar{x} \ll 1$, to give

$$W_0 = V_{0,0}|\kappa_z| + \frac{(\beta_c+\gamma_c)\, i|\kappa_z|\kappa_y}{|\kappa_z| - i\kappa_y},\ W_1 = |\kappa_z| g_1^{(0)} - \kappa_z^2\left[V_{0,0} + (\beta_c+\gamma_c)\right]\bar{\eta} \quad as \quad \eta\to\infty,$$

$$W_2 = |\kappa_z| g_2^{(0)} + \frac{i|\kappa_z|}{2} V_{0,0} + \frac{(\beta_c + \gamma_c)}{2\left(\kappa_z^2 + \kappa_y^2\right)} \left[-\kappa_z^2 \kappa_y - i|\kappa_z| \kappa_y^2 + 2\left(|\kappa_z|^3 \kappa_y^2 - i\kappa_z^2 \kappa_y^3 \right) \right.$$
$$\left. + 4\left(|\kappa_z|^5 - i\kappa_z^4 \kappa_y \right) \right] - \kappa_z^2 g_1^{(0)} \bar{\eta}$$
$$+ \left(\frac{|\kappa_z|^3}{2} V_{0,0} + \frac{(\beta_c + \gamma_c)\left(2\kappa_z^4 - 3i|\kappa_z|^3 \kappa_y - 2\kappa_z^2 \kappa_y^2 \right)}{2\left(|\kappa_z| - i\kappa_y \right)} \right) \bar{\eta}^2 \quad as \quad \eta \to \infty,$$

and

$$P_0 = -\frac{1}{|\kappa_z|} V_{0,0} - \frac{(\beta_c + \gamma_c)\, i\kappa_y}{|\kappa_z| \left(|\kappa_z| - i\kappa_y \right)}, \; P_1 = \left[V_{0,0} + (\beta_c + \gamma_c) \right] \bar{\eta} \quad as \quad \eta \to \infty,$$

$$P_2 = \frac{g_2^{(0)}}{|\kappa_z|} - \frac{(\beta_c + \gamma_c)\left(4\kappa_z^2 \kappa_y^2 + 4\kappa_y^4 - i\kappa_z^2 - 5i\kappa_y^2 \right)}{4\left(|\kappa_z| - i\kappa_y \right)\left(|\kappa_z| + i\kappa_y \right)^2}$$
$$- \left[\frac{|\kappa_z|}{2} V_{0,0} + \frac{(\beta_c + \gamma_c)\left(2\kappa_z^2 - 3i\kappa_z \kappa_y - 2\kappa_y^2 \right)}{2\left(|\kappa_z| - i\kappa_y \right)} \right] \bar{\eta}^2 \quad as \quad \eta \to \infty.$$

Appendix B

Expansion of adjoint identity

In order to obtain the CLUBR adjoint equations, the adjoint identity (3.59) needs to be expanded. The necessary steps and details are described in this Appendix.

The expansion of the adjoint identity is valid for the components $\{\bar{p}', \bar{u}', \bar{v}', \bar{w}', \bar{\tau}'\}$ and $\left\{\bar{p}^{(0)\prime}, \bar{u}^{(0)\prime}, \bar{v}^{(0)\prime}, \bar{w}^{(0)\prime}, \bar{\tau}^{(0)\prime}\right\}$. The left-hand-side expansion of the adjoint identity (3.59) is shown for the former components:

$$\left\langle \bar{\mathbf{r}}, \mathbf{Q}\left(\bar{\mathbf{q}}'\right)\right\rangle_{\mathbf{I}} = \int_{\bar{x}_i}^{\bar{x}_f}\int_0^{\infty} \bar{r}_c^H \left[\frac{\eta_c}{2\bar{x}}\frac{T'}{T}\bar{u}' + \frac{\partial \bar{u}'}{\partial \bar{x}} - \frac{\eta_c}{2\bar{x}}\frac{\partial \bar{u}'}{\partial \eta} - \frac{T'}{T^2}\bar{v}' + \frac{1}{T}\frac{\partial \bar{v}'}{\partial \eta}\right.$$
$$\left. + \bar{w}' + \left(\frac{i}{T^2} - \frac{1}{2\bar{x}}\frac{T'F}{T^2}\right)\bar{\tau}' - \frac{F'}{T}\frac{\partial \bar{\tau}'}{\partial \bar{x}} + \frac{1}{2\bar{x}}\frac{F}{T}\frac{\partial \bar{\tau}'}{\partial \eta}\right]$$
$$+ \bar{r}_x^H \left[\left(-i - \frac{\eta_c}{2\bar{x}}F'' + \kappa_z^2\mu T\right)\bar{u}' + F'\frac{\partial \bar{u}'}{\partial \bar{x}} + \left(\frac{1}{2\bar{x}}\frac{\mu T'}{T^2} - \frac{1}{2\bar{x}}F\right.\right.$$
$$\left. - \frac{1}{2\bar{x}}\frac{\mu' T'}{T}\right)\frac{\partial \bar{u}'}{\partial \eta} - \frac{1}{2\bar{x}}\frac{\mu}{T}\frac{\partial^2 \bar{u}'}{\partial \eta^2} + \frac{F''}{T}\bar{v}' + \left(\frac{1}{2\bar{x}}\frac{FF''}{T} - \frac{1}{2\bar{x}}\frac{\mu' F'''}{T}\right.$$
$$\left.\left. - \frac{1}{2\bar{x}}\frac{\mu'' T' F''}{T} + \frac{1}{2\bar{x}}\frac{\mu' T' F''}{T^2}\right)\bar{\tau}' - \frac{1}{2\bar{x}}\frac{\mu' F''}{T}\frac{\partial \bar{\tau}'}{\partial \eta}\right]$$
$$+ \bar{r}_y^H \left[\frac{1}{(2\bar{x})^2}\left(TF - \eta_c TF' + \eta_c T'F - {\eta_c}^2 TF''\right)\bar{u}' + \frac{1}{3\bar{x}}\mu' T'\frac{\partial \bar{u}'}{\partial \bar{x}}\right.$$
$$- \frac{1}{6\bar{x}}\mu\frac{\partial}{\partial \bar{x}}\left(\frac{\partial \bar{u}'}{\partial \eta}\right) + \left(\frac{\eta_c}{12\bar{x}^2}\mu' T' - \frac{\eta_c}{12\bar{x}^2}\frac{\mu T'}{T} + \frac{1}{12\bar{x}^2}\mu\right)\frac{\partial \bar{u}'}{\partial \eta}$$
$$+ \frac{\eta_c}{12\bar{x}^2}\mu\frac{\partial^2 \bar{u}'}{\partial \eta^2} + \left(-i + \frac{\eta_c}{2\bar{x}}F'' - \frac{1}{2\bar{x}}\frac{T'F}{T} + \frac{1}{2\bar{x}}F' + \kappa_z^2\mu T\right)\bar{v}'$$
$$+ F'\frac{\partial \bar{v}'}{\partial \bar{x}} + \left(-\frac{1}{2\bar{x}}F - \frac{2}{3\bar{x}}\frac{\mu' T'}{T} + \frac{2}{3\bar{x}}\frac{\mu T'}{T^2}\right)\frac{\partial \bar{v}'}{\partial \eta} - \frac{4}{3}\frac{1}{2\bar{x}}\frac{\mu}{T}\frac{\partial^2 \bar{v}'}{\partial \eta^2}$$
$$+ \frac{2}{3}\frac{1}{2\bar{x}}\mu' T'\bar{w}' - \frac{1}{3}\frac{1}{2\bar{x}}\mu\frac{\partial \bar{w}'}{\partial \eta} + \left(-FF' + \eta_c(F')^2 - \frac{T'F^2}{T} + \eta_c FF''\right.$$
$$+ \frac{1}{3\bar{x}^2}\frac{\mu' T'' F}{T} - \frac{1}{3\bar{x}^2}\frac{\mu'(T')^2 F}{T^2} + \frac{1}{3\bar{x}^2}\frac{\mu''(T')^2 F}{T} + \frac{1}{3\bar{x}^2}\frac{\mu' T' F'}{T}$$
$$\left. + \frac{\eta_c}{4\bar{x}^2}\frac{\mu' T' F''}{T} - \frac{1}{4\bar{x}^2}\mu' F'' - \frac{\eta_c}{4\bar{x}^2}\mu'' T' F'' - \frac{\eta_c}{4\bar{x}^2}\mu' F'''\right)\bar{\tau}' - \frac{1}{2\bar{x}}\mu' F''\frac{\partial \bar{\tau}'}{\partial \bar{x}}$$
$$\left. + \left(-\frac{\eta_c}{4\bar{x}^2}\mu' F'' + \frac{1}{3\bar{x}^2}\frac{\mu' T' F}{T}\right)\frac{\partial \bar{\tau}'}{\partial \eta} + \frac{1}{2\bar{x}}\frac{\partial \bar{p}'}{\partial \eta}\right]$$
$$+ \bar{r}_z^H \left[-\frac{\eta_c}{2\bar{x}}\kappa_z^2\mu' T T'\bar{u}' + \frac{1}{3}\kappa_z^2\mu T\frac{\partial \bar{u}'}{\partial \bar{x}} - \frac{\eta_c}{6\bar{x}}\kappa_z^2\mu T\frac{\partial \bar{u}'}{\partial \eta} + \kappa_z^2\mu' T'\bar{v}'\right.$$
$$+ \frac{1}{3}\kappa_z^2\mu\frac{\partial \bar{v}'}{\partial \eta} + \left(\frac{4}{3}\kappa_z^2\mu T - i\right)\bar{w}' + F'\frac{\partial \bar{w}'}{\partial \bar{x}} + \left(\frac{1}{2\bar{x}}\frac{\mu T'}{T^2} - \frac{1}{2\bar{x}}\frac{\mu' T'}{T}\right.$$
$$\left.\left. - \frac{1}{2\bar{x}}F\right)\frac{\partial \bar{w}'}{\partial \eta} - \frac{1}{2\bar{x}}\frac{\mu}{T}\frac{\partial^2 \bar{w}'}{\partial \eta^2} + \frac{1}{3\bar{x}}\kappa_z^2\mu' T' F\bar{\tau}' - \kappa_z^2 T\bar{p}'\right]$$
$$+ \bar{r}_e^H \left[-\frac{\eta_c}{2\bar{x}}T'\bar{u}' - (\gamma-1)M^2\frac{1}{\bar{x}}\frac{\mu F''}{T}\frac{\partial \bar{u}'}{\partial \eta} + \frac{T'}{T}\bar{v}' + \left(-i + \frac{1}{2\bar{x}}\frac{T'F}{T}\right.\right.$$
$$- \frac{1}{2\bar{x}}\frac{1}{\mathrm{Pr}}\frac{\mu''(T')^2}{T} - \frac{1}{2\bar{x}}\frac{1}{\mathrm{Pr}}\frac{\mu' T''}{T} + \frac{1}{2\bar{x}}\frac{1}{\mathrm{Pr}}\frac{\mu'(T')^2}{T^2} + \frac{1}{\mathrm{Pr}}\kappa_z^2\mu T$$
$$\left.\left. - (\gamma-1)M^2\frac{1}{2\bar{x}}\frac{\mu'(F'')^2}{T}\right)\bar{\tau}' + F'\frac{\partial \bar{\tau}'}{\partial \bar{x}} + \left(-\frac{1}{2\bar{x}}F - \frac{1}{\bar{x}}\frac{1}{\mathrm{Pr}}\frac{\mu' T'}{T}\right.\right.$$
$$\left.\left. + \frac{1}{2\bar{x}}\frac{1}{\mathrm{Pr}}\frac{\mu T'}{T^2}\right)\frac{\partial \bar{\tau}'}{\partial \eta} - \frac{1}{2\bar{x}}\frac{1}{\mathrm{Pr}}\frac{\mu}{T}\frac{\partial^2 \bar{\tau}'}{\partial \eta^2}\right]\mathrm{d}\eta\mathrm{d}\bar{x}.$$

Rearranging the terms and changing the order of integration accordingly leads to:

$$
\begin{aligned}
\left\langle \bar{\mathbf{r}}, \mathbf{Q}\left(\bar{\mathbf{q}}'\right)\right\rangle_{\mathbf{I}} = \int_{\bar{x}_i}^{\bar{x}_f}\int_0^{\infty} & -\bar{r}_z^H\kappa_z^2 T\bar{p}' + \Bigg[\bar{r}_c^H\frac{\eta_c}{2\bar{x}}\frac{T'}{T} + \bar{r}_x^H\left(-i - \frac{\eta_c}{2\bar{x}}F'' + \kappa_z^2\mu T\right) \\
& + \bar{r}_y^H\frac{1}{(2\bar{x})^2}\left(TF - \eta_c TF' + \eta_c T'F - {\eta_c}^2 TF''\right) - \bar{r}_z^H\frac{\eta_c}{2\bar{x}}\kappa_z^2\mu' TT' - \bar{r}_e^H\frac{\eta_c}{2\bar{x}}T'\Bigg]\bar{u}' \\
& + \Bigg[-\bar{r}_c^H\frac{T'}{T^2} + \bar{r}_x^H\frac{F''}{T} + \bar{r}_y^H\left(-i + \frac{\eta_c}{2\bar{x}}F'' - \frac{1}{2\bar{x}}\frac{T'F}{T} + \frac{1}{2\bar{x}}F' + \kappa_z^2\mu T\right) \\
& + \bar{r}_z^H\kappa_z^2\mu' T' + \bar{r}_e^H\frac{T'}{T}\Bigg]\bar{v}' + \Bigg[\bar{r}_c^H + \bar{r}_y^H\frac{2}{3}\frac{1}{2\bar{x}}\mu' T' + \bar{r}_z^H\left(\frac{4}{3}\kappa_z^2\mu T - i\right)\Bigg]\bar{w}' \\
& + \Bigg[\bar{r}_c^H\left(\frac{i}{T^2} - \frac{1}{2\bar{x}}\frac{T'F}{T^2}\right) + \bar{r}_x^H\left(\frac{1}{2\bar{x}}\frac{FF''}{T} - \frac{1}{2\bar{x}}\frac{\mu' F'''}{T} - \frac{1}{2\bar{x}}\frac{\mu'' T'F''}{T}\right. \\
& \left. + \frac{1}{2\bar{x}}\frac{\mu' T'F''}{T^2}\right) + \bar{r}_y^H\left(-\frac{T'F^2}{T} + \eta_c(F')^2 - FF' + \eta_c FF'' + \frac{1}{3\bar{x}^2}\frac{\mu' T''F}{T}\right. \\
& - \frac{1}{3\bar{x}^2}\frac{\mu'(T')^2F}{T^2} + \frac{1}{3\bar{x}^2}\frac{\mu''(T')^2F}{T} + \frac{1}{3\bar{x}^2}\frac{\mu' T'F'}{T} + \frac{\eta_c}{4\bar{x}^2}\frac{\mu' T'F''}{T} \\
& \left. - \frac{1}{4\bar{x}^2}\mu' F'' - \frac{\eta_c}{4\bar{x}^2}\mu'' T'F'' - \frac{\eta_c}{4\bar{x}^2}\mu' F'''\right) + \bar{r}_z^H\frac{1}{3\bar{x}}\kappa_z^2\mu' T'F \\
& + \bar{r}_e^H\left(-i + \frac{1}{2\bar{x}}\frac{T'F}{T} - \frac{1}{2\bar{x}}\frac{1}{\mathrm{Pr}}\frac{\mu''(T')^2}{T} - \frac{1}{2\bar{x}}\frac{1}{\mathrm{Pr}}\frac{\mu' T''}{T}\right. \\
& \left. + \frac{1}{2\bar{x}}\frac{1}{\mathrm{Pr}}\frac{\mu'(T')^2}{T^2} + \frac{1}{\mathrm{Pr}}\kappa_z^2\mu T - (\gamma-1)M^2\frac{1}{2\bar{x}}\frac{\mu'(F'')^2}{T}\right)\Bigg]\bar{\tau}'\mathrm{d}\eta\mathrm{d}\bar{x} \\
& + \int_0^{\infty}\int_{\bar{x}_i}^{\bar{x}_f}\left[\bar{r}_c^H + \bar{r}_x^H F' + \bar{r}_y^H\frac{1}{3\bar{x}}\mu' T' + \bar{r}_z^H\frac{1}{3}\kappa_z^2\mu T\right]\frac{\partial\bar{u}'}{\partial\bar{x}} + \bar{r}_y^H F'\frac{\partial\bar{v}'}{\partial\bar{x}} \\
& + \bar{r}_z^H F'\frac{\partial\bar{w}'}{\partial\bar{x}} + \left[-\bar{r}_c^H\frac{F'}{T} - \bar{r}_y^H\frac{1}{2\bar{x}}\mu' F'' + \bar{r}_e^H F'\right]\frac{\partial\bar{\tau}'}{\partial\bar{x}}\mathrm{d}\bar{x}\mathrm{d}\eta \\
& + \int_{\bar{x}_i}^{\bar{x}_f}\int_0^{\infty} -\bar{r}_y^H\frac{1}{6\bar{x}}\mu\frac{\partial}{\partial\eta}\left(\frac{\partial\bar{u}'}{\partial\bar{x}}\right)\mathrm{d}\eta\mathrm{d}\bar{x} + \int_{\bar{x}_i}^{\bar{x}_f}\int_0^{\infty}\bar{r}_y^H\frac{1}{2\bar{x}}\frac{\partial\bar{p}'}{\partial\eta} + \Big[-\bar{r}_c^H\frac{\eta_c}{2\bar{x}} \\
& + \bar{r}_x^H\left(\frac{1}{2\bar{x}}\frac{\mu T'}{T^2} - \frac{1}{2\bar{x}}F - \frac{1}{2\bar{x}}\frac{\mu' T'}{T}\right) + \bar{r}_y^H\left(\frac{\eta_c}{12\bar{x}^2}\mu' T' - \frac{\eta_c}{12\bar{x}^2}\frac{\mu T'}{T}\right. \\
& \left. + \frac{1}{12\bar{x}^2}\mu\right) - \bar{r}_z^H\frac{\eta_c}{6\bar{x}}\kappa_z^2\mu T - \bar{r}_e^H(\gamma-1)M^2\frac{1}{\bar{x}}\frac{\mu F''}{T}\Bigg]\frac{\partial\bar{u}'}{\partial\eta} + \Bigg[\bar{r}_c^H\frac{1}{T} \\
& + \bar{r}_y^H\left(-\frac{1}{2\bar{x}}F - \frac{2}{3\bar{x}}\frac{\mu' T'}{T} + \frac{2}{3\bar{x}}\frac{\mu T'}{T^2}\right) + \bar{r}_z^H\frac{1}{3}\kappa_z^2\mu\Bigg]\frac{\partial\bar{v}'}{\partial\eta} + \Bigg[-\bar{r}_y^H\frac{1}{3}\frac{1}{2\bar{x}}\mu \\
& + \bar{r}_z^H\left(\frac{1}{2\bar{x}}\frac{\mu T'}{T^2} - \frac{1}{2\bar{x}}\frac{\mu' T'}{T} - \frac{1}{2\bar{x}}F\right)\Bigg]\frac{\partial\bar{w}'}{\partial\eta} + \Bigg[\bar{r}_c^H\frac{1}{2\bar{x}}\frac{F}{T} - \bar{r}_x^H\frac{1}{2\bar{x}}\frac{\mu' F''}{T} \\
& + \bar{r}_y^H\left(-\frac{\eta_c}{4\bar{x}^2}\mu' F'' + \frac{1}{3\bar{x}^2}\frac{\mu' T'F}{T}\right) + \bar{r}_e^H\left(-\frac{1}{2\bar{x}}F - \frac{1}{\bar{x}}\frac{1}{\mathrm{Pr}}\frac{\mu' T'}{T}\right. \\
& \left. + \frac{1}{2\bar{x}}\frac{1}{\mathrm{Pr}}\frac{\mu T'}{T^2}\right)\Bigg]\frac{\partial\bar{\tau}'}{\partial\eta}\mathrm{d}\eta\mathrm{d}\bar{x} + \int_{\bar{x}_i}^{\bar{x}_f}\int_0^{\infty}\left[-\bar{r}_x^H\frac{1}{2\bar{x}}\frac{\mu}{T} + \bar{r}_y^H\frac{\eta_c}{12\bar{x}^2}\mu\right]\frac{\partial^2\bar{u}'}{\partial\eta^2} \\
& - \bar{r}_y^H\frac{4}{3}\frac{1}{2\bar{x}}\frac{\mu}{T}\frac{\partial^2\bar{v}'}{\partial\eta^2} - \bar{r}_z^H\frac{1}{2\bar{x}}\frac{\mu}{T}\frac{\partial^2\bar{w}'}{\partial\eta^2} - \bar{r}_e^H\frac{1}{2\bar{x}}\frac{1}{\mathrm{Pr}}\frac{\mu}{T}\frac{\partial^2\bar{\tau}'}{\partial\eta^2}\mathrm{d}\eta\mathrm{d}\bar{x}.
\end{aligned}
$$

The last step is to integrate by parts as many times as needed to move the partial derivatives from the state variables perturbations (i.e.: $\bar{p}'$, $\bar{u}'$, $\bar{v}'$, $\bar{w}'$ and $\bar{\tau}'$) to the adjoint variables (i.e.: $\bar{r}_c$, $\bar{r}_x$, $\bar{r}_y$, $\bar{r}_z$ and $\bar{r}_e$). Applying integration by parts twice and rearranging the terms yields the right-hand-side of the adjoint identity (3.59):

$$
\begin{aligned}
\left\langle \bar{\mathbf{R}}\left(\bar{\mathbf{r}}\right), \bar{\mathbf{q}}' \right\rangle_{\mathbf{I}} = \int_{\bar{x}_i}^{\bar{x}_f} \int_0^{\infty} & \left[-\frac{1}{2\bar{x}} \frac{\partial \bar{r}_y}{\partial \eta} - \kappa_z^2 T \bar{r}_z \right]^H \bar{p}' + \left[\frac{1}{2\bar{x}} \bar{r}_c - \frac{\partial \bar{r}_c}{\partial \bar{x}} \right. \\
& + \frac{\eta_c}{2\bar{x}} \frac{\partial \bar{r}_c}{\partial \eta} + \left(i + \kappa_z^2 \mu T + \frac{F'}{2\bar{x}} - \frac{\eta_c F''}{2\bar{x}} \right) \bar{r}_x - F' \frac{\partial \bar{r}_x}{\partial \bar{x}} \\
& + \frac{1}{2\bar{x}} \left(F + \frac{\mu T'}{T^2} - \frac{\mu' T'}{T} \right) \frac{\partial \bar{r}_x}{\partial \eta} - \frac{1}{2\bar{x}} \frac{\mu}{T} \frac{\partial^2 \bar{r}_x}{\partial \eta^2} \\
& + \frac{1}{(2\bar{x})^2} \left(TF + 2\mu' T' - \eta_c T F' + \eta_c T' F - {\eta_c}^2 T F'' \right) \bar{r}_y - \frac{\mu' T'}{2\bar{x}} \frac{\partial \bar{r}_y}{\partial \bar{x}} \\
& - \frac{\mu}{6\bar{x}} \frac{\partial}{\partial \bar{x}} \left(\frac{\partial \bar{r}_y}{\partial \eta} \right) + \frac{1}{(2\bar{x})^2} \left(\mu - \frac{\eta_c \mu T'}{3T} + \frac{\eta_c \mu' T'}{3} \right) \frac{\partial \bar{r}_y}{\partial \eta} + \frac{\eta_c \mu}{12\bar{x}^2} \frac{\partial^2 \bar{r}_y}{\partial \eta^2} \\
& + \frac{1}{6\bar{x}} \left(\kappa_z^2 \mu T - 3\eta_c \kappa_z^2 \mu' T T' \right) \bar{r}_z - \frac{1}{3} \kappa_z^2 \mu T \frac{\partial \bar{r}_z}{\partial \bar{x}} + \frac{\eta_c \kappa_z^2 \mu T}{6\bar{x}} \frac{\partial \bar{r}_z}{\partial \eta} \\
& + \left(-\frac{\eta_c T'}{2\bar{x}} + \frac{1}{\bar{x}} (\gamma - 1) M^2 \left(\frac{\mu F'''}{T} - \frac{\mu T' F''}{T^2} + \frac{\mu' T' F''}{T} \right) \right) \bar{r}_e \\
& \left. + \frac{1}{\bar{x}} (\gamma - 1) M^2 \frac{\mu F''}{T} \frac{\partial \bar{r}_e}{\partial \eta} \right]^H \bar{u}' + \left[-\frac{1}{T} \frac{\partial \bar{r}_c}{\partial \eta} + \frac{F''}{T} \bar{r}_x + \left(i + \kappa_z^2 \mu T \right. \right. \\
& \left. + \frac{1}{2\bar{x}} \left(2F' - \frac{T' F}{T} + \eta_c F'' \right) \right) \bar{r}_y - F' \frac{\partial \bar{r}_y}{\partial \bar{x}} + \left(\frac{F}{2\bar{x}} + \frac{2}{3\bar{x}} \left(\frac{\mu T'}{T^2} \right. \right. \\
& \left. \left. - \frac{\mu' T'}{T} \right) \right) \frac{\partial \bar{r}_y}{\partial \eta} - \frac{2}{3\bar{x}} \frac{\mu}{T} \frac{\partial^2 \bar{r}_y}{\partial \eta^2} + \frac{2}{3} \kappa_z^2 \mu' T' \bar{r}_z - \frac{1}{3} \kappa_z^2 \mu \frac{\partial \bar{r}_z}{\partial \eta} + \frac{T'}{T} \bar{r}_e \Bigg]^H \bar{v}' \\
& + \left[\bar{r}_c + \frac{\mu' T'}{2\bar{x}} \bar{r}_y + \frac{\mu}{6\bar{x}} \frac{\partial \bar{r}_y}{\partial \eta} + \left(i + \frac{4}{3} \kappa_z^2 \mu T + \frac{F'}{2\bar{x}} \right) \bar{r}_z - F' \frac{\partial \bar{r}_z}{\partial \bar{x}} \right. \\
& + \frac{1}{2\bar{x}} \left(F + \frac{\mu T'}{T^2} - \frac{\mu' T'}{T} \right) \frac{\partial \bar{r}_z}{\partial \eta} - \frac{1}{2\bar{x}} \frac{\mu}{T} \frac{\partial^2 \bar{r}_z}{\partial \eta^2} \Bigg]^H \bar{w}' + \left[\left(-\frac{i}{T^2} \right. \right. \\
& \left. - \frac{1}{2\bar{x}} \frac{F'}{T} \right) \bar{r}_c + \frac{F'}{T} \frac{\partial \bar{r}_c}{\partial \bar{x}} - \frac{1}{2\bar{x}} \frac{F}{T} \frac{\partial \bar{r}_c}{\partial \eta} + \frac{1}{2\bar{x}} \frac{F F''}{T} \bar{r}_x + \frac{1}{2\bar{x}} \frac{\mu' F''}{T} \frac{\partial \bar{r}_x}{\partial \eta} \\
& + \left(-F F' + \eta_c (F')^2 - \frac{T' F^2}{T} + \eta_c F F'' - \frac{\mu' F''}{2\bar{x}^2} \right) \bar{r}_y \\
& + \frac{\mu' F''}{2\bar{x}} \frac{\partial \bar{r}_y}{\partial \bar{x}} + \left(-\frac{1}{3\bar{x}^2} \frac{\mu' T' F}{T} + \frac{\eta_c \mu' F''}{4\bar{x}^2} \right) \frac{\partial \bar{r}_y}{\partial \eta} + \frac{\kappa_z^2 \mu' T' F}{3\bar{x}} \bar{r}_z \\
& + \left(i + \frac{\kappa_z^2 \mu T}{\mathrm{Pr}} + \frac{1}{2\bar{x}} \left(F' + \frac{T' F}{T} - (\gamma - 1) M^2 \frac{\mu' (F'')^2}{T} \right) \right) \bar{r}_e \\
& \left. - F' \frac{\partial \bar{r}_e}{\partial \bar{x}} + \frac{1}{2\bar{x}} \left(F + \frac{\mu T'}{\mathrm{Pr}\, T^2} \right) \frac{\partial \bar{r}_e}{\partial \eta} - \frac{1}{2\bar{x}} \frac{\mu}{\mathrm{Pr}\, T} \frac{\partial^2 \bar{r}_e}{\partial \eta^2} \right]^H \bar{\tau}' \mathrm{d}\eta \mathrm{d}\bar{x},
\end{aligned}
\tag{B.1}
$$

and

$$
\begin{aligned}
b = \int_0^{\infty} \Bigg[& \left(\bar{r}_c + F' \bar{r}_x + \frac{\mu' T'}{2\bar{x}} \bar{r}_y + \frac{\mu}{6\bar{x}} \frac{\partial \bar{r}_y}{\partial \eta} + \frac{1}{3} \kappa_z^2 \mu T \bar{r}_z \right)^H \bar{u}' + F' \bar{r}_y^H \bar{v}' \\
& + F' \bar{r}_z^H \bar{w}' + \left(-\frac{F'}{T} \bar{r}_c - \frac{\mu' F''}{2\bar{x}} \bar{r}_y + F' \bar{r}_e \right)^H \bar{\tau}' \Bigg]_{\bar{x}_i}^{\bar{x}_f} \mathrm{d}\eta \\
& + \int_{\bar{x}_i}^{\bar{x}_f} \Bigg[\frac{1}{2\bar{x}} \bar{r}_y^H \bar{p}' + \left(-\frac{\eta_c}{2\bar{x}} \bar{r}_c - \frac{1}{2\bar{x}} F \bar{r}_x + \frac{1}{2\bar{x}} \frac{\mu}{T} \frac{\partial \bar{r}_x}{\partial \eta} - \frac{\eta_c \mu}{12\bar{x}^2} \frac{\partial \bar{r}_y}{\partial \eta} \right. \\
& \left. - \frac{\eta_c \kappa_z^2 \mu T}{6\bar{x}} \bar{r}_z - \frac{1}{\bar{x}} (\gamma - 1) M^2 \frac{\mu F''}{T} \bar{r}_e \right)^H \bar{u}' - \frac{\mu}{6\bar{x}} \bar{r}_y^H \frac{\partial \bar{u}'}{\partial \bar{x}} \\
& + \left(-\frac{1}{2\bar{x}} \frac{\mu}{T} \bar{r}_x + \frac{\eta_c \mu}{12\bar{x}^2} \bar{r}_y \right)^H \frac{\partial \bar{u}'}{\partial \eta} + \left(\frac{1}{T} \bar{r}_c - \frac{F}{2\bar{x}} \bar{r}_y + \frac{2}{3\bar{x}} \frac{\mu}{T} \frac{\partial \bar{r}_y}{\partial \eta} \right. \\
& \left. + \frac{1}{3} \kappa_z^2 \mu \bar{r}_z \right)^H \bar{v}' - \frac{2}{3\bar{x}} \frac{\mu}{T} \bar{r}_y^H \frac{\partial \bar{v}'}{\partial \eta} + \left(-\frac{\mu}{6\bar{x}} \bar{r}_y - \frac{F}{2\bar{x}} \bar{r}_z + \frac{1}{2\bar{x}} \frac{\mu}{T} \frac{\partial \bar{r}_z}{\partial \eta} \right)^H \bar{w}' \\
& - \frac{1}{2\bar{x}} \frac{\mu}{T} \bar{r}_z^H \frac{\partial \bar{w}'}{\partial \eta} + \left(\frac{1}{2\bar{x}} \frac{F}{T} \bar{r}_c - \frac{1}{2\bar{x}} \frac{\mu' F''}{T} \bar{r}_x + \left(\frac{1}{3\bar{x}^2} \frac{\mu' T' F}{T} - \frac{\eta_c \mu' F''}{4\bar{x}^2} \right) \bar{r}_y \right. \\
& \left. + \frac{1}{2\bar{x}} \left(-F - \frac{\mu' T'}{\mathrm{Pr}\, T} \right) \bar{r}_e + \frac{1}{2\bar{x}} \frac{\mu}{\mathrm{Pr}\, T} \frac{\partial \bar{r}_e}{\partial \eta} \right)^H \bar{\tau}' - \frac{1}{2\bar{x}} \frac{\mu}{\mathrm{Pr}\, T} \bar{r}_e^H \frac{\partial \bar{\tau}'}{\partial \eta} \Bigg]_0^{\infty} \mathrm{d}\bar{x}.
\end{aligned}
\tag{B.2}
$$

The adjoint equations can be directly obtained from equation (B.1) by extracting the term $\bar{\mathbf{R}}(\bar{\mathbf{r}})$. However, the reader is reminded that the intended use of the dual space is to find a simpler expression for the gradient of the cost functional $\mathcal{J}$ with respect to the control variable $\bar{v}_w$. Therefore, the judicious choice of boundary conditions, terminal conditions and forcing terms is essential. Thus, the perturbed cost functional $\mathcal{J}'$ terms that do not include the control variable $\bar{v}_w'$ are added to both sides of $\left\langle \bar{\mathbf{R}}(\bar{\mathbf{r}}), \bar{\mathbf{q}}' \right\rangle_{\mathbf{I}} + b = 0$:

$$
\alpha_1 \mathcal{J}_1' + \alpha_2 \mathcal{J}_2' + \alpha_3 \mathcal{J}_3' + \alpha_4 \mathcal{J}_4' = \alpha_1 \mathcal{J}_1' + \alpha_2 \mathcal{J}_2' + \alpha_3 \mathcal{J}_3' + \alpha_4 \mathcal{J}_4' - \left\langle \bar{\mathbf{R}}(\bar{\mathbf{r}}), \bar{\mathbf{q}}' \right\rangle_{\mathbf{I}} - b. \tag{B.3}
$$

Then the right-hand-side of the equation (B.3) is used to obtain the adjoint equation system. Set

$$
\alpha_2 \mathcal{J}_2' + \alpha_4 \mathcal{J}_4' = \left\langle \bar{\mathbf{R}}(\bar{\mathbf{r}}), \bar{\mathbf{q}}' \right\rangle_{\mathbf{I}}, \tag{B.4}
$$

to extract the adjoint equations forcing, which can be written as

$$\bar{\mathbf{R}}\left(\bar{\mathbf{r}}\right) = \begin{bmatrix} 0 \\ \alpha_2 \mathbf{Q_2} \bar{u} \\ 0 \\ 0 \\ \alpha_4 \mathbf{Q_4} \bar{\tau} \end{bmatrix}. \tag{B.5}$$

The equation (B.5) turns out to be the previously derived adjoint equation (3.15b). Substituting equation (B.4) into the right-hand-side of equation (B.3) leads to

$$\alpha_1 \mathcal{J}_1' + \alpha_2 \mathcal{J}_2' + \alpha_3 \mathcal{J}_3' + \alpha_4 \mathcal{J}_4' = \alpha_1 \mathcal{J}_1' + \alpha_3 \mathcal{J}_3' - b. \tag{B.6}$$

In a similar way, the boundary conditions and terminal conditions can be extracted from the right-hand-side of equation (B.6) while considering the boundary and initial conditions (3.54)-(3.58), to yield the boundary conditions

$$\bar{r}_x = \bar{r}_y = \bar{r}_z = \frac{\partial \bar{r}_e}{\partial \eta} = 0 \quad \text{at} \quad \eta = 0, \tag{B.7}$$

$$\bar{r}_c = \bar{r}_x = \bar{r}_y = \bar{r}_z = \bar{r}_e = 0 \quad \text{as} \quad \eta \to \infty, \tag{B.8}$$

and terminal conditions

$$\bar{r}_c = \bar{r}_y = \bar{r}_z = 0 \quad \text{at} \quad \bar{x} = \bar{x}_f, \tag{B.9}$$

$$\bar{r}_x = \alpha_1 \frac{\mathbf{Q_1} \bar{u}}{F'} \quad \text{at} \quad \bar{x} = \bar{x}_f, \tag{B.10}$$

$$\bar{r}_e = \alpha_3 \frac{\mathbf{Q_3} \bar{\tau}}{F'} \quad \text{at} \quad \bar{x} = \bar{x}_f. \tag{B.11}$$

Then, the equation (B.6) is further simplified by the substitution of the boundary and terminal conditions (B.7)-(B.11) of the adjoint system. The remainder terms yield:

$$\alpha_1 \mathcal{J}_1' + \alpha_2 \mathcal{J}_2' + \alpha_3 \mathcal{J}_3' + \alpha_4 \mathcal{J}_4' = \int_{\bar{x}_i}^{\bar{x}_f} \left[\frac{1}{T} \bar{r}_c \right]_{\eta=0}^{H} \bar{v}_w' \mathrm{d}\bar{x}. \tag{B.12}$$

Equation (B.12) can then be substituted into the cost functional perturbation $\mathcal{J}'$ (3.40), to simplify it as

$$\mathcal{J}' = \int_{\bar{x}_i}^{\bar{x}_f} \left[\frac{1}{T} \bar{r}_c + \theta_v^2 \mathbf{Q_v} \bar{v}_w \right]_{\eta=0}^{H} \bar{v}_w' \mathrm{d}\bar{x}. \tag{B.13}$$

In an analogous way, an expression for the cost functional perturbation $\mathcal{J}^{(0)\prime}$ (3.41) can be found from solving the adjoint equations:

$$\bar{\mathbf{R}}\left(\bar{\mathbf{r}}\right) = \begin{bmatrix} 0 \\ \alpha_2^{(0)} \mathbf{Q_2^{(0)}} \bar{u}^{(0)} \\ 0 \\ 0 \\ \alpha_4^{(0)} \mathbf{Q_4^{(0)}} \bar{\tau}^{(0)} \end{bmatrix}. \tag{B.14}$$

with boundary conditions

$$\bar{r}_x = \bar{r}_y = \bar{r}_z = \frac{\partial \bar{r}_e}{\partial \eta} = 0 \quad \text{at} \quad \eta = 0, \tag{B.15}$$

$$\bar{r}_c = \bar{r}_x = \bar{r}_y = \bar{r}_z = \bar{r}_e = 0 \quad \text{as} \quad \eta \to \infty, \tag{B.16}$$

and terminal conditions

$$\bar{r}_c = \bar{r}_y = \bar{r}_z = 0 \quad \text{at} \quad \bar{x} = \bar{x}_f, \tag{B.17}$$

$$\bar{r}_x = 0 \quad \text{at} \quad \bar{x} = \bar{x}_f, \tag{B.18}$$

$$\bar{r}_e = 0 \quad \text{at} \quad \bar{x} = \bar{x}_f. \tag{B.19}$$

This leads to

$$\mathcal{J}^{(0)\prime} = \int_{\bar{x}_i}^{\bar{x}_f} \left[\frac{1}{T} \bar{r}_c + \theta_v^{(0)2} \mathbf{Q_v^{(0)}} \bar{v}_w^{(0)} \right]_{\eta=0}^{H} \bar{v}_w^{(0)\prime} \mathrm{d}\bar{x}. \tag{B.20}$$

Appendix C

Incompressible LUBR adjoint

The adjoint system was derived from the CLUBR equations in section §3.2, and just like the CLUBR equations, it is valid up to Mach 4. Similarly, an adjoint system can be derived for the particular case when $M = 0$ from the incompressible LUBR equations (5.2)-(5.5) in LWG [43]:

continuity equation

$$\frac{\partial \bar{u}}{\partial \bar{x}} - \frac{\eta}{2\bar{x}}\frac{\partial \bar{u}}{\partial \eta} + \frac{\partial \bar{v}}{\partial \eta} + \bar{w} = 0; \tag{C.1}$$

x-momentum equation

$$-i\bar{u} + F'\frac{\partial \bar{u}}{\partial \bar{x}} - \frac{F}{2\bar{x}}\frac{\partial \bar{u}}{\partial \eta} - \frac{\eta F''}{2\bar{x}}\bar{u} + F''\bar{v} - \frac{1}{2\bar{x}}\frac{\partial^2 \bar{u}}{\partial \eta^2} + \kappa_z^2\bar{u} = 0; \tag{C.2}$$

y-momentum equation

$$\begin{aligned} -i\bar{v} + F'\frac{\partial \bar{v}}{\partial \bar{x}} - \frac{F}{2\bar{x}}\frac{\partial \bar{v}}{\partial \eta} - \frac{1}{(2\bar{x})^2}[\eta(\eta F')' - F]\bar{u} \\ + \frac{(\eta F')'}{2\bar{x}}\bar{v} + \frac{1}{2\bar{x}}\frac{\partial \bar{p}}{\partial \eta} - \frac{1}{2\bar{x}}\frac{\partial^2 \bar{v}}{\partial \eta^2} + \kappa_z^2\bar{v} = 0; \end{aligned} \tag{C.3}$$

z-momentum equation

$$-i\bar{w} + F'\frac{\partial \bar{w}}{\partial \bar{x}} - \frac{F}{2\bar{x}}\frac{\partial \bar{w}}{\partial \eta} - \kappa_z^2\bar{p} - \frac{1}{2\bar{x}}\frac{\partial^2 \bar{w}}{\partial \eta^2} + \kappa_z^2\bar{w} = 0; \tag{C.4}$$

with boundary conditions at the wall defined as

$$\bar{u} = \bar{w} \quad \text{at} \quad \eta = 0, \tag{C.5}$$

and control wall-normal transpiration imposed by

$$\bar{v} = \bar{v}_w \quad \text{at} \quad \eta = 0. \tag{C.6}$$

A cost functional to measure the kinetic energy of the Klebanoff modes is defined as

$$\mathcal{J} = \frac{1}{2}\int_{\bar{x}_i}^{\bar{x}_f}\int_0^\infty \left(\bar{u}^H \mathbf{Q_2} \bar{u}\right) \mathrm{d}\eta \mathrm{d}\bar{x} + \frac{\theta_v^2}{2}\int_{\bar{x}_i}^{\bar{x}_f} \left(\bar{v}_w^H \mathbf{Q_v} \bar{v}_w\right) \mathrm{d}\bar{x}, \tag{C.7}$$

with weighing Hermitian matrices $\mathbf{Q_2} \geq 0$, $\mathbf{Q_v} \geq 0$. The coefficients θ_v define the weight of the cost of actuation.

The optimisation problem is thus defined as the minimisation of the cost functional $\mathcal{J}$ through the control variable $\bar{v}_w(x)$, while taking into account the LUBR equations (C.1)-(C.4) as constraints. The solution to this problem can be obtained by searching for

$$\frac{\mathrm{d}\mathcal{J}}{\mathrm{d}\bar{v}_w} = 0. \tag{C.8}$$

In order to find a simpler expression for this gradient, the use of the adjoint identity (3.59) and the inner product defined as (3.60) are used to find an explicit expression of the gradient that only depends on the control $\bar{v}_w$ and the adjoint variables.

Similar to the compressible case, the left-hand-side of the adjoint identity (3.59) is expanded as

$$\begin{aligned}
\left\langle \bar{\mathbf{r}}, \mathbf{Q}\left(\bar{\mathbf{q}}'\right)\right\rangle_{\mathbf{I}} = \int_{\bar{x}_i}^{\bar{x}_f}\int_0^\infty & \bar{r}_c^H \left[\frac{\partial \bar{u}'}{\partial \bar{x}} - \frac{\eta}{2\bar{x}}\frac{\partial \bar{u}'}{\partial \eta} + \frac{\partial \bar{v}'}{\partial \eta} + \bar{w}'\right] \\
& + \bar{r}_x^H \left[-i\bar{u}' + F'\frac{\partial \bar{u}'}{\partial \bar{x}} - \frac{F}{2\bar{x}}\frac{\partial \bar{u}'}{\partial \eta} - \frac{\eta F''}{2\bar{x}}\bar{u}' - \frac{1}{2\bar{x}}\frac{\partial^2 \bar{u}'}{\partial \eta^2} + \kappa_z^2 \bar{u}' + F''\bar{v}'\right] \\
& + \bar{r}_y^H \left[\frac{1}{2\bar{x}}\frac{\partial \bar{p}'}{\partial \eta} - \frac{1}{(2\bar{x})^2}[\eta(\eta F')' - F]\bar{u}' - i\bar{v}' + F'\frac{\partial \bar{v}'}{\partial \bar{x}} - \frac{F}{2\bar{x}}\frac{\partial \bar{v}'}{\partial \eta}\right. \\
& \left. + \frac{(\eta F')'}{2\bar{x}}\bar{v}' - \frac{1}{2\bar{x}}\frac{\partial^2 \bar{v}'}{\partial \eta^2} + \kappa_z^2 \bar{v}'\right] \\
& + \bar{r}_z^H \left[-\kappa_z^2 \bar{p}' - i\bar{w}' + F'\frac{\partial \bar{w}'}{\partial \bar{x}} - \frac{F}{2\bar{x}}\frac{\partial \bar{w}'}{\partial \eta} - \frac{1}{2\bar{x}}\frac{\partial^2 \bar{w}'}{\partial \eta^2} + \kappa_z^2 \bar{w}'\right] \mathrm{d}\eta \mathrm{d}\bar{x}.
\end{aligned}$$

The terms are rearranged, and the order of integration is changed as follows

$$
\begin{aligned}
\left\langle \bar{\mathbf{r}}, \mathbf{Q}\left(\bar{\mathbf{q}}'\right)\right\rangle_{\mathbf{I}} = & \int_{\bar{x}_i}^{\bar{x}_f}\int_0^{\infty} -\bar{r}_z^H \kappa_z^2 \bar{p}' \\
& + \left[-\bar{r}_x^H i - \bar{r}_x^H \frac{\eta F''}{2\bar{x}} + \bar{r}_x^H \kappa_z^2 - \bar{r}_y^H \frac{1}{(2\bar{x})^2}[\eta(\eta F')' - F]\right] \bar{u}' \\
& + \left[\bar{r}_x^H F'' - \bar{r}_y^H i + \bar{r}_y^H \frac{(\eta F')'}{2\bar{x}} + \bar{r}_y^H \kappa_z^2\right] \bar{v}' \\
& + \left[\bar{r}_c^H - \bar{r}_z^H i + \bar{r}_z^H \kappa_z^2\right] \bar{w}' \mathrm{d}\eta \mathrm{d}\bar{x} \\
& + \int_0^{\infty}\int_{\bar{x}_i}^{\bar{x}_f} \left[\bar{r}_c^H + \bar{r}_x^H F'\right] \frac{\partial \bar{u}'}{\partial \bar{x}} + F' \frac{\partial \bar{v}'}{\partial \bar{x}} + \bar{r}_z^H F' \frac{\partial \bar{w}'}{\partial \bar{x}} \mathrm{d}\bar{x}\mathrm{d}\eta \\
& + \int_{\bar{x}_i}^{\bar{x}_f}\int_0^{\infty} \bar{r}_y^H \frac{1}{2\bar{x}} \frac{\partial \bar{p}'}{\partial \eta} + \left[-\bar{r}_c^H \frac{\eta}{2\bar{x}} - \bar{r}_x^H \frac{F}{2\bar{x}}\right] \frac{\partial \bar{u}'}{\partial \eta} \\
& + \left[\bar{r}_c^H - \bar{r}_y^H \frac{F}{2\bar{x}}\right] \frac{\partial \bar{v}'}{\partial \eta} - \bar{r}_z^H \frac{F}{2\bar{x}} \frac{\partial \bar{w}'}{\partial \eta} \mathrm{d}\eta \mathrm{d}\bar{x} \\
& + \int_{\bar{x}_i}^{\bar{x}_f}\int_0^{\infty} -\bar{r}_x^H \frac{1}{2\bar{x}} \frac{\partial^2 \bar{u}'}{\partial \eta^2} - \bar{r}_y^H \frac{1}{2\bar{x}} \frac{\partial^2 \bar{v}'}{\partial \eta^2} - \bar{r}_z^H \frac{1}{2\bar{x}} \frac{\partial^2 \bar{w}'}{\partial \eta^2} \mathrm{d}\eta \mathrm{d}\bar{x}.
\end{aligned}
$$

Then, integration by parts is used as many times as needed to move all the derivative operators from the state variables perturbations $\bar{p}'$, $\bar{u}'$, $\bar{v}'$ and $\bar{w}'$ to the adjoint variables $\bar{r}_c$, $\bar{r}_x$, $\bar{r}_y$, $\bar{r}_z$. The result of these operations are the right-hand-side terms of the adjoint identity (3.59):

$$
\begin{aligned}
\left\langle \bar{\mathbf{R}}\left(\bar{\mathbf{r}}\right), \bar{\mathbf{q}}'\right\rangle_{\mathbf{I}} = & \int_{\bar{x}_i}^{\bar{x}_f}\int_0^{\infty} \left[-\frac{\partial \bar{r}_y}{\partial \eta}\frac{1}{2\bar{x}} - \bar{r}_z \kappa_z^2\right]^H \bar{p}' \\
& \left[\frac{1}{2\bar{x}}\bar{r}_c - \frac{\partial \bar{r}_c}{\partial \bar{x}} + \frac{\eta}{2\bar{x}}\frac{\partial \bar{r}_c}{\partial \eta} + \left(i + \kappa_z^2 + \frac{F'}{2\bar{x}} - \frac{\eta F''}{2\bar{x}}\right)\bar{r}_x \right. \\
& \left. -F'\frac{\partial \bar{r}_x}{\partial \bar{x}} + \frac{F}{2\bar{x}}\frac{\partial \bar{r}_x}{\partial \eta} - \frac{1}{2\bar{x}}\frac{\partial^2 \bar{r}_x}{\partial \eta^2} - \frac{1}{(2\bar{x})^2}[\eta(\eta F')' - F]\bar{r}_y\right]^H \bar{u}' \\
& \left[-\frac{\partial \bar{r}_c}{\partial \eta} + F''\bar{r}_x + \left(i + \kappa_z^2 + \frac{F'}{2\bar{x}} + \frac{(\eta F')'}{2\bar{x}}\right)\bar{r}_y \right. \\
& \left. -F'\frac{\partial \bar{r}_y}{\partial \bar{x}} + \frac{F}{2\bar{x}}\frac{\partial \bar{r}_y}{\partial \eta} - \frac{1}{2\bar{x}}\frac{\partial^2 \bar{r}_y}{\partial \eta^2}\right]^H \bar{v}' \\
& \left[\bar{r}_c + \left(i + \kappa_z^2 + \frac{F'}{2\bar{x}}\right)\bar{r}_z \right. \\
& \left. -F'\frac{\partial \bar{r}_z}{\partial \bar{x}} + \frac{F}{2\bar{x}}\frac{\partial \bar{r}_z}{\partial \eta} - \frac{1}{2\bar{x}}\frac{\partial^2 \bar{r}_z}{\partial \eta^2}\right]^H \bar{w}' \mathrm{d}\eta \mathrm{d}\bar{x},
\end{aligned}
\tag{C.9}
$$

and

$$
\begin{aligned}
b = & \int_0^{\infty} \left[\left(\bar{r}_c + F' \bar{r}_x \right)^H \bar{u}' + F' \bar{r}_y^H \bar{v}' + F' \bar{r}_z^H \bar{w}' \right]_{\bar{x}_i}^{\bar{x}_f} \mathrm{d}\eta \\
& + \int_{\bar{x}_i}^{\bar{x}_f} \left[\frac{1}{2\bar{x}} \bar{r}_y^H \bar{p}' + \left(-\frac{\eta}{2\bar{x}} \bar{r}_c - \frac{F}{2\bar{x}} \bar{r}_x + \frac{1}{2\bar{x}} \frac{\partial \bar{r}_x}{\partial \eta} \right)^H \bar{u}' - \frac{1}{2\bar{x}} \bar{r}_x^H \frac{\partial \bar{u}'}{\partial \eta} \right. \\
& + \left(\bar{r}_c - \frac{F}{2\bar{x}} \bar{r}_y + \frac{1}{2\bar{x}} \frac{\partial \bar{r}_y}{\partial \eta} \right)^H \bar{v}' - \frac{1}{2\bar{x}} \bar{r}_y^H \frac{\partial \bar{v}'}{\partial \eta} \\
& \left. + \left(-\frac{F}{2\bar{x}} \bar{r}_z + \frac{1}{2\bar{x}} \frac{\partial \bar{r}_z}{\partial \eta} \right)^H \bar{w}' - \frac{1}{2\bar{x}} \bar{r}_z^H \frac{\partial \bar{w}'}{\partial \eta} \right]_0^{\infty} \mathrm{d}\bar{x}
\end{aligned}
\qquad . \tag{C.10}
$$

The adjoint equations can be written from equation (C.9) by taking into account the cost functional (C.7). Thus the adjoint equations are written in a reduced form as

$$
\bar{\mathbf{R}} \left(\bar{\mathbf{r}} \right) = \begin{bmatrix} 0 \\ \mathbf{Q_2} \bar{u} \\ 0 \\ 0 \end{bmatrix} . \tag{C.11}
$$

In a similar way, the boundary conditions and terminal conditions for the adjoint system (C.11) can be found from the terms (C.10) and the boundary conditions (C.5)-(C.6), and written as

$$
\bar{r}_x = \bar{r}_y = \bar{r}_z = 0 \quad \text{at} \quad \eta = 0, \tag{C.12}
$$

$$
\bar{r}_c = \bar{r}_x = \bar{r}_y = \bar{r}_z = 0 \quad \text{as} \quad \eta \to \infty, \tag{C.13}
$$

and

$$
\bar{r}_c = \bar{r}_x = \bar{r}_y = \bar{r}_z = 0 \quad \text{at} \quad \bar{x} = \bar{x}_f. \tag{C.14}
$$

With the adjoint system fully defined, a new expression for the optimality condition (C.8) can be written as

$$
\frac{\mathrm{d}\mathcal{J}}{\mathrm{d}\bar{v}_w} = \left[\bar{r}_c + \theta_v^2 \mathbf{Q_v} \bar{v}_w \right]_{\eta=0} , \tag{C.15}
$$

where the solution of $\bar{r}_c$ is given by the adjoint equations:

$$
-\frac{1}{2\bar{x}} \frac{\partial \bar{r}_y}{\partial \eta} - \kappa_z^2 \bar{r}_z = 0;
$$

$$\frac{1}{2\bar{x}}\bar{r}_c - \frac{\partial \bar{r}_c}{\partial \bar{x}} + \frac{\eta}{2\bar{x}}\frac{\partial \bar{r}_c}{\partial \eta} + \left(i + \kappa_z^2 + \frac{F'}{2\bar{x}} - \frac{\eta F"}{2\bar{x}}\right)\bar{r}_x - F'\frac{\partial \bar{r}_x}{\partial \bar{x}} + \frac{F}{2\bar{x}}\frac{\partial \bar{r}_x}{\partial \eta}$$
$$-\frac{1}{2\bar{x}}\frac{\partial^2 \bar{r}_x}{\partial \eta^2} - \frac{1}{(2\bar{x})^2}[\eta(\eta F')' - F]\bar{r}_y = 0;$$
$$-\frac{\partial \bar{r}_c}{\partial \eta} + F"\bar{r}_x + \left(i + \kappa_z^2 + \frac{F'}{2\bar{x}} + \frac{(\eta F')'}{2\bar{x}}\right)\bar{r}_y - F'\frac{\partial \bar{r}_y}{\partial \bar{x}}$$
$$+\frac{F}{2\bar{x}}\frac{\partial \bar{r}_y}{\partial \eta} - \frac{1}{2\bar{x}}\frac{\partial^2 \bar{r}_y}{\partial \eta^2} = 0;$$
$$\bar{r}_c + \left(i + \kappa_z^2 + \frac{F'}{2\bar{x}}\right)\bar{r}_z - F'\frac{\partial \bar{r}_z}{\partial \bar{x}} + \frac{F}{2\bar{x}}\frac{\partial \bar{r}_z}{\partial \eta} - \frac{1}{2\bar{x}}\frac{\partial^2 \bar{r}_z}{\partial \eta^2} = 0.$$

Appendix D

Alternative actuators for wall-based feedback control

In chapter 3, the chosen method of actuation was blowing and suction implemented at the wall with wall-normal velocity, i.e. with an angle of attack of $\pi/2$.

Throughout this chapter, heat transfer actuators and blowing and suction along the streamwise and spanwise direction are also considered. The adjoint formulation is extended in §D.1 and the numerical findings in §3.5.

D.1 Implementation of the alternative actuators

The wall-normal transpiration implemented in the previous chapter was successful in attenuating the Klebanoff modes. In this chapter, a combination of actuators is explored. The alternative actuators include heat transfer, and blowing and suction with a direction other than wall-normal. Of the combinations considered, not all can be directly implemented in a physical experiment. However, they are still considered for the control and physical insight.

The formulation used closely follows the one described in §3.2. The inclusion of the streamwise and spanwise wall transpiration is carried out by modifying the

boundary conditions (3.18)-(3.20) defined in the previous section to

$$\bar{u} = \alpha_u \bar{u}_w \quad \text{at} \quad \eta = 0, \tag{D.1}$$

$$\bar{u}^{(0)} = \alpha_u \bar{u}_w^{(0)} \quad \text{at} \quad \eta = 0, \tag{D.2}$$

$$\bar{v} = \alpha_v \bar{v}_w \quad \text{at} \quad \eta = 0, \tag{D.3}$$

$$\bar{v}^{(0)} = \alpha_v \bar{v}_w^{(0)} \quad \text{at} \quad \eta = 0, \tag{D.4}$$

and

$$\bar{w} = \alpha_w \bar{w}_w \quad \text{at} \quad \eta = 0, \tag{D.5}$$

$$\bar{w}^{(0)} = \alpha_w \bar{w}_w^{(0)} \quad \text{at} \quad \eta = 0. \tag{D.6}$$

The variables $\bar{u}_w$, $\bar{u}_w^{(0)}$, $\bar{w}_w^{(0)}$ and $\bar{w}_w^{(0)}$ represent the modified velocities on the wall in their respective directions as $\bar{v}_w$, $\bar{v}_w^{(0)}$. Furthermore, the heat transfer actuator is added by modifying the boundary condition (2.70) as

$$\frac{\partial \bar{\tau}}{\partial \eta} = \alpha_\tau \bar{\tau}_w \quad \text{at} \quad \eta = 0, \tag{D.7}$$

$$\frac{\partial \bar{\tau}^{(0)}}{\partial \eta} = \alpha_\tau \bar{\tau}_w^{(0)} \quad \text{at} \quad \eta = 0, \tag{D.8}$$

where $\bar{\tau}_w$ and $\bar{\tau}_w^{(0)}$ represent values of heat transference induced at the wall across $\bar{x}$. The coefficients α_u, α_v, α_w and α_τ are used to select the actuator or the combination of actuators that are active during the simulation, and they satisfy the equation:

$$\alpha_u + \alpha_v + \alpha_w + \alpha_\tau \leq 4, \quad \alpha_u, \alpha_v, \alpha_w, \alpha_\tau \in \{0, 1\}.$$

The cost of the combination of actuators, is added to the cost functionals as:

$$\mathcal{J} = \alpha_1 \mathcal{J}_1 + \alpha_2 \mathcal{J}_2 + \alpha_3 \mathcal{J}_3 + \alpha_4 \mathcal{J}_4 + \mathcal{J}_u + \mathcal{J}_v + \mathcal{J}_w + \mathcal{J}_\tau \tag{D.9}$$

and

$$\begin{aligned} \mathcal{J}^{(0)} = {} & \alpha_2^{(0)} \mathcal{J}_2^{(0)} + \alpha_4^{(0)} \mathcal{J}_4^{(0)} \\ & + \mathcal{J}_u^{(0)} + \mathcal{J}_v^{(0)} + \mathcal{J}_w^{(0)} + \mathcal{J}_\tau^{(0)}, \end{aligned} \tag{D.10}$$

where

$$\mathcal{J}_u = \frac{\theta_u^2}{2} \int_{\bar{x}_i}^{\bar{x}_f} \left(\bar{u}_w^H \mathbf{Q_u} \bar{u}_w \right) \mathrm{d}\bar{x},$$

$$\mathcal{J}_v = \frac{\theta_v^2}{2} \int_{\bar{x}_i}^{\bar{x}_f} \left(\bar{v}_w^H \mathbf{Q_v} \bar{v}_w \right) \mathrm{d}\bar{x},$$

$$\mathcal{J}_w = \frac{\theta_w^2}{2} \int_{\bar{x}_i}^{\bar{x}_f} \left(\bar{w}_w^H \mathbf{Q_w} \bar{w}_w \right) \mathrm{d}\bar{x},$$

$$\mathcal{J}_\tau = \frac{\theta_\tau^2}{2} \int_{\bar{x}_i}^{\bar{x}_f} \left(\bar{\tau}_w^H \mathbf{Q}_\tau \bar{\tau}_w \right) \mathrm{d}\bar{x},$$

$$\mathcal{J}_u^{(0)} = \frac{\theta_u^{(0)2}}{2} \int_{\bar{x}_i}^{\bar{x}_f} \left(\bar{u}_w^{(0)H} \mathbf{Q_u^{(0)}} \bar{u}_w^{(0)} \right) \mathrm{d}\bar{x},$$

$$\mathcal{J}_v^{(0)} = \frac{\theta_v^{(0)2}}{2} \int_{\bar{x}_i}^{\bar{x}_f} \left(\bar{v}_w^{(0)H} \mathbf{Q_v^{(0)}} \bar{v}_w^{(0)} \right) \mathrm{d}\bar{x},$$

$$\mathcal{J}_w^{(0)} = \frac{\theta_w^{(0)2}}{2} \int_{\bar{x}_i}^{\bar{x}_f} \left(\bar{w}_w^{(0)H} \mathbf{Q_w^{(0)}} \bar{w}_w^{(0)} \right) \mathrm{d}\bar{x},$$

$$\mathcal{J}_\tau^{(0)} = \frac{\theta_\tau^{(0)2}}{2} \int_{\bar{x}_i}^{\bar{x}_f} \left(\bar{\tau}_w^{(0)H} \mathbf{Q}_\tau^{(0)} \bar{\tau}_w^{(0)} \right) \mathrm{d}\bar{x},$$

and $\mathcal{J}_1$, $\mathcal{J}_2$, $\mathcal{J}_3$, $\mathcal{J}_4$, $\mathcal{J}_2^{(0)}$, $\mathcal{J}_4^{(0)}$ are defined as in the last chapter in equations (3.23)-(3.28). The terms $\mathbf{Q_u}$, $\mathbf{Q_v}$, $\mathbf{Q_w}$, $\mathbf{Q}_\tau$, $\mathbf{Q_u^{(0)}}$, $\mathbf{Q_v^{(0)}}$, $\mathbf{Q_w^{(0)}}$ and $\mathbf{Q}_\tau^{(0)}$, are weighing Hermitian matrices that satisfy the equations $\mathbf{Q_u} > 0$, $\mathbf{Q_v} > 0$, $\mathbf{Q_w} > 0$, $\mathbf{Q}_\tau > 0$, $\mathbf{Q_u^{(0)}} > 0$, $\mathbf{Q_v^{(0)}} > 0$, $\mathbf{Q_w^{(0)}} > 0$ and $\mathbf{Q}_\tau^{(0)} > 0$. The coefficients θ_u, θ_v, θ_w, θ_τ, $\theta_u^{(0)}$, $\theta_v^{(0)}$, $\theta_w^{(0)}$ and $\theta_\tau^{(0)}$ are weights that account for the cost of actuation, as in the last chapter.

To simplify the notation, the control variables $\bar{\mathbf{c}}_\mathbf{w}(\bar{x})$ are used to represent the combination of the other actuators as

$$\bar{\mathbf{c}}_\mathbf{w} = \begin{bmatrix} \alpha_u \bar{u}_w \\ \alpha_v \bar{v}_w \\ \alpha_w \bar{w}_w \\ \alpha_\tau \bar{\tau}_w \end{bmatrix}$$

and $\bar{\mathbf{c}}_{\mathbf{w}}^{(\mathbf{0})}(\bar{x})$ to the remaining actuators as

$$\bar{\mathbf{c}}_{\mathbf{w}}^{(\mathbf{0})} = \begin{bmatrix} \alpha_u \bar{u}_w^{(0)} \\ \alpha_v \bar{v}_w^{(0)} \\ \alpha_w \bar{w}_w^{(0)} \\ \alpha_\tau \bar{\tau}_w^{(0)} \end{bmatrix}.$$

The optimisation problem can now be defined as the search of the controls $\bar{\mathbf{c}}_{\mathbf{w}}(\bar{x})$ and $\bar{\mathbf{c}}_{\mathbf{w}}^{(\mathbf{0})}(\bar{x})$ that minimise $\mathcal{J}$ and $\mathcal{J}^{(0)}$. Therefore, the optimality conditions

$$\frac{\mathrm{d}\mathcal{J}}{\mathrm{d}\bar{\mathbf{c}}_{\mathbf{w}}} = 0, \tag{D.11}$$

and

$$\frac{\mathrm{d}\mathcal{J}^{(0)}}{\mathrm{d}\bar{\mathbf{c}}_{\mathbf{w}}^{(\mathbf{0})}} = 0. \tag{D.12}$$

are the solution for the optimisation problem.

The Fréchet differentials of the cost functionals $\mathcal{J}'$ (D.9) and $\mathcal{J}^{(0)}$ (D.10) are now defined as

$$\begin{aligned} \mathcal{J}' &\equiv \lim_{h\to 0} \frac{\mathcal{J}\left(\bar{\mathbf{c}}_{\mathbf{w}} + h\bar{\mathbf{c}}'_{\mathbf{w}}\right) - \mathcal{J}\left(\bar{\mathbf{c}}_{\mathbf{w}}\right)}{h} \\ &\equiv \int_{\bar{x}_i}^{\bar{x}_f} \left(\frac{\mathrm{d}\mathcal{J}\left(\bar{\mathbf{c}}_{\mathbf{w}}\right)}{\mathrm{d}\bar{\mathbf{c}}_{\mathbf{w}}}\right)^H \mathbf{I}\bar{\mathbf{c}}'_{\mathbf{w}}\mathrm{d}\bar{x} \end{aligned}$$

and

$$\begin{aligned} \mathcal{J}^{(0)\prime} &\equiv \lim_{h\to 0} \frac{\mathcal{J}^{(0)}\left(\bar{\mathbf{c}}_{\mathbf{w}}^{(\mathbf{0})} + h\bar{\mathbf{c}}_{\mathbf{w}}^{(\mathbf{0})\prime}\right) - \mathcal{J}^{(0)}\left(\bar{\mathbf{c}}_{\mathbf{w}}^{(\mathbf{0})}\right)}{h} \\ &\equiv \int_{\bar{x}_i}^{\bar{x}_f} \left(\frac{\mathrm{d}\mathcal{J}^{(0)}\left(\bar{\mathbf{c}}_{\mathbf{w}}^{(\mathbf{0})}\right)}{\mathrm{d}\bar{\mathbf{c}}_{\mathbf{w}}^{(\mathbf{0})}}\right)^H \mathbf{I}\bar{\mathbf{c}}_{\mathbf{w}}^{(\mathbf{0})\prime}\mathrm{d}\bar{x} \end{aligned}$$

respectively. Similarly, equation (3.48) is rewritten as

$$\bar{\mathbf{q}}' \equiv \lim_{h\to 0} \frac{\bar{\mathbf{q}}\left(\bar{\mathbf{c}}_{\mathbf{w}} + h\bar{\mathbf{c}}'_{\mathbf{w}}\right) - \bar{\mathbf{q}}\left(\bar{\mathbf{c}}_{\mathbf{w}}\right)}{h},$$

and equation (3.49) as

$$\bar{\mathbf{q}}^{(\mathbf{0})\prime} \equiv \lim_{h\to 0} \frac{\bar{\mathbf{q}}^{(\mathbf{0})}\left(\bar{\mathbf{c}}_{\mathbf{w}}^{(\mathbf{0})} + h\bar{\mathbf{c}}_{\mathbf{w}}^{(\mathbf{0})\prime}\right) - \bar{\mathbf{q}}^{(\mathbf{0})}\left(\bar{\mathbf{c}}_{\mathbf{w}}^{(\mathbf{0})}\right)}{h}.$$

The cost functionals perturbations $\mathcal{J}'$ and $\mathcal{J}^{(0)\prime}$ can be expressed from (D.9) and (D.10) as

$$\mathcal{J}' = \alpha_1\mathcal{J}_1' + \alpha_2\mathcal{J}_2' + \alpha_3\mathcal{J}_3' + \alpha_4\mathcal{J}_4' + \mathcal{J}_u' + \mathcal{J}_v' + \mathcal{J}_w' + \mathcal{J}_\tau' \tag{D.13}$$

and

$$\begin{aligned}\mathcal{J}^{(0)\prime} = \alpha_2^{(0)}\mathcal{J}_2^{(0)\prime} + \alpha_4^{(0)}\mathcal{J}_4^{(0)\prime} \\ + \mathcal{J}_u^{(0)\prime} + \mathcal{J}_v^{(0)\prime} + \mathcal{J}_w^{(0)\prime} + \mathcal{J}_\tau^{(0)\prime},\end{aligned} \tag{D.14}$$

where

$$\mathcal{J}_u' = \theta_u^2 \int_{\bar{x}_i}^{\bar{x}_f} \left(\bar{u}_w^H \mathbf{Q_u} \bar{u}_w'\right) \mathrm{d}\bar{x},$$

$$\mathcal{J}_v' = \theta_v^2 \int_{\bar{x}_i}^{\bar{x}_f} \left(\bar{v}_w^H \mathbf{Q_v} \bar{v}_w'\right) \mathrm{d}\bar{x},$$

$$\mathcal{J}_w' = \theta_w^2 \int_{\bar{x}_i}^{\bar{x}_f} \left(\bar{w}_w^H \mathbf{Q_w} \bar{w}_w'\right) \mathrm{d}\bar{x},$$

$$\mathcal{J}_\tau' = \theta_\tau^2 \int_{\bar{x}_i}^{\bar{x}_f} \left(\bar{\tau}_w^H \mathbf{Q}_\tau \bar{\tau}_w'\right) \mathrm{d}\bar{x},$$

$$\mathcal{J}_u^{(0)\prime} = \theta_u^{(0)2} \int_{\bar{x}_i}^{\bar{x}_f} \left(\bar{u}_w^{(0)H} \mathbf{Q_u^{(0)}} \bar{u}_w^{(0)\prime}\right) \mathrm{d}\bar{x},$$

$$\mathcal{J}_v^{(0)\prime} = \theta_v^{(0)2} \int_{\bar{x}_i}^{\bar{x}_f} \left(\bar{v}_w^{(0)H} \mathbf{Q_v^{(0)}} \bar{v}_w^{(0)\prime}\right) \mathrm{d}\bar{x},$$

$$\mathcal{J}_w^{(0)\prime} = \theta_w^{(0)2} \int_{\bar{x}_i}^{\bar{x}_f} \left(\bar{w}_w^{(0)H} \mathbf{Q_w^{(0)}} \bar{w}_w^{(0)\prime}\right) \mathrm{d}\bar{x},$$

$$\mathcal{J}_\tau^{(0)\prime} = \theta_\tau^{(0)2} \int_{\bar{x}_i}^{\bar{x}_f} \left(\bar{\tau}_w^{(0)H} \mathbf{Q}_\tau^{(0)} \bar{\tau}_w^{(0)\prime}\right) \mathrm{d}\bar{x},$$

and the terms $\mathcal{J}_1'$, $\mathcal{J}_2'$, $\mathcal{J}_3'$, $\mathcal{J}_4'$, $\mathcal{J}_2^{(0)\prime}$, $\mathcal{J}_4^{(0)\prime}$ are obtained from equations (3.42)-(3.47).

The solution of the vectors $\bar{\mathbf{q}}'$ (3.50) and $\bar{\mathbf{q}}^{(\mathbf{0})\prime}$ (3.51) can be obtained from the CLUBR equations (2.64)-(2.68), as it was described by equations (3.52) and (3.53) in the previous chapter, with boundary conditions (3.57) as $\eta \to \infty$ and initial conditions (3.58). The wall boundary conditions necessary to solve the system of equations differs for each vector. For the vector $\bar{\mathbf{q}}'$, the equations (3.54) and (3.56) are modified as shown below

$$\bar{u}' = \alpha_u \bar{u}_w' \quad \text{at} \quad \eta = 0,$$

$$\bar{v}' = \alpha_v \bar{v}'_w \quad \text{at} \quad \eta = 0,$$

$$\bar{w}' = \alpha_w \bar{w}'_w \quad \text{at} \quad \eta = 0,$$

$$\frac{\partial \bar{\tau}'}{\partial \eta} = \alpha_\tau \bar{\tau}'_w \quad \text{at} \quad \eta = 0.$$

Similarly, the vector $\bar{\mathbf{q}}^{(\mathbf{0})\prime}$ is obtained by modifying equations (3.55) and (3.56), as follows

$$\bar{u}^{(0)\prime} = \alpha_u \bar{u}^{(0)\prime}_w \quad \text{at} \quad \eta = 0,$$

$$\bar{v}^{(0)\prime} = \alpha_v \bar{v}^{(0)\prime}_w \quad \text{at} \quad \eta = 0,$$

$$\bar{w}^{(0)\prime} = \alpha_w \bar{w}^{(0)\prime}_w \quad \text{at} \quad \eta = 0,$$

$$\frac{\partial \bar{\tau}^{(0)\prime}}{\partial \eta} = \alpha_\tau \bar{\tau}^{0\prime}_w \quad \text{at} \quad \eta = 0.$$

As shown in the previous chapter, the adjoint identity (3.59) is crucial in obtaining a system of adjoint equations that can be used to rewrite the gradients (D.11) and (D.12) to simpler expressions. The expansion of the adjoint identity (3.59) and the method to obtain the adjoint equation systems is shown in Appendix B.

The procedure is identical and thus, the cost functional perturbation $\mathcal{J}'$ (D.13) is obtained from the b terms (B.2) while considering the boundary conditions (3.54), (3.57), (D.1)-(D.1) and initial conditions (3.58), and also the adjoint boundary (B.7)-(B.8) and terminal (B.9)-(B.11) conditions. This leads to

$$\begin{aligned}\mathcal{J}' = \int_{\bar{x}_i}^{\bar{x}_f} \Bigg[& \alpha_u \left(\frac{1}{2\bar{x}} \frac{\mu}{T} \frac{\partial \bar{r}_x}{\partial \eta} - \frac{1}{\bar{x}} (\gamma - 1) M^2 \frac{\mu F''}{T} \bar{r}_e + \theta_u^2 \mathbf{Q_u} \bar{u}_w \right)^H \bar{u}'_w \\ & + \alpha_v \left(\frac{1}{T} \bar{r}_c + \theta_v^2 \mathbf{Q_v} \bar{v}_w \right)^H \bar{v}'_w + \alpha_w \left(\frac{1}{2\bar{x}} \frac{\mu}{T} \frac{\partial \bar{r}_z}{\partial \eta} + \theta_w^2 \mathbf{Q_w} \bar{w}_w \right)^H \bar{w}'_w \\ & + \alpha_\tau \left(-\frac{1}{2\bar{x}} \frac{\mu}{\mathrm{Pr}\, T} \bar{r}_e + \theta_\tau^2 \mathbf{Q}_\tau \bar{\tau}_w \right)^H \bar{\tau}'_w \Bigg]_{\eta=0} \mathrm{d}\bar{x}. \end{aligned} \tag{D.15}$$

Additionally, the cost functional perturbation $\mathcal{J}^{(0)\prime}$ (D.14) can be expressed from the boundary (3.55), (3.57), (D.1)-(D.1) and initial conditions (3.58), together with the adjoint boundary (B.15)-(B.16) and terminal (B.17)-(B.19) conditions,

yielding

$$\begin{aligned}\mathcal{J}^{(0)\prime} = \int_{\bar{x}_i}^{\bar{x}_f} \Bigg[& \alpha_u \left(\frac{1}{2\bar{x}} \frac{\mu}{T} \frac{\partial \bar{r}_x}{\partial \eta} - \frac{1}{\bar{x}} (\gamma - 1) M^2 \frac{\mu F''}{T} \bar{r}_e \right. \\ & \left. + \theta_u^{(0)2} \mathbf{Q}_{\mathbf{u}}^{(\mathbf{0})} \bar{u}_w^{(0)} \right)^H \bar{u}_w^{(0)\prime} \\ & + \alpha_v \left(\frac{1}{T} \bar{r}_c + \theta_v^{(0)2} \mathbf{Q}_{\mathbf{v}}^{(\mathbf{0})} \bar{v}_w^{(0)} \right)^H \bar{v}_w^{(0)\prime} \\ & + \alpha_w \left(\frac{1}{2\bar{x}} \frac{\mu}{T} \frac{\partial \bar{r}_z}{\partial \eta} + \theta_w^{(0)2} \mathbf{Q}_{\mathbf{w}}^{(\mathbf{0})} \bar{w}_w^{(0)} \right)^H \bar{w}_w^{(0)\prime} \\ & + \alpha_\tau \left(-\frac{1}{2\bar{x}} \frac{\mu}{\mathrm{Pr}\, T} \bar{r}_e + \theta_\tau^{(0)2} \mathbf{Q}_\tau^{(\mathbf{0})} \bar{\tau}_w^{(0)} \right)^H \bar{\tau}_w^{(0)\prime} \Bigg]_{\eta=0} \mathrm{d}\bar{x}. \end{aligned} \tag{D.16}$$

The Fréchet differential definition (D.1) is used to extract the gradient (D.11) from the cost functional perturbation $\mathcal{J}'$ (D.15), as follows

$$\frac{\mathrm{d}\mathcal{J}}{\mathrm{d}\bar{\mathbf{c}}_{\mathbf{w}}} = \begin{bmatrix} \alpha_u \left[\frac{1}{2\bar{x}} \frac{\mu}{T} \frac{\partial \bar{r}_x}{\partial \eta} - \frac{1}{\bar{x}} (\gamma - 1) M^2 \frac{\mu F''}{T} \bar{r}_e + \theta_u^2 \mathbf{Q}_{\mathbf{u}} \bar{u}_w \right]_{\eta=0} \\ \alpha_v \left[\frac{1}{T} \bar{r}_c + \theta_v^2 \mathbf{Q}_{\mathbf{v}} \bar{v}_w \right]_{\eta=0} \\ \alpha_w \left[\frac{1}{2\bar{x}} \frac{\mu}{T} \frac{\partial \bar{r}_z}{\partial \eta} + \theta_w^2 \mathbf{Q}_{\mathbf{w}} \bar{w}_w \right]_{\eta=0} \\ \alpha_\tau \left[-\frac{1}{2\bar{x}} \frac{\mu}{\mathrm{Pr}\, T} \bar{r}_e + \theta_\tau^2 \mathbf{Q}_\tau \bar{\tau}_w \right]_{\eta=0} \end{bmatrix}^T . \tag{D.17}$$

The solutions of $\bar{r}_c$, $\bar{r}_x$, $\bar{r}_z$ and $\bar{r}_e$ are obtained from solving the adjoint equations (3.64)-(3.67) with boundary conditions (B.7) and (B.8), and terminal conditions (B.9)-(B.11).

Correspondingly, the gradient (D.12) is extracted from the cost functional perturbation $\mathcal{J}^{(0)\prime}$ (D.16) using the definition (D.1), resulting in

$$\frac{\mathrm{d}\mathcal{J}^{(0)}}{\mathrm{d}\bar{\mathbf{c}}_{\mathbf{w}}^{(\mathbf{0})}} = \begin{bmatrix} \alpha_u \left[\frac{1}{2\bar{x}} \frac{\mu}{T} \frac{\partial \bar{r}_x}{\partial \eta} - \frac{1}{\bar{x}} (\gamma - 1) M^2 \frac{\mu F''}{T} \bar{r}_e + \theta_u^{(0)2} \mathbf{Q}_{\mathbf{u}}^{(\mathbf{0})} \bar{u}_w^{(0)} \right]_{\eta=0} \\ \alpha_v \left[\frac{1}{T} \bar{r}_c + \theta_v^{(0)2} \mathbf{Q}_{\mathbf{v}}^{(\mathbf{0})} \bar{v}_w^{(0)} \right]_{\eta=0} \\ \alpha_w \left[\frac{1}{2\bar{x}} \frac{\mu}{T} \frac{\partial \bar{r}_z}{\partial \eta} + \theta_w^{(0)2} \mathbf{Q}_{\mathbf{w}}^{(\mathbf{0})} \bar{w}_w^{(0)} \right]_{\eta=0} \\ \alpha_\tau \left[-\frac{1}{2\bar{x}} \frac{\mu}{\mathrm{Pr}\, T} \bar{r}_e + \theta_\tau^{(0)2} \mathbf{Q}_\tau^{(\mathbf{0})} \bar{\tau}_w^{(0)} \right]_{\eta=0} \end{bmatrix}^T . \tag{D.18}$$

For the gradient (D.18), the solutions $\bar{r}_c$, $\bar{r}_x$, $\bar{r}_z$ and $\bar{r}_e$ are derived from the adjoint equations (3.68)-(3.72) with boundary conditions (B.15) and (B.16), and terminal conditions (B.17)-(B.19).

As in the previous chapter, the controls $\bar{\mathbf{c}}_{\mathbf{w}}$ and $\bar{\mathbf{c}}_{\mathbf{w}}^{(\mathbf{0})}$ are obtained independently, and can be summed using the decomposition (2.55), such that

$$\begin{bmatrix} \bar{u}_0 \\ \bar{v}_0 \\ \bar{w}_0 \\ \frac{\partial \bar{\tau}_0}{\partial \eta} \end{bmatrix} = C^{(0)} \begin{bmatrix} \alpha_u \bar{u}_w^{(0)} \\ \alpha_v \bar{v}_w^{(0)} \\ -\alpha_w \frac{ik_x}{k_z} \bar{w}_w^{(0)} \\ \alpha_\tau \bar{\tau}_w^{(0)} \end{bmatrix} + C \begin{bmatrix} \alpha_u \frac{ik_z}{k_x} \bar{u}_w \\ \alpha_v \frac{ik_z}{k_x} \bar{v}_w \\ \alpha_w \bar{w}_w \\ \alpha_\tau \frac{ik_z}{k_x} \bar{\tau}_w \end{bmatrix} \quad \text{at} \quad \eta = 0.$$